CVD growth of pristine and N-doped graphene films for support of platinum and palladium nanoparticles in electrochemical sensing of dopamine and uric acid

By

Boitumelo Joyce Matsoso

Student Number: 823248

A thesis submitted to the Faculty of Science, University of the Witwatersrand, Johannesburg, in fulfilment of the requirements for degree of

Doctor of Philosophy in Chemistry

Supervisor: Prof Neil J. Coville

Co-Supervisors: Dr Tsenolo Lerotholi

Dr Glenn Jones

Johannesburg, November 2017

DECLARATION

I declare that this thesis is my own, and unaided work under the supervision of Professor Neil J. Coville, Doctor Tsenolo Lerotholi, and Doctor Glenn Jones (Johnson Matthey), as well as under the mentorship of Doctor Kamalakannan Ranganathan (Postdoctoral fellow). It is being submitted for the degree of Doctor of Philosophy at the University of the Witwatersrand, Johannesburg. It has not been submitted for any degree or examination in any other university.

(Signed) **Boitumelo Matsoso**

On this 6th day of November 2017

ABSTRACT

The synthesis of large-area graphene and nitrogen doped graphene films by atmospheric pressure chemical vapour deposition (APCVD), for application in electrochemical sensors provides a new platform for developing inexpensive techniques for selective and ultrasensitive detection of electroactive biomolecules. Therefore, optimum growth condition for the synthesis of good quality bilayered graphene films by APCVD technique on a Cu catalyst was developed (10 minutes growth time; 10 sccm of methane). The quality and thickness of the as-synthesized graphene films was further improved by using 3 sccm of hydrogen gas throughout the annealing and growth process. Doping of graphene with nitrogen atoms has been reported to be the most promising technique for modulating the structural and electrochemical properties of as-grown graphene films. A synthesis method for growing nitrogen doped graphene films with high nitrogen content was obtained by in-situ route using 5 sccm of ammonia. Furthermore, both overall nitrogen content (N/C) and configurations in N-doped graphene films were controlled by varying the growth times (i.e. 2, 5, 10, and 20 min). The results indicated that short growth time (2 min) led to N-graphene films that are rich in pyridinic-N and highest N/C value (4.68 %), while longer growth time (20 min) resulted in formation of graphitic-N rich films with N/C value of 2.84 %. Electrocatalytic activity of pristine and N-doped graphene films as well as pristine and N-graphene-platinum and palladium composites were investigated towards oxidation of dopamine and uric acid. Nitrogen doped based and metal-composite based electrochemical sensors showed better electrocatalytic activity and sensitivity compared to their undoped counterparts. Apart from single atom doping graphene with nitrogen atoms, co-doping with boron and nitrogen atoms was investigated for formation of semiconducting hybrid materials with tunable optical properties. By adjusting the flow rates of methane and the vaporization temperature of boric acid, two types of graphene and hexagonal boron nitride (*h*-BN) hybrid films were formed. This included novel crystalline hexagonal boron nitride (*h*-BN) quantum- and nanodots embedded in large-area boron carbon nitride (BCN) films and the atomically thin and quaternary semiconducting hybrid films of boron carbon oxynitride (BCNO).

DEDICATION

I would like to dedicate this thesis to;

My father: Lefu Paul, for playing both father and mother to me for over a decade. His outmost trust, love and motivation inspired me to give my very best in everything I do.

My late mother: Mabohlale Jerminah, for the love of science she instilled in me from a very young age.

My siblings: Bohlale and Litseoane, for their prayers, immense support and encouragement.

My niece and nephew: Mantsho and Tlhohonolofatso, for showing me that without having fun, research in total would have no course.

ACKNOWLEDGEMENTS

First and foremost, I would like to thank the Almighty God for giving me the courage, strength and His endless Grace to accomplish this task. I would like to extend my sincere gratitude to my supervisor Professor Neil J. Coville for his outstanding contribution, support and guidance to the success of this research. His prowess and research expertise were of great significance to my skills and am greatly indebted to him as my mentor.

I would like to express my great appreciation to my co-supervisors Dr. Tsenolo Lerotholi and Dr. Glenn Jones for their guidance and great support in accomplishing this task.

I would like to sincerely thank my mentor Dr. Kamalakannan Ranganathan for his support and fruitful discussions in this work. I am greatly indebted to Dr. Bridget Mutuma for her contribution, support and positive criticism throughout this research project.

My sincere gratitude to Ms Joyce Gama and Mr Thuthuka Mabaso, the third year undergraduate laboratory superintends, for their assistance with any tiny bit of equipment and reagent that were required for immediate use in my research. Further sincere gratitude goes to Dr. Riho Green, Dr. Richard Smith, and D Tugce Eralp-Erden at the Johnson Matthey Technology Center in Sonning Common in Reading, UK for assistance with the XPS analysis and data interpretation. Their inputs into this research helped to bridge the scientific knowledge, thus making the research study into novelty.

This research would not be complete without the research facilities provided by the technical support and training by the Microscopy and Microanalysis unit at the University of Witwatersrand. Special thanks to Prof. Alexander Ziegler, Dr. Deran Reddy, Dr. Manoko Maubane, Dr. Zikhona Tetana, Mr Jacques Gerber and Mrs Tutuzwa Zuma for their patience and help. Finally, the research could not have been completed without the help of Dr Caren Billing, who opened her electrochemistry facility to us for usage

To Ms Amanda Morgan, Mrs Colleen Coutts, Ms Khwezi Ndawonde, Ms Sadiya Ooni, and the late Mrs Agnes Pointeer, your great assistance in accommodation and travel arrangements during the course of my studies, have helped me to sow the rest of the scientific world the great job we are doing here at University of Witwatersrand. With the early check-ins at the

airport, although painstakingly long, I have never missed a flight, and I am very grateful for that.

To the Catalysis and Materials (CATOMAT) and Carbon Solar cells and Sensors (CSS) group members, your positive criticism and valuable suggestions have encouraged me to work hard as well as to always give my best at everything I do. I also thank Ms Mulweli Nthathe, whom I co-supervised in her honour's project. The work done we did with her has contributed a lot to this thesis.

In addition to the PhD Postgraduate Merit Award (University of the Witwatersrand) and DST-NRF Centre of Excellence in Strong Materials, this research work would not have been possible without the major financial assistance from Johnson Matthey Research Center in Pretoria.

PUBLICATIONS, AWARDS, PRESENTATIONS AND MEMBERSHIPS

Publications related to this work

- **Boitumelo Matsoso**, Kamalakannan Ranganathan, Bridget K. Mutuma, Tsenolo Lerotholi, Glenn Jones, Neil J Coville "Time-dependent evolution of the nitrogen configuration in N-doped graphene films", *RSC Adv.*, **2016,** *6,* 106914-106920.

- **Boitumelo Matsoso,** Kamalakannan Ranganathan, Bridget K. Mutuma, Tsenolo Lerotholi, Glenn Jones and Neil J Coville "Single-step synthesis of crystalline h-BN quantum-and nanodots embedded in boron carbon nitride films", *Nanotechnology*, **2017***, 28,* 105602.

- **Boitumelo Matsoso,** Kamalakannan Ranganathan, Bridget K. Mutuma, Tsenolo Lerotholi, Glenn Jones, Neil J Coville "Synthesis and XPS characterization of BCNO films by atmospheric pressure CVD", *New Journal of Chemistry,* **2017,** *41*,9497-9504.

- **Boitumelo Matsoso**, Kamalakannan Ranganathan, Bridget K. Mutuma, Tsenolo Lerotholi, Glenn Jones, Neil J Coville "The effect of N-configurations on the detection of dopamine on N-graphene/ITO electrodes", *Analyst,* **2017,** *under review.*

- **Boitumelo Matsoso**, Kamalakannan Ranganathan, Bridget K. Mutuma, Tsenolo Lerotholi, Glenn Jones, Neil J Coville "Electrochemical behaviour and detection of uric acid at indium tin oxide-coated glass electrode modified with N-doped graphene containing different N-configurations", *to be submitted.*

Publications arising from collaborations

- Bridget K. Mutuma, **Boitumelo Matsoso**, Kamalakannan Ranganathan, Daniel Wamwangi, Neil J Coville "Generation of open ended, worm like and graphene like structures from layered spherical carbon materials", *RSC Adv.*, **2016,** *6,* 20399-20408.

- Bridget K. Mutuma, Rafael Rodrigues, Kamalakannan Ranganathan, **Boitumelo Matsoso**, Daniel Wamwangi, Ivo A. Hümmelgen and Neil J. Coville "Hollow carbon spheres and hollow carbon sphere/polyvinylpyrrolidone composite as ammonia sensors", *J. Mater. Chem. A*, **2017**, *5*, 2539-2549.

- Bridget K. Mutuma, Rafael Rodrigues, Kamalakannan Ranganathan, **Boitumelo J Matsoso**, Daniel Wamwangi, Ivo A. Hümmelgen and Neil J. Coville "Hollow carbon spheres and hollow carbon sphere/polyvinylpyrrolidone composite as ammonia sensors", *J. Mater. Chem. A*, **2017**, 5, 2539-2549. **(Inside cover page)**

- Bridget K. Mutuma, **Boitumelo J Matsoso**, Kamalakannan Ranganathan, Jonathan Keartland, Daniel Wamwangi and Neil J Coville "Generation of radical species in CVD grown pristine and N-doped solid carbon spheres using H_2 and Ar as carrier gases", *RSC Adv.*, **2017**, *7*,21187-21195.

- George Chimowa, **Boitumelo J. Matsoso**, Neil Coville, Suprakas Sinha Ray and Bonex Mwakikunga "Understanding the selective adsorption of NH_3 on MWCNTs defect sites investigated using Raman Spectroscopy", *Physica Status Solidi A: Applications and Materials Science,* **2017,** 1600930 (1-7).

- Amos, A. Akande., Augusto, G. J. Machatine, Bathusile, N. Masina, George, Chimowa, **Boitumelo, J. Matsoso**, Roro Kittessa, Mart-Mari Duvenage, Hendrik Swart, Suprakas, S. Ray and Bonex, W. Mwakikunga "Blue- and red-shifts of V_2O_5 phonons in NH_3 environment by in-situ Raman spectroscopy", *Journal of Physics D: Applied Physics,* **2017, accepted**.

- Ibrahim, B. Usman, **Boitumelo J. Matsoso**, Lesias Kotane, Kamalakannan Ranganathan, Deena Naidoo, Neil, J. Coville, and Daniel Wamwangi "Synthesis and magnetic properties of aligned nitrogen-doped multi-walled carbon nanotubes", *Journal of Materials Chemistry and Physics*, **2017,** *under review*.

- Ibrahim, B. Usman, **Boitumelo J. Matsoso**, Lesias Kotane, Deena Naidoo, Kamalakannan Ranganathan, Neil, J. Coville, and Daniel Wamwangi "Synthesis of carbon-doped GaN nanostructures for application in room temperature gas sensors", **(to be submitted)**.

- Bridget K. Mutuma, Rafael Rodrigues, Kamalakannan Ranganathan, **Boitumelo J Matsoso**, Daniel Wamwangi, Ivo A. Hümmelgen and Neil J. Coville "Synthesis and characterization of N-HCSs for application in gas sensors", **(to be submitted)**.

- Bridget K. Mutuma, **Boitumelo Matsoso**, Kamalakannan Ranganathan, Daniel Wamwangi, Neil J Coville "Synthesis of asymmetric gold nanostructures and their application in hole transport layer of organic solar cells", **(to be submitted)**.

- **Boitumelo J Matsoso**, Lebogang Mosiane, Thomas Mongwe, Bridget K. Mutuma, Neil J. Coville, Manoko Maubane "Synthesis of boron and nitrogen codoped carbon nanotubes with tunable optical properties using urea and boric acid", **(to be submitted)**.

Awards

- **October 2017 –** 2nd Best PhD Oral Presentation Award (SANi- NYRS)
- **November 2016-** Best National Spectroscopy Presenter Award (SASS Symposium)
- **April 2016 -** 2nd Best PhD Poster Presentation Award (SANi- NanoAfrica)
- **March 2016 -** Postgraduate International Travel Grant (Wits University)
- **February 2016 -** Graphene 2016 Conference Student Travel Grant (Phantoms Foundations, Spain)
- **February 2015- December 2017-** PhD Postgraduate Merit Award (Wits University)
- **November 2014-** Best Poster presentation, SASS Raman Workshop

Conferences and Workshops

Oral presentations

1. "Electrochemical detection of paracetamol using pristine and N-doped graphene-modified ITO electrodes" Catalysis Society of South Africa 28th Annual Conference, Limpopo, South Africa, 19th-22nd November 2017.
2. "Electrochemical detection of paracetamol on ITO electrodes modified with pristine and N-doped graphene films", SANi National Young Researchers Symposium, Tshwanr Univesity off Technology, Pretoria, 21st October 2017.
3. "Role of N-configurations towards dopamine detection on N-doped graphene/ITO electrodes" Johnson Matthey Annual Conference, Loughborough, UK, 11th-12th April 2017.
4. "Time-dependent evolution of the nitrogen configurations in N-doped graphene" SASS Young Spectroscopist Symposium, Perkin Elmer Building, Midrand, South Africa, 15th November 2016.
5. "Electrochemical detection of paracetamol using pristine and N-doped graphene-modified ITO electrodes" Catalysis Society of South Africa 27th Annual Conference, Drakensburg Lodge, Kwazulu Natal, South Africa, 6th-9th November 2016.
6. "Time-dependent evolution of the nitrogen configurations in N-doped graphene" Johnson Matthey Academic Day, CSIR, Pretoria, South Africa, 27th October 2016.
7. "Defect-controlled synthesis of N-doped graphene films using co-growth of methane and ammonia" Wits-Sasol Academic Day, Wits University, Johannesburg, South Africa, 8th May 2016.
8. "Synthesis of *h*-BN quantum- and nanodots embedded-BCN hybrid films by APCVD" Sasol-Wits Academic Day, Sasol, Johannesburg, South Africa,12th August 2016.
9. "A facile route for the incorporation of *h*-BN nanodots in carbon films using APCVD method" Johnson Matthey Academic Day, CSIR, Pretoria, South Africa, 13th November 2015.
10. "Towards carbon supported nanoparticles: Strategies for synthesizing N-doped graphene supports" Johnson Matthey Annual Student meeting at CSIR 6th November 2014.

Poster presentations

1. "Synthesis of N-doped graphene for Organic Photovoltaic Cells Application" DST-NRF Centre of Excellence in Strong Materials, Wits University, Johannesburg, South Africa, 26th May 2016.
2. "Synthesis of *h*-BN quantum- and nano-dots embedded-BCN hybrid films by APCVD" 6th European conference & exhibition in Graphene and 2D materials, Genova, Italy, 19th-22nd April 2016.
3. "Synthesis of BN-doped graphene for transparent conducting electrode applications in organic photovoltaics (OPV's)" 6th International conference on Nanoscience & Nanotechonolgy (NanoAfrica), UNISA, Florida, South Africa, 6th – 8th April 2016.
4. "A facile method for supporting highly-dispersed, small size platinum nanoparticles on N-doped graphene films" 7th Cross Faculty Symposium, Wits University, Johannesburg, South Africa, 1st-2nd March 2016.
5. "A facile route for the incorporation of *h*-BN nanodots in carbon films using APCVD" Catalysis Society of South Africa 26th Annual Conference, Cape Town, South Africa, 15th-17th November 2015.
6. "Strategies of synthesizing N and BN doped graphene for catalytic nanoparticles support" Johnson Matthey Annual Conference, Loughborough, UK, 8th-9th April 2015.
7. "Synthesis of BN-doped graphene for transparent conducting electrode applications in organic photovoltaic cells (OPVs)" South African Raman Workshop, Wits University, Johannesburg, South Africa, 24th-25th November 2014.
8. "Synthesis of N-doped graphene for Organic Photovoltaic Cells Application" Catalysis Society of South Africa 25th Annual Conference hosted by WITS University 9th-12th November 2014
9. "CVD synthesis and DFT studies of Pt, Pd, and Pt/Pd nanoparticles supported on graphene and N-doped graphene" 5th International conference on Nanoscience & Nanotechonolgy at VUT 30th March- 2nd April 2014

Workshops

1. Postgraduate electrochemistry workshop and training, University of Cape Town, Cape Town, South Africa, 19th-25th November 2016.
2. 3rd International Workshop on "Nano Carbon", Wits University, Johannesburg, South Africa, 14th-15th January 2016.

3. Paper writing retreat at Pullen Farm (Wits University), Mpumalanga, South Africa, 5th-10th July 2015.
4. 3rd African School on 'Electron Structure Methods and Applications', Wits University, Johannesburg, south Africa, 19th -30th January 2015.
5. 2nd International Workshop on "Nano Carbon", Wits University, Johannesburg, South Africa, 15th-16th January 2015.
6. South African Raman Workshop, Wits University, Johannesburg, South Africa, 24th-25th November 2014.
7. Southern African Powder Diffraction Conference and Workshop, Wits University, Johannesburg, South Africa, 27th-31st January 2014.
8. International Workshop on "Nano Carbon", Wits University, Johannesburg, South Africa, 21st-22nd November 2013.

Memberships

- Spectroscopy Society of South Africa **(SASS)** - January 2015- present.
- South African Chemistry Institute **(SACI)** - July 2013 – present.
- South African Nanotechnology Initiative **(SANi)** – January 2014 – present.
- Catalysis Society of South Africa **(CATSA)** – January 2014 – present.
- Chemical Society **(ChemSoc), Wits University** – January 2014 – present.
- South African Electrochemistry Society **(SAES)** – June 2017 - present.

TABLE OF CONTENTS

Chapter 3: Optimizing the growth of graphene films on a Cu catalyst using atmospheric pressure CVD

Supplementary Information

LIST OF FIGURES

Chapter 2

Chapter 3

Chapter 4

Chapter 5

Chapter 6

Chapter 7

Chapter 8

Chapter 9

Chapter 10

C**hapter 11**

Supplementary Information

Appendix A

Appendix B

Appendix C

Appendix D

Appendix E

LIST OF TABLES

Chapter 7

Chapter 9

Chapter 10

Chapter 11

Appendix

ABBREVIATIONS

The following is the list of abbreviations as they appear in the thesis:

Chemical vapour deposition (CVD)

Atmospheric pressure Chemical vapour deposition (APCVD)

Poly (methyl methacrylate) (PMMA)

Standard cubic centimetres (sccm)

Transmission electron microscopy (TEM)

Atomic force microscopy (AFM)

Scanning electron microscopy (SEM)

X-ray photoelectron spectroscopy (XPS)

High resolution Transmission electron microscopy (HRTEM)

Hexagonal boron nitride (*h*-BN)

Ultraviolet visible spectroscopy (UV-Vis)

Boron carbon nitride (BCN)

Boron carbon oxynitride (BCNO)

Indium doped tin oxide (ITO)

Cyclic voltammetry (CV)

Differential pulse voltammetry (DPV)

Graphene (Gr)

Nitrogen doped graphene (NGr)

Dopamine (DA)

Uric acid (UA)

Platinum (Pt)

Palladium (Pd)

Anodic peak potential (Epa)

Cathodic peak potential (Epc)

Anodic peak current (Ipa)

Cathodic peak current (Ipc)

Chapter 1

Synopsis

1.1 Motivation of the study

Carbon based nanomaterials continue to receive tremendous interest due to their unique electrical, mechanical, physiochemical, and optical properties. Owing to the abundance of carbon, their low cost and a wide range of techniques available for synthesizing and tuning the properties of carbon-based nanomaterials, these materials have found diverse application in fields such as chemical, gas and biosensors[1-4], supercapacitors[5], fuel cells[6, 7], batteries[8] and catalysis[9]. Based on their dimensionalities, carbon-based nanomaterials can be synthesized in the form of fullerenes, carbon nanotubes (CNTs), graphene and its derivatives, as well as graphite; which represent the zero (0D)-, one (1D)-, two (2D)-, three-dimensional (3D) forms of carbon nanomaterials, respectively. Among the various dimensionalities of carbon nanomaterials, the 2D forms, especially graphene and its derivatives, have recently gained more attention in comparison with other carbon forms due to the ability of forming, at industrial scale, large area films with a high surface-to-volume ratio and excellent electrical and thermal conductivity properties [3, 10, 11]. These properties have made graphene and its derivatives very attractive and interesting materials in the nano- and microelectronic device industries, where the fabrication of robust devices, without compromising their properties and performance, is of enormous industrial importance. Consequently, graphene and its derivatives have application in the fabrication of nano- and microelectronic devices such as field effect transistors (FET) [12], chemical and biological sensors [1-4], bioimaging probes[13], dye sensitized solar cells[14], transparent conductive films for flexible electronics [15], ultra- and supercapacitors [5, 16], and graphene-polymer nanocomposites [17].

Even though graphene, an atomic thick sheet of sp^2 hybridized carbon atoms chemically bonded in the hexagonal pattern [10-12], is considered as a "*wonder material*" to the scientific community, several issues still hinder the widespread application of graphene in different fields. For instance, by definition, graphene is a chemically inert carbon nanomaterial, thus making it a very poor candidate to be employed in fields such as chemical, gas and biosensors[1-4], fuel cells[6, 7], and catalysis[9]. As a result, numerous synthesis techniques to chemically activate graphene nanostructures have been proposed including the graphitization

of SiC substrates[18], chemical reduction of graphene oxide[19], liquid exfoliation of graphite[20], and unzipping of CNTs[21]. Unfortunately, most of these methods suffer a major drawback as they fail to address critical issues such as the growth of graphene nanostructures with controlled thickness and grain size, stacking order of the layers of graphene, as well as the defect concentration. The abovementioned issues are very important as they govern various properties which enable the applicability of graphene. These include issues such as graphene's ability to homogeneously disperse and stabilize metal nanoparticles for application in catalysis and fuel cells; as well as its biocompatibility and electrochemical stability for use in chemical and biosensors.

On the other hand, catalytic chemical vapour deposition (CVD) techniques using transition metals and their alloys have been shown to be the most promising and reproducible approach for solving these critical issues [22-25]. More specifically, CVD techniques offer the ability of synthesizing industrial-scale graphene films with perfect reproducibility from gaseous, liquid or solid carbon sources. Furthermore, varying the reaction conditions for a typical CVD reactors offer the advantages of controlling the quality/defect concentration, thickness/morphology and stacking order of the graphene films. Additionally, CVD offers the ability to tune the physiochemical and optical properties of graphene via heteroatom doping with single element (N, B, S, and P) or bi-elements (N and B, or N and S) [26-30]; with N-doping receiving great attention due to its comparable atomic size of nitrogen (d_N = 70 pm) with carbon (d_C = 65 pm). Moreover, N-doping provides several advantages such as efficiently introducing chemically active sites for use in catalytic reactions, increasing biocompatibility as well as increasing anchoring sites for metal nanoparticle deposition and binding for active biomolecules [1-4]. *Thus, from this study we seek address the following questions: is it possible to control the incorporation of nitrogen atoms into the graphene lattice? How will the presence of nitrogen atoms impact the electrocatalytic activity of graphene during the detection of biomolecules? By using the electroless deposition method, can we homogeneously disperse metal nanoparticles on CVD-grown high quality graphene as well as nitrogen containing graphene films? What is the influence of metal nanoparticles and nitrogen atoms on the electrocatalytic activity of graphene for detection of biomolecules?*

1.2 Aims and objectives

The use of graphene in various electrochemical devices is very interesting; however, the use of monolayered, high quality graphene is still a necessity in many practical applications. Furthermore, in order for graphene to reach its potential applications, its electronic properties

must be improved by doping with heteroatoms. Thus, the focus of this study was to elucidate the following issues:

1. Study the optimum conditions for the synthesis of graphene films on a copper catalyst/foil by the atmospheric pressure chemical vapour deposition (APCVD) technique. The effect of varying the growth time and the methane gas flow rates on the thickness and quality of the as-grown graphene films will be investigated.

2. Investigate the influence of a reducing environment on the quality of graphene films grown at the optimised conditions. In particular, the focus will be on the effect of different flow rates of hydrogen gas at various growth stages on the quality of the as-grown graphene films.

3. Study the optimum conditions for growth of nitrogen doped graphene films using the APCVD system, and ammonia and methane gases as precursors for nitrogen and carbon atoms. The influence of varying the ammonia flow rate as well as the method of introducing ammonia into the reaction chamber on the overall nitrogen content will be studied. In addition, at optimized ammonia flow rates, the role of growth time on the type of nitrogen bonding states as well as on the overall nitrogen content will be investigated.

4. Study the influence of structural and electronic properties of graphene towards the electrochemical oxidation of biomolecules. Using pristine and N-doped graphene films grown at optimum conditions, electrochemical sensors composed of an ITO working electrode modified with pristine and N-doped graphene films will be fabricated and these will be applied for the electrochemical detection of dopamine and uric acid. Moreover, the role of different nitrogen configurations on the electrochemical performance of N-doped graphene-based ITO sensors will be investigated.

5. Study the ability of graphene and N-doped graphene films on supporting metal nanoparticles. The focus will be on the effect of the structural properties of pristine and N-doped graphene films on the stabilization and dispersion of platinum and palladium nanoparticles. Finally, the performances of ITO-based electrochemical

sensors, fabricated from composites of platinum and palladium nanoparticles on pristine and/or N-doped graphene films, towards the electrochemical oxidation of dopamine and uric acid will be investigated.

6. Investigate conditions for growing two dimensional (2D) hybrid films of graphene by studying the role of co-doping graphene with both nitrogen and boron atoms. This study will concentrate on the synthesis and characterization of hybrid films such as boron carbonitride (BCN) and boron carbon oxynitride (BCNO). The main focus will be on investigating the effect of varying the flow rate of methane gas as well as changing the vaporization temperatures of boric acid (boron source) on the atomic composition of the 2D-hybrid films.

1.3 Organization of the thesis

This thesis is written as a compilation of both fundamental experimental studies and published articles. Some of the articles have been published; others are in press or under review, and others are at the preparation phase.

Chapter 1 gives the motivation of the study, as well as the aims and objectives of this thesis.

Chapter 2 presents a background on graphene films, their doping with nitrogen atoms and with both nitrogen and boron atoms. Their ability to function as a nanoparticle support as well as their application in electrochemical sensors is also discussed.

Chapter 3 focuses on optimizing the growth conditions for formation of graphene films via the atmospheric pressure chemical vapour deposition (APCVD) technique on a copper catalyst.

Chapter 4 presents the study performed to investigate the role of hydrogen on the quality of graphene films.

Chapter 5 presents an extensive study on optimizing the conditions for incorporation of nitrogen atoms into the graphene lattice, focusing mainly on in-situ versus post doping processes.

Chapter 6 presents a study performed to investigate the electrochemical behaviour of dopamine and uric acid on pristine and N-doped graphene-ITO electrodes.

Chapter 7 focuses on the use of Pt and Pd supported nanoparticles for the electrochemical detection of dopamine and uric acid on ITO-modified electrodes.

Chapter 8 focuses on the evolution of nitrogen configurations in N-doped graphene films with time. *This chapter was published: Boitumelo J Matsoso, Kamalakannan Ranganathan,*

Bridget K. Mutuma, Tsenolo Lerotholi, Glenn Jones, Neil J Coville "Time-dependent evolution of the nitrogen configuration in N-doped graphene films", ***RSC Adv., 2016, 6, 106914-106920.***

Chapter 9 presents an extensive study on evaluating the effect of nitrogen configurations towards the detection of dopamine on ITO electrode modified with N-doped graphene films. *This chapter is to be submitted: Boitumelo J Matsoso, Kamalakannan Ranganathan, Bridget K. Mutuma, Caren Billing, Tsenolo Lerotholi, Glenn Jones, Neil J Coville "The effect of N-configurations on the detection of dopamine on N-graphene modified ITO electrodes",* ***Analyst, under review****.*

Chapter 10 reports on co-doping of graphene with both boron and nitrogen atoms in order to grow new materials. *The chapter was published: Boitumelo J Matsoso, Kamalakannan Ranganathan, Bridget K. Mutuma, Tsenolo Lerotholi, Glenn Jones, Neil J Coville "Single-step synthesis of crystalline h-BN quantum-and nanodots embedded in boron carbon nitride films",* ***Nanotechnology, 2017, 28, 105602 (1-11).***

Chapter 11 presents an extensive XPS study on co-doping of graphene with boron and nitrogen atom so as to grow new quaternary BCNO materials. *The chapter been accepted for publications: Boitumelo J Matsoso, Kamalakannan Ranganathan, Bridget K. Mutuma, Tsenolo Lerotholi, Glenn Jones, Neil J Coville "Synthesis and XPS characterization of BCNO films by atmospheric pressure CVD",* ***New Journal of Chemistry, 2017, 41,9497-9504.***

Chapter 12 gives the general conclusions and future prospects that originated from the study.

References

1. Manzetti, S., D.Vasilache, E. Francesco. *Advances in Manufacturing,* **2015,** *3*, 63-72.
2. Mutuma, B. K., R. Rodrigues, K. Ranganathan, B. J. Matsoso, D. Wamwangi, I. A. Hümmelgen, N. J. Coville. *J. Mater. Chem. A*, **2017**, *5*, 2539-2549.
3. Pumera, M., A. Ambrosi, A. Bonanni, E. L. K. Cheng, H. L. Poh. *TrAC, Trends Anal. Chem.*, **2010**, *29*, 954.
4. Brownson, D. A. C., D. K. Kampouris, C. E. Banks. *Chem. Soc. Rev.*, **2012**, *41*, 6944.
5. Wang, Q., J. Yan, Y. Wang, G. Ning, Z. Fan, T. Wei, J. Cheng, M. Zhang, X. Jing. *Carbon,* **2013,** *52*, 209-218.
6. Jackson, C., O. Conrad, P. Levecque. *Electrocatalysis,* **2017,** 1-11.
7. Antolini, E. *Appl. Cat. B.: Environ.* **2009**, *88*, 1-24.

8. Tang, K., L. Fu, R. J. White, L. Yu, M. M. Titirici, M. Antonietti, J. Maier. *Advanced Energy Materials*, **2012,** *2*, 873-877.
9. Phaahlamohlakia, T. N, D. O. Kumi, M. W. Dlamini, L. L. Jewell, N. J. Coville. *Catalysis Today*, **2016**,*275*, 76-83.
10. Geim, A. K. *Science*, **2009**, *324*, 1530–1534.
11. Geim, A.K., K. S. Novoselov, S. Morozov, D. Jiang, M. I. Katsnelson, S. Dubonos, I. Grigorieva, A. Firsov. *Nature*, **2005**, *438*, 197-200.
12. Novoselov, K. S., A. K. Geim, S. V. Morozov, D. Jiang, Y. Zhang, S. V. Dubonos, I. V. Grigorieva, A. A. Firsov. *Science*, **2004**, *306*, 666−669.
13. Dong, H., W. Gao, F. Yan, H. Ji, H. Ju. *Analytical Chemistry*, **2010,** *82*, 5511-5517.
14. Kavan, L., J. H. Yum, M. Grätzel. *ACS Nano*, **2011,** *5*, 165-172.
15. Kim, K. S., Y. Zhao, H. Jang, S. Y. Lee, J. M. Kim, K. S. Kim, J. H. Ahn, P. Kim, J. Y. Choi, B. H. Hong. *Nature*, **2009**, *457*, 706−710.
16. Stoller, M. D., S. Park, Y. Zhu Y, J. An, R. S. Ruoff. *Nano Lett*. **2008**, *8*, 3498–3502.
17. Stankovich, S, D. A. Dikin, G. H. B. Dommett, K. M. Kohlhaas, E. J. Zimney, E. A. Stach, R. D. Piner, S. T. Nguyen, R. S. Ruoff. *Nature*, **2006**, *442*, 282–286.
18. Emtsev, K. V., A. Bostwick, K. Horn, J. Jobst, G. L. Kellogg, L. Ley, J. L. McChesney, T. Ohta, S. A. Reshanov, J. Rohrl, E. Rotenberg, A. K. Schmid, D. Waldmann, H. B. Weber, T. Seyller. *Nature Mater.* **2009**, *8*, 203-207.
19. Stankovich S, D. A. Dikin, R. D. Piner, K. A. Kohlhaas, A. Kleinhammes, Y. Jia Y. *Carbon*, **2007**, *45*, 1558–1565.
20. Li, D., M. B. Muller, S. Gilje, R. B. Kaner, G. G. Wallace. *Nature Nanotechnol*. **2008**, *3*, 101–105.
21. Yang, X., X. Dou, A. Rouhanipour, L. Zhi, H. J. Rader, K. Mullen. *J. Am. Chem. Soc*. **2008**, *130*, 4216–4217.
22. Reina, A., X. Jia, J. Ho, D. Nezich, H. Son, V. Bulovic, M. S. Dresselhaus, J. Kong. *Nano Lett*. **2009**, *9*, 30-35.
23. Liao, C. D., Y. Y. Lu, S. R. Tamalampudi, H. C. Cheng, Y. T. Chen. *Phys. Chem. A.* **2013**, *117*, 9454-9461.
24. Juang, Z. Y., C. Y. Wu, A. Y. Lu, C. Y. Su, K. C. Leou, F. R. Chen, C. H. Tsai. *Carbon*, **2010**, *48*, 3169-3174.

25. Corpuz, A. R., T. S. Olson, P. Joghee, S. Pylypenko, A. A. Dameron, H. N. Dinh, K. J. O'Neill, K. E. Hurst, G. Bender, T. Gennett, B. S. Pivovar, R. M. Richards, R. P. O'Hayre. *J. Power Sources*, **2012**, *217*, 142-151.
26. Lv, R., M. Terrones. *Mater. Lett*. **2012**, *78*, 209−218.
27. Matsoso, B. J., K. Ranganathan, B. K. Mutuma, T. Lerotholi, G. Jones, N. J. Coville. *RSC Adv.*, **2016**, *6*, 106916-106920.
28. Chang, C. K., S. Kataria, C. C. Kuo, A. Ganguly, B. Y. Wang, J. Y. Hwang, W. H. Yang, S. B. Wang, C. H. Chuang, M. Chen. *ACS Nano*, **2013**, *7*, 1331-1341.
29. Shinde, P. P., V. Kumar. *Phys. Rev. B.* **2011**, *84*, 125401.
30. Bepete, G., D. Voiry, M. Chhowalla, Z. Chiguvare, N. J. Coville. *Nanoscale*, **2013**, *5*, 6552-6557.

Chapter 2

Literature Review

2.1 Background

The production of sustainable energy, the development of a sustainable environment and affordable healthcare constitute an enormously group of challenges for today's global community. For instance, due to the continuous population growth as well as the increasing improvement in the quality of life, the energy demand is predicted to increase by ~37% the year 2040 [1-3]. In most countries, including South Africa, this increasing energy demand is met by the continuous use of diminishing fossil fuels such as coal and crude oil. Unfortunately, the use of fossil fuels substantially contributes to the emission of greenhouse gases, which results in global warming. Besides global warming, these energy resources have major social and environmental impacts such as contributing to the deteriorating health of communities nearby the fossil fuel reserves. For instances, there are large emissions of the toxic sulfur dioxide and nitrogen oxide during production of coal-generated energy [1-3]. These gases are known to react with water molecules in the atmosphere to produce acid rain. Acid rain is known to have adverse impacts on forests, freshwaters and soils, killing of insects and aquatic life-forms, corrosion of steel bridges, and finally the weathering of stone buildings and statues [1-3]. Additionally, production of electrical energy from coal-fired power plants is the largest source of man-made mercury pollution [1-3]. Likewise, the production of energy from oil reservoirs results in oil spills either on land or offshore. The oil spills have been found to exhibit devastating cumulative impacts on the environment as well as contributing to chronic health effects.

As such, many countries across the globe have opted to use alternative renewable energy resources, such as wind, biomass, solar and hydro. Although the renewable forms of energy are currently being employed to offer sustainable energy resources, the current shortcomings associated with the use of renewable energy sources suggests that a balance between renewable resource and fossil fuels will play a major role, before the complete phasing –out of fossil fuel-generated energy. Some of the shortcomings include the difficulty of generating quantities of energy as large as those from fossil fuels, the current high cost of the renewable energy technology, the difficulty of storage of highly combustible fuel such as hydrogen, and

the environmental and social impacts accompanying the construction of dams for hydropower generation [4]. Since it can be seen that energy production from fossil fuels cannot be avoided for decades to come, the development of new technologies for early detection of major health and environmental impacts of fossil fuel-generated energy is a necessity. As a result, new technologies such as gas, electrochemical, and biosensors are employed to accurately detect and monitor environmental as well as health impacts related to emissions from the fossil fuel-fired energy plants. Most of these new technologies are mainly focused on the use of carbon-based nanomaterials [5-12].

2.2 Carbon nanomaterials

Carbon, the fourth most common element, is the most studied element as well as the most widely used element in numerous applications. This is due to the fact that carbon is always found in large deposits of its purest form (such as diamond, graphite, and coal); as a result it requires minimal processing prior to subsequent application [13]. Depending on the reaction conditions, carbon can be shaped into different dimensions to form different carbon-based nanomaterials, such as the zero dimensional (0D) fullerenes, one dimensional (1D) carbon nanotubes, and two dimensional (2D) graphene. As a result, different carbon-based nanomaterials have found application in various fields such as catalysis, solar cells, ultra and supercapacitors, chemical, gas and biosensors, and fuel cells [5-12]. In electrochemical applications, carbon-based nanomaterials have been of industrial importance for over a century [14]. For instance, carbon electrodes are used industrially in metallurgy, for the production of silicon-based devices, in the production of calcium carbide and yellow phosphorus, as well as for the fabrication of zinc-carbon batteries [13-17]. These applications are made possible by the excellent physical and chemical properties of carbon-based nanomaterials such as fast heterogonous electron transfer, high electrical and thermal conductivity, large surface area and excellent electrochemical stability.

Among the various carbon-based nanomaterials, graphene, an atom-thick two-dimensional (2D) allotrope of carbon in the form of sp^2-hybridized carbon atoms in a honey-comb lattice, has attracted tremendous attention [18-21]. Graphene exhibits unique structural and physiochemical properties, including the large specific surface area, excellent thermal conductivity, ultrahigh electrical conductivity, excellent chemical, thermal and electrochemical stability, and high mechanical strength [18-21]. Due to these unique properties, graphene and its derivatives, such as graphene films, graphene oxide, doped and

functionalized graphene nanomaterials, bring new prospects and perspectives to the modern electrochemistry technologies.

2.2.1 Synthesis of graphene

Similar to carbon nanotubes (CNTs), graphene have been "rediscovered" several times [22, 23], however, the successful isolation of graphene from highly orientated polymeric graphite (HOPG) in 2004[18] by Andrea Geim and Kostantin Novoselov, and the ground-breaking experiments performed to demonstrate the fascinating properties of graphene, opened new frontiers for application of graphene in different fields [18-21]. Since then, several synthesis techniques have been developed to prepare graphene nanostructures. In general, the various synthetic routes can be classified into two main approaches, as shown in scheme 2.1: (1) the top-down and (2) the bottom up approach.

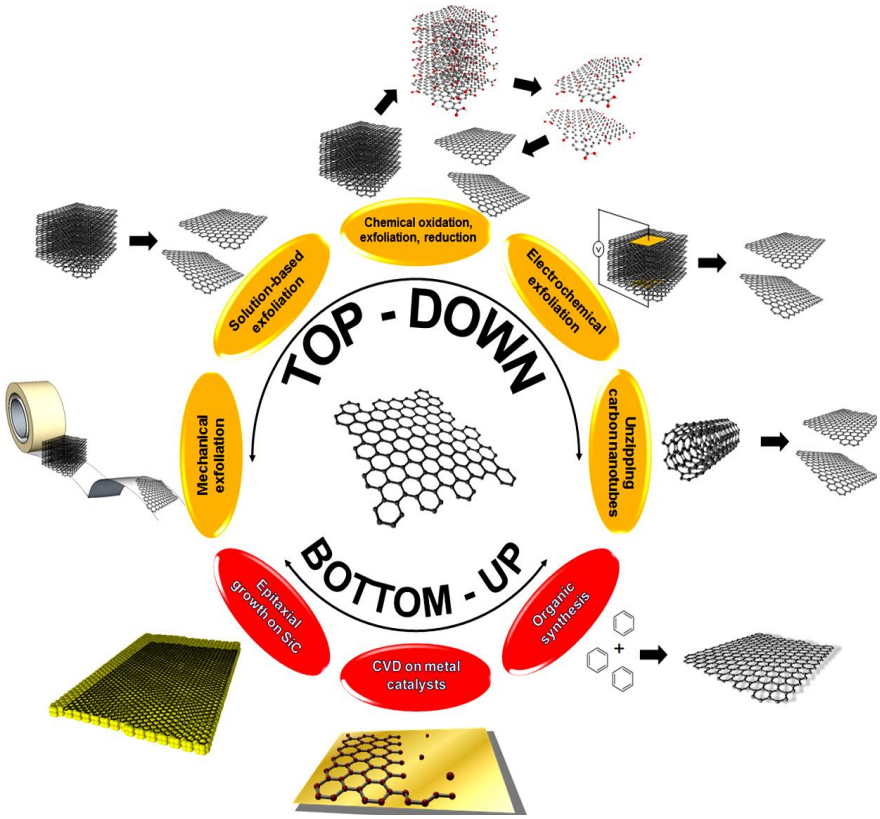

Scheme 2.1: Illustration of preparation methods of graphene and its derivatives [13].

2.2.1.1 Top-down approach

The top-down synthesis routes involves the weakening of the van der Waals forces between the layers of graphite in order to form free standing layers of graphene. These synthetic approaches includes techniques such as mechanical exfoliation of graphite (also known as the Scotch tape method) [18-21, 24], a solution-based chemical oxidation process [25], chemical

reduction of graphene oxide [26-28], unzipping of carbon nanotubes, intercalation of ions or compounds in graphite, etc. [29-31] Graphene nanostructures obtained from the mechanical exfoliation method are considered pristine and are of the highest quality [18]. The method was first described in 2004 [18] and it entails repeated peeling off of graphene layers from highly oriented pyrrolic graphite (HOPG) by means of an adhesive tape, hence the infamous 'Scotch tape' method. Monolayers of graphene are eventually transferred onto substrates of choice using either wet or dry transfer techniques [18-21]. Unfortunately, the mechanical exfoliation method can only be adopted for fundamental research studies due to the low reproducibility and the impossibility of large-scale implementation. In most cases, production of graphene by top-down synthesis routes, leads to formation of impurities in the form of amorphous carbon, and these impurities greatly influence the electrochemical properties of the as-synthesized graphene nanomaterials [24-31].

2.2.1.2 Bottom-up approach

The bottom-up synthesis routes involves the growth of single or few layered graphene from the assembly of small molecular building blocks in the form of active carbon species by means of a catalytic chemical vapour deposition (CVD) method [32-35], by thermal sublimation of SiC [36, 37], or by a solution-based catalytic growth using organic molecules [38, 39]. Most importantly, in the bottom-up synthesis methods, special conditions are required to allow active carbon molecules to combine into the sp^2-hybridized carbon network of graphene. For instance, when SiC is used to make graphene, it involves high temperatures under ultrahigh vacuum (UHV) conditions to sublime Si atom from silicon carbide (SiC) wafers. This is followed by the subsequent rearrangement of the remaining carbon atoms into graphitic layers [36, 37]. Although the use of the SiC wafer growth method to make graphene is applied in the electronics industry for the fabrication of devices, the high cost of single-crystal SiC wafers, is a limiting factor for the large-scale production of graphene by this method.

Alternatively, the use of transition metal supports such as cobalt (Co) [40], platinum (Pt) [41], iridium (Ir) [42], ruthenium (Ru) [43], nickel (Ni) [44, 45], and copper (Cu) [35, 46, 47], have been found to facilitate the growth of large-area and high quality graphene films of varying thicknesses on metal surfaces via the high-temperature catalytic chemical vapour deposition (CVD) technique. The CVD technique is a chemical process in which the carbon source, in the form of gaseous, liquid, or solid precursors, is deposited at high temperatures as a thin film on the surface of a metal catalyst or substrate [35, 40-47]. It is widely used in the semiconductor industry

as well as in the controllable growth of nanomaterials like nanowires, nanofibers, diamond like carbons, silicon nitride, and carbon nanotubes [17, 48]. Consequently, the CVD technique is considered as one of the most promising commercial techniques for the industrial-scale growth of graphene films.

2.3 Applications of graphene

Due to its unique structural and physiochemical properties, such as its large specific surface area, excellent thermal conductivity, ultrahigh electrical conductivity, excellent chemical, thermal and electrochemical stability, the application of graphene has been explored in numerous fields [18-21].

2.3.1 Graphene in energy systems

2.3.1.1 Capacitors and supercapacitors

The capacitance of carbon nanomaterials, such as graphene, carbon nanotubes and graphite, has been extensively studied; and various research reports have indicated that the excellent capacitance in carbon-based nanomaterials can be attributed to the amount of sp^2 lattice and sp^3 defects [13, 49, 50]. Furthermore, the capacitance behavior of carbon materials was found to increase with the amount of edge and plane defects as well as the amount of oxygen functionalities [13]. This suggests that carbon materials with a significantly large amount of active surface area, i.e. with defects, should theoretically exhibit a higher capacitance behavior. Due to the ease of adjusting the amount of defects in graphene, via chemical or thermal reduction techniques, a significantly high theoretical specific surface area (~2600 m^2g^{-1}), and exceptionally high electrical conductivity in graphene has been achieved. This indicates that graphene and its derivatives are promising electrode materials for the construction of capacitors and supercapacitors device [13, 51]. Unfortunately, the capacitance of electrodes fabricated from graphene nanosheets was measured in the order of only tens of Farads per gram, which is similar to that of graphite-based electrodes [13, 51, 52]. This was attributed to the restacking of graphene sheets after the fabrication of the devices, thus significantly reducing the active surface area. To circumvent such limitations and increase capacitance of graphene-based electrodes, various strategies have been developed, including introduction of spacers (water molecules, carbon nanotubes, metal nanoparticles, etc.); doping with heteroatoms (nitrogen, boron, sulphur, phosphorus); functionalization with redox

molecules; preparation of 3D graphene nanostructures; as well as growth of large area and high quality graphene films by CVD [13, 51, 52].

2.3.1.2 Solar cells

Owing to the high optical transparency (~ 97.7%) and high electrical conductivity, in combination with the tunable electron transport and work function properties graphene is an ideal material to be exploited in solar cells [53, 54]. Recent research reports have indicated that graphene and its derivatives are good candidates for substituting the expensive indium tin oxide (ITO) as well as the fluorine tin oxide (FTO) conducting electrodes in organic photovoltaic (OPV's) and dye sensitized solar cells (DSSC's) [55,56]. Besides the application of graphene as a conducting electrode, graphene and its derivatives have been employed as the active layer material in OPVs[57]. Despite the low power conversion efficiencies of most graphene-based OPV's and/or DSSC's in comparison with the ITO/FTO-based devices [55-57] the reports inevitably highlight the potential application of graphene and its derivatives in solar cells. The compromised performance of graphene-based solar cells, specifically the OPV's, was attributed to the film morphology and the quality of the interface layers of the as-fabricated devices due to increased roughness. As a result, the use of wrinkle-free CVD-grown graphene films have demonstrated improved performance [58].

2.3.1.3 Oxygen reduction reactions

The oxygen reduction reactions (ORRs) are critical reactions involved in the performance of fuel cells, and the fuel cell electrodes are conventionally made from platinum nanoparticles supported on carbon black (Pt/C) [8-11]. Unfortunately, the high cost and limited availability of platinum, coupled with the slow reaction kinetics at the Pt/C cathode, the high sensitivity of Pt to carbon monoxide poisoning, and methanol crossover, have prompted a search for alternative catalysts [8-11]. As such, graphene nanostructures have been explored as robust and inexpensive alternative materials for electrocatalysis of ORRs in fuel cells. Owing to the large theoretical specific surface area of graphene as well as the ease of tuning its electronic and chemical properties via the heteroatom doping (N, B, S and P) [13, 51], graphene has been utilized in different ORR setups. For instance, graphene has been used as a conductive support for metal/metal oxide nanoparticles in a metal-based ORR setup. In another ORR setup, doped graphene nanostructures have been used directly as electrocatalysts for improved metal-free reduction of oxygen [59]. The reports indicated that the ORR performance of metal-free graphene-based electrocatalysts exceeded that of platinum electrocatalysts, especially for the reduction of oxygen in alkaline solution [51]. However, metallic impurities

are found in ORR electrocatalysts fabricated from graphene oxide nanosheets, specifically those produced from graphite. These impurities can impede the inherent ORR performance of graphene nanostructures alone; since these impurities also catalyze the reduction of oxygen [13, 51]. As a result, new research advances have ventured into using CVD-grown graphene films, both pristine and doped. As such, these electrocatalysts provide a high specific surface area, metal impurity-free surfaces, fast electron transport kinetics, as well as fascinating intrinsic properties [13, 51].

2.3.2 Graphene in electrochemical sensing

Graphene and its derivatives have been widely exploited for the fabrication of electrochemical sensors and biosensors due to their unique electrochemical properties as well as the ease of tuning these properties via functionalization with, or incorporation of, specific elements [60-62]. Generally, voltammetric and amperometric techniques such as differential pulse voltammetry (DPV), cyclic voltammetry (CV), square-wave voltammetry (SWV), and normal pulse voltammetry (NPV), have been adopted extensively for use in electrochemical sensors. This is due to the requirement of low-cost instrumentation, simplicity of the techniques, as well as the significantly fast responses and high selectivity of these sensors. As such, electrochemical sensors find application in a variety of environmental and pharmaceutical studies, ranging from analysis of DNA and cells in biological assays to significantly high sensitive detection of important biomakers and heavy metals [63-70].

Basically, the response from the electrochemical sensor is due to the electron transfer between the sensing materials (graphene or carbon-based nanostructures) supported on the working electrode (ITO) and the electroactive species (e.g. dopamine), as shown in scheme 2.2. In essence, the electroactive species can either be the molecule and/or an element of interest, or a product which has an electrochemical response that can be correlated directly to the electroactive species of interest. In general, development of an electrochemical sensor with good performance is governed by two main factors: (i) high sensitivity and selectivity for electrochemically active species, as well as (ii) enhanced electrochemical activity at the interface of the sensing material (graphene or carbon-based nanostructures) [13, 51]. As such graphene and its derivatives are ideal sensing materials due their high specific surface area and excellent electrical conductivity; thus resulting in accelerated heterogeneous electron transfer and hence improved intensity of the output signal [60-72].

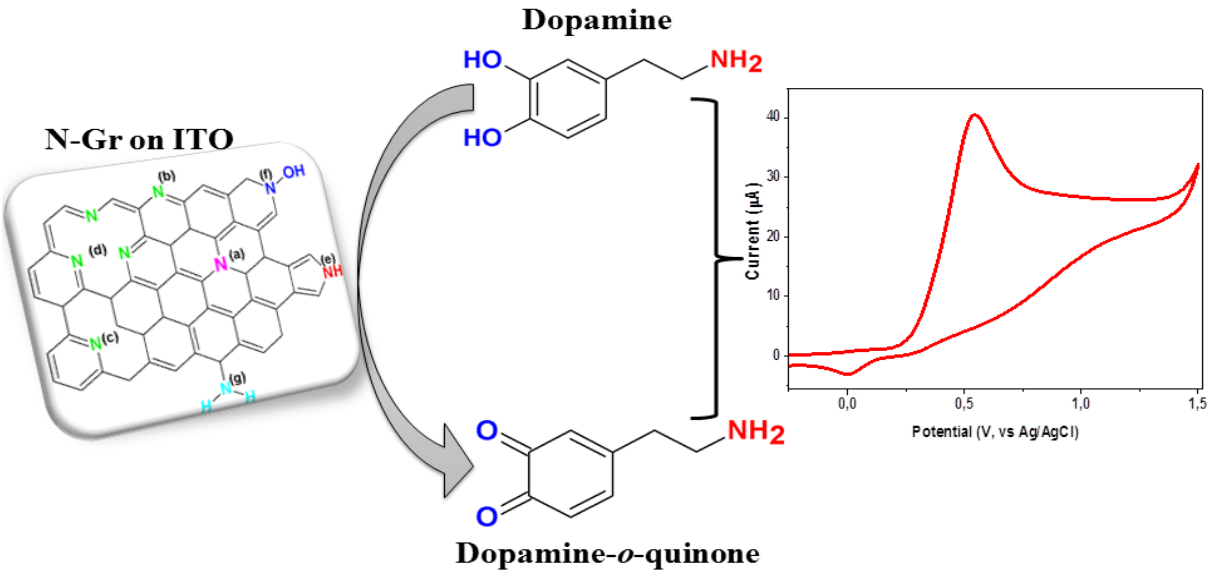

Scheme 2.2: Principles of stages during the operation of the electrochemical sensing of dopamine.

2.3.2.1 Cell and protein analysis

Graphene and related materials have been used to modify electrode surfaces with the aim of increasing the electrode surface area for loading biorecognition molecules like antibodies, and for providing a biocompatible surface for excellent adhesion of cells [51]. Owing to the high electrical conductivity and increased biocompatibility, graphene and its derivatives are promising materials for the development of ultrasensitive electrochemical sensors for direct quantification of cells as well as for the fabrication of highly sensitive immunosensors [51].

2.3.2.2 Analysis of biomakers

Over the decades, an enormous amount of research has been dedicated to the application of graphene and its derivatives for the selective and sensitive detection of biomakers, such as dopamine, uric acid, ascorbic acid, nicotinamide-adenine dinucleotide (NADH), serotonin, and glucose [66-70]. Biomakers are small molecules that are directly or indirectly related to clinical diagnosis of serious degenerative diseases [13, 51]. The sp^2 hybridized lattice, unique electrochemical properties, high electrical conductivity, and the amount of defect and oxygen functionalities on graphene have been found to facilitate the electron transfer during electrochemical detection of these biomakers via graphene-modified electrodes [13, 51, 66-70]. Recent research reports have indicated that traditional working electrodes modified with graphene nanostructures exhibit better conductivity, improved chemical stability, excellent selectivity and faster heterogeneous electron transfer rate for the determination of various

biomolecules [66-70]. The observed good electrochemical performance of most graphene nanomaterials has been attributed, not only to the presence of basal and edge plane defects and/or graphite 'nanoislands' across the graphene surface, but also to the presence of adatoms and impurities in the form of residual metal nanoparticles or amorphous carbon from the synthesis routes [13, 51, 66-70]. To avoid contributions from synthesis routes, CVD-grown graphene films have been used as promising candidates for modifying electrode surfaces. Reports have indicated that the electrocatalytic performance of CVD-graphene during detection of biomakers can be ascribed to the presence of edge plane defects and graphitic 'nanoislands' across the graphene surface [62, 73].

On the other hand, regardless of the synthesis routes used for production of graphene nanomaterials, intrinsic doping of graphene with heteroatoms ((N, B, S and P), is an effective way for tuning and tailoring the structural, surface chemistry and physiochemical properties of graphene [13, 51, 66-70]. This is beneficial as it provides efficient pathways for fast electron transfer kinetics, hence increasing the electrocatalytic activity of doped graphene materials towards detection of biomakers such as dopamine, glucose and ascorbic acid. Moreover, intrinsic doping also provides fundamental insight into new applications of doped graphene in electrochemical sensors and biosensors. Among the numerous dopants, nitrogen atoms are considered as excellent elements for chemical doping due to its comparable size (70 pm) with that of carbon (65 pm), as well as the extra lone pair of electrons on nitrogen atoms, which are available to form strong delocalised conjugated system with the sp^2 hybridized carbon lattice [61, 62]. Additionally, doping with electron-rich nitrogen atoms results in increased free charge carriers within the sp^2 hybridized carbon network [13, 51, 66-70]. Consequently, nitrogen doping of graphene leads to enhanced electrical conductivity and electrocatalytic activity [13, 51, 66-70]; thus making nitrogen doped graphene materials have great potential for applications in electrochemical sensors and biosensors.

2.4 Conclusions

Electrochemical sensors are the largest group of devices that are useful for monitoring and/or prevention of environmental and health risks, such as in the detection of heavy metals [71], high-energy explosive (2,4,6-trinitrotoluene, TNT) materials [74], degenerative disorders [66-70], and poisonous organic compounds (pesticides, ammonia) [75]. As a result, numerous research developments have bee dedicated to the construction of these devices in the laboratory and at the industrial scale. This has led to a wealth of information regarding the production of

electrochemical sensors that exhibit low detection limits, good selectivity and excellent sensitivity. The main challenge in the production of electrochemical sensors lies in the development of cost-effective and environmentally friendly methods suitable for the fabrication of electrochemical sensors with improved stability and performance. This is because most electrochemical sensors utilize nanoparticles of the expensive noble metals such as platinum, gold and silver [4, 50]. Consequently, recent advances have shown that graphene and its derivatives, without the addition of metals, are promising materials due to the intriguing electrochemistry displayed by electrodes modified with graphene nanomaterials. On the other hand, the presence of impurities in the form of metallic or carbonaceous materials in graphene derivatives (graphene oxide, graphene nanoribbons) have been reported to directly influence the performance of electrochemical sensors based on these graphene nanomaterials. As such, production of graphene nanomaterials using the CVD techniques has proved to be a trustworthy replacement for other graphene-based nanomaterials. The ease of tuning the intrinsic properties of CVD-graphene by controlled doping with heteroatoms, as well as the industrial-scale production of CVD-graphene, make graphene nanosheets grown via CVD techniques perfect materials to be employed in a wide variety of electrochemical sensors.

References

1. Armaroli, N., V. Balzani, *Angew. Chemie. Int. Ed.***, 2007,** *46(1-2)*¸52-66.
2. IEA, *World Energy Outlook,* **2014**. IEA.
3. IEA, *World Energy Outlook,* **2013**. IEA.
4. Maehlum, M. A., *Hydroelectric Energy pros and cons,* **2012,** www.energyinformative.org.
5. Manzetti, S., D.Vasilache, E. Francesco. *Advances in Manufacturing,* **2015,** *3,* 63-72.
6. Mutuma, B. K., R. Rodrigues, K. Ranganathan, B. J. Matsoso, D. Wamwangi, I. A. Hümmelgen, N. J. Coville. *J. Mater. Chem. A*, **2017**, *5*, 2539-2549.
7. Wang, Q., J. Yan, Y. Wang, G. Ning, Z. Fan, T. Wei, J. Cheng, M. Zhang, X. Jing. *Carbon,* **2013,** *52,* 209-218.
8. Jackson, C., O. Conrad, P. Levecque. *Electrocatalysis*, **2017,** 1-11.
9. Gattia, D. M., M. V. Antisari, L. Giorgi, R. Marazzi, E. Piscopiello, A. Montone, S. Bellitto, S. Licoccia, E. Traversa. *J. Power Sources*, **2009**, *194*, 243-251.
10. Antolini, E. *Appl. Cat. B.: Environ.* **2009**, *88*, 1-24.

11. Tang, K., L. Fu, R. J. White, L. Yu, M. M. Titirici, M. Antonietti, J. Maier. *Advanced Energy Materials*, **2012,** *2*, 873-877.
12. Phaahlamohlakia, T. N, D. O. Kumi, M. W. Dlamini, L. L. Jewell, N. J. Coville. *Catalysis Today*, **2016**,*275*, 76-83.
13. Von Stack, A., A. Muhlbauer, C. Kramer. *Handbook of Thermoprocessing Technologies:Fundamentals, Processes, Components, Safety.* Vulkan-Verlag:Essen, Germany, **2005,** 275.
14. Ambrosi, A., C. K. Chua, A. Bonnani, M. Pumera. *Chem.Rev.* **2014,** *114,* 7150-7188.
15. Linden, D., T. B. Reddy. *Handbook of batteries 3rd Ed,* McGraw-Hill, New York, **2002,** chapters 13 and 38.
16. Greenwood, N. N., A. Earnshaw, *Chemistry of the elements 2nd Ed,* Btterworth-Heinemann, **1997,** Oxford, 298.
17. Hideki, M., *Japanese Journal of Applied Physics,***1998,** *37,*(6R),3175.
18. Geim, A. K., K. S. Novoselov. *Nat. Mater*. **2007**, *6,* 183-191.
19. Novoselov, K. S., A. K. Geim, S. V. Morozov, D. Jiang, Y. Zhang, S. V. Dubonos, I. V. Grigorieva, A. A. Firsov. *Science*, **2004**, *306*, 666−669.
20. Geim, A. K. *Science*, **2009**, *324*, 1530–1534.
21. Geim, A.K., K. S. Novoselov, S. Morozov, D. Jiang, M. I. Katsnelson, S. Dubonos, I. Grigorieva, A. Firsov. *Nature*, **2005**, *438*, 197-200.
22. Fitzer, E., K. H. Kochling, H. P. Boehm, H. Marsh. *Pure, Appl. Chem.***,1995,** *67,*473.
23. Morgan, A. E., G. A. Somorjai, *Surf. Sci.,* **1968,** *12,* 405.
24. Balandin, A. A., S. Ghosh, W. Bao, I. Calizo, D. Teweldebrhan, F. Miao, C. N. Lau. *Nano Lett.* **2008**, *8*, 902–907.
25. Hernandez, Y., M. Lotya, D. Richard, S. D. Bergin, J. N. Coleman, *Langmuir,* **2010,** *26*, 3208.
26. Stankovich S, D. A. Dikin, R. D. Piner, K. A. Kohlhaas, A. Kleinhammes, Y. Jia Y. *Carbon*, **2007**, *45*, 1558–1565.
27. Li, D., M. B. Muller, S. Gilje, R. B. Kaner, G. G. Wallace. *Nature Nanotechnol*. **2008**, *3*, 101–105.
28. Hummers, W. S., R. E. Offeman. *J. Am. Chem. Soc.,* **1958**, *80,* 1339.
29. Yang, X., X. Dou, A. Rouhanipour, L. Zhi, H. J. Rader, K. Mullen. *J. Am. Chem. Soc*. **2008**, *130*, 4216–4217.
30. Takada, Y., R. Fujii, *Tanso,* **1985,** *1985,* 110.

31. Low, C. T., F. C. Walsh, M. H. Chakrabarti, M. A. Hashim, M. A. Hussain, *Carbon*, **2013,** ***54,*** 1.
32. Li, X., W. Cai, L. Colombo, R. S. Ruoff. *Nano Lett.*, **2009**, *9*, 4268−4272.
33. Gao, T., S. Xie, Y. Gao, M. Liu, Y. Chen, Y. Zhang, Z. Liu. *ACS Nano*, **2011**, *5*, 9194−9201.
34. Bae, S. H., Kim, Y. Lee, X. Xu, J.S. Park, Y. Zheng, J. Balakrishnan, T. Lei, H. R. Kim, Y. Song, Y. J. Kim, K. S. Kim, B. Ozyilmaz, J. H. Ahn, B. H. Hong, S. Iijima. *Nat Nanotechnol*, **2010**, *5*, 574–578.
35. Reina, A., X. Jia, J. Ho, D. Nezich, H. Son, V. Bulovic, M. S. Dresselhaus, J. Kong. *Nano Lett*, **2009**, *9*, 30–5.
36. Berger, C., Z. Song, X. Li, X. Wu, N. Brown, C. Naud, D. Mayou, T. Li, J. Hass, A. N. Marchenkov, E. H. Conrad, P. N. First, W. A. de Heer. *Science*, **2006**, *312*, 1191−1196.
37. Lin, Y. M., C. Dimitrakopoulos, K. A. Jenkins, D. B. Farmer, H. Y. Chiu, A. Grill, Ph. Avouris. *Science*, **2010**, *327*, 662.
38. Yang, X. Y., X. Dou, A. Rouhanipour, L. J. Zhi, H. J. Rader, K. J. Müllen, *Am. Chem. Soc*. **2008**, *130*, 4216.
39. Cai, J. M., P. Ruffieux, R. Jaafar, M. Bieri, T. Braun, S. Blankenburg, M. Muoth, A. P. Seitsonen, M. Saleh, X. L. Feng, K. Müllen, R. Fasel, *Nature*, **2010**, *466*, 470.
40. Wang, S., L. Qiao, C. Zhao, X. Zhang, J. Chen, H. Tian, W. Zheng, Z. Han. *New J. Chem.* **2013**, *37*, 1616-1622.
41. Cushing, G. W., V. Johanek, J. K. Navin, I. Harrison. *J. Phys. Chem. C.* **2015**, *119*, 4759-4768.
42. Locatelli, A., G. Zamborlini, T. O. Mentes. *Carbon*, **2014**, *74*, 237-248.
43. Pan, Y., H. Zhang, D. Shi, J. Sun, S. Du, F. Liu, H. Gao. *Adv. Mater*. **2009**, *21*, 2777−2780.
44. Reina A, S. Thiele, X. Jia, S. Bhaviripudi, M. S. Dresselhaus, J. A. Schaefer, J. Kong. *Nano Res*. **2009**, *2*, 509–516.
45. Garlow, J. A., L. K. Barrett, L. Wu, K. Kisslinger, Y. Zhu, J. F. Pulecio.. *Scientific Reports*, **2016**, *6*, 19804 (1-11).
46. Sun, Z., Z. Yan, J. Yao, E. Beitler, Y. Zhu, J. M. Tour. *Nature*, **2010**, *468*, 549–552.
47. Li, X. S., W. W. Cai, J.H. An, S. Kim, J. Nah, D. X. Yang, R. Piner, A. Velamakanni, I Jung, E. Tutuc, S. K. Banerjee, L. Colombo, R. S. Ruoff. *Science*, **2009**, *324*, 1312−1314.

48. Kijma, K., N. Setaka, H. Tanaka, *Journal of Crystal Growth*, **1974,** *24*, 183-187.
49. Pumera, M.,*Energy Environ. Sci.* **2011,** *4*,668.
50. Kim, T., S. Lim, K. Kwon, S. H. Hong, W. Qiao, C. Rhee, S. H. Yoon, I. Mochida, *Langmuir,* **2006,** ***22,*** **9086.**
51. Ambrosi, A., C. K. Chua, N. M. Latiff, A. H. Loo, C. H. A. Wong, A. Y. S. Eng, A. Bonanni, M. Pumera, *Chem Soc. Rev,* **2016,** ***45,*** 2458-2493**.**
52. Pumera, M., B. Smid, K. Veltruska, *J. Nanosci. Nanotechnol.* **2009,** *9*, 2671.
53. Yin, Z. Y., J. X. Zhu, Q. Y. He, X. H. Cao, C. L. Tan, H. Y. Chen, Q. Y. Yan, H. Zhang, *Adv. Energy Mater*. **2014**, *4*, 1300574.
54. Jariwala, D., V. K. Sangwan, L. J. Lauhon, T. J. Marks, M. C. Hersam, *Chem. Soc. Rev*. **2013**, *42*, 2824
55. .Xu, Y., G. Long, L. Huang, Y. Huang, X. Wan, Y. MA, Y. Chen, *Carbon*, **2010,** *48*, 3308-3311.
56. Wang, X.; L. Zhi, K. Mullen, *Nano Lett***. 2007**, *8*, 323.
57. Jun, G. H., S. B. Jin, B. Lee, B. H. Kim, W. S. Chae, S. H. Hong, S. Jeon, *Energy &Environmental Science,* **2013,** *6*, 3000-3006.
58. Park, H., P. R. Brown, V. Bulovic, J. Kong, *Nano Lett.*, **2012,** *12*,133-140.
59. Shao, Y.Y., J. H. Sui, G. P. Yin, Y. Z. Gao. *Applied Catalysis B-Environmental, 2008¸79,* 89e99.
60. Shen, Z. H., X. Q. Zheng, J. Y. Xu, W. J. Bao, F. B. Wang, X. H. Xia. *Biosensors and Bioelectronics*¸ **2012**¸ *34,* 125-131.
61. Pumera, M., A. Ambrosi, A. Bonanni, E. L. K. Cheng, H. L. Poh. *TrAC, Trends Anal. Chem.*, **2010**, *29*, 954.
62. Brownson, D. A. C., D. K. Kampouris, C. E. Banks. *Chem. Soc. Rev.*, **2012**, *41*, 6944.
63. Alwarappan, S., K. Cissell, S. Dixit, S. Mohapatra, C. Z. Li, *J. Electroanal. Chem.*, **2013,** *686*, 69-72.
64. Castillo, J. J., W. E. Svendsen, N. Rozlosnik, P. Escobar, F. Martinez, J. Castillo-Leon, *Analyst,* **2013,** *138,* 1026-1031.
65. Wang, H. W., Y. H. Wei, H. W. Guo. *Anti-Cancer Agents in Med. Chem*., **2009**, *9*, 1012-1017.
66. Wang, Z. Y., S. N. Liu, P. Wu, C. X. Cai. *Anal. Chem*., **2009**, *81*, 1638-1645.
67. Dennis, M. A., K. Michael, M. M. Khodabakhsh, N. Stuart, W. Michael. *Anal. Chem.*, **1989**, *61*, 2603-2608.

68. Xu, H. Y., J. J. Xiao, L, Yan, L. Zhu, B. H. Liu. *J. Electroanalytical Chemistry,* **2016**¸*779*, 92-98.
69. Christopher, B. J., P. M. Jennifer and V. B. Jill, *Anal. Chim. Acta,* **2010,** *622*, 105.
70. Annesh, P. K., S. R. Nambiar, T. P. Rao, A. Ajayaghosh. *Anal. Methods*, **2014**¸*6*, 5322-5330.
71. Li, M., H. Guo, I. Al-Ogaidi, N. Wu, *ACS, Sustainable Chem. Eng.,* **2013,** *1*, 713-723.
72. Kalimuthu, P., S. A. John. *Talanta,* **2010**, *80*, 1686–1691.
73. Lim, C. X., H. Y. Hoh, P. K. Ang, K. P. Loh, *Anal. Chem*. **2010**, *82*, 7387.
74. O'Mahony, A. M., J. Wang, *Anal. Method*, **2013**, *5*, 4296.
75. Wang, J. *Anal. Chim. Acta* **2004**, *507*, 3.

Chapter 3

Optimizing the growth of graphene films on a Cu catalyst using atmospheric pressure CVD

3.1 Introduction

Graphene, an allotrope of carbon with a two dimensional (2D) structure and the first example of a free-standing and stable 2D material, has attracted enormous research interest from both theoretical and experimental scientists[1, 2]. This was made possible after its mechanical isolation from highly orientated polymeric graphite (HOPG) in 2004[3], and it exhibited promising properties, mainly those related to electronic applications [4-6]. Since graphene consists of a single layer of sp^2 hybridised carbon atoms[3], it can be regarded as the basic unit for other carbon materials such as 3D graphite, a 1D CNT or the 0D fullerene[4]. Both theoretical and experimental studied have shown that electrons in graphene obey a linear dispersion relationship and behave as massless Dirac fermions[7]. This phenomenon gives rise to graphene's outstanding electrical properties such as half-integer quantum Hall effect, absence of charge localization, ultra-high charge mobility, and its charge concentration[7-12]. Additionally, the room temperature electron mobility in graphene is predicted to be ~ 200 000 $cm^2V^{-1}s^{-1}$, which is found to be 2 orders of magnitude higher than that of modern Si transistors that currently dominates the semiconductor industry[9]. Furthermore, the room temperature current density of graphene is 2.2 $g.cm^{-1}$ which is 6 orders on magnitude higher than copper[7, 9]. Other extraordinary properties of graphene include its high optical transparency (~ 97.7%), a high theoretical specific surface area (~2600 m^2g^{-1}), high thermal conductivity (5000 $Wm^{-1}K^{-1}$), mechanical stress (1060 GPa), a large Young's modulus (1.0 TPa), chemical inertness, and super hydrophobicity at the nanometre scale[1-11]. Owing to these extraordinary properties in combination with its single atom-thickness, graphene has proved to be a promising candidate for fabrication of nano- and microelectronic devices such as field effect transistors (FET) [3, 12], chemical and biological sensors [13, 14] organic solar cells [15, 16], transparent conductive films for flexible electronics [17], ultra- and supercapacitors [18, 19], and graphene-polymer nanocomposites [20].

However, for graphene to find application in electrochemical and energy storage devices, synthesis of uniform and large area graphene films on insulating substrates is a necessity[20]. As a result, different synthesis techniques have been proposed including the graphitization of SiC substrates[21], chemical reduction of graphene oxide[22], liquid exfoliation of graphite[23], catalytic chemical vapour deposition (CVD) using transition metals [24-26], and unzipping of CNTs[27]. Contrarily, most of these methods suffer a major drawback since they do not cover the critical issues such as controlled graphene thickness and grain size, stacking order, as well as defect concentration.

On the other hand, CVD techniques using transition metals have shown to be the most promising and reproducible approach for solving these critical issues, thereby resulting in the growth of high-quality, large area and conducting graphene films [26]. In particular, various transition metal catalysts such as cobalt (Co) [28, 29], platinum (Pt) [30, 31], iridium (Ir) [32, 33], ruthenium (Ru) [34], nickel (Ni) [35, 36], copper (Cu) [24,37, 38], nickel-copper alloy (Ni/Cu) [39, 40], and cobalt-copper (Co-Cu) alloy [41], have been used to facilitate the decomposition of the carbon precursors (either from gases, liquids, or solids); hence leading to the deposition of carbon atoms into planar sheets of graphene [13, 24-41]. Depending on the solubility of carbon in different transition metals, graphene films of varying thickness and quality are formed. Therefore, due to the low solubility of carbon in Cu (< 8 ppm at 1048 K) [42], single crystal and polycrystalline Cu have shown great potential for growing large area monolayered graphene films with excellent quality [24, 24,37, 38].

The catalytic CVD technique possesses numerous advantages over other growth methods. However, growth of graphene films on a Cu catalyst by CVD is known to be a complex heterogeneous catalytic process involving a number of growth parameters which play a major role in affecting the morphology, thickness, stacking order, and quality/defects of the as-synthesized graphene films. These include parameters such as the crystalinity and thermal annealing of the Cu substrate [24, 43] growth temperature [24, 44, 45], carbon source [24, 37, 44-46], exposure time of the carbon source onto the metal catalyst [47], volume ratio and flow rate of the gas mixture [48-50], as well as the operating pressure [24, ,37, 48-51].

For instance, Li *et al.* developed a three-step APCVD growth method to obtain mono-, bi- and tri-layer graphene films with a ~ 90% coverage on the Cu foil by controlling the growth temperature (900 to 1070 ^{o}C) and total gas flow rates (250 to 1500 sccm) [48]. They found that with a low methane partial pressure and with the growth temperature kept at 930 ^{o}C to 1070

^{o}C, more graphene layers were formed since graphene nucleate to give different layers. Similar behaviour was observed when the methane partial pressure was increased by a factor of 5, and when both methane and hydrogen partial pressures were doubled. Furthermore, Lavin-Lopez and co-workers [51] studied the influence of growth parameters, such as temperature (900 – 1050 ^{o}C), reaction time (5 -40 min), molar ratio of CH_4/H_2 (3 -45 %), and total gas flow (40 – 140 NmL/min) on the synthesis of bilayer graphene films using an APCVD setup. They found that graphene formation was not homogeneous in most of the samples prepared since the presence of multilayer graphene films was observed. However, optimizing to a 10 minute growth time, a growth temperature of 1050^{o}C, a CH_4/H_2 ratio of 7% and a 60 NmL/min total gas flow resulted in the growth of bilayered graphene films with good quality. They observed that at these conditions, both the defect density and graphene layers were reduced to a minimum. They attributed this to the increased mobility and good attachment of carbon atoms to more favourable active sites on the Cu surface, hence facilitating a more ordered growth of graphene domains, and formation of graphene films with fewer layers. By adjusting the total pressure within the CVD reactor ($5.8_{(\text{low pressure})}$ − $740_{(\text{near atmospheric})}$ Torr) and the individual pressures for methane and hydrogen (P_{H2} = 5.6 to 716.8 Torr and P_{CH4} = 0.2 to 25.6 Torr), Sun *et al.* obtained graphene films with thickness ranging from one, two, three, four, and up to ten layers [52]. They showed that at a very low total growth pressure (≤ 23.1 Torr), and $P_{H2} \leq 22.4$ Torr as well as $P_{CH4} \leq 1.6$ Torr, the as-grown graphene films were mainly monolayered. However, increasing the growth pressure (≈ 740 Torr), and using $P_{H2} \approx 716.8$ Torr and $P_{CH4} \approx 25.6$ Torr, the graphene films became thicker, ranging from bilayered to few layered. They attributed the observed growth mechanism to the presence of high concentrations of carbon species, hence leading to the supersaturation of C atoms on the surface layers of Cu. Finally, Vlassiouk *et al.* found that the purity and crystallographic orientation of the Cu foil influenced the density of active sites on the Cu foil, hence affecting the growth rate of graphene and the size of the graphene domains [53].

On the basis of the above studies, it is indicative that before CVD-grown graphene films are applied for device fabrication, a thorough study is necessary in order to understand and evaluate the growth parameters that would influence the growth conditions for the synthesis of high-quality and large-area graphene films. Therefore, in this work, the parameters for growing good quality graphene films on a Cu catalyst under the APCVD technique were optimized. Growth parameters that were studied in detail were methane (CH_4) flow rate and

reaction time; since these are known to play a major role in influencing the successful growth as well as the quality of CVD-grown graphene.

3.2 Experimental

3.2.1 Starting materials

Acetone (99%, gold line ACE), methanol (99.5 %), ethanol (absolute), iso-propanol (ACE, 99%), ortho-phosphoric acid (85%, LabChem), urea (99%, Promark Chemicals), chlorobenzene (99%, UniLab), sodium hydroxide pellets (98%, Merk) and poly(methyl methacrylate) (PMMA, Mw ~999 000) were purchased from Sigma-Aldrich, South Africa. The gases included argon (Ar, 99%), methane (CH_4, 99.98%), ammonia (NH_3, 10% in Ar), and hydrogen (H_2, 99.98 %), and these were supplied by Afrox, South Africa. Other materials included a copper foil (25 µm, 99.98%) from Sigma Aldrich (RSA), a silicon substrate with a 300 nm silicon oxide layer (Sigma-Aldrich), the copper plate and an iron wire (University of the Witwatersrand workshop). Distilled water was used in all the experiments.

3.2.2 Growth and Transfer of graphene films

Graphene was grown on a 3 cm × 3 cm of a 25 µm Cu foil using CH_4 gas as the carbon source, H_2 as the reducing gas, and Ar as the carrier gas. Initially, the Cu foil was cleaned in an electrochemical cell using 12.0 V for 90 sec, and in which the anode is the Cu foil and the cathode is the Cu plate (Scheme 3.1). The electropolishing solution was a solution mixture of 300 mL distilled water, 150 mL ethanol, 150 mL ortho-phosphoric acid, 30 mL isopropanol and 3.0 g urea[54]. After cleaning, the Cu foil was placed at the centre of the cylindrical quartz tube (100 cm × 20 cm) inside a horizontal CVD furnace. The furnace was heated to 1000 ^oC (ramping rate of 10 $^oC\ min^{-1}$) and held at the designated temperature for 30 minutes under 10 sccm H_2 and 300 sccm Ar atmospheres. Growth of graphene films was carried out for 2-20 minutes using various flow rates of CH_4 (5-30 sccm). Finally the reactor was ***rapidly*** cooled to room temperature under both H_2 and Ar atmospheres by pushing the quartz tube outside the furnace at the end of the reaction.

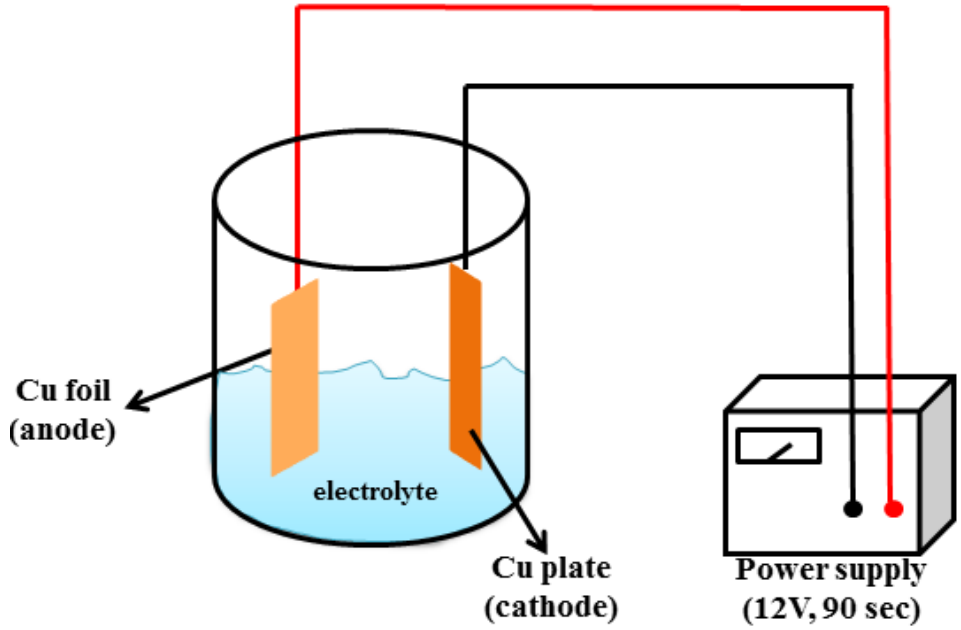

Scheme 3.1: Electropolishing of Cu foil.

For characterization, the as-grown graphene films on Cu foil were transferred onto a 300 nm SiO_2/Si substrate using the PMMA-assisted electrochemical delamination method [55](Scheme 3.2). Initially a 1.5 cm × 1.5 cm square of the as-grown graphene on Cu was spin-coated with a thin layer of PMMA (4.6 % m/v in chlorobenzene) at 2000 rpm for 60 sec. The PMMA-coated graphene/Cu foil was baked at 80 ^{o}C for 5 min to ensure good adhesion of the PMMA on the graphene/Cu. The electrochemical delamination cell consisted of a Fe wire (anode), PMMA/graphene/Cu foil (cathode), and 0.1 M NaOH electrolyte solution. The reduction of water at the PMMA/graphene/Cu electrode led to the emergence of hydrogen bubbles at the PMMA/graphene-Cu interface; which facilitated the detachment of the PMMA/graphene film from the Cu foil. The floating PMMA/graphene film was transferred onto the 300 nm SiO_2/Si substrate, and then baked at 50 ^{o}C for 20 minutes to enable good adherence of PMMA/graphene onto the substrate. Lastly, PMMA was dissolved with hot acetone, while any residual PMMA and/or acetone on the surface of the graphene surface were removed by washing with multiple volumes of methanol and distilled water.

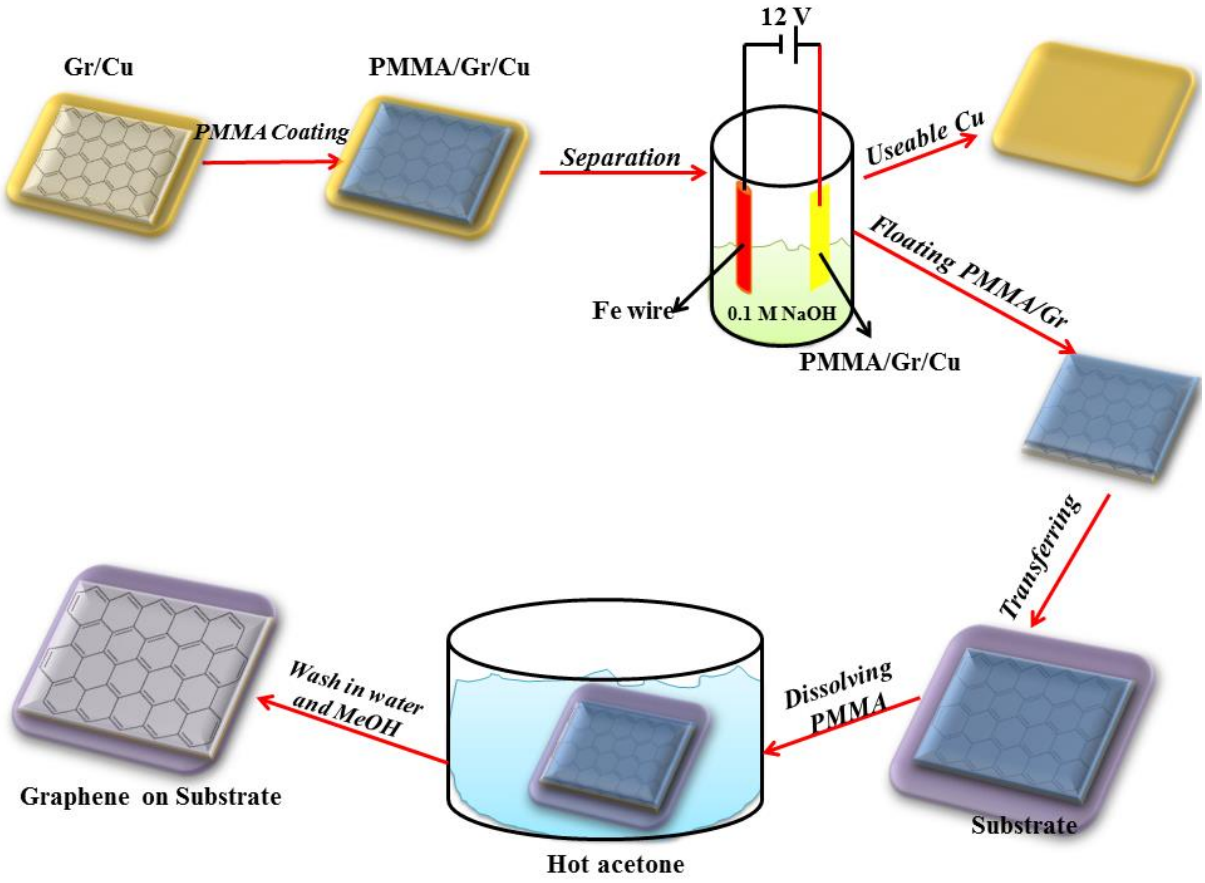

Scheme 3.2: Transfer procedure of the CVD-grown graphene films using electrochemical delamination technique.

3.2.3 Characterization

Raman spectroscopy is one of the most important characterization tools for assessing the number of layers and the quality in as-grown graphene films. Raman spectroscopic measurements were performed using a Bruker Raman Senterra spectrometer, equipped with a 20x optical objective for optical imaging. The characterization was performed with a 532 nm excitation laser using a very low laser power (0.5 mW) so as to avoid laser-induced heating of the films. The Raman measurements were collected from graphene films that were transferred onto the 300 nm SiO_2/Si substrates.

3.3 Results and discussions

For over a decade, Raman spectroscopy has been used as a convenient tool for investigating the quality and structural properties of graphene and related materials. This is because Raman spectroscopy is sensitive to the electronic structure of these materials. Additionally, with

Raman analysis it is easy to distinguish between mono-layered, bilayered, few layered and multilayered graphene sheets. The main features that are observed in the Raman spectra of graphene sheets are the G band (~1590 cm^{-1}), the 2D band (~2700 cm^{-1}), and the defect-induced D band (~1350 cm^{-1}) [56, 57]. The G band is the most prominent feature for graphitic materials, and it originates from the first-order Raman scattering process due to the in-plane vibrational modes of the sp^2-hybridized carbons in the graphene basal plane. The second-order 2D band arises from the double resonance process involving intervalley scattering by two in-plane transverse optical (TO) phonons near the *K* point of the Brillouin zone[56, 57]. Interestingly, in single-layered graphene sheets, the double resonance process results in an intense 2D band in comparison with the G band. Both G and 2D bands are present in all graphene-based materials; however their relative intensities, frequencies, and line widths are influenced by factors such as the number of graphene layers, stress, and laser excitation energy. Moreover, the occurrence of the D band in graphene sheets is related to the branches of the transverse optical phonons around the corner of the *K* point of the Brillouin zone; a process activated by intervalley double resonance involving one TO phonon and one defect [56-61]. In addition to the D band, the G band splits to give a shoulder at ~1620 cm^{-1} (D* band), which signifies the presence of more defects associated with graphene edges and/or a reduction in domain size [58, 61]. Finally, by determining the ratio of the intensity of G and 2D bands (I_G/I_{2D}), the peak width of the 2D band (full width at half maximum, FWHM), the line shape of 2D band, and the intensity ratios of D and G bands (I_D/I_G); the number of layers, stacking order, and quality of the graphene films can be obtained [62-64].

3.3.1 Influence of CH_4-flow rates on graphene films grown after a short growth time.

Figure 3.1a displays the typical Raman spectra of the individual graphene films transferred onto a 300 nm-tick SiO_2/Si wafer substrate and grown at 2 min using 5 sccm to 30 sccm CH_4 flow rates. The Raman spectra showed contributions from the first-order scattering mode (G band at 1580.2 – 1584.3 cm^{-1}), the second-order scattering mode (2D band located at 2677.3 – 2679.8 cm^{-1}) and two defect-induced modes located at 1338.4 – 1345.4 cm^{-1} and 1621.8 - 1622.9 cm^{-1} for D and D* bands, respectively (Table 3.1). The observed large D band intensity and the presence of the D* band can be attributed to the presence of disorder due to large amounts of edge defects, sp^3-bonded C-H species, and nanographitic basal plane [56-60].

Table 3.1: Peak positions and ratios for graphene films grown at 2 minutes

CH_4 flow rate (sccm)	Peak Position (cm^{-1})				Ratios	
	D	G	D*	2D	I_D/I_G	I_G/I_{2D}
5	1343.8	1584.3	1622.9	2678.9	1,10	0,930
10	1338.4	1580.2	-	2677.3	1,04	0,446
15	1345.4	1582.7	1621.8	2679.4	1,06	0,816
20	1345.2	1583.0	1622.0	2679.4	1,08	0,803
30	1345.0	1584.2	1622.8	2679.8	1,09	1,04

The ratio of the relative intensity of the G band to that of the 2D band was used to determine the thickness of the as-grown films. This was found to be in the range $0.446 < I_G/I_{2D} < 1.04$ (Fig.3.1b, red line), which indicated that there was formation of bilayered (10 sccm) to few and/or multilayered (5, 15-30 sccm) graphene films [56, 57, 59, 60]. Furthermore, a red shift of the Raman frequency of the G band by ~ 5 cm^{-1} was observed (Table 3.1), and this corroborated the formation of thicker graphene films [65-67]. The quality of the as-grown films was ascertained by calculating the ratio of the intensity of the disorder-induced D band to that of the G band, and it was observed that the as-synthesized films were highly defective as shown by the values $1.04 < I_D/I_G < 1.09$ [67-69].

Furthermore, based on the orientation of the graphene sheets, the stacking order bilayered and few layered graphene films can be classified as Bernal (AB), non-Bernal and rhombohedral (ABC) [24, 40, 51, 70-72]. This classification can be determined from the full width at half maxima of the 2D bands. For instance, the 2D band FWHM of 31.5 cm^{-1} for the graphene films grown using 10 sccm of CH_4 was characteristic of the Bernal stacking orientation found in bilayered graphene sheets [24, 51, 70-72]. In addition, FWHM's of graphene films grown using 5 sccm, 15 sccm and 20 sccm, as listed in figure 3.1a, compared well with the values obtained for Bernal (AB) stacked bilayered and/or trilayered graphene obtained by Chen *et al.* (~53 cm^{-1}) [73], Lee *et al.* (~51 cm^{-1}) [74], Fang *et al.* (~ 40-70 cm^{-1}) [71], and Madito *et al.* (~28- 53 cm^{-1}) [40]. On the other hand, the 30 sccm-grown graphene films exhibited a FWHM of ~80.4 cm^{-1}, which is characteristic to the formation of few to multilayered graphene films [24, 62].

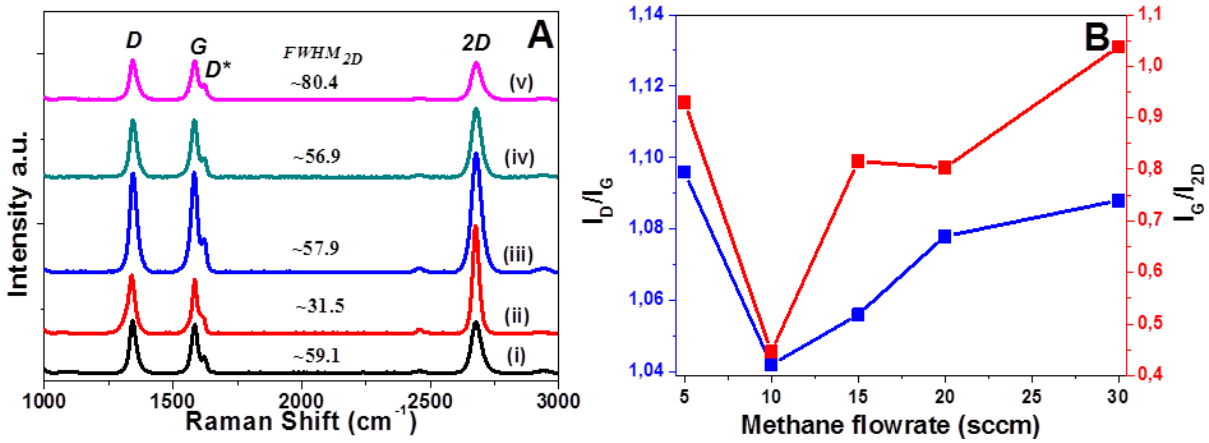

Figure 3.1:(a) Raman spectra of graphene films grown using (i) 5 sccm, (ii) 10 sccm, (iii) 15 sccm, (iv) 20 sccm, and (v) 30 sccm of CH_4, and (b) Plot of I_D/I_G and I_G/I_{2D} ratios.

Another important parameter for characterizing graphene layers is the line shape of the deconvoluted 2D peak. It is known that the 2D peak can be deconvoluted differently for single layered, bilayered, trilayered, few layered, multilayered graphene, and highly oriented pyrolytic graphite (HOPG). For instance, the 2D peak for multilayer graphene and HOPG are deconvoluted into two components ($2D_1$ and $2D_2$), into four components ($2D_{1B}$, $2D_{1A}$, $2D_{2A}$, and $2D_{2B}$) for bilayered, and into six components for trilayered. Few layered graphene can be deconvoluted into three components, and finally for monolayered graphene and turbostratic graphite, the 2D peak is fitted to a single Lorentzian peak [40, 70-72]. Finally, the shape of the 2D band is useful for further determination of the stacking order of the as-synthesized graphene films. For instance, the rhombohedral stacking order is characterized by a more asymmetric 2D peak, consisting of an enhanced main peak and a shoulder; whereas the Bernal order has a more symmetric 2D peak [24, 72].

Figure 3.2 shows in detail the deconvolution and line shapes of the 2D peaks for all graphene films grown using 5-30 sccm of CH_4. The symmetrical line shapes suggested that the films display a Bernal orientation. Further analysis showed that the 2D band of 10 sccm-grown graphene films was fitted with four Lorentzian peaks whose FWHM's represented that of a monolayered graphene sheet [70-72]. The symmetrical line shape as well as the four Lorentzian peak fittings demonstrates a Bernal or AB stacking order of bilayered graphene films. On the other hand, the 2D bands for graphene films grown using 5 sccm, 15 sccm, and 20 sccm of CH_4 flow rate were fitted with six Lorentzian peaks, which is characteristic of trilayered graphene films. Finally, formation of few layered graphene films when using 30 sccm of CH_4 was confirmed by the fitting of its 2D band with three Lorentzian peaks.

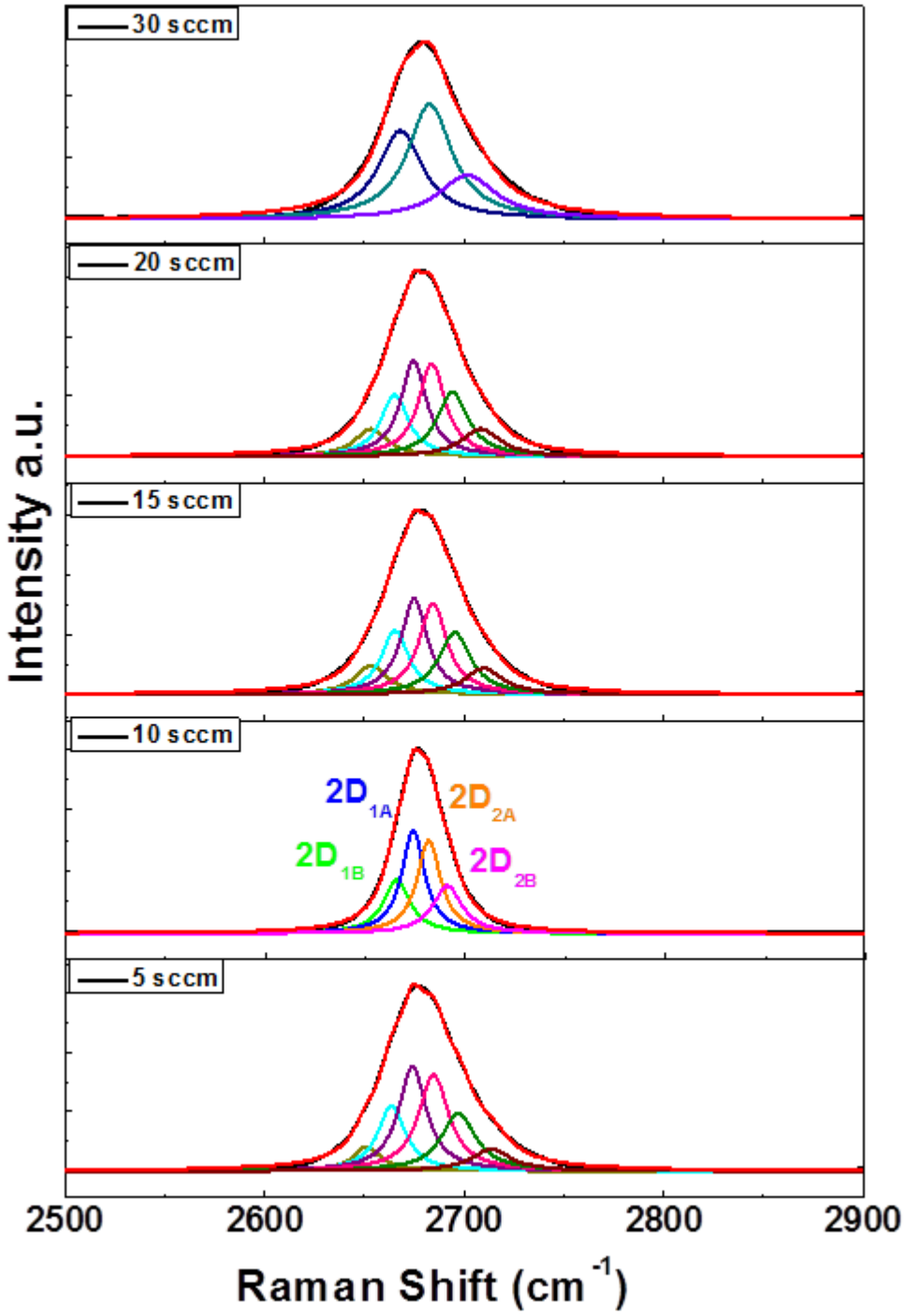

Figure 3.2: Deconvoluted 2D peaks of the graphene films grown at 2 min growth time.

In summary, the results show that when a low CH_4 flow rate (5 sccm) is used, there is a small concentration of active carbon species on the Cu surface to enable good aggregation and nucleation of carbon atoms into a continuous graphene film. As a result, these carbon species tend to only nucleate into small graphene 'islands' whose edges and defect sites act as growth sites for formation of highly defective trilayered graphene films (Fig. 3.1b). Furthermore, on increasing the CH_4 flow rate to 10 sccm, despite the very short growth time (2 min), there is a

sufficient amount of carbon species on the Cu surface to enable growth of continuous bilayered graphene films, as shown by the I_G/I_{2D} ratio value of 0.446 and the FWHM of ~31.5 cm^{-1} (Figs 3.1a and b). The high defect density (I_D/I_G = 1.04) suggests formation of incomplete coverage of the second and/or third layers onto the top of the monolayer. Finally, on increasing the CH_4 flow rate from 15 sccm to 30 sccm, the high concentration of the carbon species on the Cu foil surface leads to a competitive cracking of CH_4, adsorption, nucleation and aggregation of carbon species into graphene domains. The competitive processes result in the formation of many edge sites due to unmerged graphene domains, thereby leading to the observed high defect density (Fig. 3.1b). Moreover, the edge sites would facilitate the formation of graphene 'islands' on top of the underlying bilayered and/or trilayered graphene films.

3.3.2 Influence of CH_4 flow rates on graphene films grown after medium growth time regime.

Figure 3.3a depicts the Raman spectra of high quality graphene films grown at 10 min, with the main features corresponding to the G band (1583.3 – 1585.5 cm^{-1}) and the 2D band (2676.0 – 2678.8 cm^{-1}). The low relative intensity of the defect-sensitive D band (1341.0 – 1342.9 cm^{-1}) as well as the almost negligible D* band (~ 1620 cm^{-1}) confirmed the formation of high quality graphene films [56-60] (Table 3.2). Additionally, the high quality of the as-grown films was established from the ratio of the intensities of defect-sensitive D band and the graphitic-G band. The results showed a ratio $0.206 < I_D/I_G < 0.669$ (Fig. 3.3b, blue line), which indicated that the as-gown 10 min-graphene films exhibited very good quality [67-69]. Moreover, throughout the growth regime it was observed that the relative intensity of the graphitic-G band was almost half the height of the 2D band [56-60]. This was indicative of the growth of mainly bilayered graphene films. These results were supported by the I_{2D}/I_G ratios (Fig. 3.3b, red line) which were found to be in a $0.362 < I_G/I_{2D} < 0.598$ range. As was mentioned earlier, the 2D band FWHM was used to establish the thickness and/or orientation of graphene films; so for all the 10 min as-grown graphene films, the range was found to be ~ 25.0 cm^{-1} < FWHM < ~ 38.9 cm^{-1}. Interestingly, graphene films grown using 10 sccm of CH_4 revealed a FWHM value of ~ 25.0 cm^{-1}, which is considered with the characteristic of monolayered and/or non-Bernal bilayered graphene [24, 40, 51, 70-72]. On the contrary, the FWHM's of other films were in agreement with the reported values for Bernal (AB) oriented bilayered and/or trilayered graphene [51, 70-74].

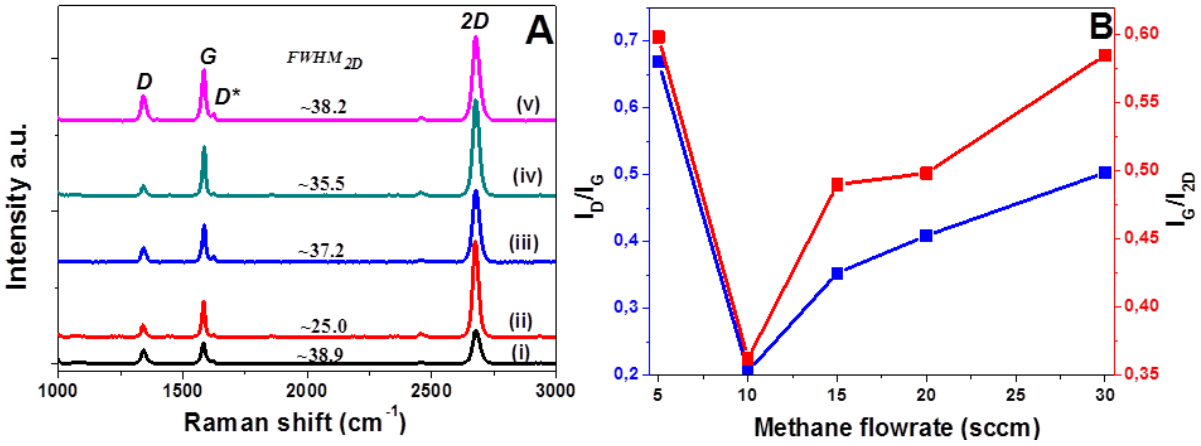

Figure 3.3: (a) Raman spectra of graphene films grown using (i) 5 sccm, (ii) 10 sccm, (iii) 15 sccm, (iv) 20 sccm, and (v) 30 sccm of CH_4, and (b) Plot of I_D/I_G and I_G/I_{2D} ratios of the as-grown films.

Table 3.2: Peak positions and Ratios for graphene films grown at 10 minutes

CH_4 flow rate (sccm)	Peak Position (cm^{-1})				Ratios	
	D	G	D*	2D	I_D/I_G	I_G/I_{2D}
5	1342.9	1583.2	-	2678.8	0,669	0,598
10	1341.0	1583.5	-	2676.0	0,206	0,362
15	1342.4	1585.5	-	2677.7	0,352	0,490
20	1342.0	1584.3	-	2677.7	0,409	0,498
30	1342.4	1583.9	-	2677.7	0,503	0,585

Since the FWHM values showed that the as-grown films exhibited a Bernal stacking order, their 2D band were then fitted with Lorentzian peaks so as to confirm the actual thickness of the as-synthesized films. For example, the 2D band of the10 sccm-grown graphene films was fitted to a single Lorentzian peak, which is representative of monolayered and/or non-Bernal bilayered graphene [40, 70-72]. Additionally, figure 3.4 shows that the 2D bands exhibited a symmetrical line and the bands were fitted to four (15 sccm and 20 sccm) and six Lorentzian peaks (5 sccm and 30 sccm); which was representative of a Bernal stacking orientation [24, 51, 70-72]. The fitting of four Lorentzian peaks for 2D bands indicated that the 15 sccm- and 20 sccm-grown graphene films contained a Bernal (AB) stacking order characteristic of bilayered graphene. Finally, the fitting with six Lorentzian peaks for the 5 sccm– and 30

sccm-grown films suggested the presence of a Bernal (ABA) orientation of trilayered graphene [24].

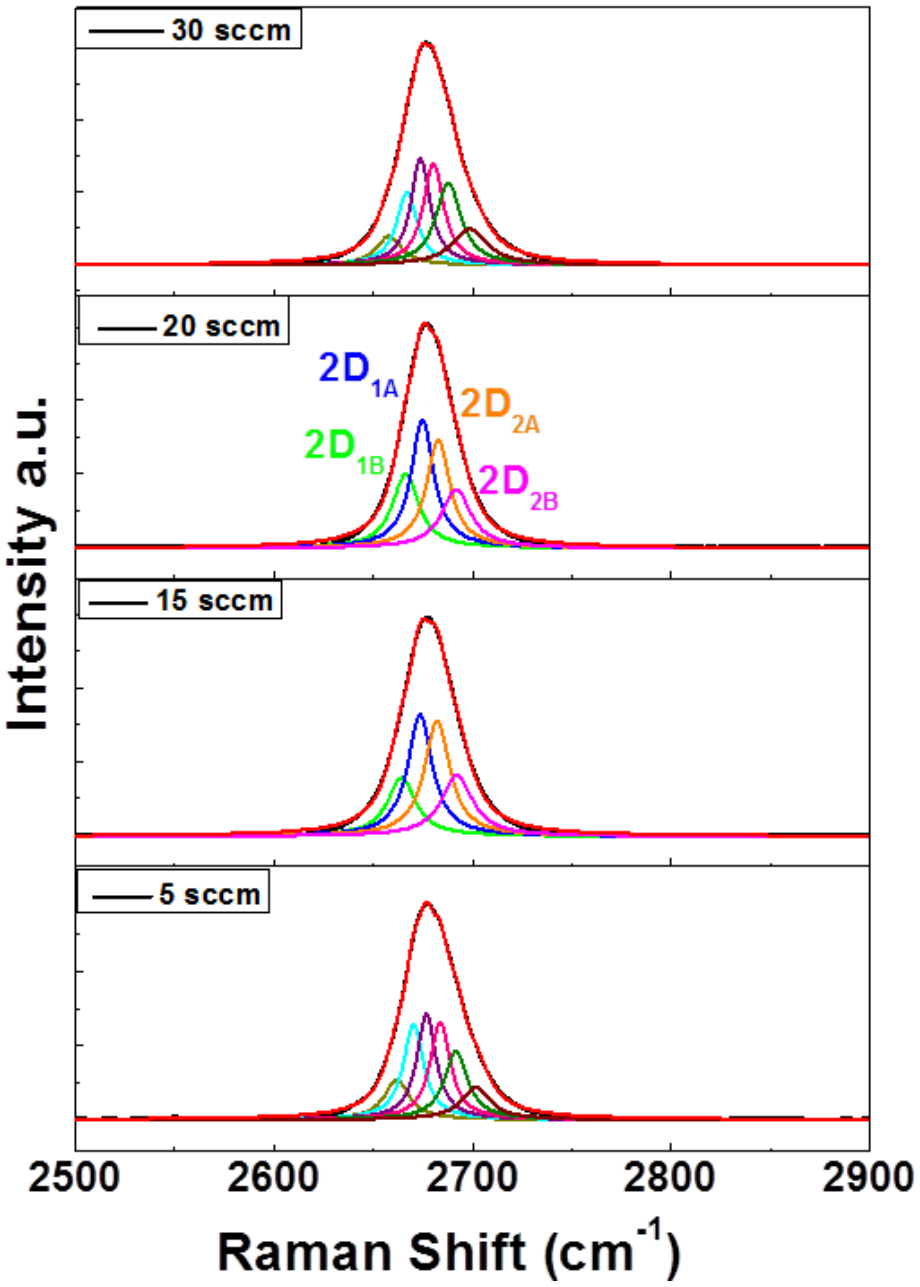

Figure 3.4: Deconvoluted 2D peaks of the graphene films grown at 10 min.

To summarise: From Raman analysis, it was observed that despite the low CH_4 flow rate (5 sccm) which led to the low concentration of active carbon species on the growth substrate, the growth time was long enough to permit good aggregation and nucleation of carbon atoms into a graphene domains. The FWHM (~38.9 cm^{-1}) and the I_G/I_{2D} (0.598) suggested the formation of trilayered graphene films. However, the high defect density (I_D/I_G = 0.669) could indicate the presence of many domain edges and defect sites from the incomplete

formation of the third graphene layer on top of the continuous bilayered graphene background. On increasing the CH_4 flow rate to 10 sccm, both the growth time and carbon concentration are sufficient to enable nucleation and coalescence of the graphene domains into a high quality (I_D/I_G = 0.206) and bilayered (I_G/I_{2D} = 0.362) graphene film. Moreover, increasing the CH_4 flow rate from 15 sccm to 20 sccm resulted in a synthesis of slightly thicker bilayered graphene films, as shown by the red shift in the Raman frequency of the G band [65, 66] for 15 sccm- (1585.5 cm^{-1}) and 20 sccm-grown (1584.34 cm^{-1}) graphene films. The observed decreasing quality of the films ($0.352_{15\ sccm} < I_D/I_G < 0.409_{20\ sccm}$) shows the effect of the competitive cracking of CH_4, adsorption and nucleation of carbon atoms on the Cu, which then prevents the coalescence of graphene domains into a continuous bilayered graphene film. Finally, when the CH_4 flow rate is increased to 30 sccm, the quality of the as-grown films further degrades (I_D/I_G = 0.503), hence indicating that the high concentration of carbon species on the growth substrate results in increased competitive cracking of CH_4, as well as adsorption and nucleation of carbon atoms. However, the 10 min growth time is still sufficient to enable the growth of bilayered graphene films. The defective second layer contains many edge sites, which would then facilitate the formation of graphene 'islands' onto top of the underlying bilayered, and thus leading to the formation of trilayered graphene films.

3.3.3 Influence of CH_4 flow rates on graphene films grown after long growth times.

The quality, thickness and the stacking orientation of the graphene films grown using a long-time regime were ascertained by analyses of their Raman spectra. Figure 3.5a displays the Raman spectra of the 20 min-grown graphene films. The observable features are two disorder-induced and Raman-forbidden peaks located at ~1342.1 – 1343.6 cm^{-1} and ~ 1623.2 – 1624.5 cm^{-1}, corresponding to the D and D* bands respectively. Additionally, the graphitic-G band (~1583.2 – 1586.0 cm^{-1}) and the lattice distortion-sensitive 2D band (~2676.4 – 2679.7 cm^{-1}) were found to be the prominent features (Table 3.3). Determination of the I_G/I_{2D} ratio ($0.404 < I_G/I_{2D} < 0.513$, Fig. 3.5b, red line) showed that bilayered and/or few layered graphene films had formed [56-60], with the quality ranging from good (10 sccm, I_D/I_G = 0.119) to very defective (15 sccm, I_D/I_G = 0.942 and other films, Fig. 3.5b, blue line). In order to establish the orientation of the as-grown films, the FWHM's of their 2D bands were determined. The results showed that all graphene films exhibited FWHM values in the range of 29.2 cm^{-1} - 50.6 cm^{-1}; and these were characteristic of bilayered graphene with a Bernal (AB) stacking order [24, 40, 51, 70-72].

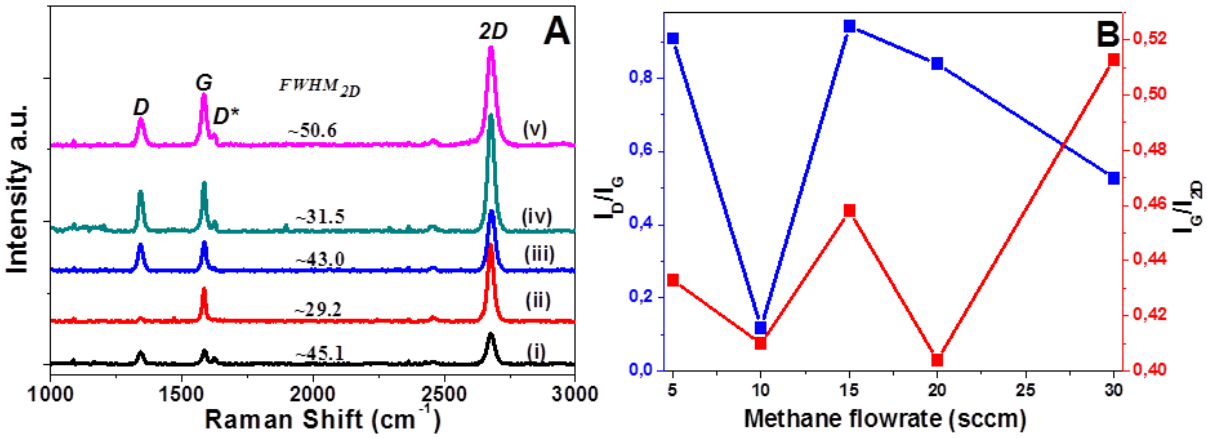

Figure 3.5: (a) Raman spectra of graphene films grown using (i) 5 sccm, (ii) 10 sccm, (iii) 15 sccm, (iv) 20 sccm, and (v) 30 sccm of CH_4, and (b) Plot of I_D/I_G and I_G/I_{2D} ratios of the as-grown films.

Table 3.3: Peak positions and Ratios for graphene films grown at 20 minutes

CH_4 flow rate (sccm)	Peak Position (cm^{-1})				Ratios	
	D	G	D*	2D	I_D/I_G	I_G/I_{2D}
5	1342.4	1586.0	1623.8	2677.5	0,909	0,433
10	1342.4	1583.2	-	2676.4	0,119	0,41
15	1342.1	1584.7	-	2679.7	0,942	0,458
20	1342.4	1583.7	1624.5	2677.7	0,839	0,404
30	1343.6	1583.3	1623.2	2678.2	0,528	0,513

Further analysis for the determination of the line shape of the 2D bands and their fitting with Lorentzian peaks was performed so as to establish the exact thickness of all 20 min-grown graphene films. Figure 3.6 showed that for both 10 sccm- and 20 sccm-grown graphene films, the 2D bands could be deconvoluted into four component peaks ($2D_{1B}$, $2D_{1A}$, $2D_{2A}$, and $2D_{2B}$), suggesting the growth of AB-stacked bilayered graphene films [70-74]. On the other hand, the rest of the graphene exhibited 2D bands that were fitted with six Lorentzian peaks, hence indicating the growth of Bernal (ABA) trilayered graphene films [24, 72]. Finally, in all cases the line shape of the 2D bands was symmetrical, which is representative of Bernal orientation in stacked graphene.

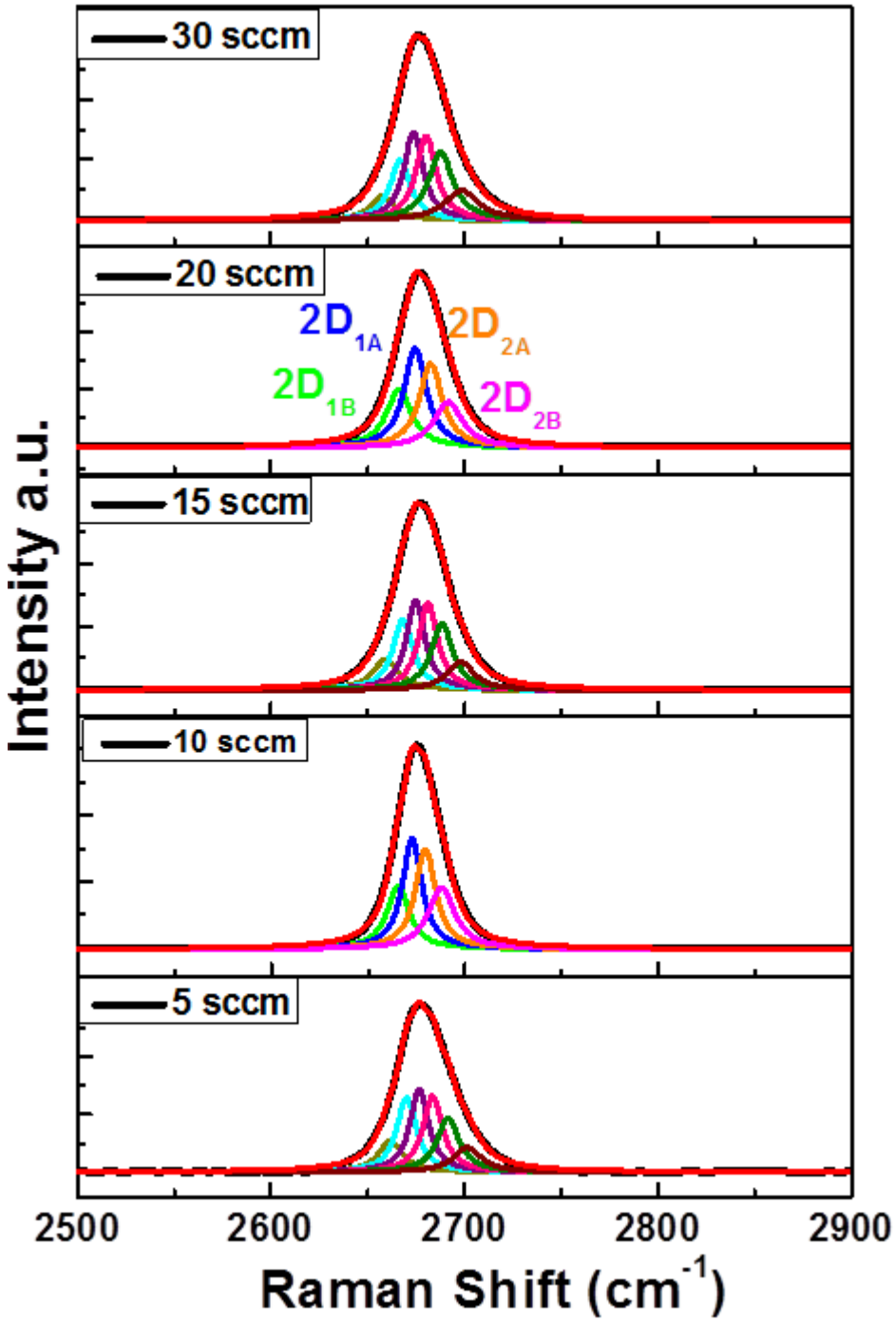

Figure 3.6: Deconvoluted 2D peaks of the graphene films grown at 20 min.

To give a brief summary: It was observed that regardless of the low concentration of carbon species (5 sccm) on the Cu surface, the growth time of 20 min is sufficient to allow the mobility of carbon atoms to move to the active site. The obtained high defect density (I_D/I_G = 0.909) could indicate that migration of carbon atoms to the active site may be limited at low concentrations, hence hindering the merging of the graphene domains into an ordered thin graphene film and therefore leading to formation of many edges sites. As a result, the

additional carbon atoms (ad-atoms) tend to nucleate on the edge defects, hence resulting in the formation of bilayered and/trilayered graphene films. The same phenomenon was observed for both 15 sccm-grown graphene films. In this case the continuous competitive decomposition of CH_4 on the active sites of Cu also led to formation of highly defective ((I_D/I_G = 0.942) bilayered and/trilayered graphene films due to the presence of edge sites and ad-atoms. However, on increasing the CH_4 flow rate (10 sccm, 20 sccm, and 30 sccm), the quality of the as-grown graphene films improved, as shown by the decreasing I_D/I_G ratio (Fig. 3.6b). Interestingly, when 10 sccm CH_4 flow rate is used, the resulting graphene films are of high quality and are bilayered. This is indicative that the migration of carbon atoms to active sites and growth of graphene domains is much faster than the addition of ad-atoms under the 10 sccm CH_4 flow rate conditions.

3.4 Conclusions

A series of experiments were conducted to optimise the growth of high quality graphene films on a Cu catalyst using atmospheric pressure CVD. Different growth times (2, 10, and 20 min) and methane flow rates (5, 10, 15, 20, and 30 sccm) were used to grow graphene films with varying thicknesses and qualities. The results showed that short growth times (2 min) led to the growth of highly defective bilayered to few layered graphene films, as shown by the defect density ratio ($1.04 < I_D/I_G < 1.09$) and the I_G/I_{2D} ratio (0.446 to 1.04). In contrast, a medium growth time (10 min) resulted in the formation of predominantly bilayered graphene films with very good quality, as indicated by the defect density in the range of $0.209 < I_D/I_G < 0.669$. Finally, a long growth time (20 min) led to the formation of mostly bi- and trilayered graphene films, which exhibited a slightly poor quality ($0.119 < I_D/I_G < 0.942$ range). In general, the results showed that growth of graphene films throughout all the time regimes followed a self-limiting reaction mechanism. This reaction mechanism can be attributed to the low carbon solubility in copper. Since the main objective was to obtain good growth conditions for the formation of good quality graphene films under an APCVD system, the 10 sccm of CH_4 was chosen as the optimum methane concentration. Additionally, the medium time regime (10 min) was selected as the optimum growth time for formation of high quality bilayered graphene films under this growth condition. Therefore, for synthesis of graphene films by the APCVD technique in future studies in our group, the optimum growth conditions were selected to be as follows: CH_4 flow rate (10 sccm), growth time (10 min), and H_2 concentration (10 sccm).

References

1. Geim, A. K., K. S. Novoselov. *Nat. Mater*. **2007**, *6*, 183-191.
2. Freitag, M., H. Y. Chiu, M. Steiner, V. Perebeinos, P. Avouris. *Nat. Nanotechnol*. **2010**, *5*, 497-501.
3. Novoselov, K. S., A. K. Geim, S. V. Morozov, D. Jiang, Y. Zhang, S. V. Dubonos, I. V. Grigorieva, A. A. Firsov. *Science*, **2004**, *306*, 666−669.
4. Geim, A. K. *Science*, **2009**, *324*, 1530–1534.
5. Geim, A.K., K. S. Novoselov, S. Morozov, D. Jiang, M. I. Katsnelson, S. Dubonos, I. Grigorieva, A. Firsov. *Nature*, **2005**, *438*, 197-200.
6. Wang, Y. Y., Z. H. Ni, T. Yu, Z. X. Shen, H. M. Wang, Y. H. Wu, W. Chen, A. T. S. Wee. *J. Phys. Chem. C*. **2008**, *112*, 10637-10640.
7. Cao, H. L., Q. Yu, L.A. Jauregui, J. Tian, W. Wu, Z. Liu, R. Jalilian, D. K. Benjamin, Z. Jiang, J. Bao, S. S. Pei, Y. P. Chen. *Appl. Phys. Lett*. **2010**, *96*, 122106.
8. Lee, C., X. Wei, J. W. Kysar, J. Hone. *Science*, **2008**, *321*, 385–388.
9. Zhang, Y., J. W. Tan, H. L. Stormer, P. Kim. *Nature*, **2005**, *438*, 201–204.
10. Balandin, A. A., S. Ghosh, W. Bao, I. Calizo, D. Teweldebrhan, F. Miao, C. N. Lau. *Nano Lett.* **2008**, *8*, 902–907.
11. Zhu, Y., S. Murali, W. Cai, X. Li, J.W. Suk, J. R. Potts, R. S. Ruoff. *Adv. Mater*. **2010**, **22**, 3906–3924.
12. Schwierz, F. *Nat. Nanotechnol*. **2010**, *5*, 487−496.
13. Ang, P. K., W. Chen, A. T. S. Wee, K. P. Loh. *J. Am. Chem. Soc*. **2008**, *130*, 14392−14393.
14. Pumera, M. *Mater. Today*, **2011**, *14*, 308−315.
15. Dodoo-Arhin D., M. Fabiane, A. Bello, N. Manyala. *Ind. Eng. Chem. Res*. **2013**, *52*, 14160-14168.
16. Wang, X., L. Zhi, K. Müllen. *Nano Lett.* **2008**, *8*, 323–327.
17. Kim, K. S., Y. Zhao, H. Jang, S. Y. Lee, J. M. Kim, K. S. Kim, J. H. Ahn, P. Kim, J. Y. Choi, B. H. Hong. *Nature*, **2009**, *457*, 706−710.
18. Stoller, M. D., S. Park, Y. Zhu Y, J. An, R. S. Ruoff. *Nano Lett*. **2008**, *8*, 3498–3502.
19. Zhang, Y. P., H. B. Li, T. Lu, L. K. Pan, Z. Sun. *J. Electrochem*. **2009**, *634*, 68-71.
20. Stankovich, S, D. A. Dikin, G. H. B. Dommett, K. M. Kohlhaas, E. J. Zimney, E. A. Stach, R. D. Piner, S. T. Nguyen, R. S. Ruoff. *Nature*, **2006**, *442*, 282–286.

21. Emtsev, K. V., A. Bostwick, K. Horn, J. Jobst, G. L. Kellogg, L. Ley, J. L. McChesney, T. Ohta, S. A. Reshanov, J. Rohrl, E. Rotenberg, A. K. Schmid, D. Waldmann, H. B. Weber, T. Seyller. *Nature Mater.* **2009**, *8*, 203-207.
22. Stankovich S, D. A. Dikin, R. D. Piner, K. A. Kohlhaas, A. Kleinhammes, Y. Jia Y. *Carbon*, **2007**, *45*, 1558–1565.
23. Li, D., M. B. Muller, S. Gilje, R. B. Kaner, G. G. Wallace. *Nature Nanotechnol*. **2008**, *3*, 101–105.
24. Reina, A., X. Jia, J. Ho, D. Nezich, H. Son, V. Bulovic, M. S. Dresselhaus, J. Kong. *Nano Lett*. **2009**, *9*, 30-35.
25. Liao, C. D., Y. Y. Lu, S. R. Tamalampudi, H. C. Cheng, Y. T. Chen. *Phys. Chem. A.* **2013**, *117*, 9454-9461.
26. Juang, Z. Y., C. Y. Wu, A. Y. Lu, C. Y. Su, K. C. Leou, F. R. Chen, C. H. Tsai. *Carbon,* **2010**, *48*, 3169-3174.
27. Yang, X., X. Dou, A. Rouhanipour, L. Zhi, H. J. Rader, K. Mullen. *J. Am. Chem. Soc*. **2008**, *130*, 4216–4217.
28. Ago, H., Y. Ito, N. Mizuta, K. Yoshida, B. Hu, C. M. Orofeo, M. Tsuji, K Ikeda, S. Mizuno. *ACS Nano,* **2010**, *4*, 7407-7414.
29. Wang, S., L. Qiao, C. Zhao, X. Zhang, J. Chen, H. Tian, W. Zheng, Z. Han. *New J. Chem.* **2013**, *37*, 1616-1622.
30. Gao, L. W. Ren, H. Xu, L. Jin, Z. Wang, T. Ma, L. P. Ma, Z. Zhang, Q. Fu, L. M. Peng, X. Bao, H. M. Cheng. *Nature Communications,* **2012**, *3*, 699 (1-7).
31. Cushing, G. W., V. Johanek, J. K. Navin, I. Harrison. *J. Phys. Chem. C.* **2015**, *119*, 4759-4768.
32. Coraux, J., A. T. N'Diaye, C. Busse, T. Michely. *Nano Lett*. **2008**, *8*, 565-570.
33. Locatelli, A., G. Zamborlini, T. O. Mentes. *Carbon,* **2014**, *74*, 237-248.
34. Pan, Y., H. Zhang, D. Shi, J. Sun, S. Du, F. Liu, H. Gao. *Adv. Mater*. **2009**, *21*, 2777−2780.
35. Reina A, S. Thiele, X. Jia, S. Bhaviripudi, M. S. Dresselhaus, J. A. Schaefer, J. Kong. *Nano Res*. **2009**, *2*, 509–516.
36. Garlow, J. A., L. K. Barrett, L. Wu, K. Kisslinger, Y. Zhu, J. F. Pulecio.. *Scientific Reports,* **2016**, *6*, 19804 (1-11).
37. Sun, Z., Z. Yan, J. Yao, E. Beitler, Y. Zhu, J. M. Tour. *Nature*, **2010**, *468*, 549–552.

38. Li, X. S., W. W. Cai, J.H. An, S. Kim, J. Nah, D. X. Yang, R. Piner, A. Velamakanni, I Jung, E. Tutuc, S. K. Banerjee, L. Colombo, R. S. Ruoff. *Science*, **2009**, *324*, 1312−1314.
39. Wan, D. Y., T. Q. Lin, H. Bi, F. Q. Huang, X. M. Xie, I. W. Chen, M. H. Jiang. *Adv. Funct. Mater*. **2012**, *22*, 1033−1039.
40. Madito, M. J., N. Manyala, A. Bello, J. K. Dangbegnon, T. M. Masikhwa, D. Y. Momodu. *RSC Adv.* **2016**, *6*, 28370-28378.
41. Lin, T. F. Huang, D. Wan, H. Bi, X. Xie, M. Jiang. *Nanoscale*, **2013**, *5*, 5847-5853.
42. Mattevi, C., H. Km, M. Chhowalla. *J. Mater. Chem.* **2011**, *21*, 3324-3334.
43. Reddy, K. M., A. D. Gledhill, C. H. Chen, J. M. Drexler, N. P. Padture. *App. Phys. Lett.* **2011**, *98*, 113117 (1-4).
44. Li, Z. P. Wu, C. Wang, X. Fan, W. Zhang, X. Zhai, C. Zeng, Z. Li, J. Yang, J. Hou. *ACS Nano*, **2011**, *5*, 3385-3390.
45. Jang, J., M. Son, S. Chung, K. Kim, C. Cho, B.H. Lee, M. H. Ha. *Scientific Reports*, **2015**, *5*, 17955 (1-7).
46. Rao, R., K. Weaver, B. Maruyama. *Mater. Express*, **2015**, *5*, 541-546.
47. Cabrero-Vilatela, A., R. S. Weatherup, P. Braeuninger-Weimer, S. Caneva, S. Hofmann. *Nanoscale*, **2016,** *8*, 2149-2158.
48. Li, J., H. Ji, X. Zhang, X. Wang, Z. Jin, D. Wang, and L. J. Wan. *Chem. Commun.* **2014**, *50*, 11012-11015.
49. Kostogrud, A. I., K. V. Trusov, D. V. Smovzh. *Adv. Mater. Inter.* **2016**, *3*, 1500823 (1-6).
50. Feng, Y., D. J. Trainer, H. Peng, Y. Liu, K. Chen. *J. Mater. Sci. Technol.* **2016**, *872*.
51. Lavin-Lopez, M. P., J. L. Valverde, M. C. Cuevas, A. Garrido, L. Sanchez-Silva, P. Martinez, A. Romero-Izquiedo. *Phys. Chem. Chem. Phys.* **2014**, *16*, 2962-2970.
52. Sun, Z. Z., A.-R. O. Raji, Y. Zhu, C. S. Xiang, Z. Yan, C. Kittrell, E. L. G. Samuel, J. M. Tour. *ACS Nano*, **2012**, *6*, 9790–9796.
53. Vlassiouk, I., M. Regmi, P. Fulvio, S. Dai, P. Datskos, G. Eres, S. Smirnov. *ACS Nano*, **2011**, *5*, 6069− 6076.
54. Jung, H. S. H. Z. Tsai, D. Wong, C. Germany, S. Kahn, Y. Kim, A. S. Aikawa, A. K. Desai, G. F. Rodgers, A. J. Bradley, J. Velasco, K. Watanabe, T. Taniguchi, F. Wang, A. Zettl, M. F. Crommie. *J. Vis. Exp.* **2015**, *101*, e52711 (1-9).
55. Wang, Y., Y. Zheng, X. Xu, E. Dubuisson, Q. Bao, J. Lu, K. P. Loh. *ACS Nano*. **2011**, 5, 9927-9933.

56. Ferrari, A. C., J. C. Meyer, V. Scardaci, C. Casiraghi, M. Lazzeri, F. Mauri, S. Piscanec, D. Jiang, K. S. Novoselov, S. Roth, A. K. Geim. *Phys. Rev. Lett*. **2006,** *97***,** 187401 (1-4).
57. Casiraghi, C., S. Pisana, K. S. Novoselov, A. K. Geim, A. C. Ferrari. *Appl. Phys. Lett*. **2007,** *91***,** 233108 (1-3).
58. Ferrari, A. C. *Solid State Commun*. **2007,** *143*, 47-57.
59. Malard, L. M., M. A. Pimenta, G. Dresselhaus, M. S. Dresselhaus. *Phys. Rep.* **2009**, *473*, 51-87.
60. Ferrari, A. C., D. M. Basko. *Nat. Nanotechnol.* **2013**, *8*, 235-246.
61. Piscanec, S., M. Lazzeri, F. Mauri, A. C. Ferrari, J. Robertson. *Phys. Rev. Lett.* **2004**, *93*, 185503-185506.
62. Hao, Y., Y. Wang, L. Wang, Z. Ni, Z. Wang, R. Wang, C. K. Koo, Z. Shen, J. T. L. Thong. *Small*, **2010**, *2*, 195-200.
63. Luo, X., X. Lu, C. Cong, T. Yu, Q. Xiong, S. Y. Quek. *Scientific reports*, **2015**, *5*, 14565 (1-13).
64. Ni, Z., Y. Wang, T. Yu, Z. Shen. *Nano. Res.* **2008**, *1*, 273-291.
65. Gupta, A., G. Chen, P. Joshi, S. Tadigadapa, P. Eklund. *Nano Lett.* **2006**, *6*, 2667-2673.
66. Kalbac, M., H. Farhat, J. Kong, P. Janda, L. Kavan, M. S. Dresselhaus. *Nano Lett.* **2011**, *11*, 1957-1963.
67. Ferrari, A. C., J. Robertson. *Phys. Rev. B.* **2011**, *61*, 14095-14107.
68. Cancado, L. G., A. Jorio, E. H. Martins- Ferreira, F. Stavale, C. A. Achete, R. B. Capaz, M. V. Moutinho, A. Lombardo, T. S. Kulmala, A. C. Ferrari. *Nano Lett.* **2011**, *11*, 3190-3196.
69. Eckmann, A, A. Felten, A. Mishchenko, L. Britnell, R. Krupke, K. S. Novoselov, C. Casiraghi. *Nano. Lett.* **2012**, *12*, 3925-3930.
70. Kim, K., S. Coh, L. Z. Tan, W. Regan, J. M. Yuk, E. Chatterjee, M. F. Crommie, M. L. Cohen, S. G. Louie, A. Zettl. *Phys. Rev. Lett.* **2012**, *108*, 246103.
71. Fang, W., A. L. Hsu, R. Caudillo, Y. Song, A. G. Birdwell, E Zakar, M. Kalbac, M. Dubey, T. Palacios, M. S. Dresselhaus, P. T. Araujo, J. Kong. *Nano Lett.* **2013**, *13*, 1541-1548.
72. Cong, C., T. Yu, K. Sato, J. Shang, R. Saito, G. Dresselhaus, M. S. Dresselhaus. *ACS Nano*, **2011**, *5*, 8760-8768.

73. Chen, S., W. Cai, R. D. Piner, J. W. Suk, Y. Wu, Y. Ren, J. Kang, R. S. Ruoff. *Nano Lett.* **2011**, *11*, 3519-3525.
74. Lee, S., K. Lee, Z. Zhong. *Nano Lett.* **2010**, *10*, 4702-4707.

Chapter 4

The effect of hydrogen on the synthesis of high quality graphene films

4.1. Introduction

Graphene is an atomic thin film of sp^2-hybridized carbon atoms [1, 2] with the honeycomb lattice, and is an important material due to its remarkably unique electronic[1, 3], optical[4], mechanical[5], chemical[4] and thermal[6] properties. Since the successful isolation of graphene sheets from highly oriented pyrolytic graphite (HOPG) in 2004[1, 2, 7], various experimental approaches have been developed to make graphene, including epitaxial growth on single crystalline SiC[8, 9], chemical reduction of exfoliated graphene oxide[10, 11], and chemical vapour deposition (CVD) on transition metals[12-14]. The recently developed CVD method on transition metals has emerged as a convenient synthetic route due to its high compatibility with possible industrial synthesis potentials and suitability for growing large-area and high-quality graphene films, while also maintaining the excellent material properties of the graphene[1, 14-18]. In particular, the copper catalyst is considered to be an excellent substrate for growing high-quality graphene films with uniform thickness due to the low solubility of carbon in Cu [15, 19, 20].

Generally, a successful CVD-growth of graphene is mainly dependent on the carbon solubility into the transition metal of interest[18, 21-24] and this synthesis technique is considered as a complicated heterogeneous catalysis process, comprising of at least six important surface reactions (Scheme 4.1). These surface reactions include [15, 25-29]: (1) adsorption and catalytic-decomposition of H_2 on the Cu surface, (2) adsorption and dissociation of a surface-bound carbon precursor into active C species, (3) diffusion and dissolution of carbon species into the metal bulk, (4) migration and segregation of C species on the metal surface, (5) surface nucleation of C species, growth of graphene domains into layers and carbon incorporation into the growing graphene layer, and finally (6) etching of the as-formed graphene domains by H_2. Due to the significantly low carbon solubility in Cu [15, 19, 20], the steps dependent on the diffusion, dissolution and segregation of carbon species are negligible (i.e. steps 3 and 4).

However, as the active species from both carbon and hydrogen co-exist on the Cu surface, the growth mechanism and kinetics of graphene films has been found to be affected and/or significantly changed by the H and C atoms. As a result, intensive research has been conducted to study and comprehensively understand the role of hydrogen in influencing the adsorption properties of carbon atoms that facilitate the growth of uniform and continuous graphene films on a copper catalyst.

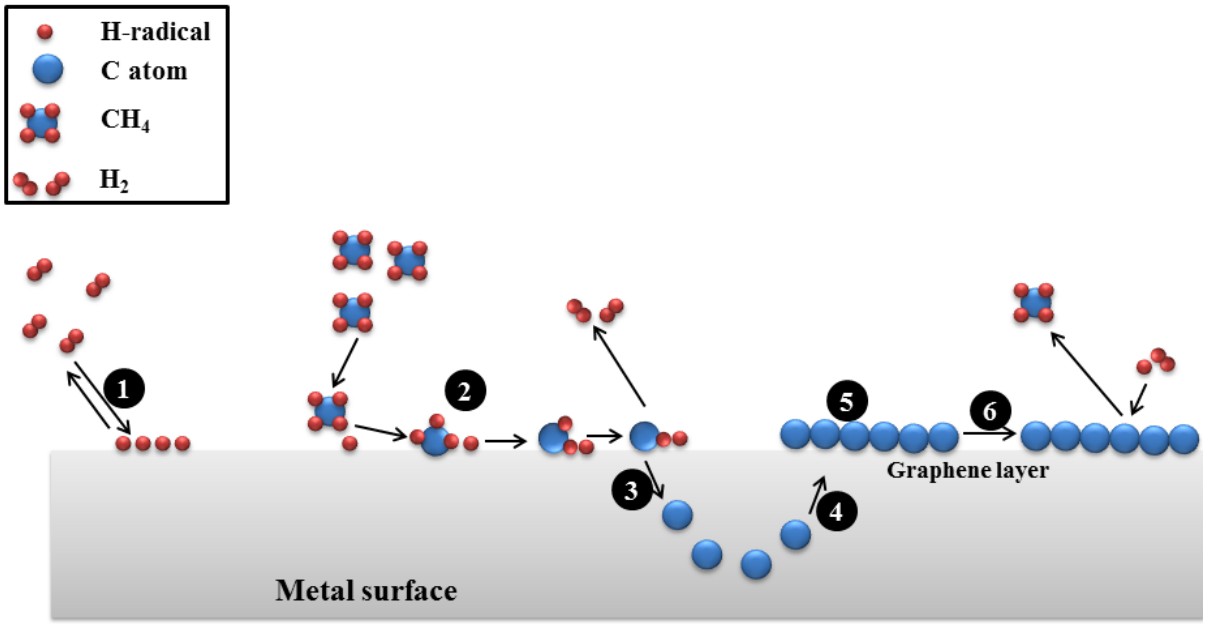

Scheme 4.1: Surface reactions of H_2 and CH_4 on Cu foil during graphene growth.

Theoretical and experimental research has shown that H_2 has two significant roles to play during the CVD-growth of graphene films. Primarily, hydrogen has been found to act as a cleaning agent by reducing the oxide layer on the Cu foil [15, 25-37]. The cleaning process leads to the exposure of the active sites for catalytic cracking of CH_4 into active carbon species, which would nucleate and coalescence into graphene films[25-37]. For instance, Gan *et al.* studied the role of H_2 during the APCVD-growth of sub-centimetre single-crystal graphene grains (~ 5.9 nm in diameter), based on the seeding of Cu nanoparticles [37]. They showed that H_2 played the main role of smoothing the Cu surface by removing oxidized surface irregularities. This resulted in the formation of large Cu nanoparticles (≥ 20 nm), which they observed to be good nucleation sites for large hexagonal domains.

The second important role of H_2 during the CVD-growth of graphene is its etching effect on the edges of the graphene domains, which leads to the introduction of more defects and/or active sites [25-37]. Interestingly, the role of H_2 as an etchant has been found to be the most

significant factor for the growth of graphene domains with controllable thickness, shape, size, edge configuration, stacking order, and crystalline quality [24-38]. Yan *et al.* indicated that the CVD-fabrication of three-dimensional (3D) hexagonal graphene onion rings followed a H_2-assisted edge-nucleation growth mechanism [38]. They suggested that the ring formation was stimulated by the hydrogenation of the graphene edges, which then facilitated the 3D growth of the new graphene layer on the edge and under the already formed graphene layer. In another research report, Vlassiouk *et al.* indicated that the size and morphology of the graphene domains was dependent on the concentration of H_2 in the total gas mixture [33]. They suggested that H_2 acted as a co-catalyst for formation of active surface-bound carbon species that are required for graphene growth, while at the same time it controlled the growth of graphene grains into a larger and well-defined hexagonal shape by etching away the weak carbon-carbon bonds. Furthermore, Zhang and co-workers systematically studied the hydrogen-induced effects on CVD-growth of high quality graphene films by regulating the growth parameters that are mainly related to hydrogen[34]. Their results demonstrated that under high hydrogen flow rates (1000 sccm), the competitive H_2 etching effect was more prominent and led to transformation of the edges of the graphene domains from straight to toothed, and then to zigzag shapes.

Although H_2 has been shown to be important for controlling the shape and dimensions of graphene domains/grains, its deleterious effect on the quality of the graphene films has also been reported[24, 39-41]. An increasing H_2 concentration has been shown to lead to an increase in the density of wrinkles and inter-island junctions, thereby contributing to the low quality of the as-grown graphene films and their resultant large sheet resistance [23, 39-41]. To circumvent this problem, Gao *et al.* synthesized high-quality graphene films using an H_2-excluded atmospheric pressure CVD (APCVD) technique [39]. They indicated that the quality and growth rate of graphene films increased dramatically with decreasing H_2 concentration. The H_2-excluded grown graphene films exhibited a mean sheet resistance of < 350 Ω/sq. and a light transmittance of 96.3 % at 550 nm. Moreover, Shin *et al.* showed that pristine monolayer graphene films can be achieved under an APCVD system in which hydrogen has been excluded in all growth steps [23]. They attributed this to the pyrolysis of CH_4 which provided the active hydrogen species, which then played a role in the growth step of graphene films [23, 39]. On the other hand, Jin and co-workers [27, 42] indicated that instead of synthesizing graphene in a H_2-excluded system, high quality graphene films can be grown by introducing hydrogen during the annealing step. They suggested that during annealing, H_2 assisted in

reconstructing the Cu surface to produce a wrinkle-like morphology suitable for graphene growth. Additionally, the H_2 would then dissociate and form a layer of active-surface bound H_2 species, which were later released during the growth process to facilitate the growth of high-quality graphene [27, 42].

In general, it can be seen that H_2 plays a significant role in controlling the sizes, morphology and quality of CVD-grown graphene films. Therefore, in this work we report on the effect of H_2 flow rate on the quality of the as-grown graphene during the annealing (A), growth (G), as well as annealing and growth (A/G) processes of APCVD-graphene. Graphene growth under the CVD system is influenced by numerous factors such as operating pressure, temperature, carbon source concentration (CH_4), partial pressures of the gases in the reaction chamber, etc. This study was thus conducted to provide optimum growth conditions for the synthesis of high-quality monolayer graphene films using the atmospheric pressure CVD (~766.71mmHg).

4.2. Experimental

4.2.1 Starting materials

Acetone (99%, gold line ACE), methanol (99.5 %), ethanol (absolute), iso-propanol (ACE, 99%), ortho-phosphoric acid (85%, LabChem), urea (99%, Promark Chemicals), chlorobenzene (99%, UniLab), sodium hydroxide pellets (98%, Merk) and poly(methyl methacrylate) (PMMA, Mw ~999 000) were purchased from Sigma-Aldrich, South Africa. The gases used included argon (Ar, 99%), methane (CH_4, 99.98%), and hydrogen (H_2, 99.98 %), and these were supplied by Afrox, South Africa. Other materials included a copper foil (25 µm, 99.98%) from Sigma Aldrich (RSA), a silicon substrate with a 300 nm silicon oxide layer (Sigma-Aldrich), a copper plate and an iron wire (University of the Witwatersrand workshop). Distilled water was used in all the experiments.

4.2.2 Growth and transfer of graphene films

Graphene films were grown on a copper foil (3 cm × 3 cm) using the atmospheric pressure chemical vapour deposition technique. The Cu foil was electrochemically cleaned[43] to remove the oxide layer (Scheme 1), and this was placed at a centre of the cylindrical quartz tube (100 cm × 20 cm) inside a horizontal furnace. The furnace was heated to the growth temperature of 1000 ^oC under 300 sccm Ar and variable flow rates of H_2 ($\boldsymbol{x}$ = 0 -100 sccm). Annealing of the Cu foil was then performed for 30 min, after which growth of the graphene

films was achieved by introducing 10 sccm of CH_4 for 10 min. After growth, the reactor was ***rapidly*** cooled to room temperature by pushing the quartz tube outside the reactor. The growth profile for the graphene films under the APCVD system is shown in scheme 4.2. To investigate the effect of H_2 on the quality and thickness of CVD-grown graphene films, three sets of experiments were conducted by introducing different flow rates of H_2 (0, 3, 10, 50, and 100 sccm) at three different growth stages. These were [1] during the annealing (A) stage only, [2] during the growth (G) stage only, and finally [3] during both the annealing and growth (A/G) stages. For characterization purposes, the as-grown graphene films were then transferred onto the 300 nm SiO_2/Si substrate, using the PMMA assisted electrochemical delamination method (Scheme 3.2)[44].

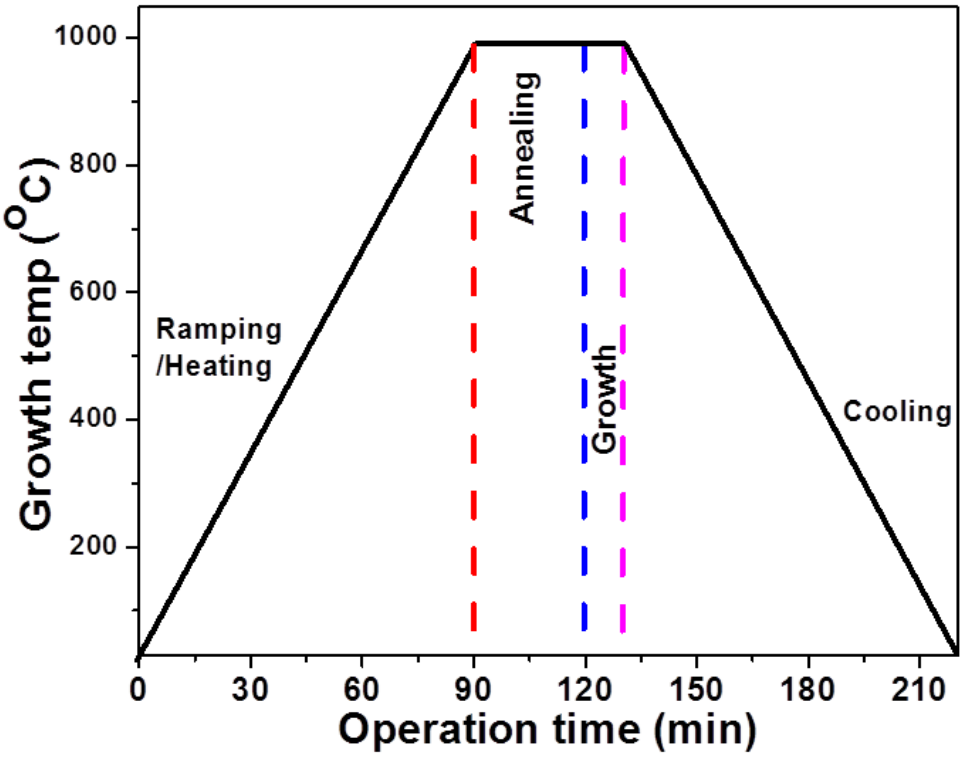

Scheme 4.2: The growth profile for the synthesis of graphene films by APCVD.

4.2.3 Characterization

Raman spectroscopy was used to assess the number of layers and quality of the as-grown films. Raman spectroscopic measurements were performed on a Bruker Raman Senterra spectrophotometer, equipped with a 20x optical objective for optical imaging. The characterization was performed with a 532 nm excitation laser at a very low laser power (0.5 mW) so as to avoid laser-induced heating of the films. The Raman measurements were collected from graphene films that were transferred onto 300 nm SiO_2/Si substrates. The

imaging of the graphene films was performed on films that were transferred onto the SiO_2/Si substrates. The optical images were collected in the bright field mode from the Olympus BX 63 Optical/Fluorescence Microscope using the 20x optical objective.

4.3 Results and discussions

During the catalytic CVD-growth of graphene films on Cu, both thermodynamic (i.e. temperature, etc.) and kinetic (i.e. C-source, H_2 concentration, substrate, etc.) factors[22, 25] are known to influence the growth mechanism. For over a decade, numerous research reports have shown that a growth temperature just below the melting point of Cu (i.e. $\leq 1085\ ^oC$) is suitable for growing good quality and large area graphene films[15]. Kinetic factors as well as the designated experimental set-up have been shown to influence the growth of graphene for both low and atmospheric pressure CVD procedures. In this study the growth temperature was kept at 1000 ^oC, CH_4 flow rate at 10 sccm, growth time at 10 min, and all other experimental parameters were fixed (such as pressure $\approx$ 766.71 mmHg). Only the flow rate of H_2 during the annealing (A), growth (G), annealing/growth (A/G) processes were varied.

4.3.1 Effect of H_2 flow rate during annealing step.

In order to investigate the influence of introducing H_2 flow rates during the annealing stage, a set of atmospheric pressure CVD experiments were conducted using different flow rates of H_2 (0-100 sccm). The optical images of as-synthesized graphene films on a 300 nm SiO_2/Si substrate (Fig. 4.1) show uniform and continuous films consisting of areas of multilayer graphene, indicated by darker purple spots. The formation of regions of multi-layer graphene can be attributed to the difficulty in adsorption of CH_4 onto the Cu surface due to the presence of surface bound hydrogen atoms. This leads to the defects on the as-grown graphene domains that act as active sites for the catalytic cracking of CH_4 and subsequent graphene growth[13-20]

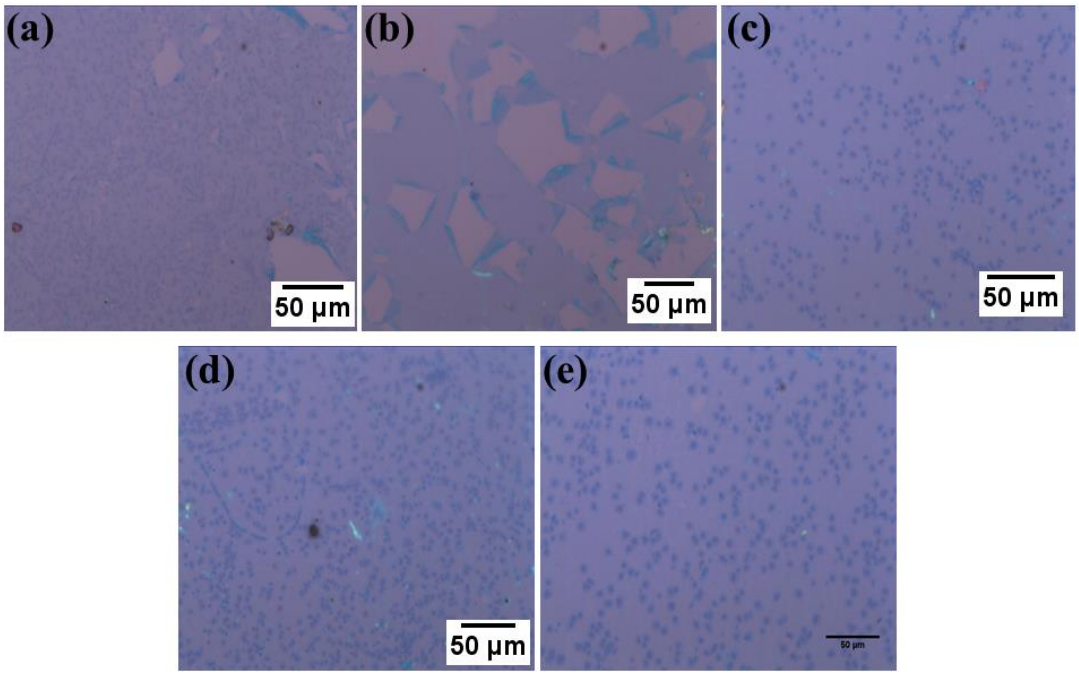

Figure 4.1: Optical images of graphene films on SiO_2/Si substrate grown using (a) 0 sccm, (b) 3 sccm, (c) 10 sccm, (d) 50 sccm, and (e) 100 sccm of H_2 during the annealing process.

To further evaluate the quality and the number of layers of the as-synthesized graphene films, Raman spectra (Fig. 4.2a) were obtained on films after they were transferred onto a 300 nm SiO_2/Si substrate. The results showed that Raman spectra exhibited the three "finger-print" Raman bands for graphene and/or graphitic carbon materials (Table 4.1). These are the sp^3 defect-induced D band (~ 1340.4 – 1345.4 cm^{-1}), the graphitization G band (~ 1583.4 – 1586.5 cm^{-1}), and the lattice-distortion sensitive 2D band (~ 2674.2 – 2685.6 cm^{-1})[45-49]. Additionally, using higher H_2 flow rates (10 - 100 sccm) the G band was observed to broaden and split and give a shoulder (1621.0 – 1621.5 cm^{-1}), which was assigned to the D* band[45-49]. The presence of the D* band together with the very intense D band for graphene films grown using medium to high H_2 flow rates (10 - 100 sccm), signified the presence of large amounts of defects in the form of edge defects, sp^3-bonded C-H species, C and H adatoms, intercalated C and H atoms, or a nanographitic basal plane[45-49].

Table 4.1: Peak positions and ratios for graphene films grown by introducing H_2 during the annealing process

H_2 flow rate (sccm)	Peak Positions (cm^{-1})				Ratios	
	D	G	D*	2D	I_D/I_G	I_G/I_{2D}
0	1343.3	1586.5	-	2675.8	0.621	0.601
3	1340.4	1583.4	-	2674.2	0.433	0.338
10	1345.1	1584.3	1621.5	2683.5	1.07	1.57
50	1345.4	1584.4	1621.4	2685.6	1.18	1.80
100	1343.7	1584.3	1621.0	2681.1	1.45	1.38

The thickness of the as-grown graphene films was determined by calculating the intensity ratio of the G band with respect to the 2D band (I_G/I_{2D}) [45, 46, 47, 49]; which was found to be in the $0.338 < I_G/I_{2D} < 1.80$ range (Fig. 4.2b, red line). The results suggested that the H_2-exclusion (0 sccm) method resulted in the formation of fairly good quality bilayered graphene films, as indicated by the I_D/I_G and I_G/I_{2D} ratio values of ~0.621 and ~0.601 respectively. The observed results were in good agreement with Hu *et al.*[21] and Gao *et al.*[39] who showed that good quality graphene films with few layers can be successfully grown in a H_2-excluded CVD system [23, 41]. They attributed the successful graphene growth to the pyrolysis of CH_4 during the growth step, which produces both active H and C species. The cracking produces active carbon species that eventually initiate the growth of graphene domains and thus their aggregation into graphene films. In addition, the catalytic cracking produces hydrogen radicals which play a major role in etching the Cu surface leading to formation of more Cu nanoparticles (Scheme 4.3a). As a result, formation of new Cu nanoparticles means the availability of new active sites for more catalytic cracking of CH_4, and further growth of graphene domains. However, due to the lack of a continuous supply of hydrogen atoms/radicals, a limited number of active sites are produced. This results in conversion of edge and defect sites on the graphene domains to adsorb, crack and provide nucleation sites for more incoming CH_4 molecules, and hence growth of a bilayered graphene film (I_G/I_{2D} ratio of 0.601). This led to formation of graphene domains which do not fully coalescence into complete and uniform graphene films, leading to the presence of many defect sites and the resultant I_D/I_G ratio of 0.621.

Interestingly, graphene films grown using low flow rates of H_2 (3 sccm) exhibited a very low intensity D band, which signified the presence of fewer defects. Additionally, the I_D/I_G and I_G/I_{2D} ratio values were found to be ~0.433 and ~0.338, respectively. The results suggested the formation of good quality bilayered graphene films, with a monolayered basal plane [45, 46, 47, 49]. When H_2 flow rates are used (3 sccm), it could be concluded that the hydrogen plays two major roles in constructing the Cu surface for the growth of good quality bilayered graphene films. The hydrogen cleans and smooths the Cu surface by removing copper oxide irregularities as well as etching the Cu surface in order to create the appropriate sizes of Cu nanoparticles (i.e. >20 nm) for graphene growth[39]. Additionally, there is the continuous supply of H_2 which also leads to formation of surface-bound active hydrogen species. The hydrogen species act as extra activators for the catalytic cracking of CH_4 as well as etching agents that control the size and morphology of the graphene domains of the graphene film (Scheme 4.3b).

On the contrary, when the H_2 flow rate was increased (10 sccm – 100 sccm) the as-grown graphene films were found to be highly defective ($I_D/I_G = 1.07_{10\ sccm}$, $1.18_{50\ sccm}$, $1.45_{100\ sccm}$) as well as also being few to multi-layered, as shown by the I_G/I_{2D} ratio values of ~1.57, ~1.80, and ~1.38 for graphene films grown using 10 sccm, 50 sccm, and 100 sccm, respectively. This could indicate that many surface-bound H-atoms were formed on the Cu surface. This would hinder the successful and efficient cracking of CH_4 into active species and thus the nucleation and aggregation of the carbon atoms into fully coalesced graphene films. Additionally, surface-bound hydrogen species increase the etching effect and hydrogenation of graphene edges, thus leading to the formation of highly defective few to multilayered graphene films (Scheme 4.3c).

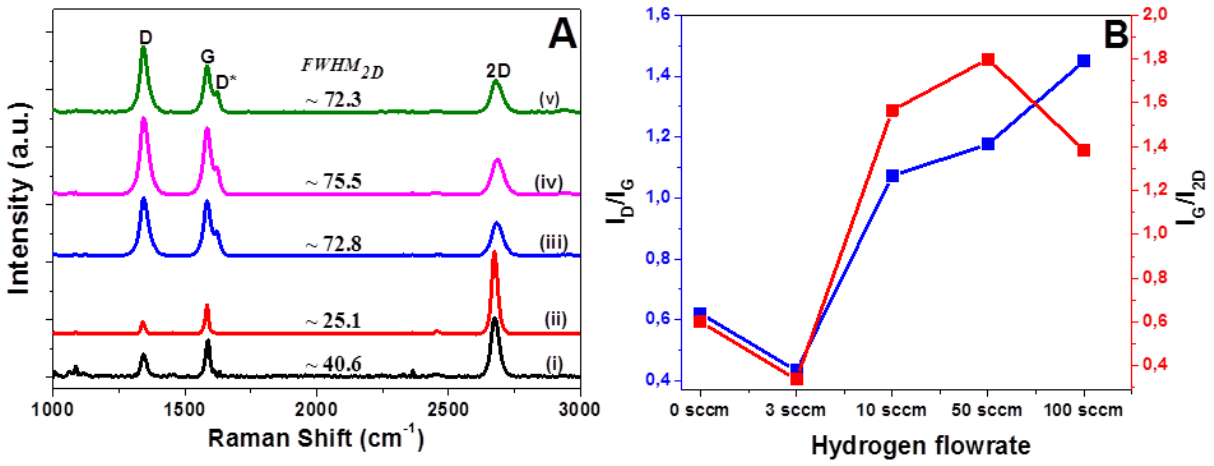

Figure 4.2: (a) Raman spectra of graphene films grown using (i) 0 sccm, (ii) 3 sccm, (iii) 10 sccm, (iv) 50 sccm, and (v) 100 sccm of H_2; (b) Plot of I_D/I_G and $I_G/I2_D$ ratios.

Finally, the orientation and thickness of the as-grown graphene films was determined from the full width at half maxima (FWHM) of the 2D bands (Fig. 4.2a), the line shapes and the Lorentzian fitting of the 2D bands (Fig. 4.3). The values of the 2D-FHWM are an important tool for determining whether the as-grown graphene films exhibit a Bernal (AB), non-Bernal or rhombohedral (ABC) arrangement of C atoms [15, 29, 50-53]. On the other hand, the line shape and the Lorentzian fitting of the 2D bands can be used to support the I_G/I_{2D} ratio values in determining the actual thickness of the as-synthesized graphene films[15, 29, 50-53]. As a result, the analysis of the 2D band of the graphene films grown in a H_2-excluded system revealed the FWHM value of ~ 40.6 cm^{-1} and a symmetrical 2D band which was fitted with four Lorentzian peaks. The observed FWHM was characteristic of a Bernal stacking orientation found in bilayered graphene films; whereas the fitting with four Lorentzian peaks confirmed the formation of bilayered graphene films[15, 29, 50-53]. Remarkably, the graphene films grown using low H_2 flow rates (3 sccm) revealed a characteristic monolayer, as exhibited by single Lorentzian peak fit. However, both the values of the I_G/I_{2D} ratio (0.601) and the FWHM (~25.1 cm^{-1}) indicated that the as-grown graphene films are bilayered, but exhibited a non-Bernal stacking orientation since the FWHM is much larger than that observed for monolayered graphene[50,52-53]. Finally, formation of few layered graphene films when using medium to higher flow rates of H_2 (10 sccm-100 sccm) was confirmed by the fitting of the 2D band with three Lorentzian peaks (Fig. 4.3) and the asymmetrical line shapes of the 2D

bands. Their observed FHWM values were found to agree well with those obtained for AB stacked few to multilayered graphene films [15, 54].

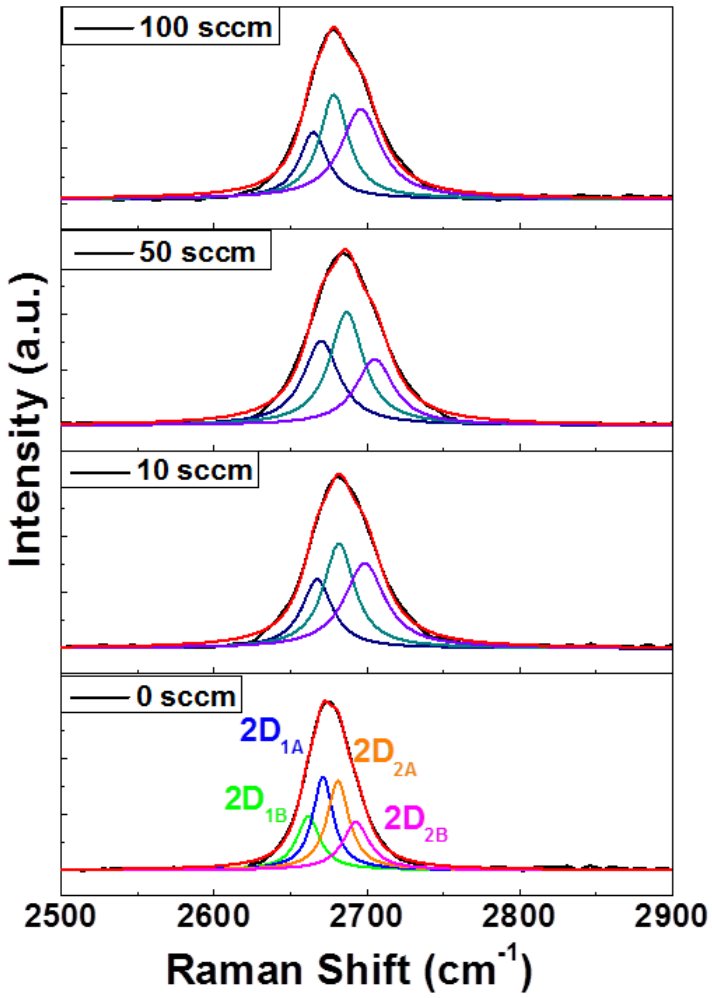

Figure 4.3: Deconvoluted 2D peaks of the graphene films grown by introducing H_2 during the annealing step only.

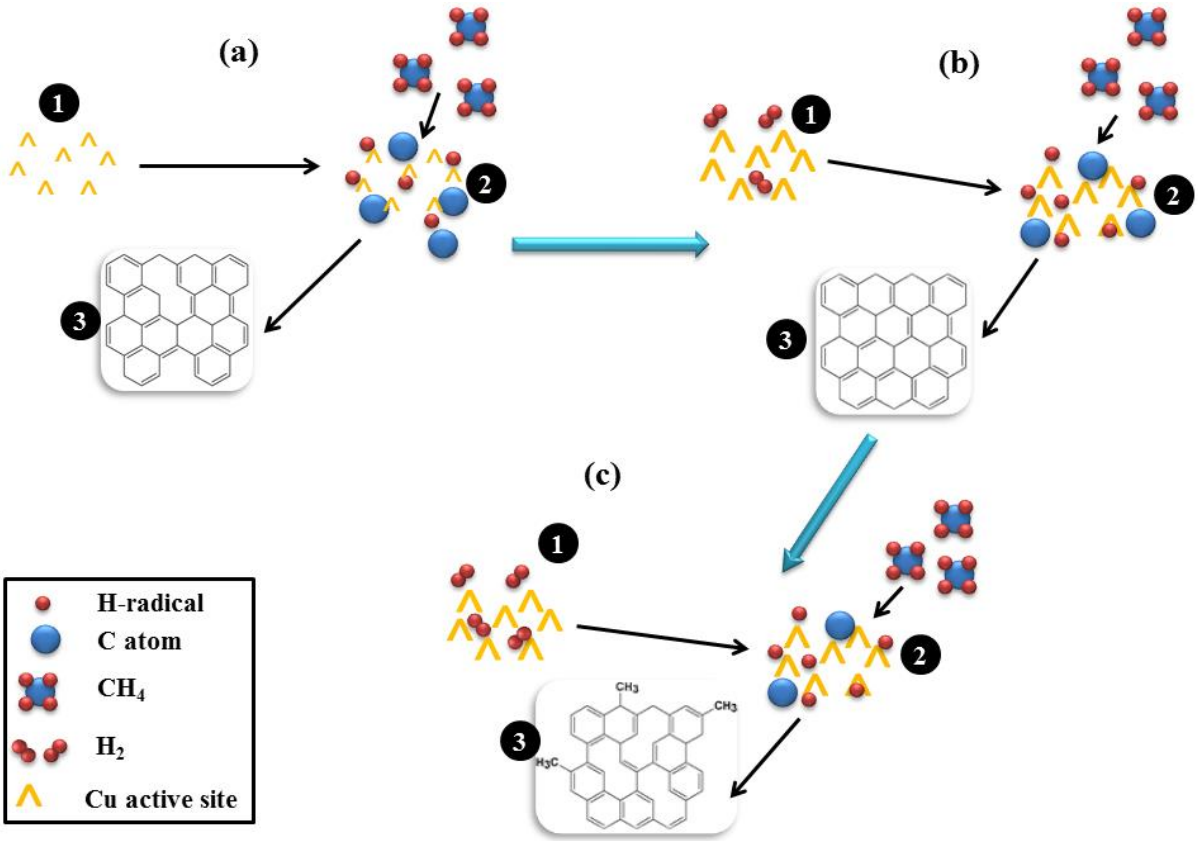

Scheme 4.3: Formation of graphene films during (a) no H_2 flow rate (0 sccm), (b) low H_2 flow rate (3 sccm), and medium – high H_2 flow rate (10 sccm – 100 sccm).

4.3.2 Effect of H_2 flow rate during the growth step.

Optical micrographs of the graphene films, after they were transferred onto the 300 nm SiO_2/Si substrates (Fig. 4.4) revealed uniform and continuous films that were decorated by regions of multilayered films. The formation of these multilayered regions could be attributed to the increased competitive adsorption and decomposition of both H_2 and CH_4 molecules on the Cu surface, which hinders the growth of good quality graphene films.

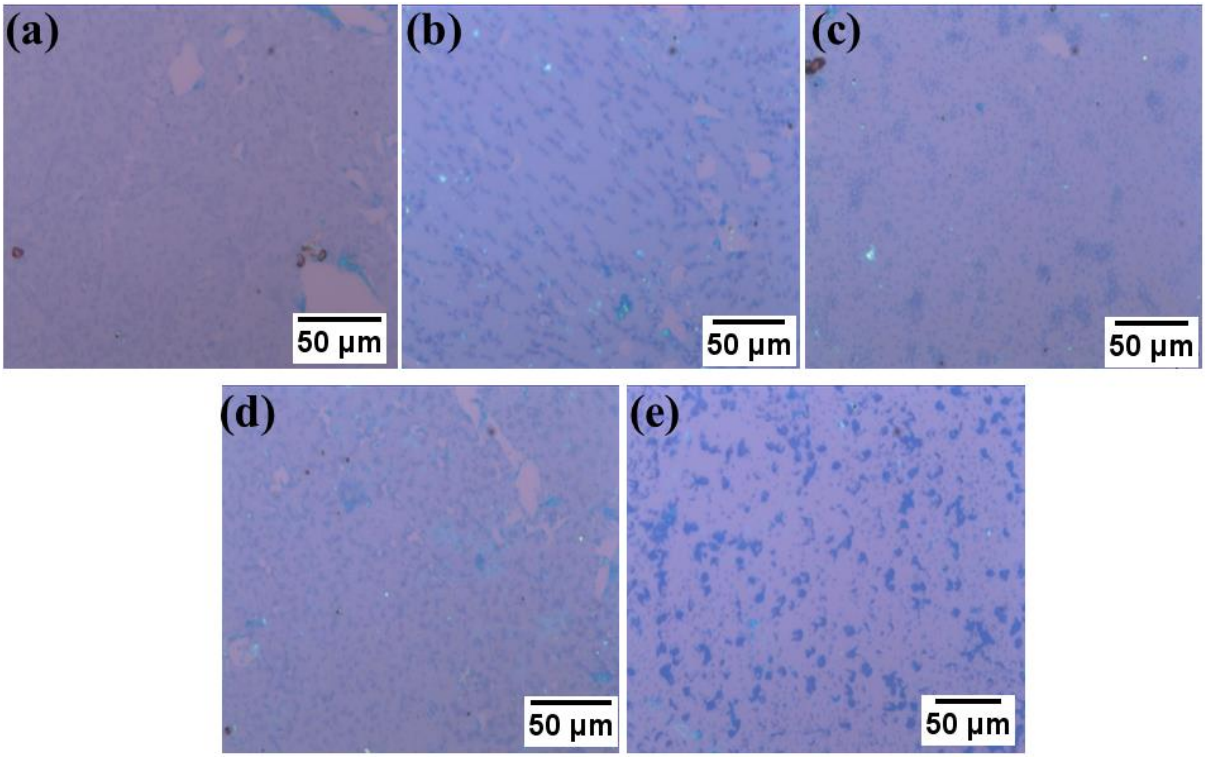

Figure 4.4: Optical images of graphene films on SiO_2/Si substrate grown using (a) 0 sccm, (b) 3 sccm, (c) 10 sccm, (d) 50 sccm, and (e) 100 sccm of H_2 during the growth process.

The defect density, quality and thickness of the as-grown graphene films were determined from the Raman analysis of these films, after they were transferred onto the 300 nm SiO_2/Si substrates. Raman spectra collected from all graphene films (Table 4.2) showed the responses from two of the Raman active modes (i.e. G band at ~1581.6 – 1586.5 cm^{-1}, and 2D band at ~2675.8 – 2684.3 cm^{-1}), as well as responses from the Raman forbidden modes (i.e. the D band at ~1342.4 – 1345.6 cm^{-1} and the D* band at ~1619.8 – 1620.5 cm^{-1}) [45-49]. An increased defect density was observed when high flow rates of H_2 (10 sccm – 100 sccm) were used. This was depicted by the appearance of the D* bands and the increasing relative intensity of the D bands (Fig. 4.5a); which could be attributed to the presence of edge defects, sp^3-bonded C-H species, C and H adatoms, intercalated C and H atoms, or a nanographitic basal plane [45-49].

Table 4.2: Peak positions and Rations for graphene films grown by introducing H_2 during the growth process

H_2 flow rate (sccm)	Peak Positions (cm^{-1})				Ratios	
	D	G	D*	2D	I_D/I_G	I_G/I_{2D}
0	1343.3	1586.5	-	2675.8	0.621	0.601
3	1342.4	1582.8	-	2678.6	0.293	0.721
10	1345.5	1582.9	1620.2	2678.2	0.647	0.806
50	1345.6	1581.6	1620.5	2682.3	0.714	1.34
100	1345.6	1586.4	1619.8	2684.3	1.17	2.14

In order to determine the thickness of the as-grown graphene films, the intensity ratio of the graphitic G band with respect to the lattice-distortion sensitive 2D band (I_G/I_{2D}) was calculated [45, 46, 47, 49], and this was found to be in the $0.601 < I_G/I_{2D} < 2.14$ range (Fig. 4.5b, red line, Table 4.2). It was indicated earlier in section 4.3.1 that the pyrolysis of CH_4 during the growth step[21, 23, 39] of the H_2-exclusion (0 sccm) method led to formation of graphene which were mostly bilayered (I_G/I_{2D} = ~0.601) and exhibited a fairly good quality (I_D/I_G = ~0.621). However, when the H_2 flow rate was slightly increased to 3 sccm, high quality (I_D/I_G = ~0.293) graphene films which are bilayered (I_G/I_{2D} = ~0.721) in nature were formed[45, 46, 47, 49]. This is shown in scheme 4.4a. Further increase of the H_2 flow rate (10 sccm – 100 sccm) resulted in the formation of more defective and thicker graphene films. This was indicated by the increasing I_D/I_G (i.e. $0.647_{10\ sccm}$, $0.714_{50\ sccm}$, $1.17_{100\ sccm}$) and I_G/I_{2D} (i.e. $0.806_{10\ sccm}$, $1.34_{50\ sccm}$, $2.14_{100\ sccm}$) ratio values. These results show that the continuous addition of H_2 molecules play two significant roles toward the successful growth of graphene films. Initially, the competitive adsorption and decomposition of both CH_4 and H_2 molecules on the Cu surface hindered the lateral growth of graphene domains. As a result, the defect sites and C-adatoms on the underlying graphene domains behaved as new nucleation sites for cracking of in-coming CH_4. This led to the formation of few to multilayered graphene films. Secondly, the termination of the edges of the graphene domains by hydrogen led to the formation of sp^3-defects, thereby resulting in the formation of highly defective graphene films, as indicated by the increasing I_D/I_G ratio values. In general, it can be concluded that growth of graphene films during the introduction of different H_2 flow rates during the growth step (A) follows a three

step mechanism (Scheme 4.4). The first step indicated the H_2-excluded method, the second step showed growth with low H_2 flow rates (3 sccm), and step three showed growth with medium to high H_2 flow rates (10 – 100 sccm).

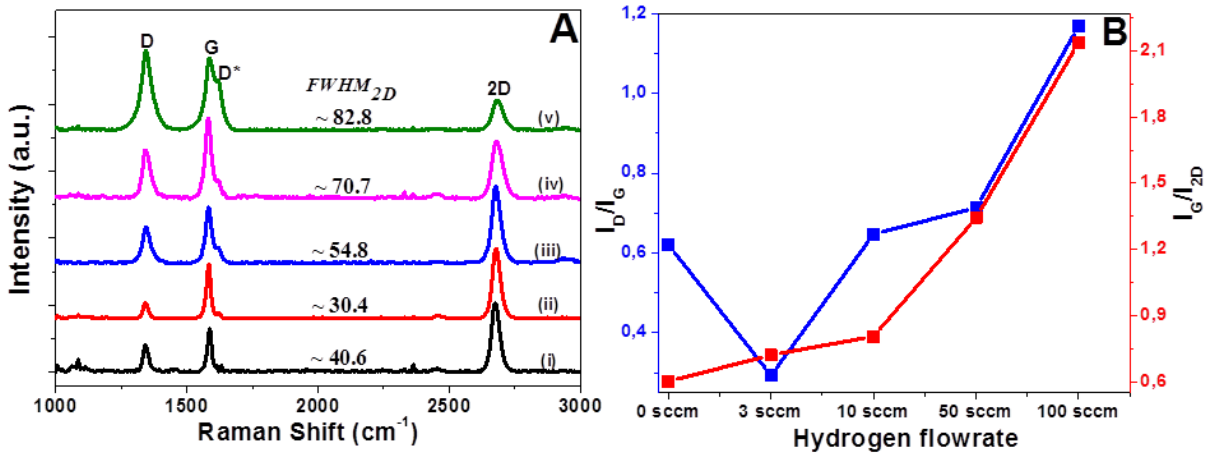

Figure 4.5: (a) Raman spectra of graphene films grown using (i) 0 sccm, (ii) 3 sccm, (iii) 10 sccm, (iv) 50 sccm, and (v) 100 sccm of H_2; (b) Plot of I_D/I_G and I_G/I_{2D} ratios.

The FWHM of the 2D band was used to establish the thickness and/or orientation (i.e. either Bernal (AB), non-Bernal or rhombohedral (ABC)), whereas both the Lorentzian peak fitting and the line shape of the 2D were used for the confirmation of the thickness of the as-grown graphene films[15, 29, 50-53]. As a result, figure 4.5a showed that when different flow rates of H_2 were introduced during the growth step only, the FWHM values varied: ~ 30.4 cm^{-1} < FWHM < ~ 82.8 cm^{-1}. For instance, graphene films grown using 0 sccm (~ 40.6 cm^{-1}) and 3 sccm (~ 30.4 cm^{-1}) H_2 flow rates exhibited symmetrical 2D bands and 2D-FWHM values which are characteristic of a Bernal bilayered graphene[15, 29, 50-53]. The fitting of the 2D bands with four Lorentzian peaks confirmed that these as-grown films are bilayered in nature (Fig. 4.6). Additionally, the 2D-FWHM (~54.8 cm^{-1}) for graphene films grown using a medium H_2 flow rate (10 sccm) was characteristic of AB-stacked bilayered graphene films [29, 50-53, 55, 56]. Furthermore, the fitting of the symmetrical 2D band of the H_2-10sccm graphene films with six Lorentzian peaks (Fig.4.6), indicated the formation of Bernal-orientated, trilayered graphene films. Contrarily, graphene films grown using 50 sccm of H_2 exhibited a large FWHM (~ 70.7 cm^{-1}), an asymmetrical line shape and the Lorentzian fitting with three peaks for the 2D band. The results indicated the formation of few layered graphene films, which exhibited a rhombohedral orientation [15, 29, 50-53]. Finally, the formation of multilayered

graphene films when 100 sccm of H_2 was used, was ascertained by a very broad 2D-FWHM (~ 82.8 cm^{-1}) as well as the fitting of the 2D band with two Lorentzian peaks (Fig. 4.6) [15, 54].

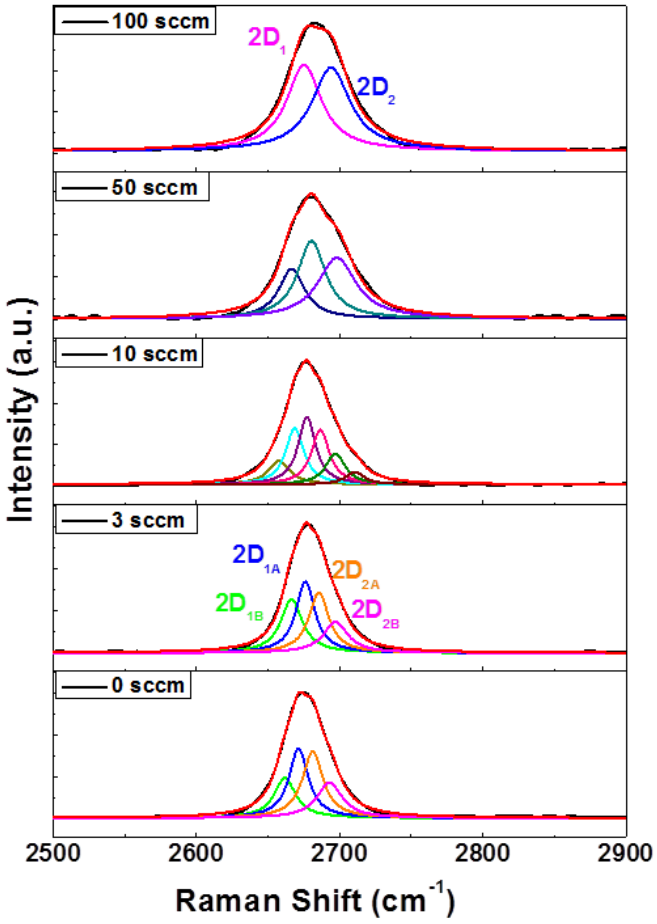

Figure 4.6: Deconvoluted 2D peaks of the graphene films grown by introducing H_2 during the growth step only.

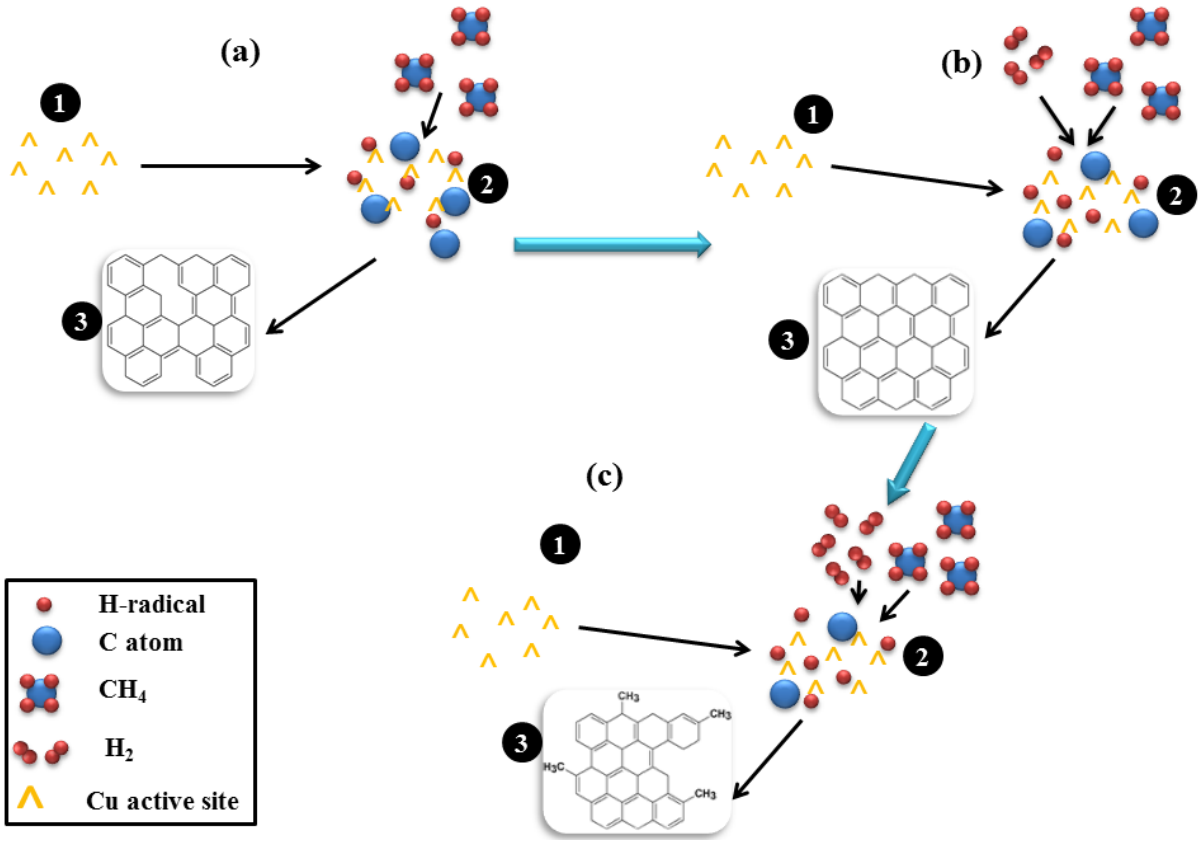

Scheme 4.4: Formation of graphene films during (a) no H_2 flow rate (0 sccm), (b) low H_2 flow rate (3 sccm), and medium – high H_2 flow rate (10 sccm – 100 sccm).

4.3.3 Effect of H_2 flow rate during annealing and growth steps.

The analysis of the as-synthesized graphene films with optical microscopy showed that smooth and large-area graphene films were grown when low (3 sccm), medium (10 sccm) and reasonably high (50 sccm) H_2 flow rates were used during both the annealing and growth steps (A/G). Furthermore, the use of high H_2 flow rates (50 - 100 sccm) was found to result in the formation of coarse multilayered graphene films. Regions of multilayered graphene films are depicted on the optical micrographs by the dark purple dots (Fig. 4.7).

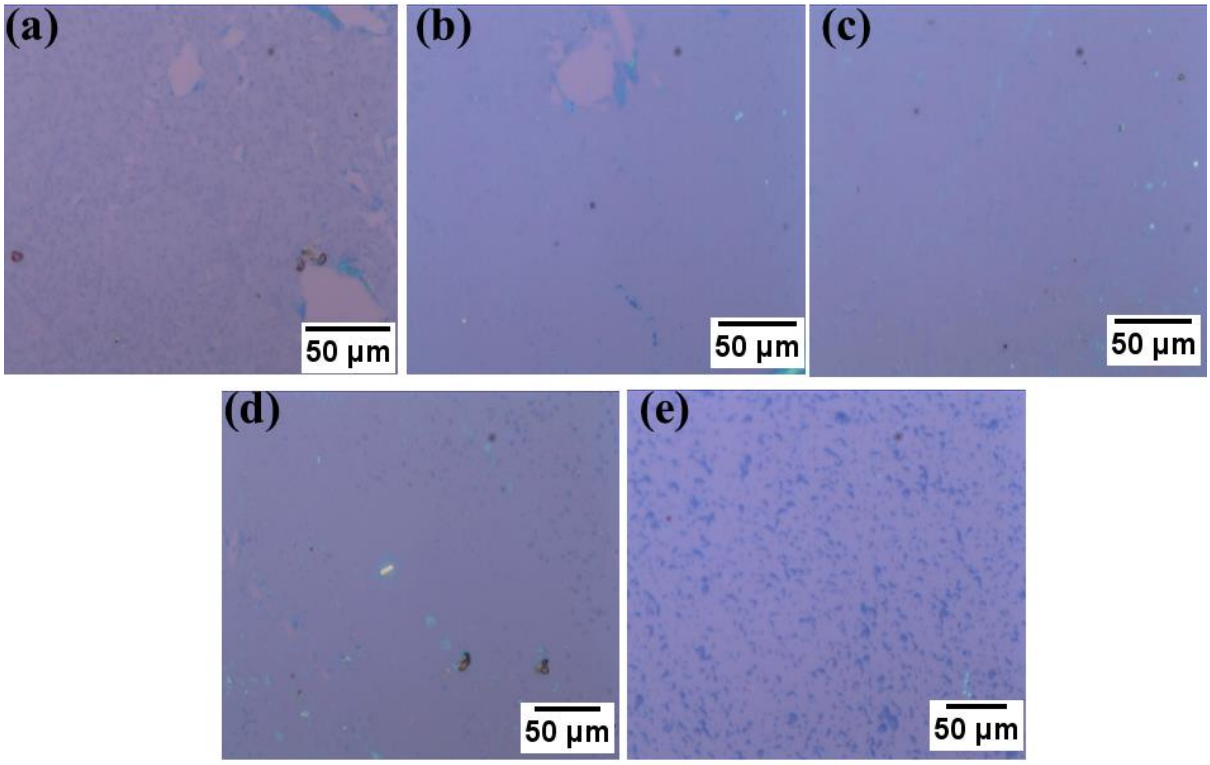

Figure 4.7: Optical images of the as-synthesized graphene films transferred onto the SiO_2/Si substrate after growth with H_2 passed during the annealing and growth process.

Raman spectroscopic analyses were performed to ascertain the defect density, quality and variation in the thickness of these as-grown graphene films. Raman spectra (Fig. 4.8a, Table 4.3) collected from graphene films grown at various H_2 flow rates exhibited three characteristic bands of graphene; the sp^3 defect- sensitive D band (~ 1340.0 – 1345.6 cm^{-1}), the graphitization G band (~ 1582.4 – 1586.5 cm^{-1}), and the lattice-distortion sensitive 2D band (~ 2673.9 – 2682.3 cm^{-1}). Similar to other growth conditions (Sections 4.3.1 and 4.3.2), at higher flow rates (50 and 100 cm), the G peak was observed to split into two peaks, with the extra peak detected at ~ 1622.1 cm^{-1} (D^* band). The splitting can be attributed to the increased defect density in the form of vacancies, adatoms, or distortions of the graphene lattice [15, 45-49].

Table 4.3: Peak positions and Rations for graphene films grown by introducing H_2 during the annealing and growth processes

H_2 flow rate (sccm)	Peak Positions (cm^{-1})				Ratios	
	D	G	D*	2D	I_D/I_G	I_G/I_{2D}
0	1343.3	1586.5	-	2675.8	0.621	0.601
3	1340.0	1582.4	-	2673.9	0.184	0.265
10	1341.0	1583.5	-	2676.0	0.206	0.362
50	1345.6	1581.6	1620.5	2682.3	0.614	1.34
100	1343.0	1584.1	1622.1	2677.6	1.66	1.59

Evaluation of the quality of the as-grown films was determined from the I_D/I_G ratios (Fig. 4.8b, blue), while their thickness was determined from the ratio of the G band to 2D band intensities (I_G/I_{2D}, Fig. 4.8b, red) [45-49]. It was observed that the pyrolysis of CH_4 during the growth step [21, 23, 29, 39] was the main contributing factor for the growth of mostly bilayered and fairly good quality graphene films during the H_2-exclusion (0 sccm) system. An increase of the H_2 flow rate to 3 sccm, revealed a sharp symmetric 2D band with fwhm of ~23.1 cm^{-1}, a very low intensity G band and a diminished D band. The I_G/I_{2D} ratio of 0.265 suggested the formation of monolayered graphene films, while the I_D/I_G ratio of 0.184 signified the formation of very high quality graphene films with a low defect density. Moreover, further increase of the H_2 flow rate to 10 sccm, revealed the I_D/I_G and I_G/I_{2D} ratios of 0.206 and 0.364, respectively, suggesting the growth of a high quality bilayer graphene film. The better quality and decreased thickness of the as-grown graphene films at both 3 sccm and 10 sccm H_2 flow rates, can be attributed to the better availability of active sites on the Cu surface and less crowding of active hydrogen and carbon species. As a result, nucleation of carbon species in graphene domains and aggregation of the domains into a continuous and high quality graphene film was permitted. Finally, with higher H_2 flow rates (50 sccm and 100 sccm) the competitive adsorption and decomposition of both carbon and hydrogen molecules on the Cu active sites led to the growth of highly defective few- and/or multilayered graphene films ($I_G/I_{2D} = 1.34_{50\ sccm}$ and $1.59_{100\ sccm}$). This is because high H_2 flow rates can facilitate the etching effect on the already formed graphene domains and/or layers by hydrogenating the graphene edges and resulting in formation of sp^3-type defects[21-35]. Additionally, high flow

rates of H_2 led to intercalation of hydrogen and/or carbon atoms in between the graphene layers resulting in increased lattice distortion. In conclusion, an evaluation of the growth of graphene films when H_2 was introduced during the entire growth system (A/G) also showed a three step growth mechanism (Scheme 4.5): step one representing growth with the no H_2 flow rate (0 sccm), step two with the low - medium H_2 flow rate (3 – 10 sccm), and step three with high H_2 flow rate (50 sccm – 100 sccm).

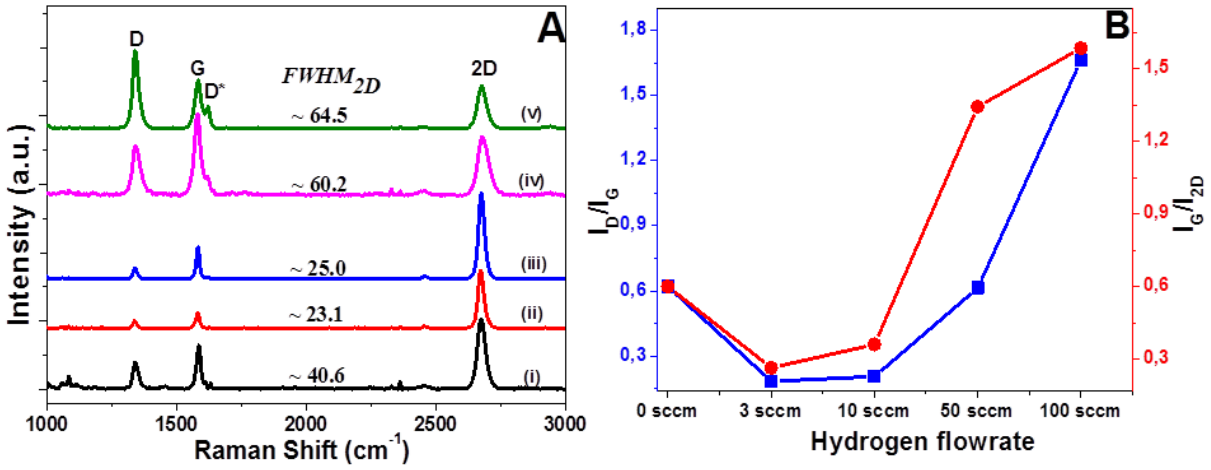

Figure 4.8: Raman analysis of graphene films grown using various H_2 flow rates during the annealing and growth process.

Finally, the FWHM (Fig. 4.8a), line shape and the Lorentzian peak fitting of the 2D bands (Fig. 4.9) were used to determine the orientation of the as-grown films as well as to confirm their actual thickness. The graphene films grown with low H_2 flow rates (3 sccm) revealed a characteristic monolayer by exhibiting a single Lorentzian peak fitting, a narrow 2D-FWHM (~23.1 cm^{-1}), and a sharp symmetric 2D band[50-53, 55-57]. Interestingly, growth of graphene with 10 sccm H_2 revealed a characteristic monolayer, as depicted by a single 2D-Lorentzian peak fitting and a sharp symmetric 2D band. However, the 2D-FWHM (~25.1 cm^{-1}) was observed to be larger than the reported value for monolayered graphene (≤ 24 cm^{-1})[50-53], suggesting that the $10sccm_{H2}$-grown graphene films exhibited a non-Bernal stacking order[50-53, 55-57]. Lastly, the Lorentzian peak fitting of three peaks and the broad 2D-FWHM (~ 60.2 cm^{-1} and ~ 64.5 cm^{-1}) for graphene films grown with 50 sccm and 100 sccm of H_2 indicated the formation of few layered graphene films[50-53]. Most importantly, the asymmetrical line shapes for their 2D bands suggested that the as-grown films exhibited a rhombohedral stacking orientation[50-53, 55-57].

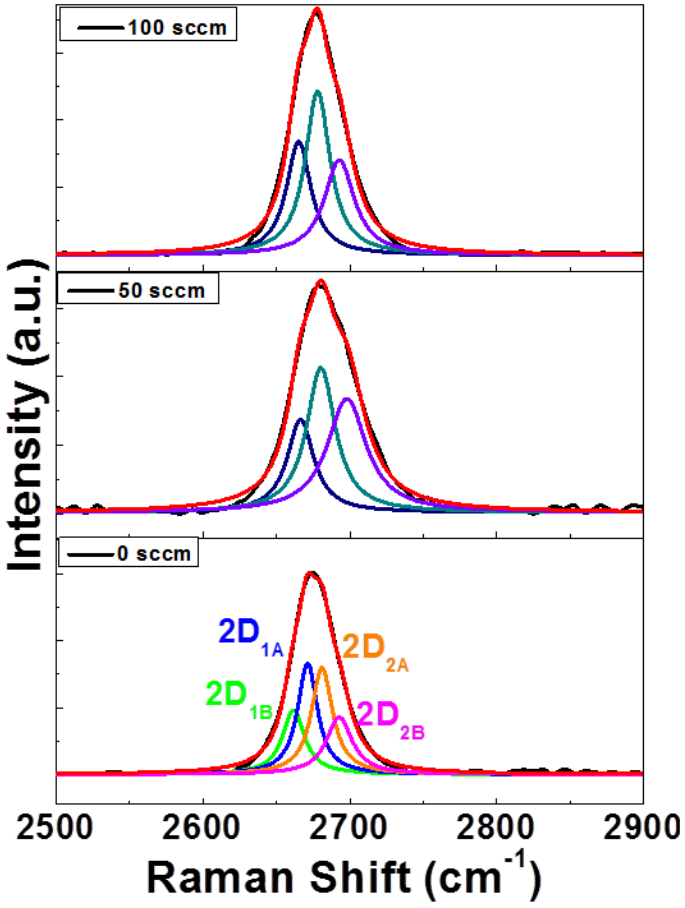

Figure 4.9: Deconvoluted 2D peaks of the graphene films grown by introducing H_2 during the annealing and growth steps.

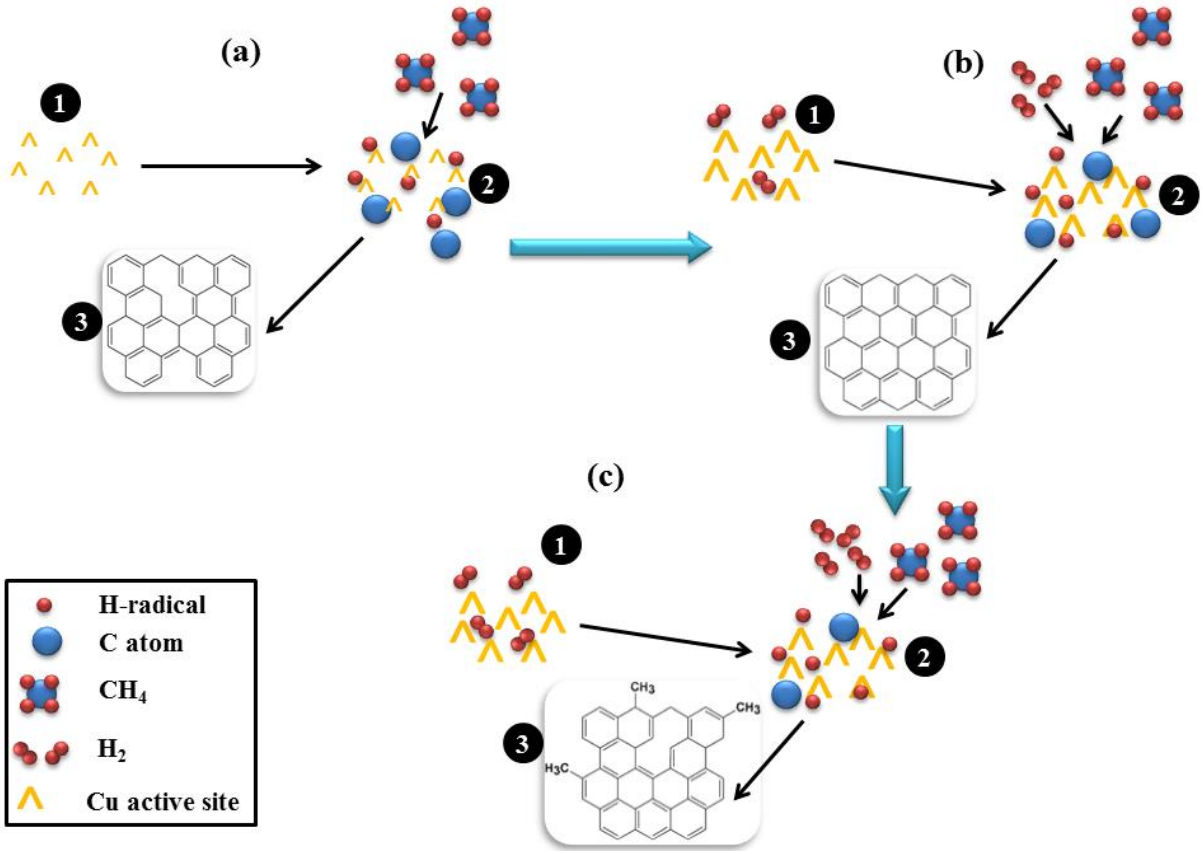

Scheme 4.5: Formation of graphene films during (a) no H_2 flow rate (0 sccm), (b) low - medium H_2 flow rate (3 – 10 sccm), and high H_2 flow rate (50 sccm – 100 sccm).

4.4. Conclusions

The influence of hydrogen concentration on the quality and thickness of the graphene films during the annealing (A), growth (G), and both annealing/growth (A/G) processes was studied. Despite the research reports [23, 39] indicating that the H_2-excluded system could provide an optimal process for growing large-area graphene films, our results show that the presence of small concentrations of H_2 inside the reaction chamber can generate excellent quality graphene films. These results are thus consistent with what has been reported previously [22, 29]. However, the influence of low H_2 flow rate on the graphene quality has not been extensively reported. For instance, monolayered (I_G/I_{2D} = 0.265) graphene films of very good quality (I_D/I_G = 0.184) were obtained when low flow rates of H_2 (3 sccm) were introduced throughout the synthesis process (A/G). Similarly, good quality bilayered graphene films were grown when low flow rates of H_2 were introduced during the annealing (A) and growth (G) steps only (i.e. $I_D/I_G = 0.433_{\boldsymbol{A}}$, $I_G/I_{2D} = 0.338_{\boldsymbol{A}}$, $I_D/I_G = 0.293_{\boldsymbol{G}}$, and $I_G/I_{2D} = 0.721_{\boldsymbol{G}}$). Interestingly, using medium H_2 flow rates (10 sccm) during the A/G step led to the

formation of good quality and non-AB stacked bilayered graphene films, as indicated by I_D/I_G and I_G/I_{2D} ratio values of ~0.206 and ~0.362, respectively. On the other hand, using both medium (10 sccm) and high (50 sccm – 100 sccm) flow rates of H_2 during the A and G steps led to the growth of highly defective and few to multilayered graphene films. Similar results were observed when high flow rates of H_2 were used during the A/G step. This was attributed to the competitive adsorption and decomposition of both CH_4 and H_2 molecules on the available Cu active sites.

Since the growth conditions in which 3 sccm of H_2 was introduced throughout the entire synthesis process (A/G) resulted in the formation of good quality monolayered graphene films, this flow rate was chosen as the optimum hydrogen flow rate for the growth of graphene films under the APCVD system in future chapters. The results indicate the presence of H_2; even in small concentrations is crucial for the growth of high quality graphene films. This correlates well with theoretical results which indicated that H_2 is very significant for the synthesis of graphene films by CVD [15, 25-37].

References

1. Novoselov, K S., A. K. Geim, S. V. Morozov, D. Jiang, Y. Zhang, S. V. Dubonos, I. V. Grigorieva, A. A. Firsov. *Science*, **2004**, *306*, 666−669.
2. Geim, A. K., Novoselov, K. S. *Nat. Mater*. **2007**, *6*, 183−191.
3. Morozov, S.V., K. S. Novoselov, M. I. Katsnelson, F. Schedin, D. C. Elias, J. A. Jaszczak, A. K. Geim. *Phys Rev Lett*, **2008**, *100*, 016602.
4. Elias, D. C., R. R. Nair, T. M. G. Mohiuddin, S. V. Morozov, P. Blake, M. P. Halsall, A. C. Ferrari, D. W. Boukhvalov, M. I. Katsnelson, A. K. Geim, K. S. Novoselov. *Science*, **2009**, *323*, 610–613.
5. Gomez-Navarro, C., M. Burghard, K. Kern. *Nano Lett*, **2008**, *8*, 2045–2049.
6. Balandin, A.A., S. Ghosh, W. Bao, I. Calizo, D. Tewelderbrhan, F. Miao, C.N. Lau. *Nano Lett*, **2008**, *8*, 902–907.
7. Geim, A. K. *Science*, **2009**, *324*, 1530−1534.
8. Berger, C., Z. Song, X. Li, X. Wu, N. Brown, C. Naud, D. Mayou, T. Li, J. Hass, A. N. Marchenkov, E. H. Conrad, P. N. First, W. A. de Heer. *Science*, **2006**, *312*, 1191−1196.
9. Lin, Y. M., C. Dimitrakopoulos, K. A. Jenkins, D. B. Farmer, H. Y. Chiu, A. Grill, Ph. Avouris. *Science*, **2010**, *327*, 662.

10. Becerril, H. A., J. Mao, Z. Liu, R.M. Stoltenberg, Z. Bao, Y. Chen. *ACS Nano*, **2008**, *2*, 463−470.
11. Yang, D., A. Velamakanni, G. Bozoklu, S. Park, M. Stoller, R. D. Piner, S. Stankovich, I. Jung, D. A. Field, C. A. Ventrice, R. S. Ruoff. *Carbon*, **2009**, *47*, 145−152.
12. Li, X., W. Cai, L. Colombo, R. S. Ruoff. *Nano Lett.*, **2009**, *9*, 4268−4272.
13. Gao, T., S. Xie, Y. Gao, M. Liu, Y. Chen, Y. Zhang, Z. Liu. *ACS Nano*, **2011**, *5*, 9194−9201.
14. Bae, S. H., Kim, Y. Lee, X. Xu, J.S. Park, Y. Zheng, J. Balakrishnan, T. Lei, H. R. Kim, Y. Song, Y. J. Kim, K. S. Kim, B. Ozyilmaz, J. H. Ahn, B. H. Hong, S. Iijima. *Nat Nanotechnol*, **2010**, *5*, 574–578.
15. Reina, A., X. Jia, J. Ho, D. Nezich, H. Son, V. Bulovic, M. S. Dresselhaus, J. Kong. *Nano Lett*, **2009**, *9*, 30–5.
16. Li, X., W. Cai, J. An, S. Kim, J. Nah, D. Yang, R. Piner, A. Velamakanni, I. Jung, E. Tutuc, S. K. Banerjee, L. Colombo, R. S. Ruoff. *Science*, **2009**, *324*, 1312–1314.
17. Kim, K. S., Y. Zhao, H. Jang, S. Y. Lee, J. M. Kim, K. S. Kim, J. H. Ahn, P. Kim, J. Y. Choi, B. H. Hong. *Nature*, **2009**, *457*, 706–710.
18. Yan, K., L. Fu, H. Peng, Z. Liu. *Acc. Chem. Res.*, **2013**, *46*, 2263− 2274.
19. Mattevi, C., H. K, M. Chhowalla. *J. Mater. Chem.* **2011**, *21*, 3324-3334.
20. Li, X. S., W. W. Cai, J. H. An, S. Kim, J. Nah, D. X. Yang, R. Piner, A. Velamakanni, I Jung, E. Tutuc, S. K. Banerjee, L. Colombo, R. S. Ruoff. *Science*, **2009**, *324*, 1312−1314.
21. Hu, B., Y. Jin, D. Guan, Z. Luo, B. Shang, Q. Fang, H. Ruan. *J. Phys. Chem. C.*, **2015**, *119*, 24124-24131.
22. Mei, Q. Z. Ren, Y. Jiao, Y. Zhou, X. Xu, W. Li, J. Li, X. Zheng, J. Bai. *J. Phys. Chem.*, **2013**, *117*, 14348-14353.
23. Shin, Y. C., J. Kong. *Carbon*, **2013**, *59*, 439-447.
24. Li, X., W. Cai, L. Colombo, R. S. Ruoff. *Nano Lett.*, **2009**, *9*, 4268–4272.
25. Ago, H., Y. Ogawa, M. Tsuji, S. Mizuno, H. Hibino. *J. Phys. Chem. Lett.*, **2012**, *3*, 2228–2236.
26. Zhang, X., J. Ning, X. Li, B. Wang, L. Hao, M. Liang, M. Jin, L. Zhi. *Nanoscale*, **2013**, *5*, 8363–8366.
27. Jung, D. H., C. Kang, M. Kim, H. Cheong, H. Lee, J. S. Lee. *J. Phys. Chem. C*, **2014**, *118*, 3574–3580.

28. Yan, J., B. Hu, Z. Wei, Z. Luo, D. Wei, Y. Xi, Y. Zhang, Y. Liu. *J. Mater. Chem. A*, **2014**, *2*, 16208-16216.
29. Lavin-Lopez, M. P., J. L. Valverde, M. C. Cuevas, A. Garrido, L. Sanchez-Silva, P. Martinez, A. Romero-Izquiedo. *Phys. Chem. Chem. Phys.* **2014**, *16*, 2962-2970.
30. Wu, B., D. Geng, Z. Xu, Y. Guo, L. Huang, Y. Xue, J. Chen, G. Yu, Y. Liu. *NPG Asia Mater.*, **2013**, *5*, e36.
31. Zhang, Y., Z. Li, P. Kim, L. Zhang, C. Zhou. *ACS Nano*, **2012**, *6*, 126−132.
32. Geng, D., B. Wu, Y. Guo, B. Luo, Y. Xue, J. Chen, G. Yu, Y. Liu *J. Am. Chem. Soc.*, **2013**, *135*, 6431− 6434.
33. Vlassiouk, I., *M.* Regmi, P. Fulvio, S. Dai, P. Datskos, G. Eres, S. Smirnov. *ACS Nano*, **2011**, *5*, 6069−6076.
34. Zhang, X., J. Ning, X. Li, B. Wang, L. Hao, M. Liang, M. Jin, L. Zhi. *Nanoscale*, **2013**, *5*, 8363−8366.
35. Losurdo, M., M. M. Giangregorio, P. Capezzuto, G. Bruno. *Phys. Chem. Chem. Phys.*, **2011**, *13*, 20836-20843.
36. Ma, T., W. Ren, X. Zhang, Z. Liu, Y. Gao, L. C. Yin, X. L. Ma, F. Ding, H. M. *Proc. Natl. Acad. Sci. U. S. A*, **2013**, *110*, 20386−20391.
37. Gan, L., Z. Luo. *ACS Nano*, **2013**, *7*, 9480−9488.
38. Yan, Z., Y. Liu, J. Lin, Z. Peng, G. Wang, E. Pembroke, H. Zhou, C. Xiang, A. R. O. Raji, E. L. G. Samuel, T. Yu, B. I. Yakobson, J. M. Tour. *J. Am. Chem. Soc.*, **2013**, *135*, 10755−10762.
39. Gao, L., W. Ren, J. Zhao, L. P. Ma, Z. Chen. *Appl. Phys. Lett.*, **2010**, *97*, 183109−183109-3.
40. Mohsin, A., L. Liu, P. Liu, W. Deng, I. N. Ivanov, G. Li, O. E. Dyck. G. Duscher, J. R. Dunlap, K. Xiao, G. Gu. *ACS Nano*, **2013**, *7*, 8924−8931.
41. Bhaviripudi, S., X. Jia, M. S. Dresselhaus, J. Kong. *Nano Lett.*, **2010**, *10*, 4128-4133.
42. Jin, Y., B. Hu, Z. Wei, Z. Luo, D. Wei, Y. Xi, Y. Zhang, Y. Liu *J. Mater. Chem. A.*, **2014**, *2*, 16208-16216.
43. Jung, H. S. H. Z. Tsai, D. Wong, C. Germany, S. Kahn, Y. Kim, A. S. Aikawa, A. K. Desai, G. F. Rodgers, A. J. Bradley, J. Velasco, K. Watanabe, T. Taniguchi, F. Wang, A. Zettl, M. F. Crommie. *J. Vis. Exp.* **2015**, *101*, e52711 (1-9).
44. Wang, Y., Y. Zheng, X. Xu, E. Dubuisson, Q. Bao, J. Lu, K. P. Loh. *ACS Nano*. **2011**, 5, 9927-9933.

45. Ferrari, A. C., J. C. Meyer, V. Scardaci, C. Casiraghi, M. Lazzeri, F. Mauri, S. Piscanec, D. Jiang, K. S. Novoselov, S. Roth, A. K. Geim. *Phys. Rev. Lett*. **2006,** *97***,** 187401 (1-4).
46. Casiraghi, C., S. Pisana, K. S. Novoselov, A. K. Geim, A. C. Ferrari. *Appl. Phys. Lett*. **2007,** *91***,** 233108 (1-3).
47. Ferrari, A. C. *Solid State Commun*. **2007,** *143*, 47-57.
48. Malard, L. M., M. A. Pimenta, G. Dresselhaus, M. S. Dresselhaus. *Phys. Rep.* **2009**, *473*, 51-87.
49. Ferrari, A. C., D. M. Basko. *Nat. Nanotechnol.* **2013**, *8*, 235-246.
50. Madito, M. J., N. Manyala, A. Bello, J. K. Dangbegnon, T. M. Masikhwa, D. Y. Momodu. *RSC Adv.***2016**, *6*, 28370-28378.
51. Kim, K., S. Coh, L. Z. Tan, W. Regan, J. M. Yuk, E. Chatterjee, M. F. Crommie, M. L. Cohen, S. G. Louie, A. Zettl. *Phys. Rev. Lett.* **2012**, *108*, 246103.
52. Fang, W., A. L. Hsu, R. Caudillo, Y. Song, A. G. Birdwell, E Zakar, M. Kalbac, M. Dubey, T. Palacios, M. S. Dresselhaus, P. T. Araujo, J. Kong. *Nano Lett.* **2013**, *13*, 1541-1548.
53. Cong, C., T. Yu, K. Sato, J. Shang, R. Saito, G. Dresselhaus, M. S. Dresselhaus. *ACS Nano*, **2011**, *5*, 8760-8768.
54. Hao, Y., Y. Wang, L. Wang, Z. Ni, Z. Wang, R. Wang, C. K. Koo, Z. Shen, J. T. L. Thong. *Small*, **2010**, *2*, 195-200.
55. Chen, S., W. Cai, R. D. Piner, J. W. Suk, Y. Wu, Y. Ren, J. Kang, R. S. Ruoff. *Nano Lett.* **2011**, *11*, 3519-3525.
56. Lee, S., K. Lee, Z. Zhong. *Nano Lett.* **2010**, *10*, 4702-4707.
57. Sun, Z. Z., A.-R. O. Raji, Y. Zhu, C. S. Xiang, Z. Yan, C. Kittrell, E. L. G. Samuel, J. M. Tour. *ACS Nano*, **2012**, *6*, 9790–9796.

Chapter 5

Optimizing the synthesis conditions for incorporation of nitrogen atoms into graphene films (in-situ vs. post nitrogen doping)

5.1. Introduction

Graphene, a single layer of sp^2 hybridized carbons and the first example of a stable free-standing 2D material, is one of the amazing materials in modern science that has attracted a wide-range of research interest from both theoretical and experimental scientists[1-3]. With its unique properties, such as high surface area, good thermal and electrical conductivity, strong Young's modulus, ultrahigh carrier mobility, charge concentration, and many other properties[1, 4-10], graphene has been intensively studied over the past decade. Consequently, these unique properties render graphene a very good candidate for a wide range of applications, such as in energy conversion and storage [11, 12], chemical and biological sensors [13, 14] organic solar cells [15, 16], transparent conductive films for flexible electronics [17], ultra- and supercapacitors [18, 19], and field effect transistors (FET) [1, 20]. However, as a zero-band gap semiconducting material with an inert surface, applications of pristine graphene in the next generation electronic devices is limited [2, 21]. This is because its electrical conductivity cannot be completely controlled when compared with the classical semiconductors (such as silicon, germanium, gallium arsenide, silicon carbide, etc.). To tackle this issue, much research effort has been focused on the development of new and reliable methods for modifying and fine-tuning the electrochemical properties of graphene[22, 23]. Among the many proposed methods for modification of the intrinsic characteristics and semiconducting properties of graphene, techniques such as the functionalization of the surface of graphene with gaseous molecules, metals, organic molecules [24-27]; geometrical confinement of graphene to nanoribbons and quantum dots [28, 29]; interaction with substrates like SiC or SiO_2 [30, 31]; creation of corrugated surfaces [32, 33]; application of electric or magnetic or electromagnetic fields [16]; and chemical substitution of foreign atoms [34-39] have been used. For instance, Haberer *et al.* showed that treatment of graphene with atomic hydrogen atoms led to hydrogenation of sp^2 to sp^3 carbons at the graphene edges, and this resulted in opening of the graphene band gap to ~1.0 eV [40]. Unfortunately, most of the proposed methods for modulating the electrochemical properties

of graphene suffer major deficiencies when considering the operation costs, scalability and reproducibility.

To circumvent the complications associated with most proposed methods, theoretical and experimental reports have indicated that chemical substitution or doping of foreign atoms into the graphene lattice can be a promising and feasible approach for effectively tailoring the electrochemical properties and electronic band structure of pristine graphene [34-39]. Doping is also an effective way to modify the local chemical activity of pristine graphene for future applications. Recently, intense and continuous research interests have focused on either single or co-substitution of heteroatoms such as nitrogen, phosphorus, sulphur, nitrogen/sulphur, or nitrogen/boron into the graphene lattice, so as to induce a p- or n-type semiconducting behaviour as well as to open its band gap[34-39]. Among the various heteroatoms/dopants, nitrogen is the most widely used due to its comparative atomic size (d_N = 70 pm_N vs. d_C = 65 pm_C) and also due to the extra electron in its outer shell. In addition, doping with nitrogen atoms effectively changes the spin density and charge distribution of neighbouring carbons, thus enhancing novel electronic properties in nitrogen doped graphene nanomaterials. As a result, N-doped graphene has shown promising catalytic activity towards oxygen reduction reactions (ORR) in fuel cells [41, 42]. Moreover, due to the lone pair of electrons from N atoms, the electrical conductivity of N-doped graphene can be easily modulated by controlling the amount of the dopant (nitrogen atoms). This makes N-doped graphene a suitable material for application in dye sensitized solar cells [43], field-effect transistors [1, 14, 44], batteries [45], supercapacitors [18, 19], and biochemical sensors [13, 14].

Therefore, a better understanding of the effect of nitrogen doping in many electrochemical device fabrication as well as the ability to control the degree of doping and the type on nitrogen bonding states is a prerequisite to further extend the applications of graphene. Similar to other carbon materials like carbon nanotubes (CNTs), doping of graphene with nitrogen atoms can be achieved by following two general synthesis routes. The first method is the bottom-up or in-situ approach, and it involves the growth of N-doped graphene from the recombination of carbon and nitrogen atoms into a continuous matrix [42]. The commonly used synthesis techniques for fabrication of N-doped graphene via this route include chemical vapour deposition (CVD) of hydrocarbons in the presence of nitrogen-rich precursors such as gaseous ammonia [35, 46, 47], solid melamine or urea [48, 49], or liquid organics [50, 51]. In-situ doping via the CVD technique is the promising and feasible method for controlling the doping level, the type of bonding states for nitrogen atoms as well as the band structure of the as-grown

doped materials [35, 46, 47]. For instance, using the ammonia-assisted CVD techniques, we have shown that the doping content and types of nitrogen configurations in N-doped graphene films can be controlled by adjusting the graphene growth time (2 min- 20 min) [35]. At long growth times (20 min), pyridinic-rich graphene films were grown with nitrogen content (N/C) of ~2.84 %. Using melamine as a sole solid source for carbon and nitrogen, Wang *et al.* showed that during the CVD-synthesis of N-doped graphene [48], the nitrogen content and configuration were dependent on mainly of the growth temperature (930 ^{o}C – 1050 ^{o}C). They reported that growth of graphitic-rich graphene with a maximum overall nitrogen incorporation of ~5.6 at.% (990 ^{o}C) resulted in high charge carrier mobility (~74 $cm^2V^{-1}s^{-1}$). Moreover, Zhang and co-workers successfully synthesized pyrrolic-rich N-graphene films with a total nitrogen content of ~3.72 at.% using urea as a solid nitrogen source [49]. Using a liquid-based CVD technique, Capasso *et al.* studied the effect of growth temperature and gas flow rates on the growth of N-graphene from ethanol and pyridine as carbon and nitrogen sources [50]. At 1000 ^{o}C, pyridinic-rich N-graphene films contained the maximum nitrogen content of ~3%, and exhibited an electrical conductivity of 14.5 $\times 10^5$ S/m, which was ~40% larger than that of ethanol-CVD grown graphene films.

The second synthesis route for incorporation of nitrogen atoms into the graphene lattice is post-treatment of graphene nanomaterials with nitrogen-containing precursors. Techniques such as thermal or high power electrical annealing in NH_3 [52, 53], N_2 plasma treatment [54], ammonia annealing after ion irradiation [55], arc-discharge treatment with a nitrogen-containing precursor [56], treatment with hydrazine (N_2H_4) [57] and hydrothermal treatment with a polymer [58] are among the methods used to achieve N-doping of graphene through the post doping synthesis route. For instance, Long *et al.* showed that treatment of graphene oxide (GO) with a solution mixture of NH_3 and N_2H_4 (3:1) at different temperatures (160 - 200 ^{o}C) modulated the overall N-content and morphology of the as-synthesized N-doped reduced graphene oxide (N-rGO) flakes [57]. Furthermore, Wang and co-workers indicated that by adjusting the exposure time (20 – 100 min) and plasma strength (100 W) during plasma treatment of graphene or GO in an atmosphere of N_2 led to incorporation of nitrogen atoms at the edge defects created by the plasma as well as introducing a significant amount of oxygen species [54]. They indicated that an increase in reactivity was displayed by carbon atoms neighbouring the edges defects created by the plasma. Recently, Zhang *et al.* reported a new feasible post doping approach using the hydrothermal thermal treatment of GO with dicyandiamide [58]. They showed that by using low temperatures (180 ^{o}C), the composition and type of nitrogen

bonding configurations in the as-synthesized N-rGO nanosheets could be controlled for effective ORR. Unfortunately, most of these synthesis approaches suffer major draw-backs related to the difficulty of producing large-scale and reproducible intrinsically N-doped graphene nanomaterials. Additionally, for some synthesis techniques, the difficulty of maintaining a high vacuum give rise to inhomogeneities in the gas pressure in the reaction chamber, hence affecting the overall degree of doping and the bonding states of nitrogen atoms. Contrarily, thermal treatment of as-grown graphene in a nitrogen-rich atmosphere, such as NH_3 or melamine, through the CVD technique has shown to be the most promising method for post-doping graphene. For example, the N-content and configurations can be easily controlled by adjustment of the annealing temperature (800 – 1100 ^oC) [35, 46, 47], exposure time (2 – 20 min) [35] and concentration of the precursor material [59, 60].

Regardless of the synthesis route used to grow N-doped graphene nanomaterials, incorporation of nitrogen into the sp^2-hybridized carbon lattice of graphene and other carbon nanomaterials is known to lead to the creation of different types of impurities or defects. These defects result in formation of different bonding configurations between nitrogen and carbon atoms, as shown in scheme 5.1. Theoretical and X-ray photoelectron spectroscopy experiments have indicated that nitrogen atoms can be directly substituted into the lattice [61, 62](Scheme 5.1a). Moreover, nitrogen atoms can be incorporated on the edges of either six-membered carbon rings [61, 62] (Scheme 4.1b-d) or five-membered carbon rings [61, 62] (Scheme 5.1e). Other bonding configurations include the oxidized pyridinic-N (Scheme 5.1f), the amine type (Scheme 5.1g) and the presence of nitrogen adatoms [61, 62]. Each of these bonding configurations is known to impact differently on the electronic and transport properties of N-doped graphene and other carbon materials. For example, doping of graphene with the pyridinic-N and pyrrolic-N types has been reported to induce a p-type semiconducting behaviour [63, 64]. On the other hand, the graphitic-N bonding configuration has been found to induce a strong n-type effect, thus preserving the high charge carrier mobility due to lack of defect formation [63-65]. Interestingly, based on the different thermal stabilities of the nitrogen configurations, growth conditions can be used to effectively control the bonding configurations of nitrogen atoms. For example, Pels *et al.* reported that increasing the growth temperature decreased both the total nitrogen content and the percentage of pyrrolic-N, while it increased both the pyridinic- and graphitic-N bonding configurations [66]. Furthermore, Usachov *et al.* showed prolonged heat treatment led to transformation of pyridinic-N to the graphitic configuration [22].

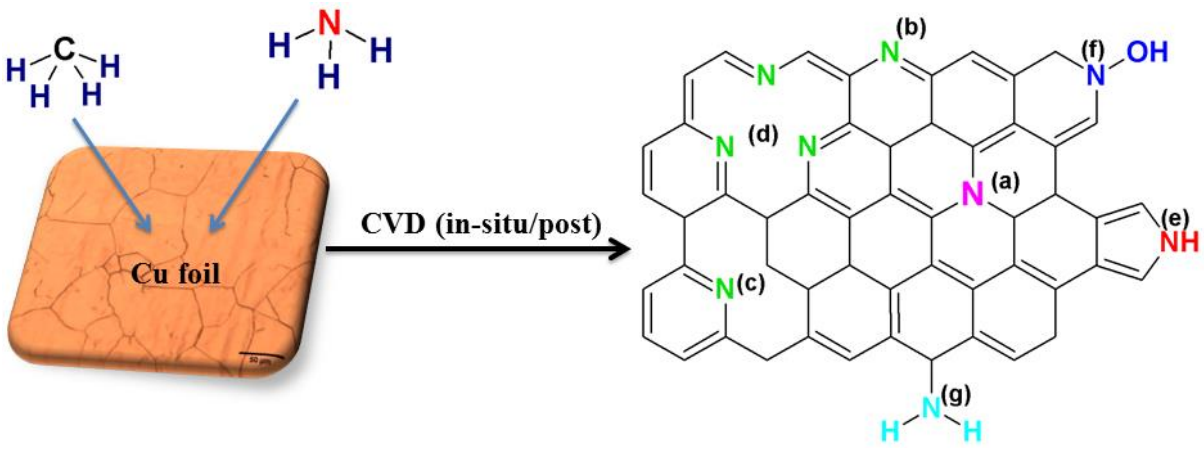

Scheme 5.1: Schematic representation of nitrogen configurations in N-doped graphene: (a) **graphitic-N**, (b) **pyridinic-N**, (c) single vacancy **pyridinic-N**, (d) triple vacancy **pyridinic-N**, (e) **pyrrolic-N**, (f) oxidized **pyridinic-N**, and (g) **amine-N**.

Thus, it is of great importance to precisely control the nitrogen configurations embedded in the graphene lattice. This control would provide a new and meaningful platform for investigating the factors that influence the application of N-doped graphene in devices such as fuel cells, dye-sensitized solar cells, field-effect transistors, etc. [1, 14, 41-44]. Since the CVD technique is the most used synthesis method for producing large-area graphene films with controlled thickness and morphology, the use of CVD method for incorporation of more nitrogen atoms into the graphene lattice without compromising the structural and electronic properties of graphene is an interesting area of research for materials scientists. Most studies have indicated that the growth of N-doped graphene using the CVD technique, either via in-situ or post doping approach, is dependent on the concentration of the N-precursors material and the growth temperature [35, 46, 47]. However, most of these studies have been performed independently and little or no research has been done to study the side-by-side comparison between in-situ and post N-doping of graphene by CVD. This approach could be useful for investigating the major factors that influence the application of N-graphene in different electronic devices. As a result, this work will focus on investigating and studying the best doping technique for incorporating nitrogen atoms into the graphene lattice, without compromising the structural properties. The comparison between in-situ doping and post nitrogen doping techniques was studied using two different flow rates (5 sccm and 10 sccm) of NH_3, as the nitrogen precursor.

5.2. Experimental

5.2.1 Starting materials

Acetone (99%, gold line ACE), methanol (99.5 %), ethanol (absolute), iso-propanol (ACE, 99%), ortho-phosphoric acid (85%, LabChem), urea (99%, Promark Chemicals), chlorobenzene (99%, UniLab), sodium hydroxide pellets (98%, Merk) and poly(methyl methacrylate) (PMMA, Mw ~999 000) were purchased from Sigma-Aldrich, South Africa. The gases used included argon (Ar, 99%), methane (CH_4, 99.98%), ammonia (NH_3, 10% in Ar), and hydrogen (H_2, 99.98 %), and these were supplied by Afrox, South Africa. Other materials included a copper foil (25 µm, 99.98%) from Sigma Aldrich (RSA), a silicon substrate with a 300 nm silicon oxide layer (Sigma-Aldrich), a copper plate and an iron wire (University of the Witwatersrand workshop). Distilled water was used in all the experiments.

5.2.2 Synthesis and transfer of films

Nitrogen doped graphene films were synthesized by atmospheric pressure CVD (APCVD) on a copper foil in a quartz tube furnace. The samples were grown with 10 sccm CH_4, 3 sccm H_2, 300 sccm Ar, and varying flow rates of NH_3 (5 and 10 sccm). Initially, the Cu foil was electrochemically cleaned by using a solution of 300 mL distilled water, 150 mL ethanol, 150 mL ortho-phosphoric acid, 30 mL isopropanol and 3.0 g urea [67]. After cleaning, the Cu foil was placed at the center of a cylindrical quartz tube (100 cm × 20 cm) inside a horizontally oriented CVD furnace. The furnace was heated to 1000 ^oC at a ramping rate of 10^oC/min in H_2 and Ar atmospheres, and then held at the designated temperature for 30 minutes. For growth of the in-situ N-doped graphene films, 10 sccm of CH_4 and different flow rates of NH_3 (5 and 10 sccm) were introduced into the reaction chamber for 10 min. For growth of post N-doped graphene films, initially, growth of pristine graphene was achieved by passing 10 sccm of CH_4 for 10 min; after which the CH_4 was turned off and varying flow rates of NH_3 were passed over the prepared graphene for another 10 min. Finally the reactor was *rapidly* cooled to room temperature by pushing the quartz tube outside the reactor. After growth and for characterization purposes, the as-grown graphene films were then transferred onto the 300 nm SiO_2/Si substrate, using the PMMA assisted electrochemical delamination method (Scheme 3.2)[68]. The as-grown films were labelled as N-5sccm$_{in\text{-}situ}$ and N-10sccm$_{in\text{-}situ}$ for films grown under in-situ conditions, as well as N-5sccm$_{post}$ and N-10sccm$_{post}$ for N-doped films grown under post doping conditions.

5.2.3 Characterization

Raman spectroscopy, optical microscopy, and X-ray photoelectron spectroscopy (XPS) were the main characterization techniques used to assess the structure, quality and doping levels of the as-grown films. The structural characterization of the as-grown N-doped graphene films was studied using a Raman spectrometer. Raman spectra of all films were collected on a Bruker Raman Senterra spectrometer (Bruker, South Arica) using a 532 nm excitation laser and at a very low laser power (0.5 mW) to avoid laser-induced heating which can damage the films. The Raman measurements were collected from graphene films that were transferred onto 300 nm SiO_2/Si substrates. The imaging of the graphene films was performed on films that were transferred onto the SiO_2/Si substrates. The optical images were collected in the bright field mode from an Olympus BX 63 Optical/Fluorescence Microscope using the 20x optical objective. The chemical composition of the prepared films was studied by X-ray photoelectron spectroscopy (XPS) at the Thermo Scientific factory in UK. The ex-situ XPS study was carried out on films grown on a Cu foil with a Thermo Escalab 250. The radiation used was determined from a monochromatised aluminium Kα radiation with a 400 μm spot size and a 'pass' energy of 60 eV.

5.3. Results and discussions

The structural characterization of the as-grown films was determined by studying their optical images and Raman spectra; while the degree of N-doping and type of N-configurations were confirmed by studying their XPS spectra.

5.3.1. Microstructural measurements of the films

Optical microscopy imaging was used to ascertain the structural/morphological properties of the as-grown pristine and N-doped graphene films. The typical optical micrographs of all the films, after transference onto 300 nm SiO_2/Si substrates (Fig. 5.1), revealed large-area, continuous and uniform films for both the pristine and post N-doped films, whereas the in-situ N-doped films exhibited a broken morphology. Furthermore, comparison of the morphologies of pristine graphene films and doped graphene films revealed that the N-doped graphene films exhibited regions of multilayers embedded within a uniform and continuous film. These multilayer regions could be ascertained by formation of the dark spots. The thickness of the graphene films on a 300 nm SiO_2/Si substrate could be verified by the colour contrast of the substrate due to the light interference effect[2, 3]. The darker the colour of the graphene film, the thicker the graphene film [69]. The formation of multilayers can be attributed

to the etching effect of NH_3 on the Cu foil. The NH_3 etching thus lead to formation of "pits" (shown in Fig. 5.1 inserts), which then enable deposition of more carbon and/or nitrogen atoms, resulting in growth of multilayered regions.

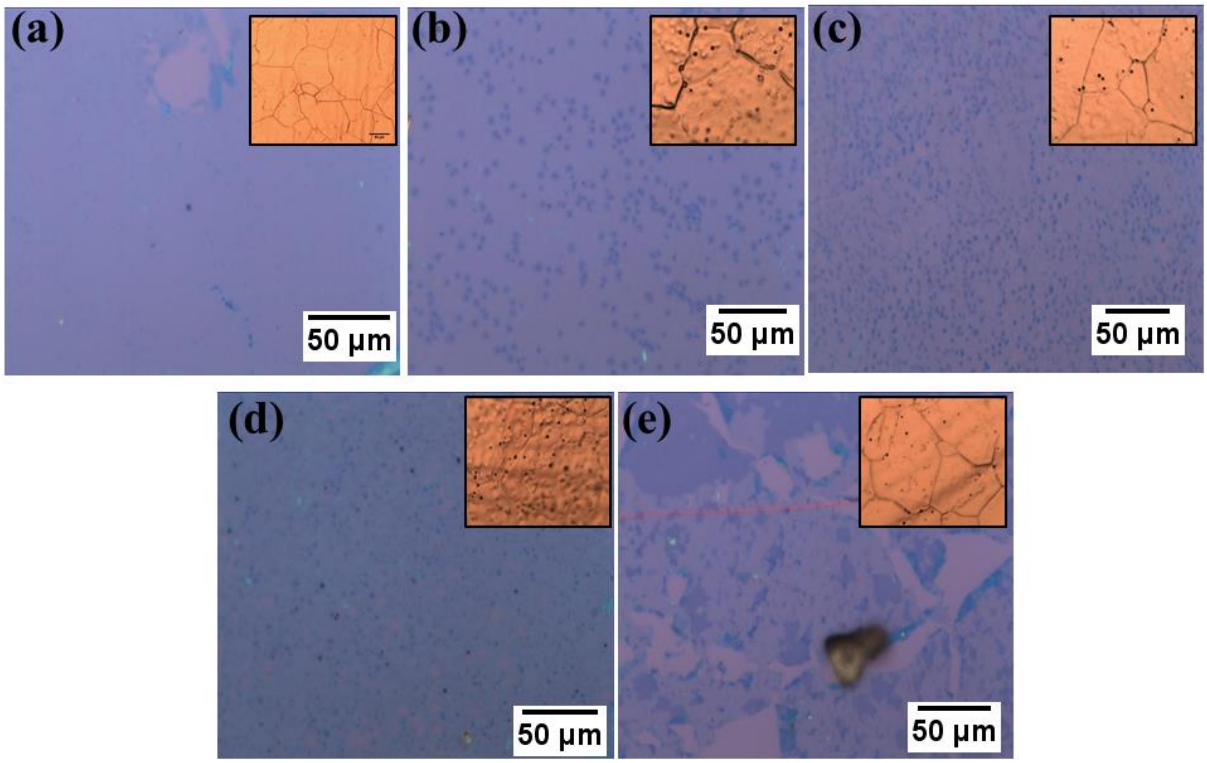

Figure 5.1: Optical images of (a) pristine, (b) N-5sccm$_{in\text{-}situ}$, (c) N-5sccm$_{post}$, (d) N-10sccm$_{in\text{-}situ}$, and (e) N-10sccm$_{post}$ graphene films. Insert: images of films on the Cu foil (Scale bar- 50 µm).

5.3.2. Raman Analysis of the films

Raman spectra of pristine samples were compared with in-situ and post N-doped graphene films grown with various NH_3 flow rates. The Raman spectra were performed on films transferred onto a 300 nm SiO_2/Si substrate (Fig. 5.2). In all spectra, broad D bands (~1340.01 cm^{-1}- 1350.5 cm^{-1}), G bands (~1583.5 cm^{-1} – 1590.4 cm^{-1}) and the 2D bands (~2675.5 cm^{-1} – 2681.5 cm^{-1}) [70-74] were observed. The positions of the peaks are shown in table 5.1.

Table 5.1: Band positions for pristine and N-doped graphene films

Sample	Peak position (cm^{-1})			
	D	**G**	**D***	**2D**
Pristine	1340,0	1583,5	-	2675,5
N-5sccm$_{in-stu}$	1350,2	1590,3	1622,6	2680,0
N-5sccm$_{post}$	1350,2	1590,4	1623,1	2679,3
N-10sccm$_{in-situ}$	1350,5	1590,1	1622,0	2681,5
N-10sccm$_{post}$	1342,4	1583,6	1623,9	2676,1

The presence of the Raman-forbidden D peak in all the graphene films indicated the presence of structural defects and disordered structures at the edges of the sp^2 domains due to the occurrence of single-phonon intervalley scattering processes [70-74]. Additional analysis of the Raman spectra showed that N-doped graphene films exhibited another Raman-forbidden band, the D^* band centred at ~1622.02 cm^{-1} – 1623.9 cm^{-1}, which can be attributed to the intravalley, defect-induced double-resonance processes [70-74]. On the other hand, both G and 2D bands are known to satisfy the Raman selection rule. The G band arises from the first-order doubly degenerate E_{2g} phonons at the Brillouin zone and can be ascribed to the vibrational modes of sp^2C atoms in the bulk of the graphitic layers. Furthermore, the 2D band is known to be sensitive to lattice distortions and it corresponds to the second-order double-resonance process which is related to the zone boundary phonons [70-74]. Due to lattice distortions induced by incorporation of nitrogen atoms into the graphene lattice, the relative intensity of the 2D band in N-doped graphene films, specifically the in-situ doped and N-5sccm$_{post}$ doped films, is significantly reduced to almost zero. Similarly, lattice disorder as a result of N-doping in the N-10sccm$_{post}$ doped films was found to slightly suppress the 2D band, whereas the relative intensity of the D band was significantly increased.

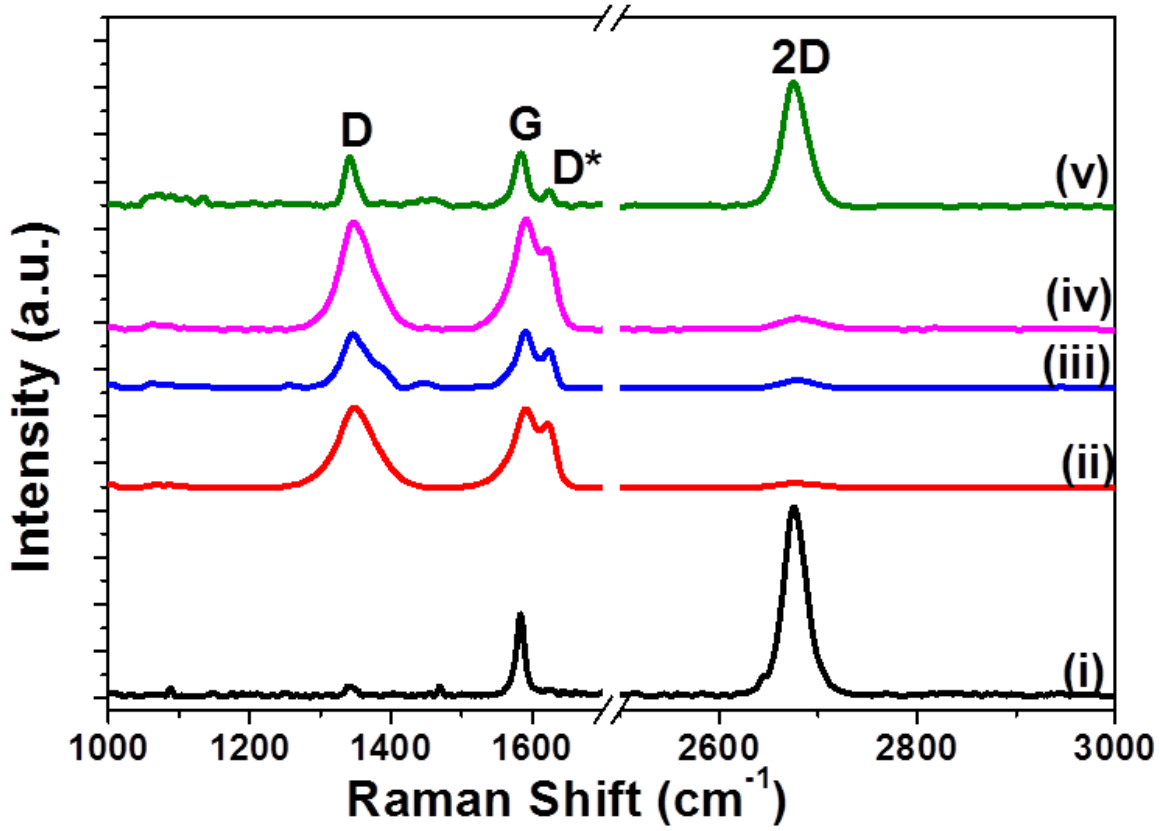

Figure 5.2: Raman spectra of (i) pristine, (ii) N-5sccm$_{in\text{-}situ}$, (iii) N-5sccm$_{post}$, (iv) N-10sccm$_{in\text{-}situ}$, and (v) N-10sccm$_{post}$ graphene films grown using varying flow rates of NH3.

Normally for pristine graphene films, the intensity ratio of the D band with respect to that of the G band (I_D/I_G) is used to probe the level of disorder either in the form of sp^3-C bond or lattice vacancies [75-78]. Similarly, in nitrogen doped graphene films, the I_D/I_G ratio is used for determining the degree of doping, since doping induces defects into the graphene lattice [75-78]. Thus, the I_D/I_G ratios were determined for both pristine and doped graphene films, and were plotted as shown in figure 5.3a. It was observed that pristine graphene films exhibited I_D/I_G ratio of ~0.271, which signified the growth of high quality graphene films [70-78]. However, upon introduction of both the carbon (CH_4, 10 sccm) and nitrogen (NH_3, 5 sccm or 10 sccm) precursors during the growth, so as to synthesize in-situ doped graphene films, the quality of the films was compromised and the degree of disorder was found to significantly increase, as shown by the I_D/I_G ratios of ~1.086$_{N\text{-}5sccm}$ and ~1.042$_{N\text{-}10sccm}$. The results show that incorporation of nitrogen atoms via the in-situ route led to sufficient of lattice distortion, and this was corroborated by the suppressed intensity of the lattice distortion-sensitive 2D band (Fig. 5.2(ii) and (iv)). Similarly, when 5 sccm of NH_3 was introduced after the growth of

pristine graphene, a relatively high defect density (I_D/I_G ratio of ~0.975) and a significantly suppressed intensity of the 2D band (Fig. 5.2(iii)) were observed. This indicates that utilization of low flow rate of NH_3, even during post nitrogen doping, also results in facile distortion of the graphene lattice.

On the contrary, post nitrogen doping with 10 sccm of NH_3 was observed to result in fewer lattice distortions as indicated by the I_D/I_G ratio of ~0.939. The prominent 2D band in the Raman spectra of N-10sccm-post doped graphene films (Fig. 5.2(v)) suggests the restoration of the hexagonal lattice of graphene, regardless of incorporation of nitrogen atoms. The results indicate that with high flow rates of NH_3, there is less chance for nitrogen atoms to be incorporated into the graphene lattice. Consequently, this led to increased competition for the catalytic decomposition of NH_3 on the graphene defects, and hence increased loss of NH_3 molecules into the carrier gas.

Finally, the nature of the defects in doped graphene films was established by determining the ratio of the two defect-induced bands (Fig. 5.3b, I_D/I_{D*}). Recently, numerous research reports have shown that Raman spectroscopy can be used as an important tool for probing the nature of defects in both pristine and doped graphene [72-78]. The studies showed that the I_D/I_{D*} is at a maximum (~13) for sp^3 hybridization defects at graphene/graphite edges and grain boundaries, and that the value decreased to ~7 for on-site/vacancy-like defects. Furthermore, the studies indicated that the I_D/I_{D*} ratio finally reached a minimum of ~3.5 for defects located at grain/domain boundaries. Therefore, analysis of both in-situ grown and N-$5sccm_{post}$ doped graphene films suggested that the nature of the defects was predominately associated with grain/domain boundary defects, as shown by the ratio range of $\sim 1.68 \leq I_D/I_{D*} \leq 1.91$. Interestingly, N-$10sccm_{post}$ doped graphene films exhibited on-site/vacancy-like defects as indicated by the I_D/I_{D*} ratio of ~3.82.

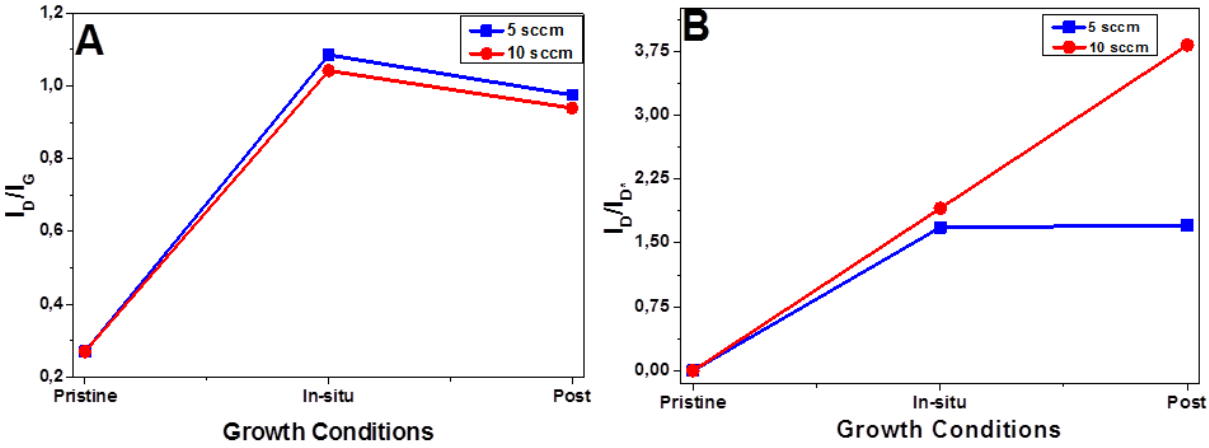

Figure 5.3: Evolution of (a) the I_D/I_G ratio for both pristine and N-doped graphene films and (b) the I_D/I_{D*} for N-doped graphene films.

The shift in the positions of both the G and 2D band is another important parameter used to determine the effect of doping on the electronic properties of nitrogen doped graphene [72-78]. Recent reports have indicated that upon doping of graphene with nitrogen atoms, the G band is expected to blue shift due to increased electron doping, whereas the 2D band can either blue or red shift due to the increased electron doping and compressive/tensile strains in the C-C bonds [79, 80]. The degree of lattice distortion and the electronic properties of the N-doped graphene films can be ascertained by determining the shift of the G band. Thus analysis of the position for the doped graphene (Fig. 5.4a), with respect to the pristine graphene films, revealed that the G band blue shifted by ~ 6.84 cm^{-1}, 6.58 cm^{-1}, and 6.91 cm^{-1} for the N-5sccm$_{in\text{-}situ}$, N-10sccm$_{in\text{-}situ}$, and N-5 sccm$_{post}$ grown N-doped graphene films, respectively. The blue shift of the G band could be attributed to the increased electron doping, as a result of the stiffening of the phonons in the G band [79, 80]. Remarkably, a mild electron doping was found to be induced into the graphene structure when 10 sccm of NH_3 was used to synthesize post nitrogen doped graphene films. The results are in good agreement with the observed Raman spectra of these films, which was characterized by a prominent 2D band, suggesting a lower level of doping and a better restoration of the graphene lattice.

Additionally, the position of the 2D band was used to further investigate and understand the electronic and structural properties of N-doped graphene films [75-80]. As such, analysis of the 2D position in the doped graphene films, showed a blue shift of ~ 4.52 cm^{-1}, 5.98 cm^{-1}, and 3.80 cm^{-1} for the N-5sccm$_{in\text{-}situ}$, N-10sccm$_{in\text{-}situ}$, and N-5 sccm$_{post}$ grown films, respectively (Fig. 5.4b). A minor blue shift of ~ 0.55 cm^{-1} was observed for post doped graphene films grown using 10 sccm of NH_3. In addition to increased electron doping, the results suggest

that compressive/tensile strains on the C-C bonds could also contribute to the observed blue shift of the 2D band. Theoretical calculations have indicated that due to the different nitrogen configurations found in N-doped graphene, compressive and/or tensile stains play an important role in the shift of the 2D band [81]. For instance, shorter C-N bond lengths in pyridinic and pyrrolic bonding configurations (~ 1.32 Å and ~ 1.37 Å respectively) exert more compressive strains on the C-C bonds in the graphene lattice, hence leading to a blue shift in the 2D band. Additionally, reports from Dettori *et al.* [82] showed that defects associated with bond reconstruction (Stone Wales defects) within the graphene lattice as a result of nitrogen doping (Fig. 5.4c)[83] also exert a major contribution on the strain fields that affect the positions of both G and 2D bands. These Stone Wales defects could be found in the following forms: 5-8-5 (pentagon-octagon-pentagon), 55-77 (two pentagons-heptagons), etc. Therefore based on the observed results, it can be ascertained that a blue shift of both G and s2D bands is mainly due to both electron doping and compressive strain on C-C bonds.

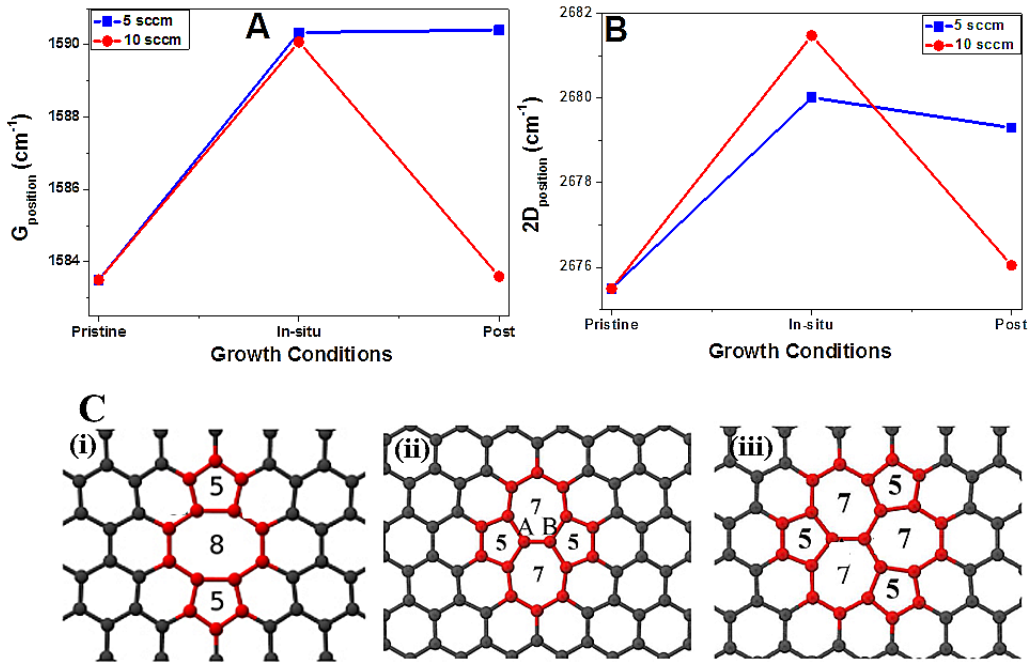

Figure 5.4: Peak positions for the (a) G and (b) 2D bands for N-doped graphene films with respect to pristine graphene films. Pictorial representation of reconstruction defects: (i) 5-8-5, 55-77, and 555-777 [83].

5.3.3. XPS measurements of the films

The X-ray photoelectron spectroscopy, a surface-sensitive technique, was used to determine the overall doping content as well as the bonding states of the nitrogen atoms in the as-grown films. By taking the integrated peak areas of the C1s and O1s from the survey XPS spectra

(Fig. 5.5a), the overall atomic percentages from pristine and doped graphene films were found to decrease for carbon (85.1 at.% - 60.4 at.%) atoms and increasing for oxygen atoms (10.5 at% - 29.1 at.%), as shown in table 5.2. The high oxygen content in doped graphene films correlates well with the Raman data which showed an increased defect density ratio upon doping. This is because an increased defect density indicates increased decoration of graphene edges and defects with oxygen atoms. Moreover, the increased oxygen content in doped graphene films indicates stronger oxygen ability on N-doped films, thus suggesting a great potential for application of the doped films in fuel cells for oxygen reduction reactions (ORR) [41, 42].

Table 5.2: Atomic compositions of the pristine and N-doped graphene films

Sample	Elemental composition (at.%)				N/C
	C	N	O	Cu	
Pristine	85,1	--	10,5	4,40	-
N-5sccm$_{in-situ}$	69,5	2,26	17,3	10,9	3,25
N-5sccm$_{post}$	60,4	1,44	25,1	13,0	2,38
N-10sccm$_{in-situ}$	66,0	0,71	21,3	12,0	1,08
N-10sccm$_{post}$	60,8	0,11	29,1	9,98	0,181

Analysis of the integrated peak areas of the N1s spectra revealed that the highest nitrogen atomic percentage was found for in-situ grown graphene films. The ratio of the integrated peak area of N1s to that of the C1s (i.e. N/C ratio, Fig. 5.5b) was used to calculate the overall nitrogen content in the films, and this was found to be 3.25%, 2.38%, 1.08%, and 0.181% for the N-5sccm$_{in-situ}$, N-5 sccm$_{post}$, N-10sccm$_{in-situ}$, and N-10scccm$_{post}$ graphene films, respectively. In general, the results showed that the maximum nitrogen content was dependent on the flow rate of the nitrogen precursor as well as the synthesis route. The most intriguing results were observed for the post doped graphene films. To be more specific, the high degree of doping in N-5sccm$_{post}$ graphene films suggested that with low flow rates of NH_3, the equilibrium between the adsorption and desorption processes was reached on the available active sites on the graphene edges and/or defects. This would then permit large incorporation of N atoms at the edges or grain boundaries. However, with high NH_3 flow rates, incorporation of nitrogen atoms into the graphene lattice is more difficult due to the increased equilibrium for adsorption and decomposition. Furthermore, an increase in NH_3

concentration led to the formation of the more stable N_2 molecules, which are then liberated by the buffer gas. In addition to this, since the reactions occur in the presence of hydrogen gas, any unstable C-NH_2 bonds are susceptible to being broken. This leads to formation and release of more N_2 molecules. Consequently, incorporation of nitrogen atoms is compromised and a low N/C content is observed.

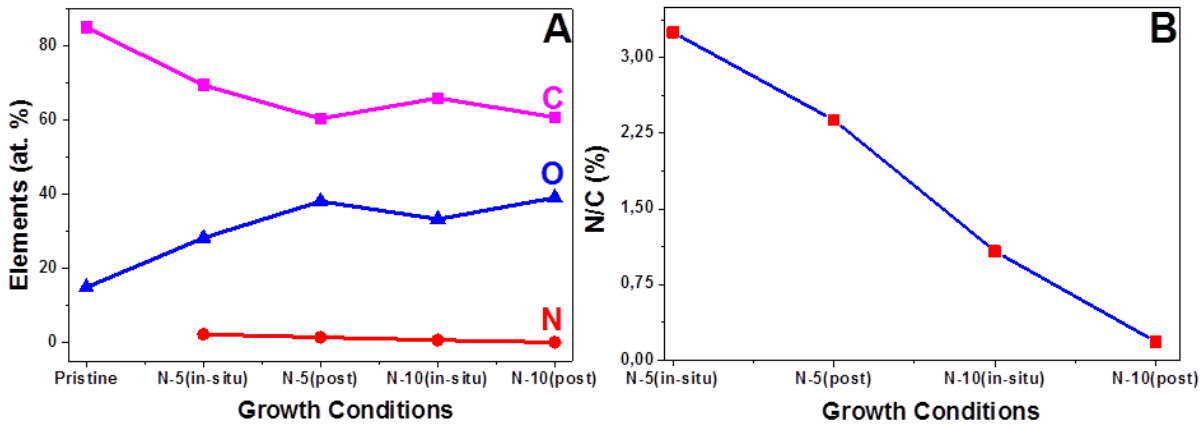

Figure 5.5: (a) Atomic composition analysis from the XPS survey spectra and (b) N/C content in N-doped graphene films.

The determination of the electronic bonding states of the C atoms in both pristine and N-doped graphene films was achieved by deconvolution of the high-resolution XPS spectra, as shown in figure 5.6. The C1s spectrum of pristine graphene films (Fig. 5.6e) exhibited three component peaks centred at ~284.0 eV, ~284.8 eV, and ~287.6 eV, respectively. The main component peak at ~284.0 eV is attributed to the presence of sp^2C-C bonds found in graphite [83, 84]. The peak center at ~284.8 eV can be attributed to the contribution from the defective sp^3C atoms, whereas the component peak at higher binding energies can be assigned to the presence of oxygenated carbon bonds[83, 84]. Upon doping with nitrogen atoms, the C1s spectra (Figs. 4.6a-d) were found to tail and could be fitted to at least four component peaks located at 284.0 - 284.3 eV(**C1**), 284.6 – 285.1 eV (**C2**), 285.8 – 286.1 eV (**C3**), and 287.6 – 288.0 eV (**C4**) [83-86]. The main component peaks (284.0 - 284.3 eV) displayed a broader full width at half maximum (N-5sccm$_{in\text{-}situ}$ =1.127 eV, N-5sccm$_{post}$ =1.275 eV, N-10sccm$_{in\text{-}situ}$ =1.25 eV, and N-10sccm$_{post}$ =1.23 eV) in comparison with that of graphite [87] and our as-grown graphene films (1.04 eV). This can be ascribed to the bonding of carbon atoms to the more electronegative nitrogen atoms [83-86]. The main peak indicated that in N-doped graphene films, most carbon atoms were still arranged in a conjugated honeycomb lattice structure. The two small peaks located at 284.6 – 285.1 eV and 285.8 – 286.1 eV were found to correspond to

sp^2N-C/ sp^3C-C and sp^3N-C bonds, respectively [83-86]. The contribution from these bonds indicates the successful substitutional incorporation of nitrogen atoms as well as incorporation of nitrogen atoms at the edges and defects sites of the graphene domains. Finally, the C1s component peak at higher binding energies (287.6 – 288.0 eV) was ascribed to oxygenated carbon atoms due to the oxygen atoms at the defect sites on the graphene surface [86].

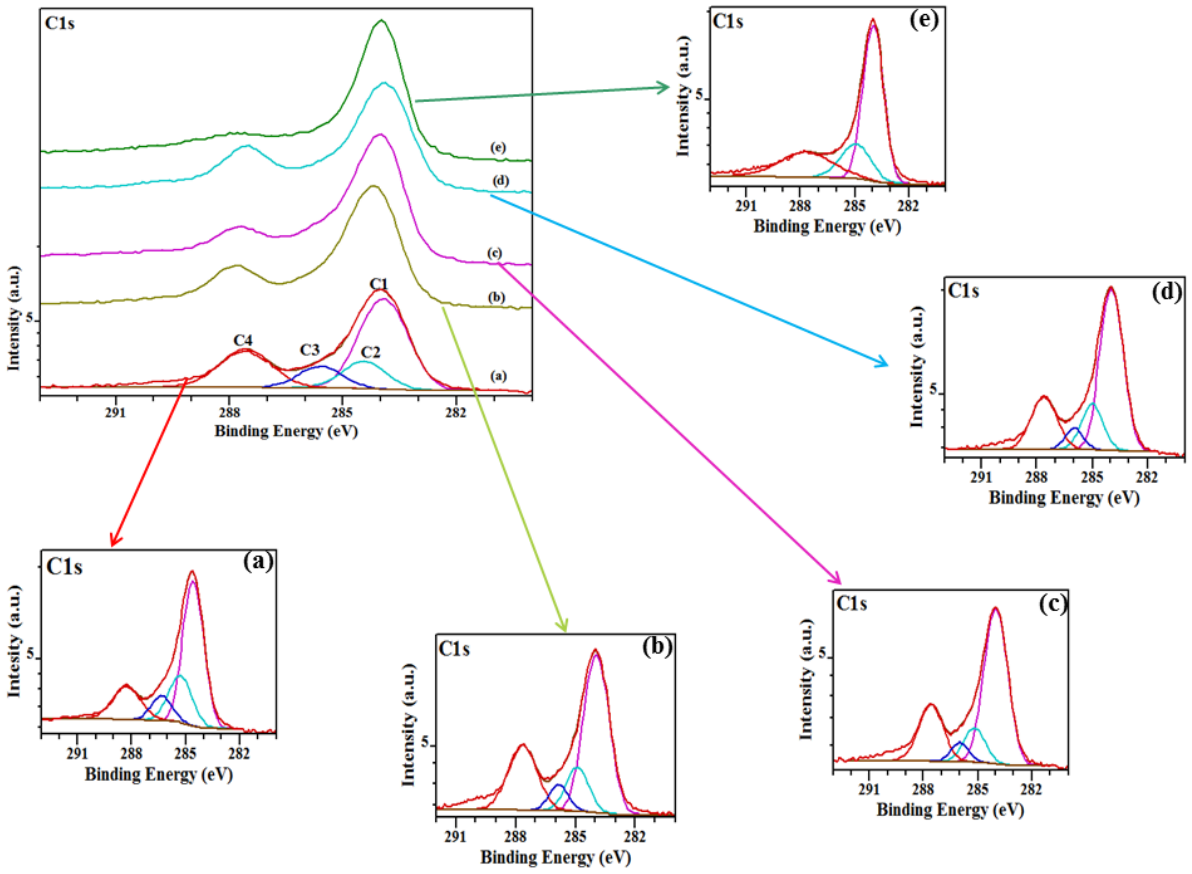

Figure 5.6: C1s core-shell XPS spectra of pristine and N-doped graphene films: (a) N-5sccm$_{in\text{-}situ}$, (b) N-5sccm$_{post}$, (c) N-10sccm$_{in\text{-}situ}$, (d) N-10sccm$_{post}$, and (e) pristine graphene films.

The deconvolution of the high-resolution N1s XPS spectra was used to determine the chemical environments of N atoms in the as-grown films (i.e. the nitrogen configurations). The N1s spectra of N-5sccm$_{in\text{-}situ}$ films (Fig. 5.7a) was deconvoluted into at least four component peaks attributed to pyridinic-N (~397.8 eV), pyrrolic-N (~399.7 eV), substitutional/graphitic-N (~400.6 eV), and the oxidized pyridinic-N (NO_x, ~402.7 eV), respectively [84-87]. Upon post doping with 5 sccm of NH_3 (Fig. 4.7b), the N1s was only fitted

to three peaks assigned to pyridinic-N (~397.9 eV), pyrrolic-N (~399.3 eV), and graphitic-N (~400.6 eV). The relatively high intensities of the peaks corresponding to pyridinic- and pyrrolic-N is indicative of the incorporation of nitrogen atoms at the edges and defect sites of the as-grown graphene films. In-situ nitrogen doping with 10 sccm NH_3 revealed N1s spectra (Fig. 5.7c) which was also deconvoluted into three component peaks assigned to formation of pyridinic-N (~397.8 eV), pyrrolic-N (~398.8 eV), graphitic-N (~400.1 eV). The high relative intensity of the pyrrolic-N bonding state reflects the formation of defects that are associated with reconstruction of the graphene lattice [82]. This can be attributed to the high concentration of nitrogen atoms in the reaction chamber, which compete with carbon atoms on the active sites, resulting in the growth of a deformed graphene lattice. Finally, N1s spectra for the N-10$sccm_{post}$ graphene films (Fig. 5.7d) could be fitted with only two component peaks corresponding to pyridinic-N (~398.1 eV) and pyrrolic-N (~399.7 eV). Due to the high concentration of NH_3, the difficulty of substitutional incorporation of nitrogen into the graphene lattice was observed by the absence of graphitic-N bonding configuration. However, the presence of both pyridinic-N and pyrrolic-N bonding configurations showed the placement of nitrogen atoms at the on-site/vacancy-like defects as indicated by the I_D/I_{D*} ratio (~3.82). Generally, the reasonably high relative intensities of pyridinic- and pyrrolic-N bonding states in all doped graphene is consistent with the theoretical prediction which indicated that N atoms are more thermodynamically stable at the graphene edges [22].

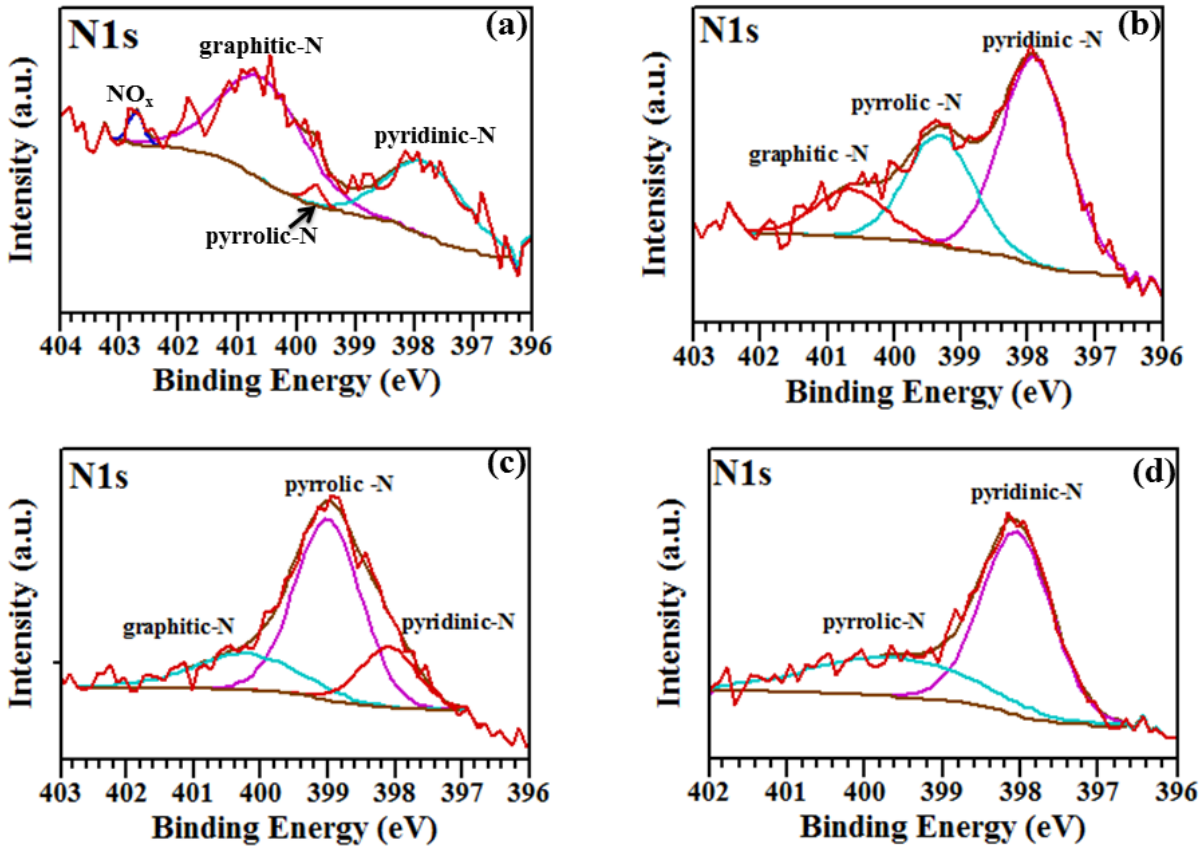

Figure 5.7: N1s core-shell XPS spectra of N-doped graphene films: (a) N-5sccm$_{in\text{-}situ}$, (b) N-5sccm$_{post}$, (c) N-10sccm$_{in\text{-}situ}$, and N-10sccm$_{post}$ graphene films.

5.3.4 Summary of growth of N-doped graphene films

From the above characterizations and analyses, a summary for the proposed growth mechanism of the doped films is shown in scheme 5.2. During in-situ doping with 5 sccm of NH_3 (Scheme 5.2a), it was found that the doped graphene films contained all the known configurations for nitrogen (i.e. pyridinic-, pyrrolic-, graphitic-N and NO_x). The domination of the graphitic-N bonding configuration thus indicates that with low concentrations of N atoms, there is easy incorporation of nitrogen into the graphene lattice. This is because of the simultaneous decomposition of both CH_4 and NH_3 on the Cu active sides, then as the active carbon species nucleate and aggregate into graphene domains, the active nitrogen species also nucleate and become incorporated into the graphene domains. In addition, some of the active nitrogen species become stabilized at the defect sides (vacancies and edges) to form the pyridinic-, pyrrolic-N and NO_x bonding configurations. This gives rise to an increased defect density. Upon post doping with 5 sccm NH_3 (Scheme 5.2b), it can be observed that the only available positions for facilitating the decomposition of NH_3 molecules are the defect sides (vacancies, adatoms and edges); hence the observed high relative concentrations of pyridinic-

and pyrrolic-N configurations. The presence of graphitic-N bonding states can be attributed to the healing effect of the graphene lattice. Theoretical studies have shown that with prolonged growth time at high temperatures [22], the graphene lattice relaxes and this process leads to the conversion of pyridinic-N into the substitutionally incorporated nitrogen atoms. When 10 sccm of NH_3 is used for growing in-situ doped graphene films, the predominant nitrogen bonding states was found to be the pyrrolic-N type. This can be attributed to the presence of high concentration of nitrogen atoms in the reaction chamber; which would then compete with the carbon atoms for nucleation and aggregation on the available active sites. Consequently, this resulted in reconstruction of the lattice and an increased lattice distortion. Although there is reconstruction of the lattice in order to form the pyrrolic-N bonding configuration, it was further found that some nitrogen atoms became stabilized at the edges (pyridinic-N) and others were successfully incorporated into the graphene lattice. Finally, post doping with high flow rates of NH_3 (10 sccm, Scheme 5.2d) showed the difficulty of incorporating nitrogen atoms into lattice, as there was lack of the graphitic-N bonding states. The results indicate that prolonged growth time has little effect on the conversion of pyridinic-N atoms into substitutionally incorporated nitrogen atoms due to the high concentration of the nitrogen precursor. The presence of only pyridinic- and pyrrolic-N bonding configurations suggests that the defects sites formed during the growth step of pristine graphene films act as active sites for the adsorption and decomposition of NH_3 molecules.

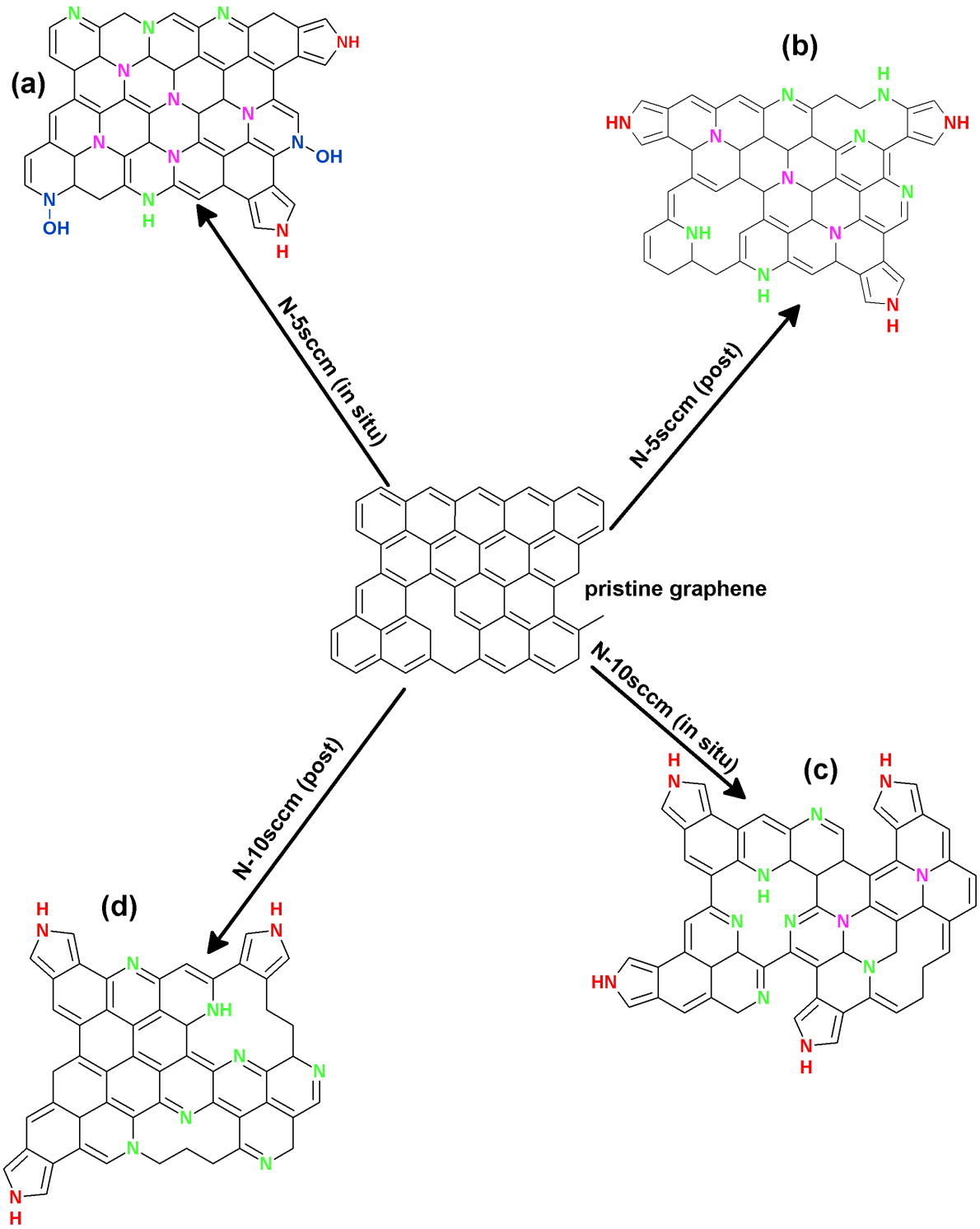

Scheme 5.2: Pictorial representation for the N-doped graphene films (N-configurations: pyridinic-N, pyrrolic-N, graphitic-N, oxidized pyridinic-N).

5.4. Conclusions

Optimization for doping graphene films with nitrogen atoms was successfully achieved by following in-situ and post doping routes. Using ammonia gas at different flow rates (5 sccm and 10 sccm) during both in-situ and post doping, allowed for the nitrogen atoms to be incorporated into the graphene lattice with varying configurations as well as at different concentrations. Characterization techniques such as optical microscopy, Raman and X-ray photoelectron spectroscopies were used to investigate the structural and electronic properties of the as-grown pristine and N-doped graphene films. For instance, the maximum N/C content of 3.25 at% was noted for doped graphene films grown from an in-situ synthesis route using 5 sccm NH_3. Raman analysis corroborated the XPS data analysis for these N-5sccmin-situ films by showing the highest defect density (I_D/I_G) ratio of ~1.09; which indicated an increased lattice distortion due to incorporation of more nitrogen atoms. Moreover, the lowest N/C content of 0.61 at% was noted for the N-10sccm post doped graphene films. Thus, it can be concluded that N/C content depends mainly on the flow rate of NH_3 ($N/C_{5sccm} > N/C_{10sccm}$), and to a lesser extent on the synthesis method ($N/C_{in\text{-}situ} > N/C_{post}$). Interestingly, the type and amount of the detected N-configurations (pyridinic, pyrrolic, graphitic and NO_x) were also found to be influenced by the flow rate of NH_3 as well as the synthesis method. To be more specific, the N-5$sccm_{in\text{-}situ}$ graphene films were characterized predominantly by graphitic-N and pyridinic-N bonding configurations, as well as small amounts of pyrrolic-N and NO_x bonding configurations. In contrast, N-10$sccm_{in\text{-}situ}$ graphene films contained large amounts of pyrrolic-N bonding states and fewer graphitic- and pyridinic-N configurations. Remarkably, in both N-5$sccm_{post}$ and N-10$sccm_{post}$ graphene films the pyridinic- and pyrrolic-N bonding configurations dominated, indicating the thermodynamic stability of nitrogen atoms at the edges of graphene domains. Therefore, since a maximum N/C content was obtained using the in-situ doping route, with low flow rates of NH_3 (5 sccm), the this process was chosen as the optimum growth condition for synthesizing future N-doped graphene.

References

1. Novoselov, K. S., A. K Geim, S. V. Morozov, D. Jang, Y. Zhang, D. Jang, Y. Zhang, S. V. Dubonos, I. V. Grigorieva, A. A. Firsov. *Science*, **2004**, *306*, 666-669.
2. Geim, A. K., K. S. Novoselov. *Nat. Mater*, **2007**, *6*, 183-191.
3. Geim, A. K. *Science*, **2009**, *324*, 1530-1534.

4. Castro Neto, A. H., F. Guinea, N.M.R. Peres, K.S. Novoselov, A.K. Geim. *Rev. Mod. Phys.*, **2009**, *81***,** 109-162.
5. Balandin, A. A., S. Ghosh, W. Bao, I. Calizo, D. Tewelderbrhan, F. Miao, C. N. Lau. *Nano Lett*., **2008**, *8*, 902-907.
6. Nika, D. L., A.A. Balandin. *J. Phys. Condens. Matter*., **2012**, *24*, 23320-23323.
7. Chen, S. D., Y. Zhang, J. Wang. *Sci China-Phys Mech Astron*., **2013**, *56*, 1466-1471.
8. Novoselov, K. S., Z. Jiang, Y. Zhang. *Science*, **2007,** *315*, 1379-1381.
9. Cao, H. L., Q. Yu, L.A. Jauregui, J. Tian, W. Wu, Z. Liu, R. Jalilian, D. K. Benjamin, Z. Jiang, J. Bao, S. S. Pei, Y. P. Chen. *Appl. Phys. Lett*. **2010**, *96*, 122106.
10. Zhu, Y., S. Murali, W. Cai, X. Li, J.W. Suk, J. R. Potts, R. S. Ruoff. *Adv. Mater*. **2010**, **22**, 3906–3924.
11. Kamat, P. V. *J. Phys. Chem. Lett.* **2011**, *2*, 242-251.
12. Pumera, M. *Energy Environ. Sci*.., **2011**, *4*, 668-674.
13. Pumera, M.. *Mater. Today*, **2011**, *14*, 308−315.
14. Shao, Y., J. Wang, H., H. Wu, J. Liu, I. A. Aksay, Y. Lin. *Electroanalysis*, **2010**, 22, 1027-1036.
15. Dodoo-Arhin D., M. Fabiane, A. Bello, N. Manyala. *Ind. Eng. Chem. Res*. **2013**, *52*, 14160-14168.
16. Wang, X., L. Zhi, K. Müllen. *Nano Lett.* **2008**, *8*, 323–327.
17. Kim, K. S., Y. Zhao, H. Jang, S. Y. Lee, J. M. Kim, K. S. Kim, J. H. Ahn, P. Kim, J. Y. Choi, B. H. Hong. *Nature*, **2009**, *457*, 706−710.
18. Stoller, M. D., S. Park, Y. Zhu Y, J. An, R. S. Ruoff. *Nano Lett*. **2008**, *8*, 3498–3502.
19. Huang, X., Z. Yin, S. Wu, X. Qi, Q. He, Q. Zhang, Q. Yan, F. Boey, H. Zhang. *Small*, **2011**, *7*, 1876-1902.
20. Schedin, F., A. K. Geim, S. V. Morozov, E. W. Hill, P. Blake, M. I. Katsnelson. *Nat Mater*., **2007**, *6*, 652-655.
21. Castro, E. V., K. S. Novoselov, S. V. Morozov, N. M. R. Peres, J. M. B. L. dos Santos, J. Nilsson, F. Guinea, A. K. Geim, A. H. C. Neto. *Phys. Rev. Lett.* **2007**, *99*, 216802.
22. Usachov, D., O. Vilkov, A. Gruneis, D. Haberer, A. Fedorov, V. K. Adamchuk, A. B. Prebrajenski, P. Dudin, A. Barinov, M. Oehzelt, C. Laubschat, D. V. Vyalikh. *Nano Lett.*, **2011**, *11*, 5401-5407.
23. Giovannetti, G., P. A. Khomyakov, G. Brocks, V. M. Karpan, J. van den Brink, P. J. Kelly, *Phys Rev Lett*., **2008**, *101*, 026803-1-4.

24. Dong, X. C., D.L. Fu, W.J. Fang, Y.M. Shi, P. Chen, L.J. Li. *Small*, **2009**, *5*, 1422-1426.

25. Berashevich, J., T. Chakraborty. *Phys Rev B.*, **2009,** *80*, 033404.
26. Bermudez, V. M.; Robinson, J. T. *Langmuir*, **2011**, *27*, 11026− 11036.
27. Kim, S.-S., J. Y. Choi, K. Kim, B. H. Sohn. *Nanotechnology*, **2012**, *23*, 125301.
28. Ritter, K. A., J.W. Lyding. *Nature Materials*, **2009,** *8*, 235–242.
29. Cheng, R., J. Bai, L. Liao, H. Zhou, Y. Chen, L. Liu, Y. C. Lin, S. Jiang, Y. Huang, X. Duan. *Proc. Nat. Acad. Sci.*, **2012,** *109*, 11588-11592.
30. Giovannetti, G., P. A. Khomyakov, G. Brocks, P. J. Kelly, J. van de Brink. *Phys. Rev B.*, **2007,** *76*, 073103.
31. Wang, F., Y. Zhang, C. Tian, C. Girit, A. Zettl, M. Crommie, Y. R. Shen. *Science*, **2008,** *320*, 206-209.
32. Papagno, M., S. Rusponi, P. M. Sheverdyaeva, S. Vlaic, M. Etzkorn, D. Pacile, P. Moras, C. Carbone, H. Brune. *ACS Nano*, **2012**, *6*, 199−204.
33. Liu, H., Y. Liu, D. Zhu. *J. Mater. Chem*. **2011**, *21*, 3335−3345.
34. Lv, R., M. Terrones. *Mater. Lett*. **2012**, *78*, 209−218.
35. Matsoso, B. J., K. Ranganathan, B. K. Mutuma, T. Lerotholi, G. Jones, N. J. Coville. *RSC Adv.*, **2016**, *6*, 106916-106920.
36. Chang, C. K., S. Kataria, C. C. Kuo, A. Ganguly, B. Y. Wang, J. Y. Hwang, W. H. Yang, S. B. Wang, C. H. Chuang, M. Chen. *ACS Nano*, **2013**, *7*, 1331-1341.
37. Shinde, P. P., V. Kumar. *Phys. Rev. B.* **2011**, *84*, 125401.
38. Yang, Z., Z. Yao, G. Li, G. Fang, H. Nie, Z. Liu, X. Zhou, X. Chen, S. Huang. *ACS Nano*, **2012**, *6*, 205−211.
39. Some, S., J. Kim, K. Lee, A. Kulkarni, Y. Yoon, S. Lee, T. Kim, H. Lee. *Adv. Mater.* **2012**, *24*, 5481−5486.
40. Haberer, D., D. V. Vyalikh, S. Taioli, B. Dora, M. Farjam, J. Fink, D. Marchenko, T. Pichler, K. Ziegler, S. Simonucci, M. S. Dresselhaus, M. Knupfer, B. Buchner, A. Gruneis. *Nano Lett*. **2010**, *10*, 3360–3366.
41. Lai, L., J. R. Potts, D. Zhan, L. Wang, C. K. Poh, C. Tang, H. Gong, Z. Shen, J. Lin, R. S. Ruoff. *Energy Environ. Sci.* **2012**, *5*, 7936−7942.
42. Wang, H., M. Xie, L. Thai, A. Fisher, X. Wang. *J. Phys. Chem. Lett.*, **2014**, *5*, 119-125.

43. Hou, S., X. Cai, H. Wu, X. Yu, M. Peng, K. Yan, D. Zou. *Energy Environ. Sci*., **2013**, *6*, 3356−3362.
44. Lu, Y. F., S. T. Lo, J. C. Lin, W. Zhang, J. Y. Lu, F. H. Liu, C. M. Tseng, Y. H. Lee, C. T. Liang, L. J. Li. *ACS Nano*, **2013**, *13*, 6522−6532.
45. Sahoo, N. G., Y. Pan, L. Li, S. H. Chan. *Adv. Mater*. **2012**, *24*, 4203−4210.
46. Wei, D., Y. Liu, Y. Wang, H. Zhang, L. Huang, G. Yu. *Nano Lett*. **2009**, *9*, 1752−1758.
47. Zhang, C., L. Fu, N. Liu, M. Liu, Y. Wang, Z. Liu. *Adv. Mater*. **2011**, *23*, 1020−1024.
48. Wang, Z., P. Li, Y. Chen, J. Liu, H. Tian, J. Zhou, W. Zhang, Y. Li. J. *Mater, Chem*. C, **2014**, *2*, 7396-7401.
49. Zhang, C., W. Lin, Z. Zhao, P. Zhuang, L. J. Zhan, Y. H. Zhou, W. Cai. S*ci China-Phys. Mech Astron*., **2015**, *58*, 107801(1-6).
50. Capasso, A., T. Dikonimos, F. Sarto, A. Tamburrano, G. de Bellis, M. S. Sarto, G. Faggio, A. Malara, G. Messina, N. Lisi. *Beilstein J. Nanotechnol*, **2015**, *6*, 2028-2038.
51. Gao, H., L. Song, W. Guo, L. Huang, D. Yang, F. Wang, Y. Zuo, X. Fan, Z. Liu, W. Gao, R. Vajtai, K. Hackenberg, P. M. Ajayan. *Carbon*, **2012**, *50*, 4476-4482.
52. Wang, X., X. Li, L. Zhang, Y. Yoon, P. K. Weber, H. Wang, J. Guo, H. Dai. *Science*, **2009**, *324*, 768-771.
53. Li, X., H. Wang, J. T. Robinson, H. Sanchez, G. Diankov, H. Dai. *J. Am. Chem. Soc*. **2009**, *131*, 15939−15944.
54. Wang, Y., Y. Shao, D. W. Matson, J. Li, Y. Lin. *ACS Nano*, **2010**, *4*, 1790-1798.
55. Guo, B., Q. Liu, E. Chen, H. Zhu, L. Fang, J. R. Gong. *Nano Lett.*, **2010**, *10*, 4975-4980.
56. Panchakarla, L. S., K. S. Subrahmanyam, S. K. Saha, A. Govindaraj, H. R. Krishnamurthy, U. V. Waghmare, C. N. R. Rao. *Adv Mater*, **2009**, *21*, 4726–4730.
57. Long, D., W. Li, L. Ling, J. Miyawaki, I. Mochida, S. H. Yoon. *Langmuir*, **2010**, *26*, 16096−16102.
58. Zhang, Y., K. Fugane, T. Mori, L. Niu, J. Ye. *J. Mater. Chem*., **2012,** *22*, 6575−6580.
59. Qu, L., Y. Liu, J.B. Baek, L. Dai, *ACS Nano,* **2010,** *4*, 1321-1326.
60. Luo, Z., S. Lim, Z. Tian, J. Shang, L. Lai, B. MacDonald., *J. Mater. Chem.*, **2011**, *21*, 8038-8044.
61. Luo, Z., S. Lim, Z. Tian, J. Shang, L. Lai, B. MacDonald, C. Fu, Z. Shen, T. Yu, J. Lin. *J. Mater. Chem.*, **2011**, *21*, 8038−8044

62. Meng, F., J. Li, S. K. Cushing, M. Zhi, N. Wu. *J. Am. Chem. Soc.* **2013**, *135*, 10286−10289.
63. Lu, Y. F., S. T. Lo, J. C. Lin, W. Zhang, J. Y. Lu, F. H. Liu, C. M. Tseng, Y. H. Lee, C. T. Liang, L. J. Li. *ACS Nano*. **2013**, *8*, 6522-6532.
64. Jalili, S., R. Vaziri. *Mol. Phys.* **2011**, *109*, 687–694.
65. Lherbier, A., X. Blase, Y. M. Niquet, F. Triozon, S. Roche. *Phys. Rev. Lett*. **2008,** *101*, 036808.
66. Pels, J. R., F. Kapteijn, J. A. Moulijn, Q. Zhu, K. M. Thomas. *Carbon*, **1995**, *33*, 1641−1653.
67. Jung, H. S., H. Z. Tsai, D. Wong, C. Germany, S. Kahn, Y. Kim, A. S. Aikawa, A. K. Desai, G. F. Rodgers, A. J. Bradley, J. Velasco, K. Watanabe, T. Taniguchi, F. Wang, A. Zettl, M. F. Crommie. *J. Vis. Exp.* **2015**, *101*, e52711 (1-9).
68. Wang, Y., Y. Zheng, X. Xu, E. Dubuisson, Q. Bao, J. Lu, K. P. Loh. *ACS Nano*. **2011**, 5, 9927-9933.
69. Malard, L. M., M. A. Pimenta, G. Dresselhaus, M. S. Dresselhaus. *Phys. Rep.* **2009**, *473*, 51-87.
70. Ferrari, A. C. *Solid State Commun.*, **2007**, *143*, 47-57.
71. Ferrari, A. C., J. C. Meyer, V. Scardaci, C. Casiraghi, M. Lazzeri, F. Mauri, S. Piscanec, D. Jiang, K. S. Novoselov, S. Roth, A. K. Geim. *Phys. Rev. Lett*. **2006,** *97***,** 187401 (1-4).
72. Casiraghi, C., S. Pisana, K. S. Novoselov, A. K. Geim, A. C. Ferrari. *Appl. Phys. Lett*. **2007,** *91***,** 233108 (1-3).
73. Ferrari, A. C. *Solid State Commun.* **2007,** *143*, 47-57.
74. Ferrari, A. C., D. M. Basko. *Nat. Nanotechnol.* **2013**, *8*, 235-246.
75. Piscanec, S., M. Lazzeri, F. Mauri, A. C. Ferrari, J. Robertson. *Phys. Rev. Lett.* **2004**, *93*, 185503-185506.
76. Ferrari, A. C., J. Robertson. *Phys. Rev. B.* **2011**, *61*, 14095-14107.
77. Cancado, L. G., A. Jorio, E. H. Martins- Ferreira, F. Stavale, C. A. Achete, R. B. Capaz, M. V. Moutinho, A. Lombardo, T. S. Kulmala, A. C. Ferrari. *Nano Lett.* **2011**, *11*, 3190-3196.
78. Eckmann, A, A. Felten, A. Mishchenko, L. Britnell, R. Krupke, K. S. Novoselov, C. Casiraghi. *Nano. Lett.* **2012**, *12*, 3925-3930.
79. Das, S., B. Pisana, S. Chakraborty, S. K. Piscanec, U. V. Saha. Waghmare. *Nat Nanotechnol*., **2008**, *3*, 210-215.

80. Zafar, Z., Z. H. Ni, X. Wu, Z. X. Shi, H. Y. Nan, J. Ba. *Carbon*, **2013,** *61*, 57-62.
81. Allen, F. H., O. Kennard, D. G. Watson, L. Brammer, A. G. Orpen, R. Taylor, *J Chem Soc*, *Perkin Trans 2*, **1987**, *12*, S1-S19.
82. Dettori, R., E. Cadelano, L. Colombo, *J Phys: Condens Matter.*, **2012**, *24*, 104020-1-10.
83. Jansen, R. J. J., H. Vanbekkum, *Carbon*, **1995**, *33*, 1021-1027.
84. Nakayama, Y., F. Soeda, A. Ishitani, *Carbon*, **1990**, *28*, 21-26.
85. Lv, R. T., Q. Li, A.R. Botello-Me´ndez, T. Hayashi, B. Wang, A. Berkdemir. *Sci Rep*., **2012**, *2***,** 586-1-8.
86. Venezuela, P., M. Lazzeri, F. Mauri, *Phys Rev B.*, **2011**, *84*, 035433-1-25.
87. Xie, W., N. M. Kai, L. T. Weng, C. M. Chan. *RSC. Adv*, **2016**, *6*, 80649-80654.

Chapter 6

Electrochemical behaviour and detection of dopamine and uric acid over pristine and N-doped graphene modified ITO electrodes

6.1 Introduction

Over the decades, the ever growing demand for ultrasensitive detection of biomolecules in biological matrixes, such as blood, urine as well as extracellular fluids, has led to the development of many techniques that can enhance the response of electrochemical sensors. The development of electrochemical sensors have been widely studied as inexpensive techniques for selective and sensitive detection of a large number of electroactive biomolecules, including nicotinamide-adenine dinucleotide (NADH) [1], serotonin [2], glucose [3], dopamine [4-6], ascorbic acid [6-9], uric acid [6, 8-11], and so on. Among them, dopamine (DA) or 4-(2-aminoethyl) benzene-1,2-diol, a neurotransmitter, has received considerable attention in clinical and/or pharmaceutical research fields due to its indispensable role in the renal, cardio vascular, hormonal and central nervous systems of humans. It has been found that abnormally high or low levels of DA in the human body is associated with the development of serious neurodegenerative diseases such as schizophrenia, epilepsy, phenylketonuria, Alzheimer's disease, Parkinson's syndrome, Huntington's disease, and attention deficiency hyperactivity disorder (ADHD) [12-18]. Thus, the rapid, selective and sensitive detection of DA levels in physiological and biological samples is of great significance for early diagnosis of various neurological disorders as well as providing the development of pharmaceutical drugs for therapeutic purposes. Recent approaches for the direct detection and quantitative determination of DA include, but are not limited to UV-vis spectroscopy [19], fluorometry [20, 21], capillary electrophoresis [22, 23], chemiluminescence [24, 25], high performance liquid chromatography [26, 27], microdialysis [20, 28], and electrochemical techniques [29-33]. Among the various methods, the electrochemical techniques have been reported to be the most promising approach for determination of DA due to the electroactive nature of DA [29-35]. Additionally, electrochemical methods offer several advantages over other methods, such as low cost, environmental friendliness, quick responses, high sensitivity, easy operation, capability to be used in turbid and coloured fluids, availability for both in vitro and/or in vivo DA detection, and most importantly, the feasibility for miniaturization for use in hand-held analysers [29-35].

However, there are major problems associated with the electrochemical determination of DA in physiological and biological samples, as selective and sensitive detection of DA suffers interference from other biomolecules such as uric acid.

Uric acid (2,6,8-trihydroxypurine, UA) is the principal end-product of purine metabolism in humans, and it is mainly excreted by the kidneys and to a lesser extent by the liver. Thus, determination off the concentration of UA in the human blood or urine has great clinical importance since it is a powerful indicator for the diagnosis of several diseases such as gout, hyperuricemia, Lesch-Nyhan syndrome, urolithiasis, kidney damage, leukaemia, and lymphoma [35-38]. Until now, various methods such as adsorption or medium exchange, enzyme-based, as well as electrochemical techniques have been used for determination of UA in biological samples [35-40]. As UA shows electrochemical activity, the electrochemical methods have been widely used for determination of UA. This has involved their use in chemically modified electrodes as well as electrochemically pre-treated electrodes [38-40]. Although electrochemical oxidation procedures for the determination of UA have shown good selectivity and sensitivity, the interference from other neurochemical compounds like DA, results in an overlap of their voltammetric responses due to their very close oxidation potentials [35-40]. Apart from the interference issues, electrochemical detection of UA suffers other drawbacks such as the requirement of large overpotentials, frequent replacement of the electrode due to fouling, as well as pre-concentration of UA prior to measurements [38-40]. Since both sensitivity and selectivity for electrochemical detection of DA and UA, either individually or simultaneously, are of equal importance for practical applications, research approaches have been devoted to improving the electrode surface, with the key focus being on suitable materials for modifying this surface.

As such, recent progress in nanotechnology has led to the production of biologically compatible materials, such carbon-based nanomaterials [41], metal and metal oxide nanoparticles [42], quantum dots [43], magnetic nanoparticles [44], and polymeric nanoparticles [45], which can be used to modify the electrode surface of electrochemical sensors. Among the newly developed biocompatible materials, carbon-based nanomaterials have gained more attention in comparison with other nanomaterials, since these materials have shown improved electrochemical performance with amplified detection signals as well as good selectivity [46]. Additionally, their good biocompatibility with amino acids and proteins, chemical stability and excellent catalytic activity are some of the properties that make carbon-based

nanomaterials good candidates for electrode surface modifiers. Although various carbon-based nanomaterials have been applied in electrochemical sensors, graphene, a two-dimensional carbon material with an atomically thick honeycomb lattice [47], has attracted enormous interest from various scientific communities, as a promising candidate nanoelectronics, catalysis, nanophotonics, and sensors [48-50]. Owing to its unique structural and physiochemical properties, including large specific surface area, outstanding thermal conductivity, and extremely high electric conductivity [48-50], graphene has been intensively employed for modification of different electrode surfaces in electrochemical sensors [45, 51, 52]. This is because the modification of the electrode surface with graphene has been shown to accelerate the electron transfer rate by providing a highly conductive interface with improved electrocatalytic activity [51, 52].

In spite of the extraordinary properties exhibited by graphene, the main drawback for practical applications of graphene is the difficulty in growing high quality monolayer graphene, since monolayer graphene is known to exhibit a high surface area and high electrocatalytic activity. As such, researchers have spent much effort in developing methods to improve the surface area as well as to enhance the electrocatalytic activity of graphene coated electrodes. For instance, Shuang *et al*. reported that the fabrication of porous graphene provided channels that accelerated the diffusion of the electrolyte and promoted the mass transfer process [53]. They observed that the presence of these channels remarkably enhanced the electrocatalytic performance of graphene. However, the use of corrosive chemicals during the synthesis steps of the porous graphene led to loss of the surface area as well as a lowered degree of reduction of this porous carbon nanomaterial. On the other hand, some researchers showed that the issues associated with a lowered surface area could be solved by using reduced graphene oxide. However, the aggregation of the graphene nanosheets during electrode preparation led to loss of electrocatalytic activity towards the oxidation of biomolecules [8, 10]. Furthermore, other studies have indicated that the use of graphene composites, including composites such as graphene/metal oxide nanocomposites [32, 45, 53] and graphene-carbon nanotube hybrid composites [46], can greatly enhance the electrochemical detection of biomolecules, such as DA and/or UA. Although good electrocatalytic performances with very small detection limits for DA and/or UA have been reported for the graphene composite-based electrochemical sensors; the tedious preparation techniques, use of expensive precious metal nanoparticles, and leaching of the nanoparticles out of the composites limits their applications.

To circumvent these problems, incorporation or doping of non-metallic elements such as nitrogen, boron, or both nitrogen and boron, have been found to provide an excellent method for enhancing the electrocatalytic performance of graphene [6, 39] regardless of whether the parent graphene material is used as monolayered films, graphene oxide or reduced graphene oxide nanosheets. Doping with nitrogen atoms is the commonly used method for tailoring the structural and electronic properties of graphene. Since the nitrogen atom has a comparable size to the carbon atom and it contains an extra electron, its extra valence electron is available to form a strong delocalised conjugated system with the sp^2 hybridized carbon lattice. This leads to improved reactivity, strengthened electrical conductivity and greatly enhanced electrocatalytic performance for graphene [51, 52]. Furthermore, the presence of nitrogen atoms in the graphene lattice enhances the biocompatibility and sensitivity in biosensing applications, by providing abundant binding sites for biomolecules such as DA, UA, ascorbic acid, glucose, etc. [51, 52] It has been reported that nitrogen atoms increase the biocompatibility of graphene through hydrogen bonding between the N-doped graphene lattice and the biomolecules; this results in accelerated charge transfer kinetics of the biomolecule on the surface of N-doped graphene [51, 52] As a result, it is apparent that N-doped graphene has great potential for application in electrochemical sensors.

Electrochemical sensors provide an inexpensive technique for the selective and sensitive detection of electroactive biomolecules. However, a drawback that researchers are facing is to design or fabricate an electrochemical sensor with excellent performance based on the working electrode that is both sensitive and selective to DA and UA. Generally, a variety of working electrodes[51, 52], including a glassy carbon electrode (GCE), carbon paste electrode, pyrolytic graphite electrode and gold electrode, have been used for individual or simultaneous detection of DA and UA. The GCE is the commonly used electrode at the laboratory scale due to the ease of modifying it with sensing materials. Additionally, the GCE provides advantages of good conductivity, good chemical stability, high intensity and rigidity [51, 52]. Although the GCE can be easily fabricated into an electrochemical sensor, it is not easy to scale up industrially. To solve this problem, recent research reports have shown that indium-doped tin oxide-coated glass (ITO or $InSnO_x$) is a promising candidate for replacing the GCE as a working electrode in electrochemical sensors [54, 55]. ITO-coated glass is a low-cost photoelectric material with excellent optical transparency and satisfactory electrical conductivity; thus making it a good material to be employed as a working electrode. Owing to its remarkable physical and chemical properties and the ease of mass production for

practical purposes, ITO has found application in various fields, such as light-emitting diodes (LEDs), solar cells, transistors, biosensors, electroluminescence devices, and liquid crystal displays (LCDs). Additionally, ITO can be etched, patterned and micro-arrayed in order to attain a desired surface functionalization for the required immobilization of biomolecules [57]. Thus, in comparison with the GCE and other working electrodes, the use of ITO in electrochemical sensing can provide a new platform for development of sensors exhibiting significantly enhanced performance due to its many desirable properties such as high surface-to-volume ratio and improved electronic conductivity. To the best of our knowledge, research reports on the use and development of modified ITO electrodes for electrochemical detection of DA and/or UA are limited [54-56].

In this research, pristine and N-doped graphene films were used to modify ITO electrodes, and the as-fabricated Gr/ITO and NGr/ITO electrodes were applied as sensitive electrochemical sensors for the detection of UA and DA. The aim of the work was to study the electrocatalytic activity of ITO electrodes towards oxidation of DA and UA, after the electrodes have been modified with pristine and N-doped graphene films. Both electrode modifiers are expected to exhibit different electrochemical responses due to their different structural and electronic properties. In this study, we investigated how each electrode modifier interacted with the biomolecules; to elucidate the influence of different structural and electronic properties on the electrochemical responses. Additionally, pristine graphene films were grown by APCVD, a technique that permits the easy control of graphene thickness. As a result, the study aims to address the application of graphene films with known thickness in electrochemical sensors.

6.2 Experimental

6.2.1 Chemicals and reagents

Dopamine hydrochloride (DA, ≥ 99%), uric acid (UA, ≥ 99%), sodium hydroxide pellets (98%, Merk), potassium dihydrogen phosphate (KH_2PO_4, 99.99%), hydrochloric acid (HCl, 32.0 w/v %), potassium ferricyanide ($K_3[Fe(CN)_6]$, Merck, 99.98%), potassium chloride (KCl, Merck, 98.5%) and poly(methyl methacrylate) (PMMA, Mw ~999 000) were purchased from Sigma-Aldrich, South Africa. The indium tin oxide (ITO)-coated glass slides (surface resistance 30 to 60 Ω/sq., thickness 1.1 mm, and optical transmittance of > 84%, refractive index of 1.517) and copper foils (25 µm, 99.98%) were also received from Sigma-

Aldrich, South Africa. The gases used included argon (Ar, 99%), methane (CH_4, 99.98%), ammonia (NH_3, 10% in Ar), nitrogen (N_2, 99.98%) and hydrogen (H_2, 99.98 %), and these were supplied by Afrox, South Africa. All other reagents were of analytical grade and were used without further purification. For the voltametric experiments, the deionized and high quality water (>18.2 MΩ.cm^2) used was purified through a Millipore ultrapure (type 1) water system (Bedford, MA, USA). Potassium ferricyanide stock solution (4 mM) was prepared with 1.0 M KCl. Stock solutions of DA (4 mM) and UA (4 mM) were prepared in 0.1 M phosphate buffer solution ((PBS) at pH 6.02, and PBS was used as supporting electrolyte. The PBS was prepared by dissolving KH_2PO_4 in deionized water and the pH was adjusted by addition of 0.1 M NaOH or 0.1 M HCl solutions. Fresh solutions of DA and UA were prepared daily. Other standard solutions of DA and UA were prepared by appropriate dilutions of the stock solutions in PBS.

6.2.2 Instrumentation

Electrochemical measurements (i.e. cyclic voltammetry (CV), differential pulse voltammetry (DPV), and amperometry) were performed using a μAutolab potentiostat/galvanostat, running with the GPES software (version 4.900B) from Eco Chemie (Utrecht, Netherlands). The conventional three-electrode cell assembly employing a Ag/AgCl (3 M KCl) reference electrode and a platinum wire auxilliary electrode was used for the electrochemical measurements (Scheme 6.1). The working electrode (geometric area = 0.42 cm^2) was either an unmodified ITO-coated glass or the ITO-coated glass modified with pristine and/N-doped graphene films. All potentials are reported against the Ag/AgCl reference electrode. The pH measurements of the PBS were performed on a Eutech Instruments bench pH/ion/mV-meter (Model pH/ion 510, Singapore). Prior to the electrochemical measurement, the electrode modifying materials were characterised using a Bruker Raman Senterra spectrophotometer (Bruker, South Arica) and XPS date were collected on a Thermo Escalab 250 X-ray photoelectron spectrometer (XPS).

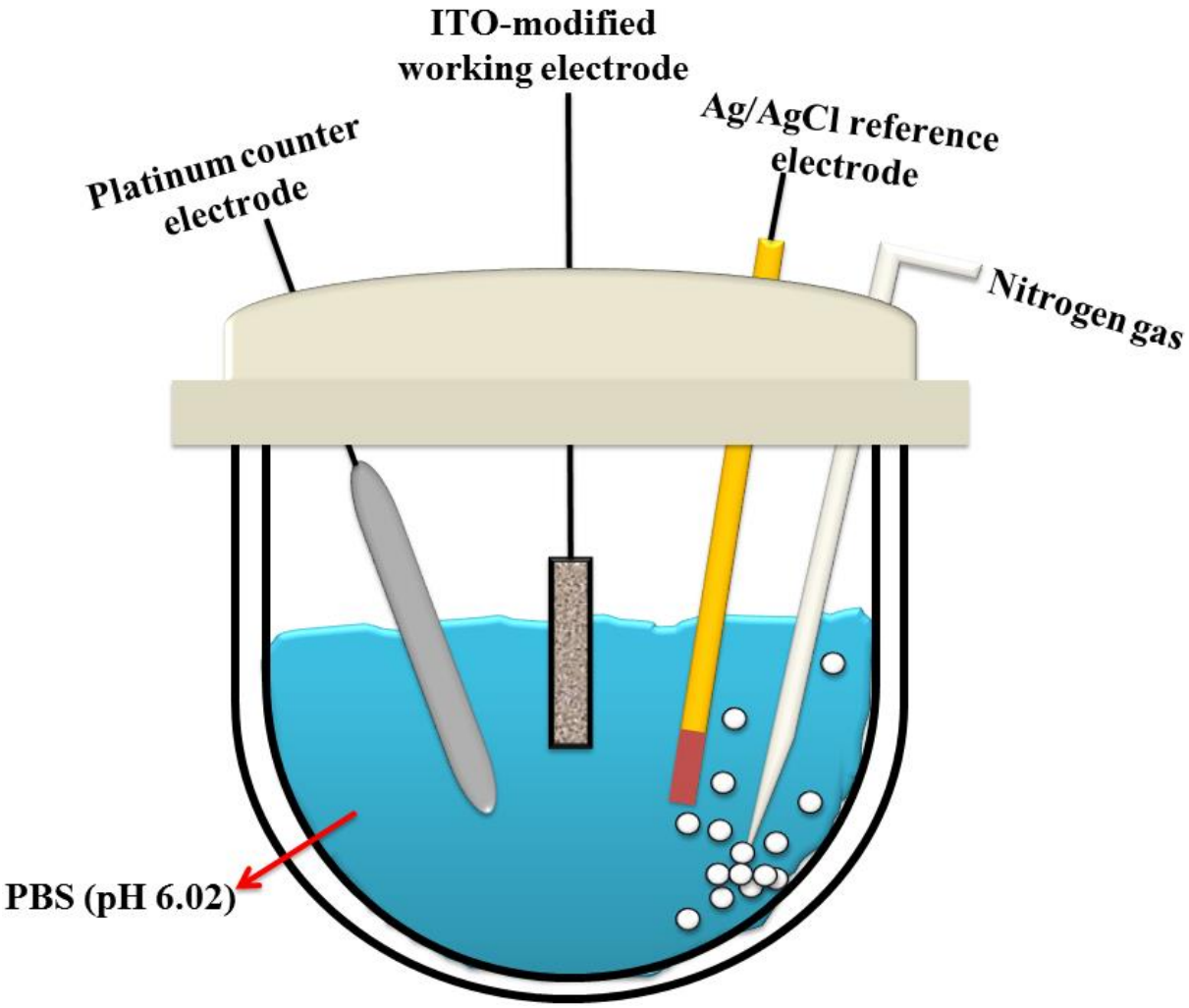

Scheme 6.1: The schematic representation of the three-electrode electrochemical cell.

6.2.3 Preparation of electrodes and the electrochemical procedure

Nitrogen doped and pristine graphene films were synthesized by atmospheric pressure CVD (APCVD) on a copper foil in a quartz tube furnace. The pristine graphene films were grown with 10 sccm CH_4 in 3 sccm H_2 and 300 sccm Ar atmospheres. On the other hand, the N-doped films were grown with 10 sccm CH_4 and 5 sccm NH_3 under 3 sccm H_2 and 300 sccm Ar atmospheres. All samples were grown for 10 min at a designated growth temperature of 1000 ^{o}C. For preparation of the modified electrodes, the as-grown graphene films were then transferred onto the ITO-coated glass using the PMMA assisted electrochemical delamination method (Scheme 3.2)[58]. Prior to modification, the ITO-coated glass was cut to 0.6 cm × 0.9 cm and was sonicated in a solution mixture of acetone, ethanol and distilled water, after which the floating PMMA/graphene films were transferred onto the electrode. PMMA was then dissolved with acetone and the modified electrode was lightly rinsed with multiple

volumes of methanol and water. These electrodes were labelled as Gr-ITO and NGr-ITO for the ITO electrodes modified with pristine and N-doped graphene films, respectively.

In a typical experimental measurement, 20.0 mL of 0.1 M PBS (pH 6.02) as supporting electrolyte in a three-electrode cell was deoxygenated by purging with nitrogen gas for 30 min prior to the start of each experiment. The cyclic voltammograms were recorded by scanning between -1.0 V and 1.0 V at the step potential of ~0.005 V. The operating parameters for obtaining the quantitative analysis of the analytes (DA and UA) by differential pulse voltammetry (DPV) were set as follows: modulation amplitude of 25.05 mV, initial potential of -0.25 V, end potential of 1.0 V, step increment potential of 1.95 mV, and sensitivity of 100 nA/V. Electrochemical behaviour and voltammetric detection of DA and UA, either as individual or in mixed solutions, were obtained by addition of a defined volume of the respective stock solution to the electrochemical cell. The voltammograms were then recorded. The detection limit (DL) was determined from, $DL = \frac{3\sigma}{s}$, where σ is the standard deviation of three low concentration measurements, and *s* is the slope of the linear relationship plot of Ipa vs. concentration (C) [55]. Furthermore, the sensitivities of the modified electrodes were calculated by dividing the slope of the calibration curve by the geometrical area of the electrode (0.42 cm^2) [54].

6.3 Results and discussions

6.3.1 Structural properties of the electrode materials

The structural and electronic properties of the electrode materials, which are pristine and N-doped graphene films, were investigated with Raman analysis. Raman spectra of the films were characterized by the Raman-active G bands (~1583.5 cm^{-1} – 1590.3 cm^{-1}) and the 2D bands (~2675.5 cm^{-1} – 2680.0 cm^{-1}) as well as the Raman-forbidden D bands (~1340.0 cm^{-1}-1350.2 cm^{-1}) [59-62] The spectra and peak positions are shown in figure 6.1 and table 6.1, respectively. The presence of the broad D band in N-doped graphene films (Fig. 6.1 (ii)) indicated an increase in lattice distortions due to incorporation of nitrogen atoms into the graphene lattice. This was further corroborated by the relative intensity of the 2D band which was reduced to almost zero. In addition to the D band, another defect-induced peak was observed as a shoulder on the G band of the Raman spectrum of the N-doped graphene films. The presence of the shoulder, known as the D* band and located at ~1622.6 cm^{-1} (Fig.

6.1(ii)), is indicative of an increased lattice distortion caused by doping with nitrogen atoms.

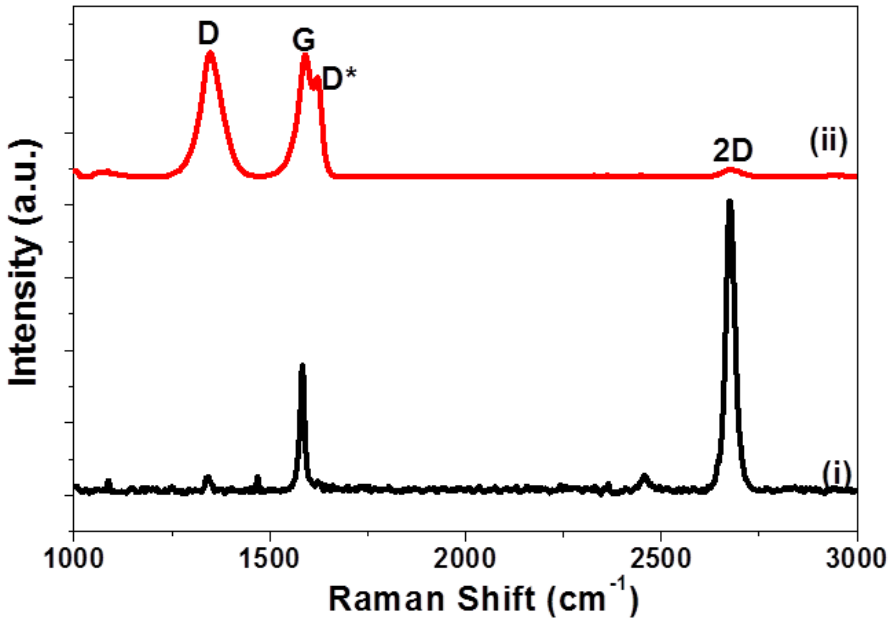

Figure 6.1: Raman spectra of (i) pristine and (ii) N-doped graphene films.

To investigate the level of disorder in the pristine graphene films as well as to probe the degree of doping in N-graphene films, the relative intensity ratios of the D band with respect to that of the G band (I_D/I_G) were determined (Table 6.1). The pristine graphene films exhibited an I_D/I_G ratio of ~0.271, which indicated the presence of few defects either in the form of sp^3-C bond or lattice vacancies [59-62]. The low defect density ratio signified the growth of high quality graphene films [59-62]. Upon doping, the I_D/I_G ratio increased to ~1.086, thus indicating that the quality of the film was compromised and the degree of disorder was found to significantly increase. The results show that incorporation of nitrogen atoms led to lattice distortion, and this was corroborated by the suppressed intensity of the lattice distortion-sensitive 2D band (Fig. 6.1(ii)).

Table 6.1: Band positions for pristine and N-doped graphene films

Sample	Peak position (cm^{-1})				Ratio	
	D	G	D*	2D	I_D/I_G	I_G/I_{2D}
Pristine	1340.0	1583.5	-	2675.5	0.271	0.41
N-doped	1350.2	1590.3	1622.6	2680.0	1.086	15.51

X-ray photoelectron spectroscopy (XPS) data were used to determine the overall doping content as well as the bonding states of both carbon and nitrogen atoms in the as-grown films. Figure 6.2(i) showed that the survey spectra of pristine graphene films consisted of C1s (~284 eV), O1s (~531 eV) and Cu2p (~933 eV) peaks. In addition to the C1s, O1s and Cu2p, the survey spectra of N-doped graphene films exhibited a weak N1s peak (~398 eV).

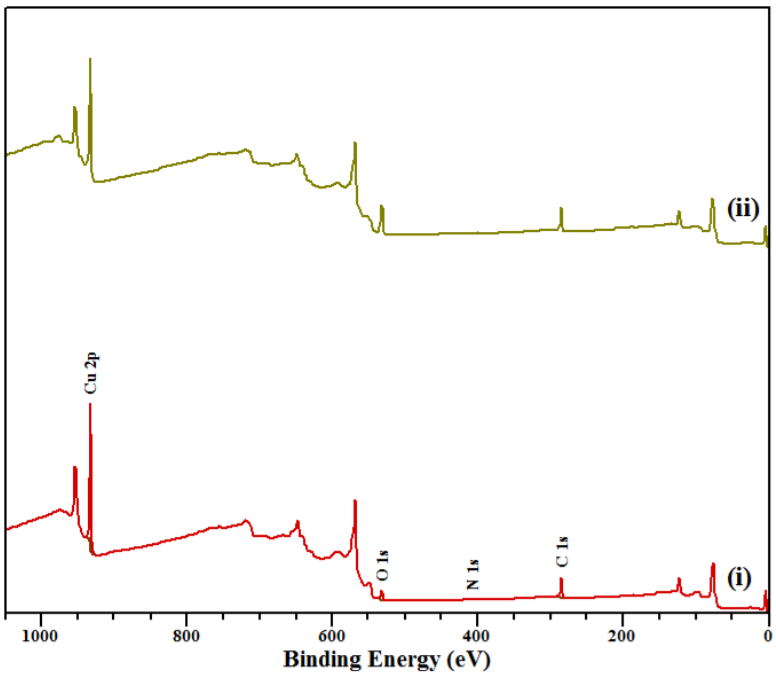

Figure 6.2: XPS survey spectra of (i) pristine and (ii) N-doped graphene films grown showing the C1s, N1s, O1s and Cu2p peaks.

The integrated areas under the peaks give the atomic percentages of each element in the as-grown films (Table 6.2). A decrease in carbon content was observed from pristine graphene films (85.1 at. %) to N-doped films (69.5 at. %), thus indicating the successful incorporation of nitrogen atoms into the graphene lattice. On the other hand, both oxygen (10.5 – 17.3 at. %) and copper (4.40 – 10.9 at. %) contents were found to increase upon doping. The high oxygen content in doped graphene films correlates well with the Raman data which showed an increased defect density ratio upon doping. This is because an increased defect density indicates increased decoration of graphene edges and defects with oxygen atoms. Furthermore, the increasing Cu content suggests that lattice distortion due to nitrogen doping results in formation of more vacancies in the graphene network, hence exposing the underlying Cu support.

Table 6.2: Atomic compositions of the pristine and N-doped graphene films

Sample	Elemental composition (at. %)				N/C
	C	N	O	Cu	
Pristine	85.1	-	10.5	4.40	-
N-doped	69.5	2.26	17.3	10.9	3.25

The chemical environments of the C atoms in both pristine and N-doped graphene films were determined by deconvolution of the high-resolution C1s XPS spectra, as reported in chapter 5 (Figs. 5.6a and e). It was observed that deconvolution of C1s spectra of pristine graphene films exhibited three component peaks centred at ~284.0 eV, ~284.8 eV, and ~287.6 eV, which corresponded to sp^2C-C bonds, defective sp^3C bonds, and oxygenated carbon bonds, respectively [63-65]. Upon incorporation of nitrogen atoms, the C1s spectra were deconvoluted with at least five component peaks. These were attributed to sp^2C-C bonds (284.3 eV), sp^2C-N bonds (285.1 eV), sp^3C-N and/or defective, sp^3C bonds (286.1 eV), and oxygenated carbon bonds (288.0 eV) [63-65]. Interestingly, the peak position of sp^2C-C bonds in N-doped films was upshifted slightly in comparison to the peak position in pristine films (Fig. 6.3a), and this is due to the bonding of carbon atoms to the more electronegative nitrogen atoms. Furthermore, deconvolution of the N1s XPs spectra was used to determine the bonding states of nitrogen atoms in the doped films. Figure 6.3b showed that at least four nitrogen configurations could be determined from the deconvolution of the N1s spectra. These are pyridinic-N (~397.7 eV), pyrrolic-N (~399.9 eV), substitutional/graphitic-N (~400.7 eV), and the oxidized pyridinic-N (NO_x, ~402.7 eV), respectively [63-65]. Finally, data analysis of the Cu2p spectra (Fig.6.3c) revealed a Cu(I) oxidation state in both pristine and doped graphene films.

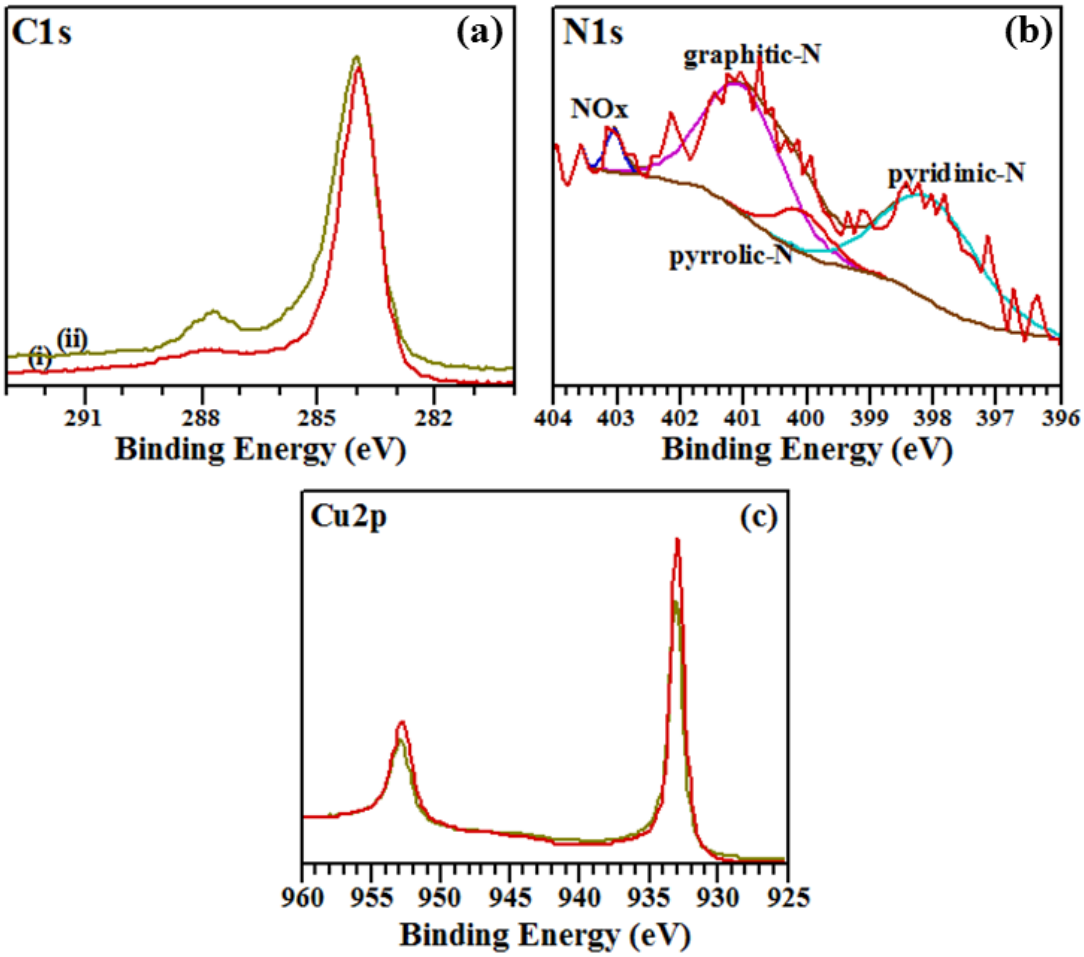

Figure 6.3: XPS data showing (a) C1s spectra of pristine (red) and N-doped (green) graphene films, (b) N1s spectra of N-doped graphene films, and (c) Cu2p spectra of both films.

6.3.2 Electrochemistry of the electrodes

The electrochemical activity of pristine and N-doped graphene modified ITO electrodes in comparison with the unmodified ITO electrodes was examined by investigating the electrochemical catalytic reaction between $[Fe(CN)_6]^{3-}$ and $[Fe(CN)_6]^{4-}$. Figure 6.4 shows the CVs of the unmodified and modified ITO electrodes in 4 mM potassium ferricyanide solution, with 1.0 M KCl as the supporting electrolyte, at a scan rate of 50 mV s^{-1}. It can be seen that the oxidation peak ascribed to the oxidation of $[Fe(CN)_6]^{4-}$ and the reduction peak attributed to reduction of $[Fe(CN)_6]^{3-}$ were observed on the bare ITO at 363.6 mV and 197.3 mV, respectively. The peak potential difference (ΔEp) of 166.3 mV (Table 6.2) indicated a quasi-reversible redox reaction. Upon modification with pristine graphene films, a slightly decreased current response of the $[Fe(CN)_6]^{3-/4-}$ redox couple was observed at the Gr/ITO (red curve). This can be attributed to the presence of oxygen functional groups on the graphene films, which then repel the negatively charged ferricyanide molecules. Interestingly, the

$[Fe(CN)_6]^{3-/4-}$ redox couple on Gr/ITO electrode exhibited a decreased peak-to-peak separation (ΔEp = 125.6 mV, Table 6.2). The results indicated that on Gr/ITO, there is improved electron transfer, although very little enhancement in electrochemical activity is observed. However, modification of the ITO with N-doped graphene films results in a much increased peak current (blue curve). The results indicated that the presence of N-graphene on the electrode surface greatly enhanced the electrochemical responses. This can be attributed to the structural properties of N-graphene which leads to an electrode surface with increased electrical conductivity, resulting in an accelerated electron transfer rate. In general, the results strongly indicated that for good sensing applications, N-graphene films are better candidate materials.

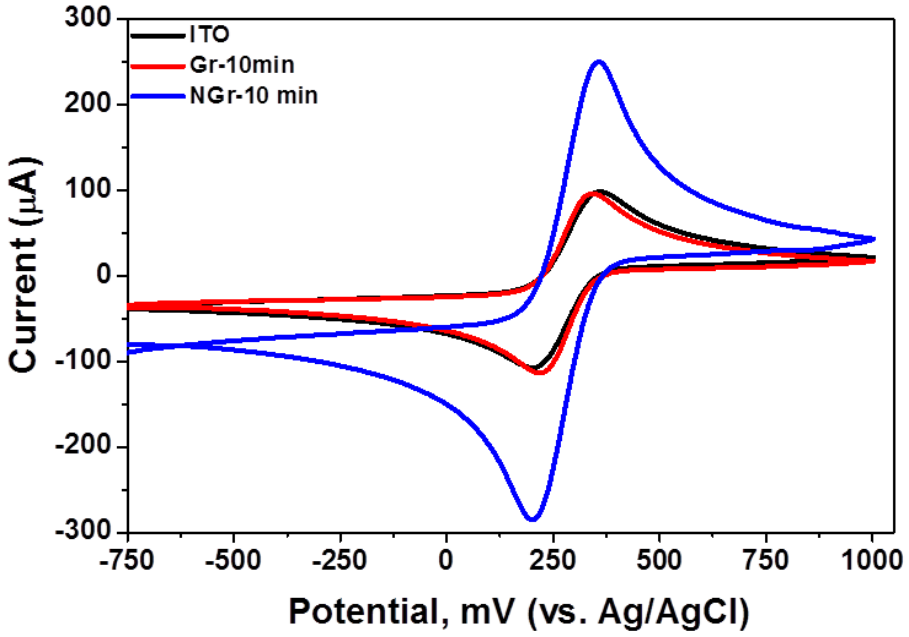

Figure 6.4: Cyclic voltammograms of ITO (black), Gr/ITO (red), and NGr (blue) in the presence of 4 mM $K_3[Fe(CN)_6]$ at the scan rate of 50 mV s^{-1}.

Table 6.3: Peak potentials and currents of $[Fe(CN)_6]^{3-/-4}$ on bare and modified ITO electrodes at a scan rate of 50 mV s^{-1}

Electrode	Ep (mV)		Ip (μA)		ΔE
	Ep_a	Ep_c	Ip_a	Ip_c	
ITO	363.6	197.3	98.89	-108.2	166.3
Gr-10min/ITO	341.3	215.7	95.71	-112.7	125.6
NGr-10min/ITO	355.1	250.5	198.7	-287.2	156.4

6.3.3 Electrochemical behaviour of DA and UA on modified electrodes

The electrocatalytic activity of pristine and N-doped graphene ITO electrodes against dopamine (DA) and uric acid (UA) was investigated by cyclic voltammetry. The CVs of 0.13 mM DA on the bare and modified ITO electrodes in PBS at pH = 6.02 are shown in figure 6.5a. On the bare ITO electrode, a pair of peak currents corresponding to the redox couple of DA was observed around 617.3 mV (Epa) and -137.4 mV (Epc), respectively. The peak current at 617.3 mV is ascribed to the oxidation of DA to the open-chain quinine, whereas the peak current at -137.4 mV is assigned to the reduction of the quinine back to DA (Scheme 6.2) [66]. Notably, both oxidation and reduction peaks currents of DA on Gr/ITO and NGr/ITO electrodes shifted negatively and positively, respectively (Table 6.3). The results demonstrated that there is excellent electrocatalytic performance of the modified ITO electrodes for the detection of DA. Furthermore, the peak currents of DA on NGr/ITO were found to be higher than that of DA on the Gr/ITO electrode (Table 6.3). This indicated that the electrochemical redox reactions of DA on NGr/ITO was improved, owing to the increased electrochemical active sites provided by the incorporation of nitrogen atoms into the graphene lattice. Additionally, the values of ΔEp were calculated to be 754.7 mV (ITO), 577.5 mV (Gr/ITO), and 640.8 mV (NGr/ITO).

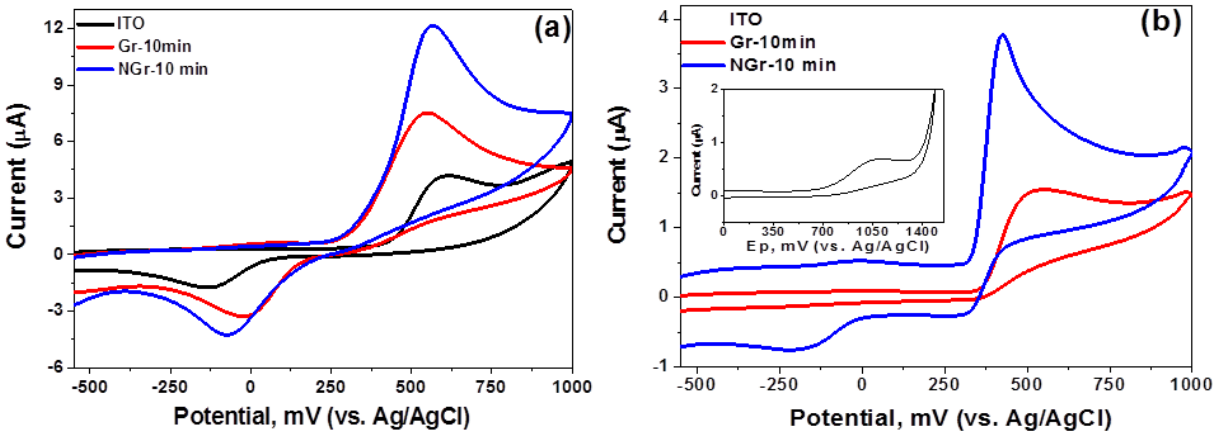

Figure 6.5: Cyclic voltammograms of (a) 0.13 mM DA and (b) 0.13 mM UA in PBS (pH = 6.02) on bare and modified ITO electrodes at scan rate of 50 mV s^{-1}.

Table 6.4: Peak positions of 0.13 mM DA in PBS (pH = 6.02) on bare and modified ITO electrodes at scan rate of 50 mV s^{-1}

Electrode	Ep (mV)		Ip (µA)		ΔE
	Ep_a	Ep_c	Ip_a	Ip_c	
ITO	617.3	-137.4	4.190	-1.779	754.7
Gr/ITO	550.3	-27.19	7.530	-3.288	577.5
NGr/ITO	566.8	-73.96	12.22	-4.258	640.8

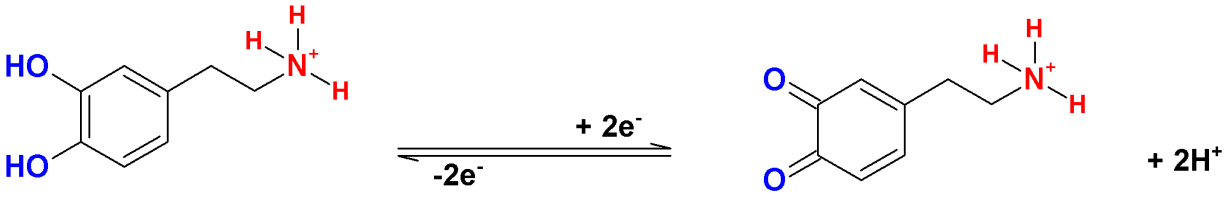

Scheme 6.2: A schematic representation of the redox reaction of dopamine to dopamine-o-quinone (dopaquinone).

Figure 6.5b shows the cyclic voltammograms of 0.13 mM uric acid (UA) on bare and modified ITO electrodes in PBS of pH = 6.02. The CVs revealed that oxidation of uric acid on bare and electrodes can be considered to be an irreversible process, as indicated by the presence of the anodic peak currents (Ipa) and lack of the cathodic peak current (Ipc). The electrochemical response of UA on the bare ITO, and the oxidation current peak (Ipa) of 0.9317 µA was located at 1113.8 mV. Furthermore, the oxidation current peak of UA on Gr/ITO of 1.555 µA at 550.3 mV indicated that Gr/ITO improved the sensing performances of ITO electrodes for electrochemical oxidation of UA. On both bare and Gr/ITO electrodes, the voltammetric peak was rather broad, indicating that the electron transfer kinetics were slow. In contrast, a well-defined oxidation peak of UA on NGr/ITO was observed at 424.1 mV with a significantly increased peak current of 3.819 µA. The peak was higher and more negatively shifted than that on bare ITO and Gr/ITO electrode. Additionally, a weak reduction peak of -0.7457 µA was observed at -222.3 mV. The results indicate that the presence of N-graphene on ITO greatly enhanced the catalytic activity of NGr/ITO towards electrochemical oxidation of uric acid. Due to the extra electrons on the N-doped graphene, the doped graphene films act as promoters to increase the rate of electron transfer, which then

lowers the overpotential of UA oxidation at the bare ITO electrode, and this led to more negatively shifted oxidation peak potential. The irreversibility of the electrochemical oxidation of UA on both electrodes can be summarised as shown in scheme 6.3. The oxidation proceeds as a two-electron-two-proton process (Scheme 6.3), and leads to the formation of an unstable diimine species, which is susceptible attack by water molecules to produce an imine alcohol and the finally the uric acid-4,5 diol [67]. The lack of a reduction peak suggests a slow electron transfer process. It is known that oxidation of UA on metal electrodes is known to be irreversible [55].

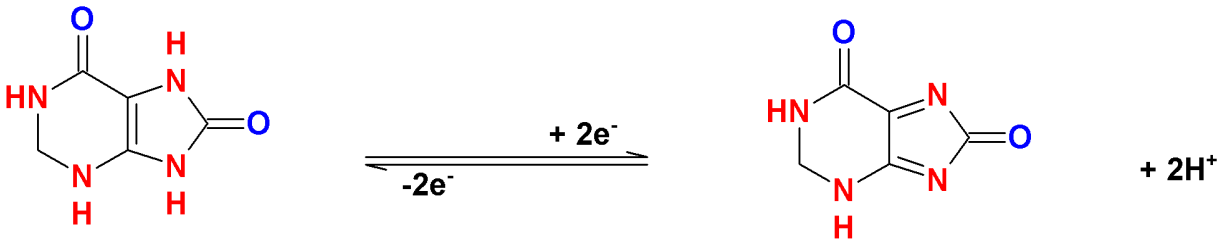

Scheme 6.3: A schematic representation of redox of uric acid to uric acid-4,5 diol.

Table 6.5: Peak positions of 0.13 mM UA in PBS (pH = 6.02) on bare and modified ITO electrodes at scan rate of 50 mV s^{-1}

Electrode	Ep_a (mV)	Ip_a (µA)
ITO	1113.8	0.9317
Gr/ITO	550.3	1.555
NGr/ITO	424.1	3.819

6.3.4 Influence of scan rate on the detection of DA

The reaction kinetics of DA on ITO electrodes modified with pristine and N-doped graphene films were investigated by studying the influence of scan rate (υ) on the electrochemical responses of DA. Figures 6.6 (a and b) illustrate the cyclic voltammograms of 0.13 mM DA on pristine and N-doped graphene modified ITO electrodes, respectively, during the variation of scan rates from 10 to 100 mV s^{-1}. It can be observed that as the scan rate is increased, both anodic (Ipa) and cathodic (Ipc) peak currents gradually increased, and this is attributed to the heterogeneous reaction kinetics at the electrode surface. Additionally, the peak potentials were found to shift slightly more negatively (Epc) and positively (Epa), respectively. The shift in peak potentials generated an increased potential separation (ΔEp), which is characteristic of a quasi-reversible reaction.

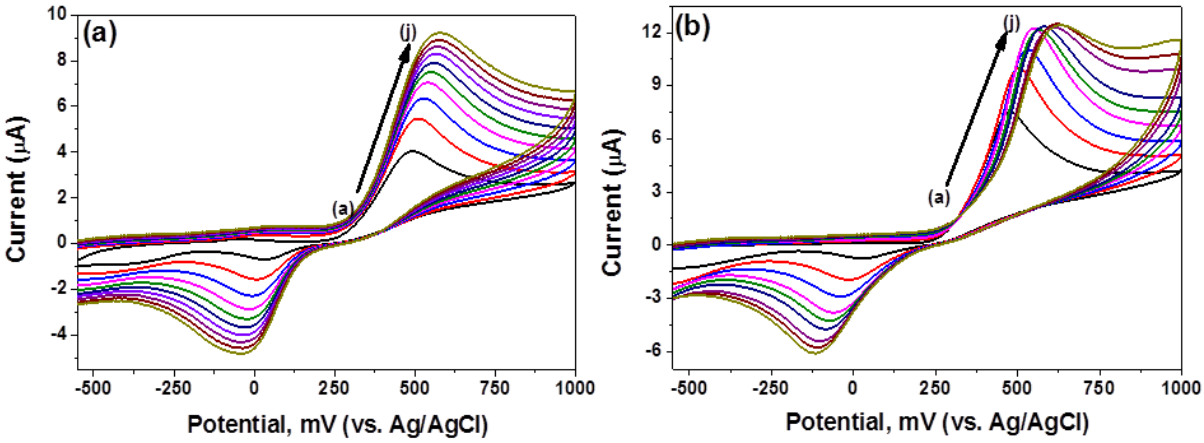

Figure 6.6: Cyclic voltammograms of (a) Gr/ITO and (b) NGr/ITO in PBS (pH =6.02) containing 0.130 mM DA at scan rate range of 10 -100 mV s^{-1} (a-j).

With the increase of scan rate, a good linear dependence of the redox peak currents of DA (I_{pa} and I_{pc}) with the square root of the scan rate (√υ), was obtained (Figs. 6.7a and b), indicating a diffusion-controlled process for the detection of DA on both modified electrodes. The results showed a faster electrochemical oxidation of DA on the N-doped graphene modified ITO electrode as compared to the oxidation on the pristine graphene modified electrode. Furthermore, the calculations from a linear plot of log υ vs. log Ipa resulted in the determination of the electron transfer coefficients (α) of 0.316 and 0.453, for DA on pristine and N-doped modified electrodes, respectively. These were found to be close to the theoretical value of 0.5 for a quasi-reversible process [54-56]. The linear regression equations for ITO electrodes modified with pristine graphene (Fig. 6.7a) were obtained to be as follows;

$$Ip_a(\mu A) = 21.81\nu^{1/2}(Vs^{-1}) + 2.495(R^2 = 0.9915)$$
$$Ip_c(\mu A) = -18.99\nu^{1/2}(Vs^{-1}) + 1.084(R^2 = 0.9952) \quad \text{.....[1]}$$

On N-doped modified electrodes (Fig. 6.7b), the linear regression equations were obtained as follows;

$$Ip_a(\mu A) = 47.29\nu^{1/2}(Vs^{-1}) + 2.835(R^2 = 0.9969)$$
$$Ip_c(\mu A) = -24.80\nu^{1/2}(Vs^{-1}) + 1.551(R^2 = 0.9976) \quad \text{.....[2]}$$

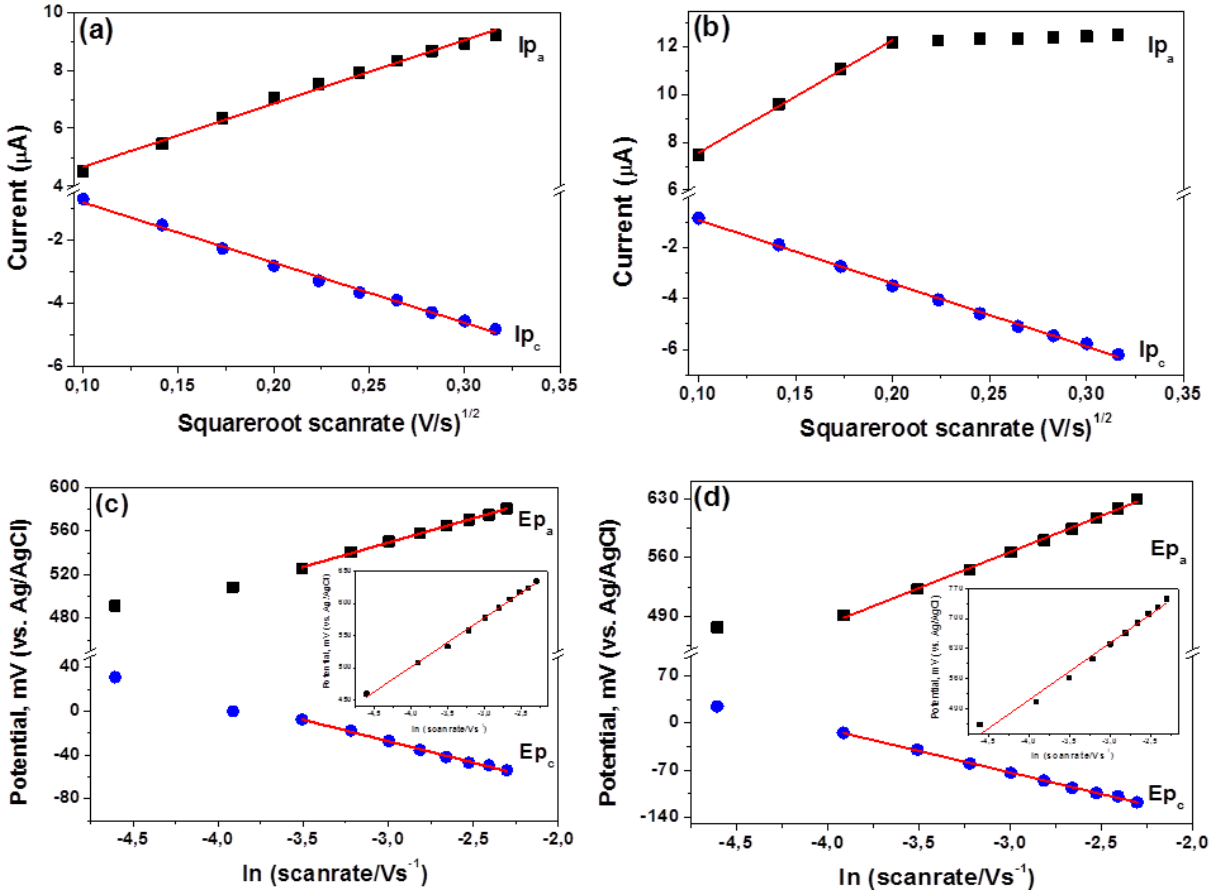

Figure 6.7: Linear relationships between Ip vs. square root of scan rate on (a) Gr/ITO and (b) NGr/ITO. Linear plots of Ep vs. ln υ on (c) Gr/ITO and (d) NGr/ITO. Inserts: (c) and (d) ΔEp vs. ln υ.

The relationship between the redox peak potentials and ln v was determined (Fig. 6.7c and d) and it was observed that a linear relationship was obtained at high scan rates (30-100 mV s^{-1}) for pristine (equation 3) and N-doped modified electrodes (equation 4):

$$Ep_a(mV) = 44.64n\,\nu(Vs^{-1}) + 683.2(R^2 = 0.9990)$$
$$Ep_c(mV) = -39.25\ln\nu(Vs^{-1}) - 145.0(R^2 = 0.9959).....[3]$$

$$Ep_a(mV) = 85.86\ln\nu(Vs^{-1}) + 824.0(R = 0.9983)$$
$$Ep_c(mV) = -63.90\ln\nu(Vs^{-1}) - 264.8(R = 0.9987).....[4]$$

Therefore, using the slopes and based on the Nicholson's models [68] (shown below, eqns. 5 and 6), the number of electrons in the reaction was determined to be 1.4 ± 0.9 and 2.7 ± 0.2 for pristine and N-doped modified electrodes, respectively. The results indicated that there are more electrons involved in the redox reaction of DA on NGr/ITO due to the presence of nitrogen atoms.

$$Ep_a = E^{0'} + \frac{RT}{(1-\alpha)nF}\ln\frac{(1-\alpha)nF}{RTk_s} + \frac{RT}{(1-\alpha)nF}\ln\nu \text{ ..... [5]}$$

$$Ep_c = E^{0'} - \frac{RT}{\alpha nF}\ln\frac{\alpha nF}{RTk_s} - \frac{RT}{\alpha nF}\ln\nu \text{ .....[6],}$$

where R is the gas constant (8.3145 $J.K^{-1}mol^{-1}$), F is the Faraday's constant (96487 $C.mol^{-1}$), n is the reaction number of electrons, α is the electron transfer coefficient, k_s is the heterogeneous transfer rate constant, and T is the reaction temperature (295.05 K).

Rearrangements of equations [5] and [6] in order to determine ΔE are shown below (eqn.7). The intercept of a plot of ΔEp against ln v (Figs. 6.7a and b, inserts) gave the apparent heterogeneous transfer rate constant (k_s) of 1.14×10^{-3} s^{-1} for pristine-graphene modified electrode and 10.1×10^{-3} s^{-1} for the N-doped graphene modified electrodes. On the bare ITO electrode, the heterogeneous transfer rate constant (k_s) was found to be 2.21×10^{-4} s^{-1}. The results indicated that a fairly fast electron transfer was observed on the N-doped modified electrode due to the increased electron density as a result of nitrogen incorporation into the graphene lattice.

$$\Delta Ep = \frac{RT}{(1-\alpha)nF}\left[\alpha\ln(1-\alpha) + (1-\alpha)\ln\alpha - \ln\frac{RT}{nF} - \ln k_s\right] + \frac{RT}{(1-\alpha)nF}\ln\nu \text{ .....[7]}$$

6.3.5 Influence of scan rate on the detection of UA

The influence of the scan rate on the electrochemical responses of UA on Gr/ITO and NGr/ITO electrodes was investigated by cyclic voltammetry. Figure 6.8 shows the CVs obtained at pristine and N-doped graphene modified ITO electrodes in PBS (pH 6.02) containing 0.13 mM UA at different scan rates (between 10 and 300 mV s^{-1}). As the scan rate was increased, the Ipa was observed to increase while the Epa shifted slightly in the positive direction (Figs 6.8a and b). Furthermore, a good linearity between the anodic peak current (Ipa) and the square root of the scan rate (√υ) was obtained for UA (Fig. 6.9a and b). The results indicate that the charge transfer on the modified electrodes is a diffusion-controlled process. The linear relationships were found to obey equations [8] and [9] for Gr/ITO and NGr/ITO electrodes, respectively:

$$Ip_a(\mu A) = 4.095\nu^{1/2}(Vs^{-1}) + 0.6604(R^2 = 0.9993)\text{.....[8]}$$

$$Ip_a(\mu A) = 9.931\nu^{1/2}(Vs^{-1}) + 1.626(R^2 = 0.9987)\text{.....[9]}$$

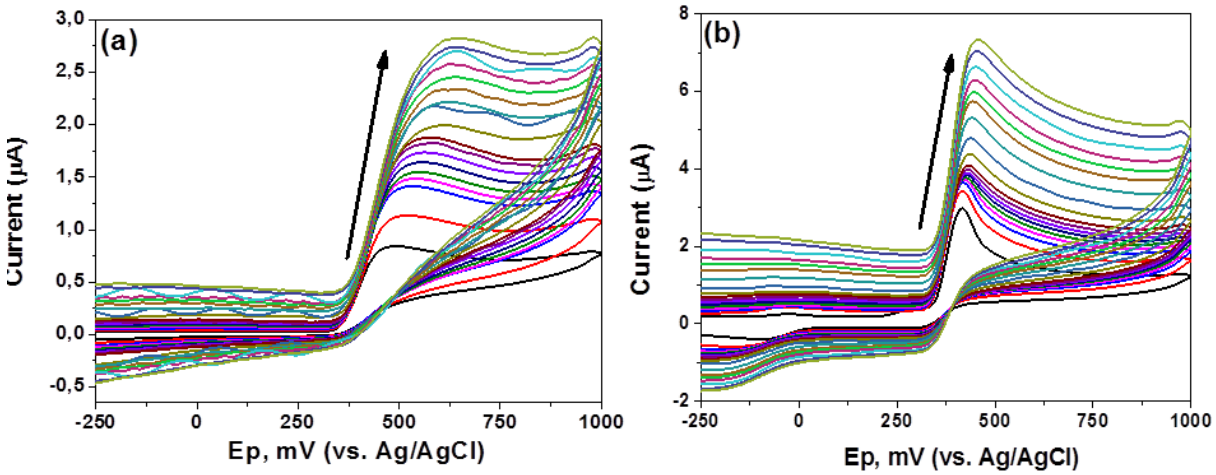

Figure 6.8: CVs of (a) Gr/ITO and (b) NGr/ITO in PBS (pH = 6.02) containing 0.130 mM UA at scan rate range of 10-300 mV s^{-1}.

The relationship between the redox peak potentials and ln υ was determined, as shown in figures 6.9c and d, and it was observed that a linear relationship was obtained at high scan rates (30-100 mV s^{-1}) and was expressed as for pristine (eqn. 10) and N-doped modified electrodes as (eqn. 11):

$$Ep_a(mV) = 61.95 \ln \nu(Vs^{-1}) + 732.1 (R^2 = 0.9994) \text{.....[10]}$$

$$Ep_a(mV) = 16.95 \ln \nu(Vs^{-1}) + 473.8 (R^2 = 0.9977) \text{.....[11]}$$

The slopes of the log Ip_a vs. log υ was used to determine the electron transfer coefficient (α) [54-56] and these were found to be 0.30 and 0.50 for Gr/ITO and NGr/ITO electrodes, respectively. This further suggested that the electron transfer reaction of UA on the modified electrodes was controlled by the diffusion process [54-56, 67]. This can be attributed to the structural properties of both pristine and N-doped graphene films. This is indicative that more electrons are being injected by the presence of nitrogen atoms on the electrode surface. Furthermore, the large slope of the Ipa vs. $\upsilon^{1/2}$ linear plot (9.93 µA sV^{-1} on NGr/ITO versus 4.10 µA $s.V^{-1}$ on Gr/ITO) also corroborated an increased electron transfer on NGr/ITO, which indicated a faster electrochemical oxidation of UA on the NGr/ITO electrode. Moreover, the broad CV's on Gr/ITO suggested a slow electron transfer, hence the fewer number of reaction electrons were observed in comparison with those required in the NGr/ITO electrochemical process. Finally, the number of electrons used in the reaction was calculated to be 1.06 and 1.76 for Gr/ITO and NGr/ITO electrodes, respectively. The number of electrons on NGr/ITO is very close to the theoretical reaction number of electrons (i.e. ~2, Scheme 6.3) [54-56]. In summary, the results indicated reasonably fast electron transfer on N-

doped modified electrode due to the increased electron density as a result of incorporation of nitrogen atoms into the graphene lattice.

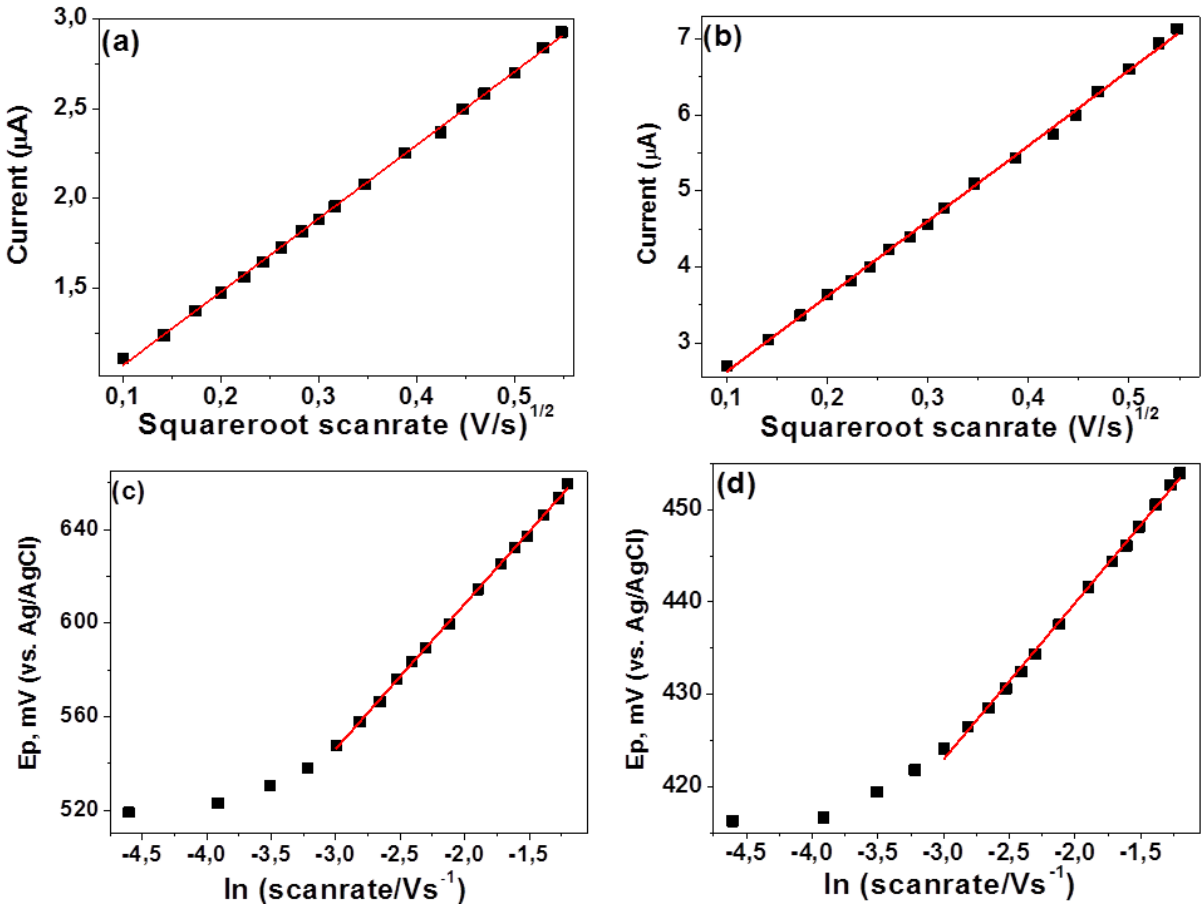

Figure 6.9: Linear relationships between Ip vs. square root of scan rate of UA on (a) Gr/ITO and (b) NGr/ITO. Linear plots of Ep vs. ln υ at (c) Gr/ITO and (d) NGr/ITO.

6.3.6 Influence of pH of the buffer solution

The influence of the pH of the PBS buffer on the electrochemical responses of 0.13 mM DA and 0.13 mM UA was investigated using differential pulse voltammetry (DPV), due to the DPV method having high sensitivity and exhibiting minimal background noise. The pH studies were performed since both DA and UA exhibited a two electron and two proton processes on the modified electrodes [66, 67]. Therefore, the pH value should have a great impact on the electrocatalytic responses of both biological molecules. Figure 6.10 illustrates the oxidation peak currents differential pulse voltammetric responses of DA in the pH range of 3.05 to 9.04 at pristine and N-doped graphene modified ITO electrodes.

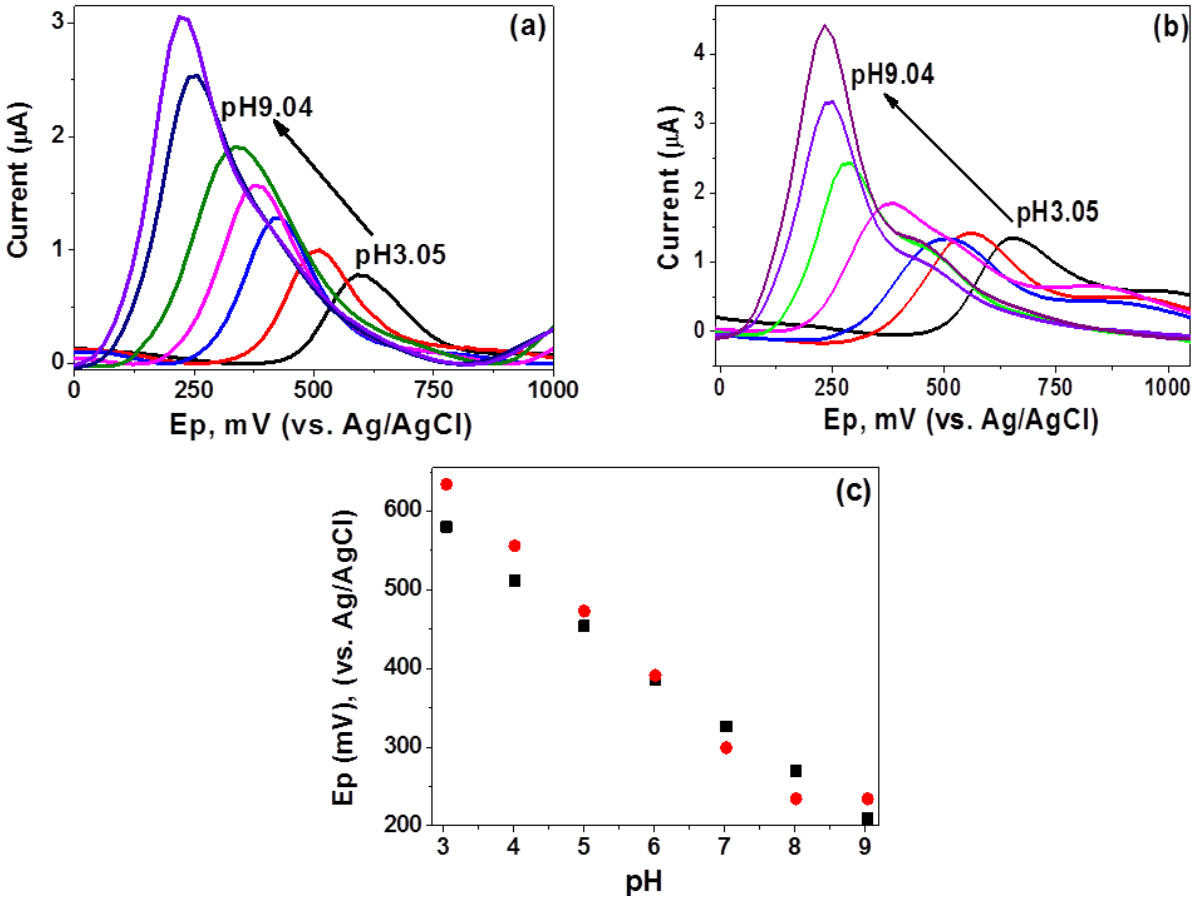

Figure 6.10: DPVs of DA at various pH values PBS on (a) Gr/ITO and (b) NGr/ITO electrodes. (c) Linear relation between peak potential (Epa) and different pH values on Gr/ITO (black squares) and NGr/ITO (red dots).

As shown in figures 6.10a and b, the oxidation current peaks of DA increased with increasing pH, thus indicating that high pH values are favourably driving the oxidation reaction of DA forward. Furthermore, the peak potentials shifted to the more negative direction with increasing buffer pH, indicating an increased electron transfer during the electrocatalytic oxidation of DA. Additionally, the small amperometric responses at ≤ pH 5.01 suggest that successful detection of DA is not possible for both electrodes. A linear relationship between the oxidation potentials (Ep_a) and PBS pH was obtained in the range of 3.05 – 9.04 for Gr/ITO (Fig. 6.10c, black squares) and 3.05 – 8.02 for NGr/ITO (Fig. 6.10c, red dots). The values of the slopes of the linear plots were calculated to be -61.7 mV pH^{-1} and -81.8 mV pH^{-1} for Gr/ITO and NGr/ITO, respectively. The measured slope for Gr/ITO is very close to the theoretical Nernst value of -59 mV pH^{-1}, thus suggesting that the electrochemical oxidation of DA at the Gr/ITO electrode involves an equal number of electrons and protons [66]. On the other hand, the measured slope of NGr/ITO was found to be larger than the theoretical Nernst

value of -59 mV pH^{-1}. This indicated that the oxidation process of DA occurred faster due to increased electron transfer, and this was also indicated by the negative shift of the oxidation peak potentials.

Thus the mechanism depicting the electrochemical behaviour of DA on the modified electrodes in buffer solutions with different pH values is shown in scheme 6.4. In general, the electrocatalytic oxidation of DA is known to occur via a two-electron and two-proton transfer process, as shown in step 1 of scheme 6.4. Initially, the parent DA molecule is oxidized to form *o*-dopaquinone by the loss of two protons from the hydroxyl groups, which is then accompanied by loss of two electrons. However, during the oxidation of dopamine in buffer solutions of alkaline pH values, a major deprotonation of the *o*-dopaquinone can occur [54, 69-71]. This protonation reaction is then followed by a cyclization reaction of *o*-dopaquinone to form the leucodopaminochrome through a proton-assisted intramolecular 1,4-Michael addition reaction (step 2) [54, 69-71]. The resultant leucodopaminochrome is more easily oxidized than the parent DA molecule, and undergoes a further two-electron oxidation to form dopaminochrome (step 3) [54, 69-71]. As a result, it is expected that the electrochemical responses for the oxidation of DA at the modified electrodes will be dependent on pH media of the buffer solution. As a result, in acidic media (pH 3.05 – 6.02), a low peak current response is observed for oxidation of DA at both Gr/ITO and NGr/ITO (Figs. 6.10 (a) and (b)), indicating a reversible reaction (step 1). The slightly increasing oxidation peak currents in acidic media can be attributed to the dissociation of the surface-bound acidic groups as well as the increased electrostatic attraction between the DA molecules and the modified electrodes. However, in neutral to alkaline media (pH 7.03 – 9.04), an increase in oxidation peak is observed in figure 6.10, suggesting that the oxidation reaction leading to the formation of dopaminochrome is more favourable.

Additionally, apart from the buffer solution media, it is noteworthy to mention that the structural properties of the modified electrodes also had an impact on the electrochemical responses of DA. For instance, the electrochemical performance of Gr/ITO towards detection of DA can be correlated to the good π-π interaction between the phenyl structure of DA and the sp^2 conjugated carbon lattice of the graphene. In addition to the π-π interaction between DA and the 2D hexagonal structure of graphene, the presence of pyridinic-N and pyrrolic-N in N-doped graphene (Fig. 6.3b), is suggesting that the NGr/ITO electrode surface contained a much more stable π-conjugated delocalised system, which is very active towards electrophiles. Thus, the electron-rich NGr/ITO, which acted as an excellent nucleophile,

would exhibit better electron transfer properties as well as facilitating the oxidation of DA at lower oxidation potentials than those observed on Gr/ITO (Fig. 6.10c), especially within pH ranges that are closer to the physiological conditions (i.e. ~pH 7).

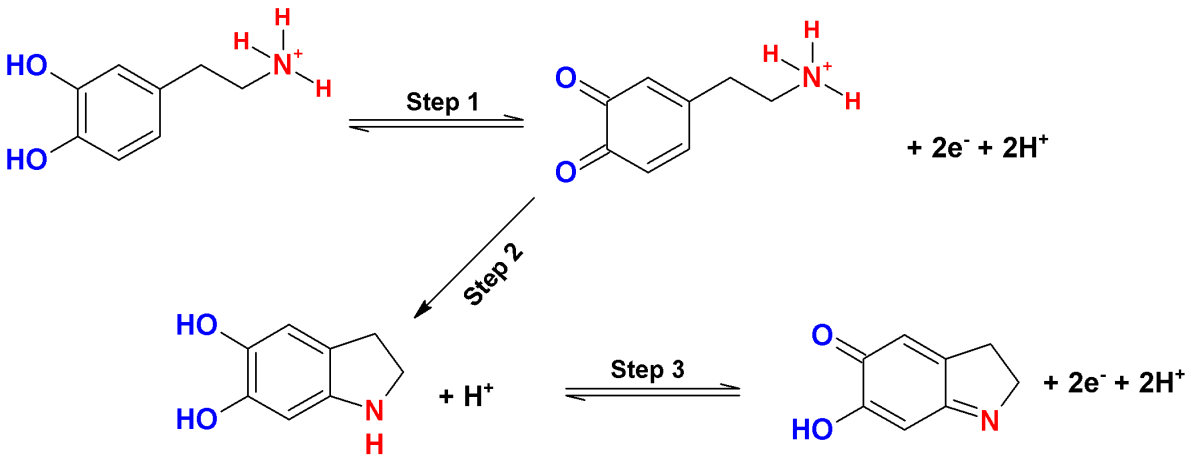

Scheme 6.4: The general mechanism for the electrochemical oxidation of DA at different pH values of the buffer solution.

The effect of pH of the buffer solution on the oxidation peak currents and potentials of UA at the modified ITO electrodes was also investigated. An interesting trend in the oxidation peak potentials was observed on Gr/ITO; with a negative shift seen in acidic media (pH 3.05 – 5.01) while a positive shift was observed in neutral to alkaline media (pH 6.02 – 9.04). On the other hand, the oxidation potentials of UA at NGr/ITO were observed to shift negatively with increasing pH of the buffer solution. This is indicative of improved electron transfer during the electrocatalytic oxidation of UA. A plot of the oxidation peak potentials (Epa) against the PBS buffer pH is shown in figures 6.11c. The slopes of the linear plots of Epa vs. pH were calculated to be -49.9 mV pH^{-1} and +68.2 mV pH^{-1} for Gr/ITO in the range of pH 3.05 to 5.02 and pH 6.02 to 9.04, respectively. The increasing slopes in alkaline pH as well as positive shift in oxidation peak potentials could suggest adsorption of impurities on the electrode surface; thus indicating that more energy is required to remove them. Moreover, the slope for the linear plot of Epa vs. pH at the NGr/ITO was calculate to be -54.4 mV pH^{-1}. Since the values of the slopes were found to be closer to the theoretical Nernst value of -59 mV $pH,^{-1}$ this is indicative that the uptake of electrons is accompanied by an equal number of protons being used during the electrocatalytic reaction of UA [67].

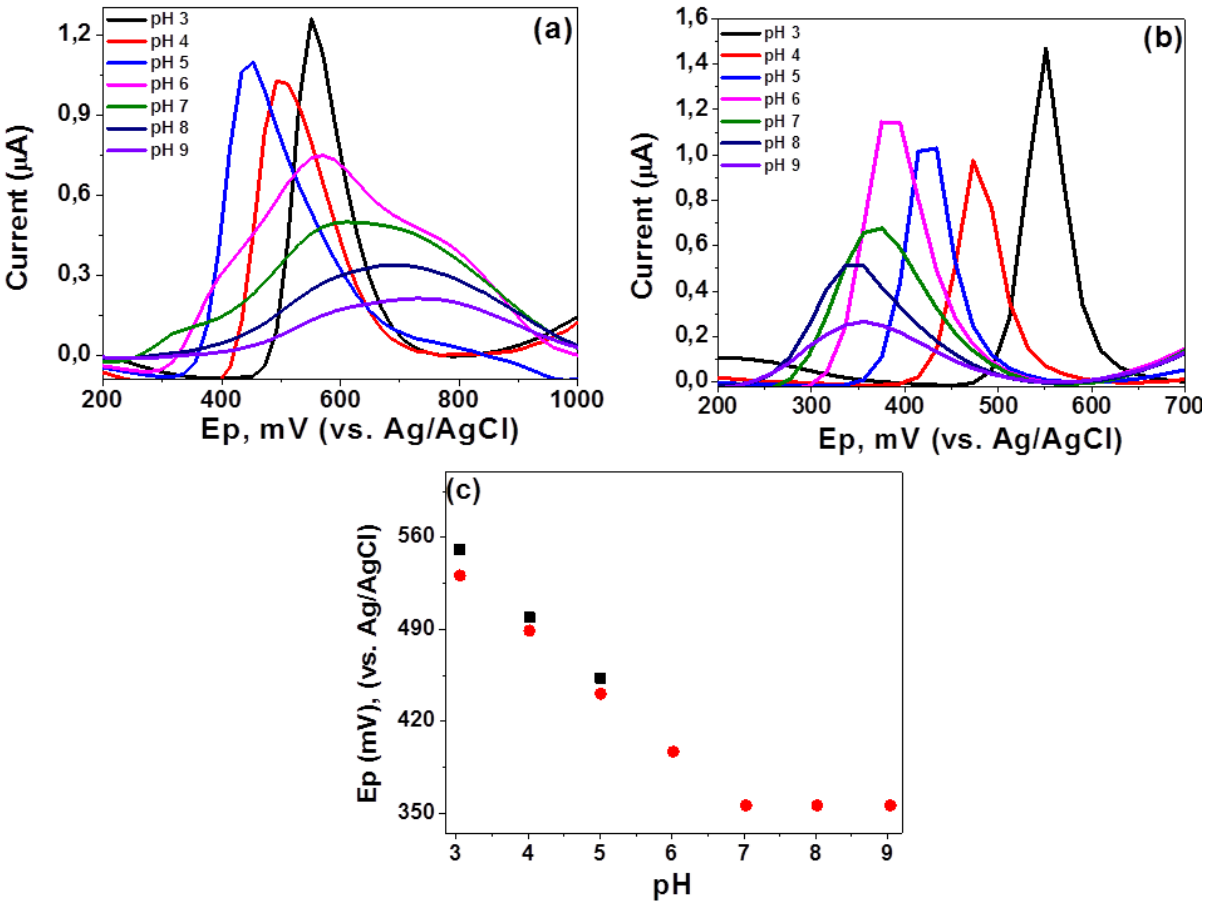

Figure 6.11: DPVs of UA at various pH values PBS on (a) Gr/ITO and (b) NGr/ITO electrodes. (c) Linear relation between peak potential (Epa) and different pH values on Gr/ITO (black dots) and NGr/ITO (red dots).

The mechanism for understanding the electrochemical behaviour of UA on the modified electrodes in buffer solutions with different pH values is shown in scheme 6.5. Generally, oxidation of uric acid is known to be a two-electron two-proton transfer process, as shown in stage 1 of scheme 6.5. This two-electron process which is the followed by protonation (also known as tautomerization) occurs at pH values of ≤ 5.4, which closer to the pKa value of UA [67, 72]. As a result, increased oxidation peak current responses are observed at pH values ≤ 5.02. Therefore, it can be concluded that in acidic media, the reverse reaction, stage 1, is more favoured. On the other hand, in neutral and/or basic media, UA becomes deprotonated and its anionic form is repelled from the electrode. As the buffer solution becomes more alkaline, more negatively charged UA molecules are formed, either in monoanionic or dianionic form. This leads to a decrease in the oxidation peak currents (stage 2) as the UA loses more protons and becomes a charged molecule[67, 72].

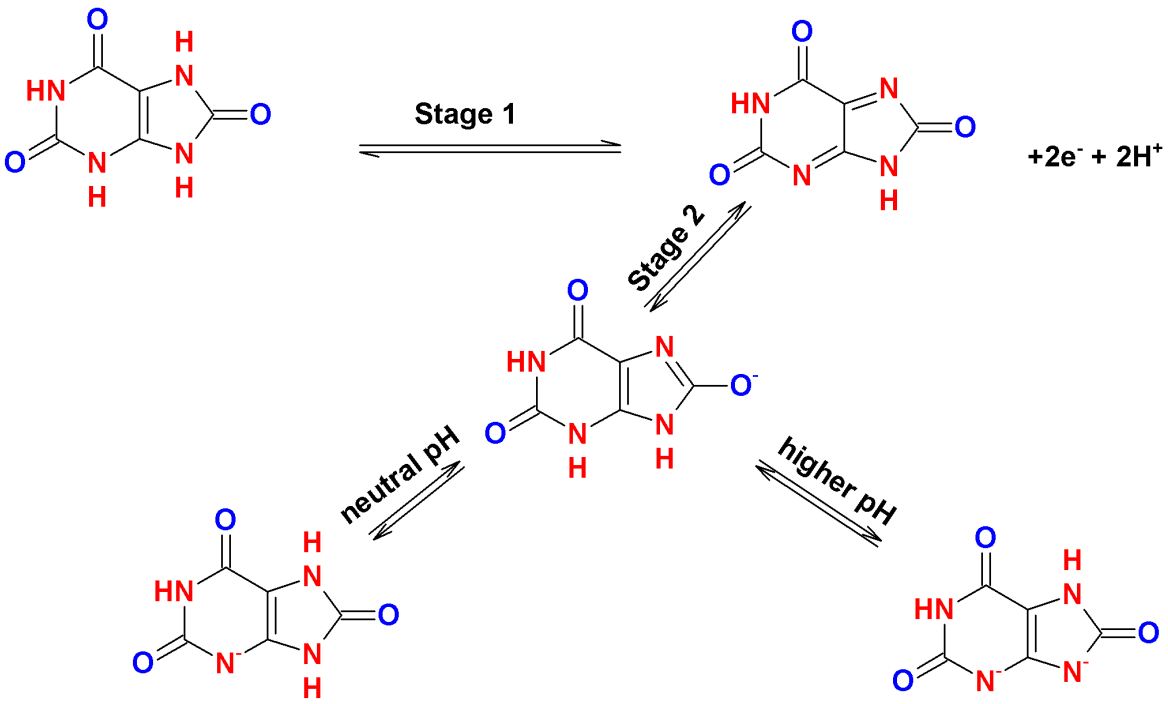

Scheme 6.5: The general mechanism for the electrochemical oxidation of UA at different pH values of the buffer solution.

6.3.7 Concentration studies

Differential pulse voltammetry (DPV) was used for the determination of the detection limits of DA and UA sensors based on Gr/ITO and NGr/ITO. Figure 6.12a illustrates the DPVs at Gr/ITO in 1.0 mM PBS containing 100 µM UA and different concentrations of DA. Figure 6.12b shows the DPVs of different DA concentrations in the absence of UA at NGr/ITO in 1.0 mM PBS. At the NGr/ITO electrode, poor oxidation potential separation was observed between DA and UA. This is due to the increased electrochemical oxidation of UA at the N-doped modified electrode, as observed by the negatively shifted oxidation potential. The enhancement of the peak currents corresponding to the oxidation of DA was observed with increasing concentration. A linear relationships between Ipa and DA concentration was observed in the concentration range of 8 – 190 µM and 2 – 150 µM on Gr/ITO (eqn. 14) and NGr/ITO (eqn. 15) electrodes, respectively.

$$Ip_a(\mu A) = 0.01235C(\mu molL^{-1}) + 0.2594(R^2 = 0.9991).....[14]$$

$$Ip_a(\mu A) = 0.03321C(\mu molL^{-1}) + 0.6920(R^2 = 0.9991).....[15]$$

The detection limits were determined to be 4.13 µM and 0.154 µM on Gr/ITO and NGr/ITO, respectively, at a signal-to-noise ratio of 3. Moreover, the sensitivities were found to be $2.94\times10^{-2}\,\mu A\mu M^{-1}cm^{-2}$ and $7.91\times10^{-2}\,\mu A\mu M^{-1}cm^{-2}$ for DA on Gr/ITO and NGr/ITO, respectively.

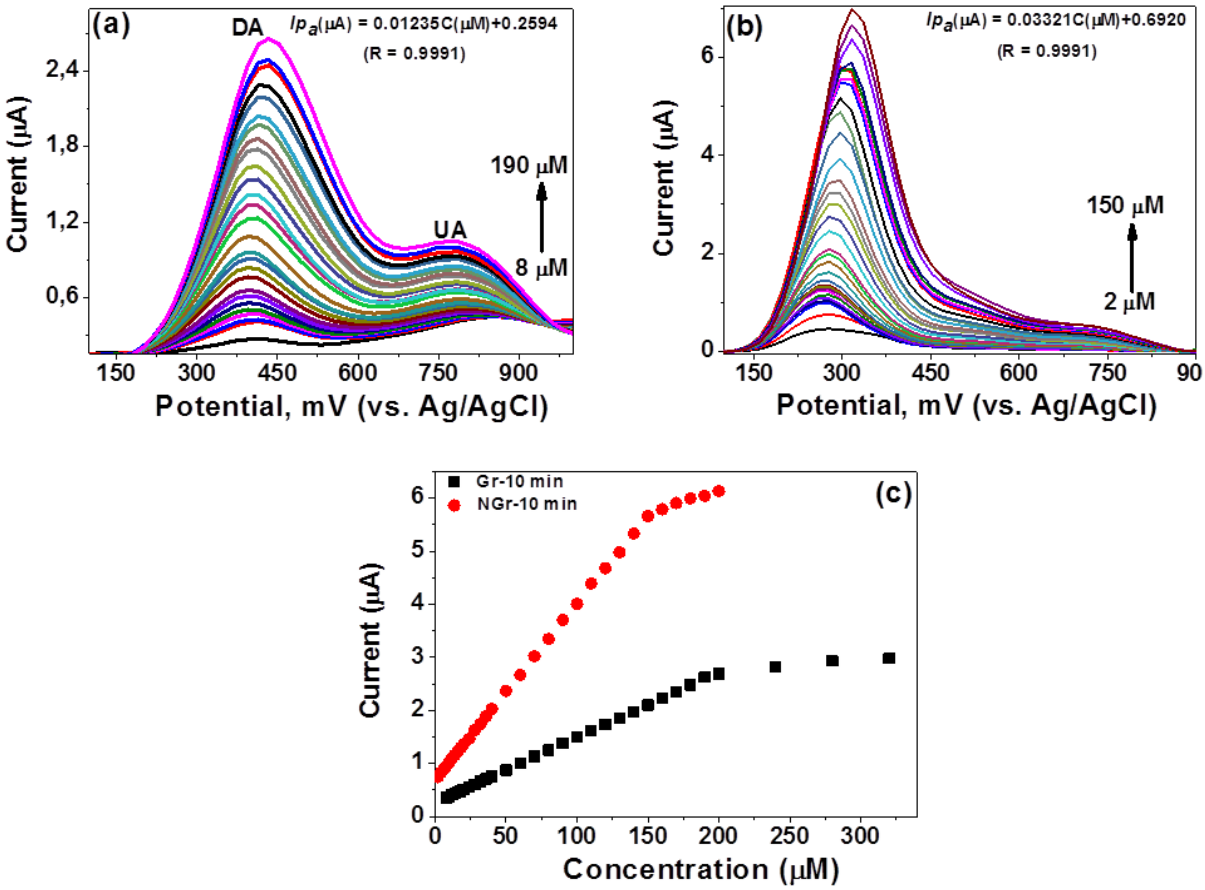

Figure 6.12: Concentration studies of DA on (a) pristine and (d) N-doped graphene modified ITO electrodes at buffer pH 6.02. (c) Linear concentration ranges of DA at Gr/ITO (black) and NGr/ITO (red) electrodes at buffer pH 6.02.

Finally, the sensing performances of our modified ITO electrodes were compared with the previously reported sensors carbon-based electrodes for either the individual or simultaneous detection of dopamine (Table 6.6). It can be seen that the linear range for DA at NGr/ITO (2 – 150 μM) was larger than that at ITO electrode modified with rGO-CNTs hybrids [55], the pyrolytic graphite electrode [74], as well as being larger than that obtained for the screen printed carbon electrode (SPCE) modified with reduced graphene oxide [42] The detection limit for the DA at NGr/ITO electrode was higher than most of the reported data, such as for the rGO-CNT/ITO [55], the NGr/GCE [6], Au-GO/ITO [54], and the N-CNRs-Nafion/GCE [75]. This is indicative that the structural properties of the modified electrode plays a major role in improving the electrocatalytic oxidation of DA by dictating the rate of electron transfer as well as the interaction of the DA molecule with the electrode surface. In summary, it can be seen that both pristine and N-doped graphene films produced detection limits that are quite comparable with those obtained at other similar electrodes modified with their powdered

counterparts (i.e. CNTs, rGO). Additionally, the key point from this study illustrated the possibility of using films for fabrication of sensors, which can also be easy to produce at an industrial scale.

Table 6.6: Comparison of electrocatalytical data for the determination of DA

Electrode	Linear range (µM)	Detection limit (µM)	Reference
Gr/ITO	8 - 190	4.13	This study
NGr/ITO	2 - 150	0.15	This study
rGO-CNT/ITO	0.2 – 8.0	0.04	55
Gr/GCE	N/A	1.86	30
GO/GCE	N/A	0.27	8
Au/ITO	0.001 – 500	0.001	72
Au-GO/ITO	10 – 1000	0.06	54
PGE	1.0 – 20	0.011	74
N-CNRs-Nafion/GCE	0.008 – 15.0	0.0089	75
NGO/GCE	0.5 - 170	0.25	6
rGO/SPCE	0.20 – 80	0.1	42

**Gr-> graphene films, ITO -> indium tin oxide, NGr -> N-doped graphene film, rGO -> reduced graphene oxide nanosheets, CNT -> carbon nanotubes, GCE -> glassy carbon electrode, GO -> graphene oxide nanosheets, Au -> gold nanoparticles, N-CNRS -> N-doped carbon nanorods, PGE -> pyrolytic graphite electrode, SPCE -> screen printed carbon electrode.*

Figure 6.13a shows the DPVs of different UA concentrations in the presence of 20 µM DA on Gr/ITO in 1.0 mM PBS. Figure 6.13b shows the DPVs of different UA concentrations in the absence of DA at NGr/ITO in 1.0 mM PBS. A poor separation was observed at the NGr/ITO electrode. However, a gradual enhancement of the oxidation peak current for UA was observed over the UA concentration range. The calibration curves (Figs. 6.13c) showed a linear relationship between Ipa and the concentration in the range of 40 - 560 µM and 6 – 140 µM for UA on Gr/ITO (eqn. 16) and NGr/ITO (eqn. 17), and the curves obeyed the following equations;

$$Ip_a(\mu A) = 0.00264C(\mu molL^{-1}) - 0.03001(R = 0.9994).....[16]$$

$$Ip_a(\mu A) = 0.02154C(\mu molL^{-1}) + 0.8394(R = 0.9995).....[17]$$

Furthermore, and under the optimized DPV conditions, the detection limits (S/N=3) of UA on Gr/ITO and NGr/ITO electrodes were determined to be 5.9387 µM and 0.7264 µM, respectively, whereas the sensitivities of the Gr/ITO and NGr/ITO electrodes towards the detection of UA were found to be $6.29\times10^{-3}\,\mu A\mu M^{-1}cm^{-2}$ and $51.29\times10^{-3}\,\mu A\mu M^{-1}cm^{-2}$ on Gr/ITO and NGr/ITO, respectively.

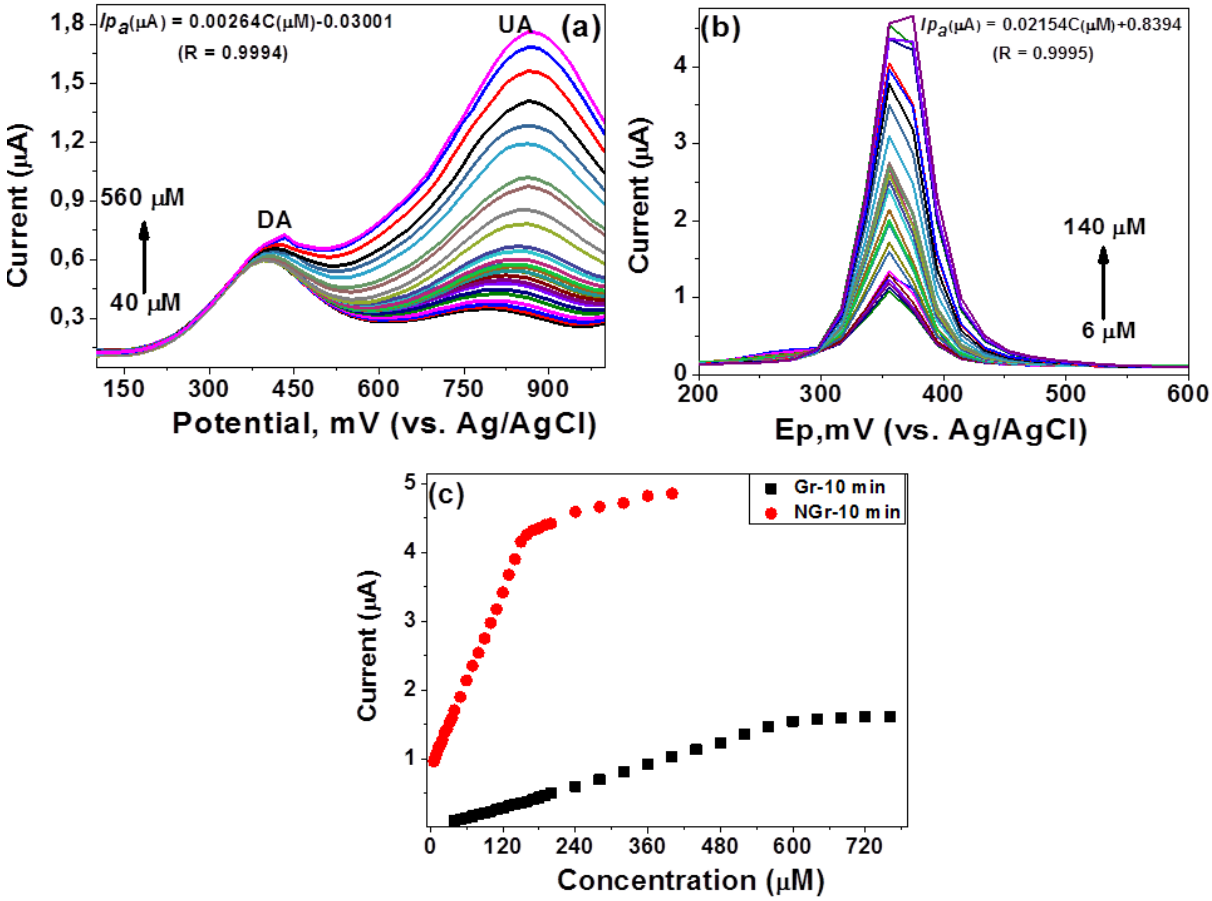

Figure 6.13: Concentration studies of UA on (a) pristine and (d) N-doped graphene modified ITO electrodes at buffer pH 6.02. (c) Linear concentration ranges of UA on pristine (black) and N-doped graphene (red) modified ITO electrodes at buffer pH 6.02.

Comparison of the electrochemical performance of our modified ITO electrodes and reported carbon-based electrodes towards the detection of uric acid was also investigated (Table 6.7). It is noteworthy to mention that very few studies on the electrochemical detection of uric acid have been performed on modified ITO electrodes. Thus, this study comprises one of the few reports that focus on the use of ITO electrodes. It can be seen that the linear range for UA at NGr/ITO (6 – 140 µM) was larger than that at ITO electrode modified with rGO-CNTs hybrids [55] and also for data reported for most of the carbon nanomaterial-based glassy carbon

electrodes. Moreover, the detection limit for UA at NGr/ITO (0.73 µM) electrode was also found to be comparable to that of other reported studies, indicating that with further improvement in the structural properties of the electrodes, lower detection limits for uric acid can be achieved. Remarkably, the linear range of UA at Gr/ITO was large, which is favourable for a good sensor. However, the large detection limit (5.94 µM) was indicative of a poor interaction between the UA molecule and the planar sp^2 conjugated carbon structure of the graphene-modified electrode.

Table 6.7: Comparison of electrocatalytical data for the determination of UA

Electrode	Linear range (µM)	Detection limit (µM)	Reference
Gr/ITO	40 -560	5.94	This study
NGr/ITO	6 - 140	0.73	This study
rGO-CNT/ITO	0.2 - 16.0	0.17	55
PGE	2.5 – 20	1.4	74
rGO/GCE	0.8 – 100	0.6	8
NGO/GCE	0.1 – 20	0.045	6
rGO/SPCE	10 – 3000	0.35	42
MWCNT/GCE	0.55 – 90	0.014	76
PLL-GO/GCE	0.5 – 20	0.031	77
NCNF/GCE	5 – 200	0.992	78

**Gr-> graphene films, ITO -> indium tin oxide, NGr -> N-doped graphene film, rGO -> reduced graphene oxide nanosheets, CNT -> carbon nanotubes, GCE -> glassy carbon electrode, NGO -> N-doped graphene oxide nanosheets, PGE -> pyrolytic graphite electrode, SPCE -> screen printed carbon electrode, MWCNT -> multiwalled carbon nanotubes, NCNF-> N-doped carbon nanofibers, PLL -> poly-L-lysine.*

6.3.8 Stability, reproducibility and repeatability of modified electrodes

To investigate the stability, differential pulse voltammograms of 0.13 mM solutions of DA and UA were recorded on modified electrodes after two weeks of storage at room temperature in ambient conditions. It was observed that a 2.4 % and 1.9 % loss of the peak current was recorded for DA, while a 5.5 % and 3.7 % were recorded for UA at the Gr/ITO and NGr/ITO electrodes, respectively. This indicates good stability for both molecules at NGr/ITO electrodes. The reproducibility was estimated from the DPVs of PBS containing 0.13 mM DA and 0.13 mM UA at five independent electrodes that were prepared in a similar

way. The relative standard deviations (RSDs) of 3.5 % and 4.7 % were obtained for DA and UA on Gr/ITO, whereas RSDs of 1.5 % and 2.3 % were obtained for DA and UA on NGr/ITO electrodes. Finally, the repeatability of the electrodes was studied by recording ten successive DPVs on the same electrode using the buffer solution (pH 6.02) containing 0.13 mM DA and UA. Satisfactory RSDs of 3.7 % and 3.5% were calculated for DA and UA on Gr/ITO, while RSDs of 1.6 % and 2.8 % were obtained for DA and UA on NGr/ITO. In summary (Table 6.8), the results indicated that NGr/ITO electrodes exhibited better stability, reproducibility and repeatability as compared to their undoped graphene counterparts.

Table 6.8: Stability, reproducibility and repeatability values of DA and UA on modified ITO

Electrode	Stability (% Loss)		Reproducibility (RSD, %)		Repeatability (RSD, %)	
	DA	**UA**	**DA**	**UA**	**DA**	**UA**
Gr/ITO	2.4	5.5	3.5	4.7	3.7	3.5
NGr/ITO	1.9	3.7	1.5	2.3	1.6	2.8

6.4 Conclusions

In summary, the study presents the use of pristine and N-doped graphene films in ITO–based electrochemical sensors for detection of DA and UA. The use of both graphene and ITO in sensing applications is due to the combination of desirable properties exhibited by both of these materials, such as the high surface-to-volume ratio, large surface area, high electrocatalytic activity, fast electron transfer kinetics, good electron conductivity and the ability to form good large area films. Raman analysis suggested the growth of high quality (I_D/I_G = 0.271) and bilayered (I_G/I_{2D} = 0.410) pristine graphene films. Furthermore, XPS data analysis showed that the N-doped graphene films had an overall N/C content of ~3.25 % and that they contained all four nitrogen configurations (i.e. graphitic-, pyrrolic-, pyridinic-N, and NO_x). The electrochemical behaviours as well as the electrochemical oxidations of DA and UA were determined to be diffusion controlled at both Gr/ITO and NGr/ITO electrodes. Under optimized DPV conditions, Gr/ITO electrode exhibited wide linear ranges, fairly reasonable stability and reproducibility, as well as good selectivity for both DA and UA. However, the Gr/ITO suffered poor sensitivity and high detection limits (S/N =3) for DA and UA, with the limits of detection determined to be 4.23 µM and 5.94 µM, respectively. Thus,

the results showed that with the observed selectivity, indicated by well-defined oxidation peak separations, and further improvements, Gr/ITO electrodes are promising candidates for simultaneous determination of DA and UA.

On the other hand, the NGr/ITO electrode exhibited reasonable linear ranges, high sensitivity, excellent long-term stability and reproducibility, as well as low detection limits (S/N =3) for DA and UA, with the limits of detection calculated to be 0.15 μM and 0.73 μM, respectively. Although the NGr/ITO electrodes suffered poor selectivity, the excellent electrocatalytic activity towards oxidation of DA and UA and observed lower overpotentials, with enhanced electrochemical response, can be attributed to the unique structural and electronic properties, as well as the increased effective surface area. XPS showed the presence of all four nitrogen configurations (i.e. graphitic-, pyrrolic-, pyridinic-N, and NO_x), thus a much more stable π-conjugated delocalised system was formed, which then led to faster electron transfer kinetics compared to bare ITO and Gr/ITO electrodes. Additionally, the good π-π and hydrogen bond interactions between DA and UA and the N-doped graphene surface led to improved electrocatalytic activity. In general, the present work provides a simple, cost-effective and environmentally friendly method for designing high performance electrochemical sensors based on N-doped graphene films on ITO electrodes, although it is apparent more work is required to their selectivity.

References

1. Wang, H. W., Y. H. Wei, H. W. Guo. *Anti-Cancer Agents in Med. Chem*., **2009**, *9*, 1012-1017.
2. Li, J., X. Q. Lin. *Sens. Actuators, B*, **2007**, *124*, 486-493.
3. Wang, Z. Y., S. N. Liu, P. Wu, C. X. Cai. *Anal. Chem*., **2009**, *81*, 1638-1645.
4. Dennis, M. A., K. Michael, M. M. Khodabakhsh, N. Stuart, W. Michael. *Anal. Chem.*, **1989**, *61*, 2603-2608.
5. Xu, H. Y., J. J. Xiao, L, Yan, L. Zhu, B. H. Liu. *J. Electroanalytical Chemistry,* **2016**¸*779*, 92-98.
6. Shen, Z. H., X. Q. Zheng, J. Y. Xu, W. J. Bao, F. B. Wang, X. H. Xia. *Biosensors and Bioelectronics*¸ **2012**¸ *34*, 125-131.
7. Christopher, B. J., P. M. Jennifer and V. B. Jill, *Anal. Chim. Acta,* **2010,** *622*, 105.
8. Annesh, P. K., S. R. Nambiar, T. P. Rao, A. Ajayaghosh. *Anal. Methods*, **2014**¸*6*, 5322-5330.

9. Wang, L., O. Huang, J. Bai, H. Wang, X. Wu, Y. Zhao. *Int. J. Electrochem. Sci.*, **2006**, *1*, 334-342.
10. Liu, G., W. Ma, Y. Luo, D. M., Sun, S. Shao. *J. Anal. Methods. Chem.*, **2014**¸ *984314*, 1-10.
11. Zhao, Y., J. Bai, L. Wang, E. XuHong, P. Huang, H. Wang, L. Zhang. *Int. J. Electrochem. Sci.*, **2006**, *1*, 363-371.
12. Ye, F., C. Feng, J. Jiang, S. Han. *Electrochim. Acta*, **2015,** *182*, 935–945.
13. Wightman, R. M., L. J. May, A. C. Michael. *Anal. Chem*., **1988**, *60*, 769A–793A.
14. Kapur, S., D. Mamo. *Prog. Neuro-Psychopharmacol. Biol. Psychiatry*, **2003**, *27*, 1081.
15. Volkow, N. D., J. S. Fowler, G. J. Wang. *Behav. Pharmacol*. **2002**, *13*, 355.
16. Kim, J. H., J. M. Auerbach, J. A. R. Gomez, I. Velasco, D. Gavin, N. Lumelsky, S. H. Lee, J. Nguyen, R. S. Pernaute, K. Bankiewicz, R. McKay. *Nature*, **2002**, *418*, 50.
17. Gowrishankar, R., M. K. Hahn, R. D. Blakely. *Neurochem. Int.* **2014**, *73*, 42–48.
18. Camardese, G., D. Giuda, M. Nicola, F. Cocciolillo, A. Giordano, L. Janiri, R. Guglielmo. *J. Psychiatr. Res.* **2014**, *51*, 7–18.
19. Abbaspour, A., A. Khajehzadeh, A. Ghaffarinejad. *Analyst*, **2009,** *134*, 1692–1698.
20. Shou, M., C. R. Ferrario, K. N. Schultz, T. E. Robinson, R. T. Kennedy, *Anal. Chem.*, **2006,** *78*, 6717–6725.
21. Chen, J. L., X.-P. Yan, K. Meng, S.-F. Wang. *Anal. Chem*., **2011,** *83*, 8787–8793.
22. Williams, K.R., B. Adhyaru, I. German and T. Russell, *J. Chem. Educ.*, **2002**, *79*, 1475.
23. Szantai, E., A. Szilagyi, A. Guttman, M. Sasvari-Szekely, Z. Ronai. *J. Chromatogr. A*, **2004**, *1053*, 241–245.
24. Swamy B. E., B. J. Venton. *Analyst*, **2007**, *132*, 876–884.
25. Huang, C., X. Chen, Y. Lu, H. Yang, W. Yang. *Biosens. Bioelectron*. **2015**, *63*, 478–482.
26. Carrera, V., E. Sabater, E. Vilanova, M .A. Sogorb. *J. Chromatogr. B.,* **2007,** *847*, 88–94.
27. Zhou, Y., H. Yan, Q. Xie, S. Huang, J. Liu, Z. Li, M. Ma, S. Yao, *Analyst*, **2013,** *138*, 7246–7253.
28. Watson, C. J., B. J. Venton, R. T. Kennedy. *Anal. Chem*. **2006,** *78*, 1391–1399.
29. Kim, Y. R., S. Bong, Y.-J. Kang, Y. Yang, R. K. Mahajan, J. S. Kim, H. Kim. *Biosens. Bioelectron.* **2010,** *25*, 2366–2369.

30. Qi, S., B. Zhao, H. Tang, X. Jiang. *Electrochim. Acta*. **2015,** *161*, 395–402.
31. Jackowska, K., P. Krysinski. *Anal. Bioanal. Chem.* **2012,** *405*, 3753–3771.
32. Niu, L. M., K. Q. Lian, H. M. Shi, Y. B. Wu, W. J. Kang, S. Y. Bi. *Sensors Actuators B Chem.* **2013,** *178*, 10–18.
33. Sajid, M. S., M. K. Nazal, M. Mansha, A. Alsharaa, S. M. S. Jillani, C. Basheer. *TrAc Trends Anal. Chem*. **2016**, *76*, 15–29.
34. Wu, L., L. Feng, J. Ren, X. Qu. *Biosens. Bioelectron*. **2012**, *34*, 57–62.
35. Liu, S., X. Xing, J. Yu, W. Lian, J. Li, M. Cui, J. Huang. *Biosens. Bioelectron*. **2012**, *36*, 186–191.
36. Dutt, V. V. S. E., H. A. Mottola. *Anal. Chem*. **1974**, *46*, 1777–1781.
37. Chen, X., G. Wu, Z. Cai, M. Oyama, X. Chen. *Microchimica Acta*, **2014,** *181*, 689–705.
38. Yu, J., S. Wang, L. Ge, S. Ge. *Biosensors and Bioelectronics*, **2011,** *26*, 3284–3289.
39. Sheng, Z. H., X. Q. Zheng, J. Y. Xu, W. J. Bao, F. B. Wang, X. H. Xia. *Biosens. Bioelectron.* **2012**, *34*, 125–131.
40. Wang, L., X. Lu, C. When, Y. Xie, L. Miao, S. Chen, H. Li, P. Li, Y. Song, *J. Mater. Chem. A*, **2015**, *3*, 608–616.
41. Cinti, S., F. Ardunini, M. Carbone, L. Sansone, I. Cacciotti, D. Moscone, G. Palleschi. *Electroanalysis* **2015**, *27*, 2230–2238.
42. Shakkthivel, P., S. Chen. *Biosens. Bioelectron*. **2007**, *22*, 1680–1687.
43. Jiang, G. T. Jiang, H. Zhou, J. Yao, X. Kong. *RSC Adv***.,** 2015, ***5*****,**9064-9068.
44. Welch, C.W., R. G. Compton. *Anal. Bioanal. Chem*. **2006**, *384*, 601–619.
45. Kalimuthu, P., S. A. John. *Talanta*, **2010**, *80*, 1686–1691.
46. Abdelwahab, A. A., Y.-B. Shim. *Sensors Actuators B Chem*. **2015,** *221*, 659–665.
47. Geim, A. K., K. S. Novoselov. *Nat. Mater.* **2007**, *6*, 183-191.
48. Novoselov, K. S., A. K. Geim, S. V. Morozov, D. Jiang, Y. Zhang, S. V. Dubonos, I. V. Grigorieva, A. A. Firsov. *Science*, **2004**, *306*, 666−669.
49. Geim, A. K. *Science*, **2009**, *324*, 1530–1534.
50. Geim, A.K., K. S. Novoselov, S. Morozov, D. Jiang, M. I. Katsnelson, S. Dubonos, I. Grigorieva, A. Firsov. *Nature*, **2005**, *438*, 197-200.
51. Pumera, M., A. Ambrosi, A. Bonanni, E. L. K. Cheng, H. L. Poh. *TrAC, Trends Anal. Chem.*, **2010**, *29*, 954.
52. Brownson, D. A. C., D. K. Kampouris, C. E. Banks. *Chem. Soc. Rev.*, **2012**, *41*, 6944.

53. Shuang, R., H. Wang, Y. Zhang, Y. Sun, L. Li, H. Zhang, Z. Shi, M. Li, M. Li. *Analyst,* **2016,** *141*, 2741-2747.
54. Yang, J., J. R. Strickler, S. Gunasekaran. *Nanoscale*, **2012,** *4*, 4594-4602.
55. Zhang, Y. Y. Ji, z. Wang, S. Liu, T. Zhang. *RSC Adv.*, **2015,** *5*, 106307-106314.
56. Thiagarajan, S., S. M. Chen, *Talanta*, **2007,***74*,212-222.
57. Grisotto, F., R. Metaye, B. Jousselme, B. Geffroy, S. Palacin, J. Charlier. *J. Mater.Chem.*, **2011,** *21*, 15962-15968.
58. Wang, Y., Y. Zheng, X. Xu, E. Dubuisson, Q. Bao, J. Lu, K. P. Loh. *ACS Nano*. **2011**, *5*, 9927-9933.
59. Ferrari, A. C., J. C. Meyer, V. Scardaci, C. Casiraghi, M. Lazzeri, F. Mauri, S. Piscanec, D. Jiang, K. S. Novoselov, S. Roth, A. K. Geim. *Phys. Rev. Lett*. **2006,** *97***,** 187401 (1-4).
60. Casiraghi, C., S. Pisana, K. S. Novoselov, A. K. Geim, A. C. Ferrari.. *Appl. Phys. Lett.* **2007,** *91***,** 233108 (1-3).
61. Ferrari, A. C. *Solid State Commun*. **2007,** *143*, 47-57.
62. Malard, L. M., M. A. Pimenta, G. Dresselhaus, M. S. Dresselhaus. *Phys. Rep.* **2009**, *473*, 51-87.
63. Xie, W., N. M. Kai, L. T. Weng, C. M. Chan. *RSC. Adv*, **2016**, *6*, 80649-80654.
64. Jansen, R. J. J., H. Vanbekkum. *Carbon*, **1995**, *33*, 1021-1027.
65. Nakayama, Y., F. Soeda, A. Ishitani. *Carbon*, **1990**, *28*, 21-26.
66. Medintz, I. L., M. H. Stewart, S. A. Trammell, K. Susumu, J. B. Delehanty, B. C. Mei, J. S. Melinger, J. B. Blanco-Canosa, P. E. Dawson, H. Mattoussi, *Nat. Mater.*, **2010,** *9*, 676-684.
67. Jayakumar, C., C. M. Magdalane, K. Kanimozhi, K. Kaviyarasu, B. Jeyaraj, *J. Nanostruct*¸**2017,** *7*, 155-164.
68. Nicholson, R. S., S. Irving. *Anal Chem.*, **1964,** *36*, 706–723.
69. Wang, X., B. JIn, X. Lin, *Anla, Sci.*, **2002,** *18*, 931-933.
70. Zhao, H., Y. Zhang, Z. Yuan, *Anal. Chim. Acta*, **2001,** *441*, 117-122.
71. Bernmann, F., V. Ball, F. d. r. Addiego, A. Ponche, M. Michel, J. J. d. A. Gracio, V. r. Toniazzo, D. Ruch, *Langmuir*, **2011,** *27*, 2819-2825.
72. Nematollahi, S. M., J. Golabi, *Electroanal. Chem*, **1996,** *405*, 133-140.
73. Goyal, R. N., V. K. Gupta, M. Oyama, N. Bachheti. *Talanta*, **2007,** *72*, 976-983.
74. Da Silva, R. P., A. W. O. Lima, S. H. P. Serrano. *Analytica Chimica Acta*, **2008**¸*612*, 89-98.

75. Yuan, D. S., X. Yuan, S. Zhou, W. Zou, T. Zhou. *RSC Adv.*, **2012,** *2*, 8157-8163.
76. Kumar, S. A., S. Ranganathan. *Anal Methods*, **2011,** *3*, 2088-2094.
77. Zhang, Y., W. Lei, Y. Xu, X. Xia, Q. Hao. *Nanomaterials*, **2016,** *6*, 1-17.
78. Sun, J., L. Li, X. Zhang, D. Liu, S. Lv, D. Zhu, T. Wu, T. You. *RSC Adv.*, **2015, *5,*** 11925-11932.

Chapter 7

Electrochemical behaviour and detection of dopamine and uric acid over Pt and Pd- graphene/ITO composites

7.1 Introduction

Dopamine (4-(2-aminoethyl) benzene-1,2-diol, DA) and uric acid (2,6,8-trihydroxypurine, UA) are biomolecules that play very vital roles in the human body (Scheme 7.1a and b). Both DA and UA coexist in biological matrixes of the human body, such as blood, urine as well as extracellular fluids. As a member of the catecholamine family that is produced in the brain and kidneys, DA is an important neurotransmitter in the mammalian renal, hormonal, cardiovascular, and central nervous systems. Recent research reports have suggested that DA plays a significant role in the treatment of depression and Alzheimer's disease [1]. Additionally, abnormal concentrations of DA are linked to neurological disorders such as schizophrenia, epilepsy, phenylketonuria, Huntington's disease, attention deficiency hyperactivity disorder (ADHD), as well as loss of muscle control (Parkinson's syndrome) [2-8]. Thus, restoration of DA levels in the human body is important for control or elimination of various neurological disorders as well as for providing the development of pharmaceutical drugs for therapeutic purposes. On the other hand, uric acid (UA, scheme 7.1b) is the primary end metabolic product of purine metabolism that is produced in mammalian blood and serum, and excreted from the human body in urine and sweat. Similarly, an abnormal concentration of UA in the human body is related to various diseases such as arthritis, gout, hyperuricemia, kidney lesion, gouty nephropathy, anaemia, and Lesch-Nyhan syndrome [9-12]. Therefore, accurate detection of UA in the human blood or urine has great clinical importance since it is a powerful indicator for the diagnosis of several diseases. As both DA and UA coexist in biological samples, for clinical diagnosis and treatment of the aforementioned diseases, determination of DA and UA with satisfactory accuracy, low limits of detection and the high sensitivity is critically important.

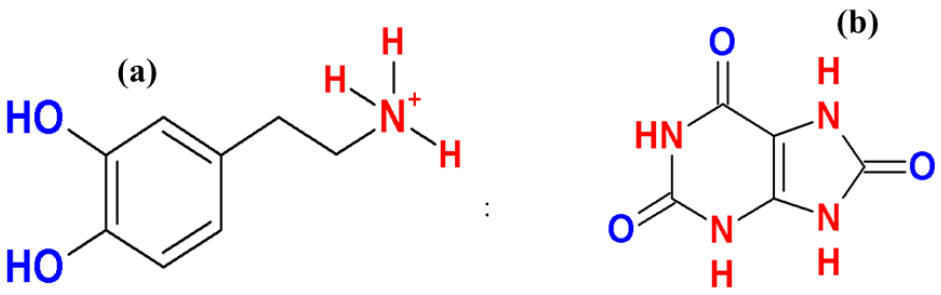

Scheme 7.1: Schematic representations of (a) dopamine, DA, and (b) uric acid, UA.

Due to the bioactivity of DA and UA, electroanalytical or electrochemical techniques have attracted great attention as promising techniques for the determination of biomolecules [9-22]. This is because electrochemical methods offer numerous advantages over other techniques in terms of quick responses, low cost, high sensitivity, ease of handling and ease of fabrication of the electrochemical sensors as well as relatively cheaper instrumentation [12-22]. However, the major drawback for accurate detection of DA and UA on traditional electrodes, such as the bare glassy carbon electrode (GCE), is the overlapping oxidation peaks for both biomolecules due to similar heterogeneous electron transfer kinetics [15-22]. Additionally, fouling of the traditional electrodes by either oxidation and/or reduction products from the electrocatalytic oxidation of these biomolecules (DA and/or UA) contribute largely to some disadvantages of the electrochemical techniques [21, 22]. Thus, it is essential that the development of simple, selective and highly sensitive voltammetric techniques for the determination of DA and UA is a necessity. As a result, a variety of biologically compatible materials, such carbon-based nanomaterials [23], metal and metal oxide nanoparticles [24], quantum dots [25], magnetic nanoparticles [26], and polymeric nanoparticles [27], have been used to modify the electrode surface of electrochemical sensors employed in the selective and sensitive determination of DA and UA. Among them, carbon-based nanomaterials have been intensively studied as excellent candidate materials for electrode modifiers due to their extraordinary properties such as good biocompatibility with amino acids and proteins, chemical stability and excellent catalytic activity [28].

Recently, graphene, an atom-thick two-dimensional (2D) allotrope of carbon in the form of sp^2-hybridized carbon atoms in a honey-comb lattice, has attracted tremendous attention due to its unique structural and physiochemical properties, including large specific surface area, excellent thermal conductivity, and ultrahigh electric conductivity, high mechanical strength, and excellent chemical, thermal and electrochemical stability [29-32]. As a result, these unique

properties make graphene and its derivatives promising materials to be used for modifying different electrode surfaces for applications in the determination of electroactive biomolecules such as dopamine and uric acid [27, 33, 34]. For instance, recent research reports have indicated that traditional glassy carbon electrodes modified with graphene exhibited an enhanced electrocatalytic activity, and accelerated electron transfer rates resulting in increase in the electrical conductivity [16, 27, 28, 35]. The graphene-modified electrodes also demonstrated excellent potential for wide applications in the individual and simultaneous detection of various biomolecules [27, 33-35]. In addition to its high electrochemical stability, the structural properties, specifically the presence of edge- and plain-like defects within its lattice have made graphene a good support to immobilize noble metal nanoparticles in various applications such as catalysis, biomedicine, fine chemicals, and sensors [36-40].

Reports have indicated that composites of noble metal nanoparticles and graphene are receiving great attention in various fileds such as in the chemical and biosensors fabrication [36-40]. This is due to the excellent electronic, optical, and magnetic properties as well as the high effective surface area of metal nanoparticles which are very different from their bulk materials. Moreover, noble metal nanoparticles are used in electrochemical sensors to enhance the heterogeneous electron transfer kinetics as well as to increase the sensitive and selective determination of bioactive molecules. For instance, Wang *et al.* developed an electrochemical sensor based on cubic palladium (c-Pd) nanoparticles immobilized on reduced graphene oxide (rGO) nanosheets [43]. Their c-Pd/rGO composite, which was assembled on the surface of the GCE, exhibited good sensitivity, reasonable selectivity and an outstanding stability towards the determination of dopamine and uric acid. Moreover, Sun and co-workers reported that platinum (Pt) nanoparticles supported on reduced graphene oxide nanosheets led to the development of the GCE-based electrodes with excellent sensitivity and selectivity for the electrocatalytic oxidation of dopamine and uric acid [44]. The electrochemical responses of the composites of the noble metal nanoparticles and graphene were attributed to the synergetic effects of graphene and the nanoparticles such as: (1) the ability of graphene to facilitate good dispersion of the nanoparticles, thus resulting in increased surface area; and (2) the ability of graphene to facilitate the electrocatalytic oxidation of the DA and/or UA on its edge- and plane-like binding sites, hence making detection of DA and/or UA easier and faster.

Although, electrochemical sensors based on graphene-metal composites exhibit promising potential applications, most of these sensors suffer major drawbacks in terms of

biocompatibility and sensitivity as a result of the properties of the support material. Consequently, tailoring of the intrinsic properties of graphene by doping with nitrogen atoms or functionalization with nitrogen containing compounds has been found to be an excellent method for enhancing the electrocatalytic performance of graphene-based sensors. For example, Brownson *et al.* showed that glassy carbon electrode (GCE) modified nitrogen doped graphene nanosheets exhibited an enhanced electrocatalytic activity towards the oxidation of ascorbic acid, dopamine, and uric acid in comparison with the bare and the undoped graphene modified-GCE [34]. Han *et al.* reported that modification of the GCE with chitosan-functionalized graphene showed excellent sensitivity and selectivity towards the electrocatalytic oxidation of dopamine, uric acid and ascorbic acid [45]. Furthermore, Wu *et al.* indicated that the presence of nitrogen active sites in a porphyrin-functionalized graphene resulted in highly selective and sensitive sensors for the detection of dopamine [46]. These research reports, and many more in the literature, highlight that the enhanced biocompatibility and sensitivity of nitrogen doped graphene in electrochemical sensors can be attributed to the presence of nitrogen atoms which provide a large amount of edge- and plane-like binding sites for biomolecules [12-23]. As the incorporation of nitrogen atoms into the lattice of carbon nanostructures leads to creation of large amount of edge- and plane-like defect sites, N-doped graphene has also been employed as a good support for immobilizing noble metal nanoparticles in various applications. For instance, a glassy carbon electrode modified with palladium (Pd) nanoparticles supported on nitrogen doped graphene nanosheets showed enhanced electrocatalytic oxidation and selective detection of dopamine, ascorbic acid and uric acid [47].

In this work, the electrochemical determination of dopamine and uric acid was performed on electrochemical sensors based on indium tin oxide electrodes modified with Pt and Pd nanoparticles supported on pristine and N–doped graphene films. To investigate the influence of the as-synthesized graphene-metal nanoparticle composite on the electrochemical detection processes of DA and UA, as the intuitionistic parameter of the electrocatalytic process on the electrode surface, was carried out using cyclic and differential pulse voltammetric techniques. Therefore, the electrochemical behaviour of DA and UA at the modified ITO electrodes was carefully investigated and the electrochemical parameters of each biomolecule were determined. As a result, the objective of the study was to investigate the interaction of each biomolecule with the electrode surface modified with composite materials, as well as to determine the influence of the presence of each metal nanoparticle on

the electrochemical responses of DA and UA. This is because theoretical studies have shown that Pt and Pd show different binding behaviour on the surface of graphene, with Pt showing a weak physisorption binding energy of < 0.5 eV and Pd demonstrating a strong chemisorption binding energy of > 0.8 eV [45]. Finally, the study illustrates for the first time the use of the electroless deposition of metal nanoparticles on APCVD-grown graphene surfaces, their successful deposition on the ITO electrodes, as well as their successful application in electrochemical sensors.

7.2 Experimental

7.2.1 Apparatus and reagents

Dopamine hydrochloride (DA, ≥ 99%), uric acid (UA, ≥ 99%), sodium hydroxide pellets (98%, Merk), potassium dihydrogen phosphate (KH_2PO_4, 99.99%), hydrochloric acid (HCl, 32.0 w/v %), potassium ferricyanide ($K_3[Fe(CN)_6]$, Merck, 99.98%), sodium palladium chloride (Na_2PdCl_4, 99.98%), hexachloroplatinic (IV) acid hydrate (H_2PtCl_6 xH_2O, 98.99%), potassium chloride (KCl, Merck, 98.5%) and poly(methyl methacrylate) (PMMA, Mw ~999 000) were purchased from Sigma-Aldrich, South Africa. The indium tin oxide (ITO)-coated glass slides (surface resistance 30 to 60 Ω/sq., thickness 1.1 mm, and optical transmittance of > 84%, refractive index of 1.517) and copper foils (25 µm, 99.98%) were also received from Sigma-Aldrich, South Africa. The gases used included Ar (99%), CH_4 (99.98%), NH_3 (10% in Ar), N_2 (99.98%) and H_2 (99.98 %), and these were supplied by Afrox, South Africa. All other reagents were of analytical grade and were used without prior purification. For the voltammetric experiments, deionized, high-quality water (>18.2 $M\Omega.cm^2$) was used and it was purified through a Millipore ultrapure (type 1) water system (Bedford, MA, USA). A $K_3[Fe(CN)_6]$ stock solution (4 mM) was prepared with 1.0 M KCl. 0.05 mM Pt and Pd standard solutions were prepared by dilution of appropriate volumes of their stock solutions with 0.1 M HCl. Stock solutions of DA (4 mM) and UA (4 mM) were prepared in 0.1 M phosphate buffer solution ((PBS) at pH 6.02. The PBS was prepared by dissolving KH_2PO_4 in deionized water and the pH was adjusted by addition of 0.1 M NaOH or 0.1 M HCl solutions. Fresh solutions of DA and UA were prepared daily. Other standard solutions of DA and UA were prepared by appropriate dilutions of the stock solutions in PBS.

7.2.2 Instrumentation and characterization

The topological information of the films was acquired using a JEM 2800 scanning transmission electron microscope (STEM) operating at 200 kV with 70 and 40 µm C2

apertures. The compositional analysis of the films was determined by X-ray emission detection in the scanning mode, while the dark-field imaging was performed in scanning mode using an off-axis annular detectorfor the high angle annular dark field scanning transmission electron microscopy (HAADF-STEM) analysis. The atomic composition and degree of doping of the electrode modifying materials were characterised by a Thermo Escalab 250 X-ray photoelectron spectroscopy (XPS), using a monochromatised aluminium Kα radiation with a 650 μm spot size to maximise signal. Charge compensation was provided by an in-lens electron flood gun and separate low-energy argon ion source. Electrochemical measurements (i.e. cyclic voltammetry (CV) and differential pulse voltammetry (DPV)) were performed using a μAutolab potentiostat/galvanostat, running with the GPES software (version 4.900B) from Eco Chemie (Utrecht, Netherlands). The conventional three-electrode cell consisted of an Ag/AgCl (3 M KCl) reference electrode, a platinum wire auxilliary electrode, and a working electrode (geometric area = 0.42 cm^2) made from the modified ITO-coated glass. All potentials are reported against the Ag/AgCl reference electrode. The pH measurements of the PBS were performed on a Eutech Instruments bench pH/ion/mV-meter (Model pH/ion 510, Singapore).

7.2.3 Preparation of electrodes and procedure

Pristine and N-doped graphene films were grown on a copper foil in a quartz tube furnace using APCVD. Pristine graphene films were grown using 10 sccm CH_4, 3 sccm H_2, 300 sccm Ar, while N-doped films were synthesized by introducing both 10 sccm CH_4 and 5 sccm NH_3 during the growth process [48]. For preparation of the modified electrodes, the deposition of Pt and Pd nanoparticles on the as-grown graphene films was performed by electroless deposition using copper substratre as the reducing agent [49]. The electroless process depends on the reduction potential of metal on interest to be higher than that of coper (+0.34 V). The films were immersed in similar concentration (0.05 mM) of Pt and Pd salt solutions for 30 sec, rinsed with ionised water and were then transferred onto the ITO-coated glass, using the PMMA assisted electrochemical delamination method[50] (see Scheme 3.2). The ITO-coated glass was cut to 0.60 cm × 0.70 cm and was sonicated in a solution mixture of acetone, ethanol and distilled water, after which the floating PMMA/graphene film was transferred onto the electrode. PMMA was then dissolved with acetone and the modified electrode was cleaned lightly with multiple volumes of methanol and water. The samples were labelled as Pt/Gr, Pd/Gr, Pt/NGr, and Pd/NGr for ITO electrodes modified with pristine and N-doped graphene films decorated with platinum and palladium nanoparticles, respectively.

In a typical experimental measurement, 20.0 mL of 0.1 M PBS (pH 6.02) as supporting electrolyte in a three-electrode cell was deoxygenated by purging with nitrogen gas for 30 min. The cyclic voltammograms were recorded by scanning two cycles between -1.0 V and 1.0 V at the step potential of 0.004889 V. The operating parameters for obtaining the quantitative analysis of the analytes (DA and UA) by DPV were set as follows: modulation amplitude of 25.05 mV, initial potential of -0.25 V, end potential of 1.0 V, step increment potential of 1.95 mV, and sensitivity of 100 nA/V. Electrochemical behaviour and voltammetric detection of DA and UA, either as individual or in mixed solutions, were obtained by addition of a defined volume of the respective stock solution to the electrochemical cell. The detection limit (DL) was determined as follows, $DL = \frac{3\sigma}{s}$, where σ is the standard deviation of three measurements of low concentrations, and *s* is the slope of the linear relationship plot of Ipa vs. concentration (C) [51]. Furthermore, the sensitivities of the modified electrodes were calculated by dividing the slope of the calibration curve by the geometrical area of the electrode (0.42 cm^2) [52].

7.3 Results and discussion

7.3.1 Morphology analysis of the electrode material

The morphologies of the platinum and palladium nanoparticles immobilized on pristine and N-doped graphene films were characterized using transmission electron microscopy (TEM), as shown in figure 7.1. Low magnification TEM images (Figs. 7.1 a-d) show that the samples are comprised of randomly dispersed clusters of nanoparticles, with the averages sizes of 29 ± 9 nm (Pt-Gr), 54 ±13 nm (Pd-Gr), 36 ± 11 nm (Pt-NGr), and 21 ± 6 nm (Pd-NGr). High resolution TEM images (Figs. 7.1 e-h) showed that the clusters are formed from individual nanoparticles with the averages sizes of 5 ± 3 nm (Pt-Gr), 22 ± 7 nm (Pd-Gr), 3 ± 1 nm (Pt-NGr), and 7 ± 3 nm (Pd-NGr). Interestingly, Pt and Pd nanoparticles supported on N-graphene exhibited better dispersion than nanoparticles supported on pristine graphene films. Formation of nanoclusters can be attributed to the electroless deposition method, which was used to immobilize the nanoparticles on graphene samples. During the deposition technique, nucleation and ultimately the sizes of the nanoparticles is governed by numerous factors. These can include the concentration of the salt solution, immersion time, as well as the structural properties of graphene, in terms of the amount of nucleation sites [49, 53-54]. For

instance, more nucleation sites on the graphene in the form of defects (i.e. vacancies, edges, folds or nitrogen atoms) provide more anchoring sites for nucleation and growth of metal nanoparticles [12-23]. Thus, the presence of fewer defects, as in the case of the pristine graphene which exhibited a very low defect density ratio (I_D/I_G = 0.271, see chapter 4), results in aggregation and growth of bigger nanoparticles via the seed-initiated growth mechanism [55]. However, on the surface of N-graphene, there is an increase in the amount of defects, as indicated by the large value of the defect density ratio (I_D/I_G = 1.086, chapter 5); hence resulting in nucleation of smaller nanoparticles with satisfactory dispersion. Moreover, the increased electron density due to the incorporation of nitrogen atoms could have facilitated faster reduction of the ionic forms of Pt and Pd into the metallic form.

Elemental mapping images from the high angle annular dark field scanning transmission electron microscopy (HAADF-STEM) analysis and the corresponding scanning profiles of the nanoclusters (Figs. S7.1- S7.4) illustrated the homogenous distribution of Pt and Pd throughout the clusters. However, the presence of the unreduced forms of the platinum and palladium salts is indicated by the sodium and/or chloride scanning profiles. In summary, the HAADF-STEM elemental mapping images suggest the presence of different oxidation phases of platinum and/or palladium nanostructures.

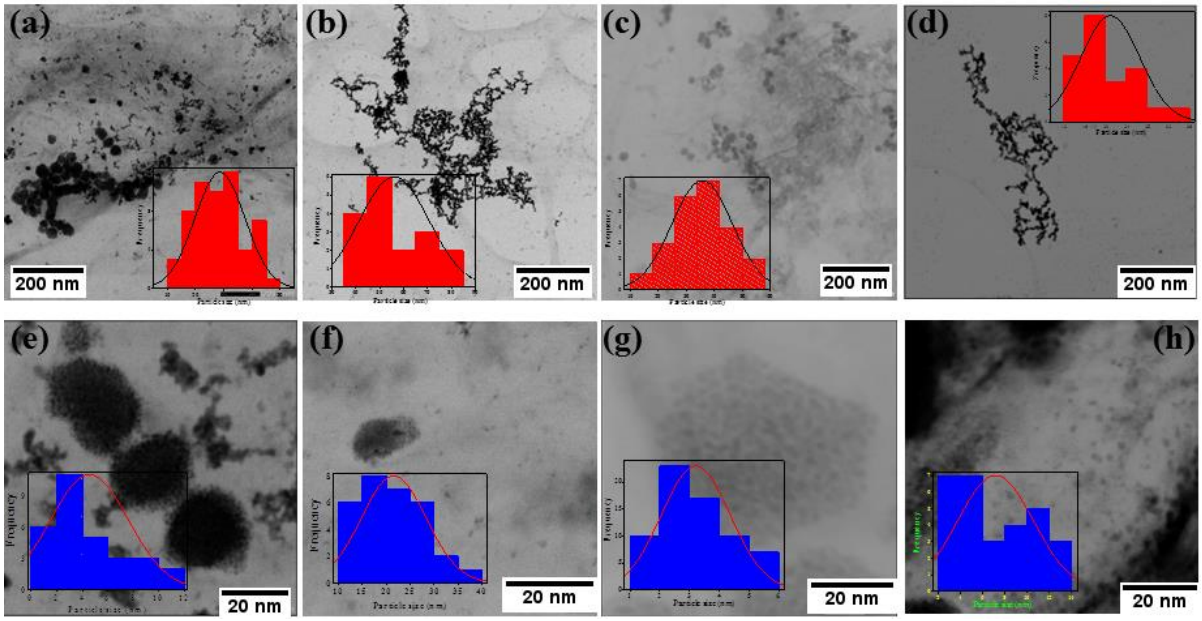

Figure 7.1: (a) – (d) Low magnification TEM and (e) – (h) High resolution TEM images of pristine and N-doped films decorated with Pt and Pd nanoparticles.

The surface elemental compositions (at. %) of the graphene-metal nanoparticle composites as well as the oxidation states of the metal nanoparticles were determined using X-ray photoelectron spectroscopy (XPS) analysis. The XPS survey analysis of the composites showed peaks corresponding to carbon (C1s = ~283.5 eV), nitrogen (N1s = ~398.4 eV), palladium (Pd3d = ~335.6 eV), platinum (Pt4f = ~71.5 eV), oxygen (O1s = ~ 530.5 eV), and copper (Cu2p = ~932.5 eV). The atomic percentages of the constituent elements in each composite are listed in table 7.1. It can be observed that the elemental compositions of the composites varied slightly with those of the non-composites graphene films. Notably, the oxygen content increased on the metal composite films, and this can be ascribed to the presence of the oxide layers on the metal nanoparticles.

Table 7.1: Atomic compositions of pristine, N-doped, as well as Pt and Pd-graphene/N-graphene composites

Samples	Elements (at. %)					
	C	**N**	**O**	**Pt**	**Pd**	**Cu[a]**
Gr	85.1	-	10.5	-	-	4.40
NGr	69.5	2.26	17.3	-	-	10.9
Pt-Gr	80.6	-	11.5	0.34	-	7.64
Pd-Gr	75.9	-	13.9	-	0.42	9.88
Pt-NGr	68.9	1.87	25.1	0.23	-	3.87
Pd-NGr	67.6	1.66	24.8	-	0.12	5.82

[a]*Cu -> from the copper foil*

The different oxidation of Pt and Pd were determined by peak fitting of the high resolution Pt4f and Pd3d XPS spectra (Figs. 7.2 c and d), and the positions of the component peaks are listed in table 7.2. Furthermore, the different bonding states for carbon, nitrogen and oxygen atoms were determined by deconvolution of the C1s, N1s and O1s spectra, respectively. Deconvolution of the C1s spectra (Fig. 7.2a) resulted into peak fitting with at least five component peaks corresponding to sp^2C-C (284.0 – 284.1), sp^2N-C/ sp^3C-C (284.8 – 285.1 eV), sp^3N-C (285.5 – 285.7 eV), C=O (286.2 – 286.5 eV), and O-C=O (288.1 – 288.4 eV) bonds [48, 56-63]. Moreover, peak fitting of the N1s spectra (Fig.7.2b) revealed four component peaks attributed to pyridinic-N (398.1 – 398.6 eV), pyrrolic-N (399.2 – 399.5 eV),

substitutional/graphitic-N (400.1 – 400.4 eV), and the oxidised pyridinic-N (NO_x, 401. 8 eV) [48, 56-63].

Analysis of the high-resolution Pt 4f spectra (Fig. 7.2c) showed a doublet structure with peaks corresponding to the Pt $4f_{7/2}$ and Pt $4d_{5/2}$ spin states [44]. For both Pt-Gr and Pt-NGr composite samples, the peaks for each spin states are fitted with three component peaks indicating the presence of metallic Pt, platinum oxide (PtO) and platinum hydroxide ($Pt(OH)_4$) phases. From peak fitting of the Pt 4f spin states, the peaks representing the metallic Pt phase are located at 70.9 – 71.2 eV (Pt^0 $4f_{7/2}$) and 71.8 – 72.4 eV (Pt^0 $4f_{5/2}$) [44]. Furthermore, extra peaks corresponding to the platinum oxide (PtO, Pt^{2+}) and hydrated platinum (Pt^{4+}) phases are observed at 73.3 – 73.2 eV (Pt^{2+} $4f_{7/2}$), 75.1 – 75.4 eV (Pt^{2+} $4f_{5/2}$), 76.1 eV (Pt^{4+} $4f_{7/2}$) and 77.2 eV (Pt^{4+} $4f_{5/2}$) binding energies [44].

In the Pd-Gr and Pd-NGr samples, the high resolution XPS spectra of Pd 3d (Fig. 7.2d) also revealed a doublet structure with two peaks representing the presence of Pd $3d_{5/2}$ and Pd $3d_{3/2}$ spin states located at ~335 eV and ~340 eV, respectively [43]. Similarly, the peaks for each spin states are fitted with three component peaks indicating the presence of metallic Pd, palladium oxide (PdO) and palladium hydroxide ($Pd(OH)_4$) phases [43]. The metallic Pd phase is represented by a pair of peaks at 334.8 – 335.1 eV (Pd^0 $3d_{5/2}$) and 340.1 – 340.3 eV (Pd^0 $3d_{3/2}$); while the PdO phase is represented by a pair of peaks at 336.6 – 336.7 eV (Pd^{2+} $3d_{5/2}$) and 341.9 – 342.1 eV (Pd^{2+} $3d_{3/2}$); and finally the $Pd(OH)_4$ is represented by a pair of peaks at 337.2 – 337.7 eV (Pd^{4+} $3d_{5/2}$) and 343.2 – 343.7 eV (Pd^{4+} $3d_{3/2}$) [43]. Notably, the relative concentrations of the peaks corresponding to metallic Pd and Pt were larger for the N-doped graphene composite in comparison with the pristine graphene composites. The results indicated that there is an efficient reduction of ionic platinum and/or palladium into their metallic phases on the N-doped graphene surface, which can be attributed to the increased electron density due to the presence of nitrogen atoms. The ease of reducibility of the metal nanoparticles on the N-doped graphene surface was further indicated by the decrease of the relative concentrations of the Pt (II)/Pd (II) and Pt (IV)/Pd (IV) phases. The relative concetrations of different oxidation states of Pt and Pd nanoparticles on pristine and N-doped graphene films are shown tables S7.1 and S7.2, respctivley.

The analysis of the O1s core-shell XPS spectra of the Pt- and Pd-graphene and N-graphene composites was used to determine the bonding states of oxygen atoms. Figure S7.6 illustrates that the high resolution O1s XPS spectra were fitted with three component peaks, centred at

~531 eV, ~532 eV, and ~534 eV. The peaks located at 530.8 – 531.9eV are ascribed to the to the oxide layer on the surfaces of Pt and Pd nanoparticles, respectively [43, 44] The binding energy corresponding to the Pd $3p_{3/2}$ spin state [43] was observed at 532.1 – 532.5 eV. Finally, the component peaks at higher binding energies (533.8 – 534.1 eV) can be assigned to the oxygen atoms, especially carboxyl groups, bonded to the graphene support [48, 56-63].

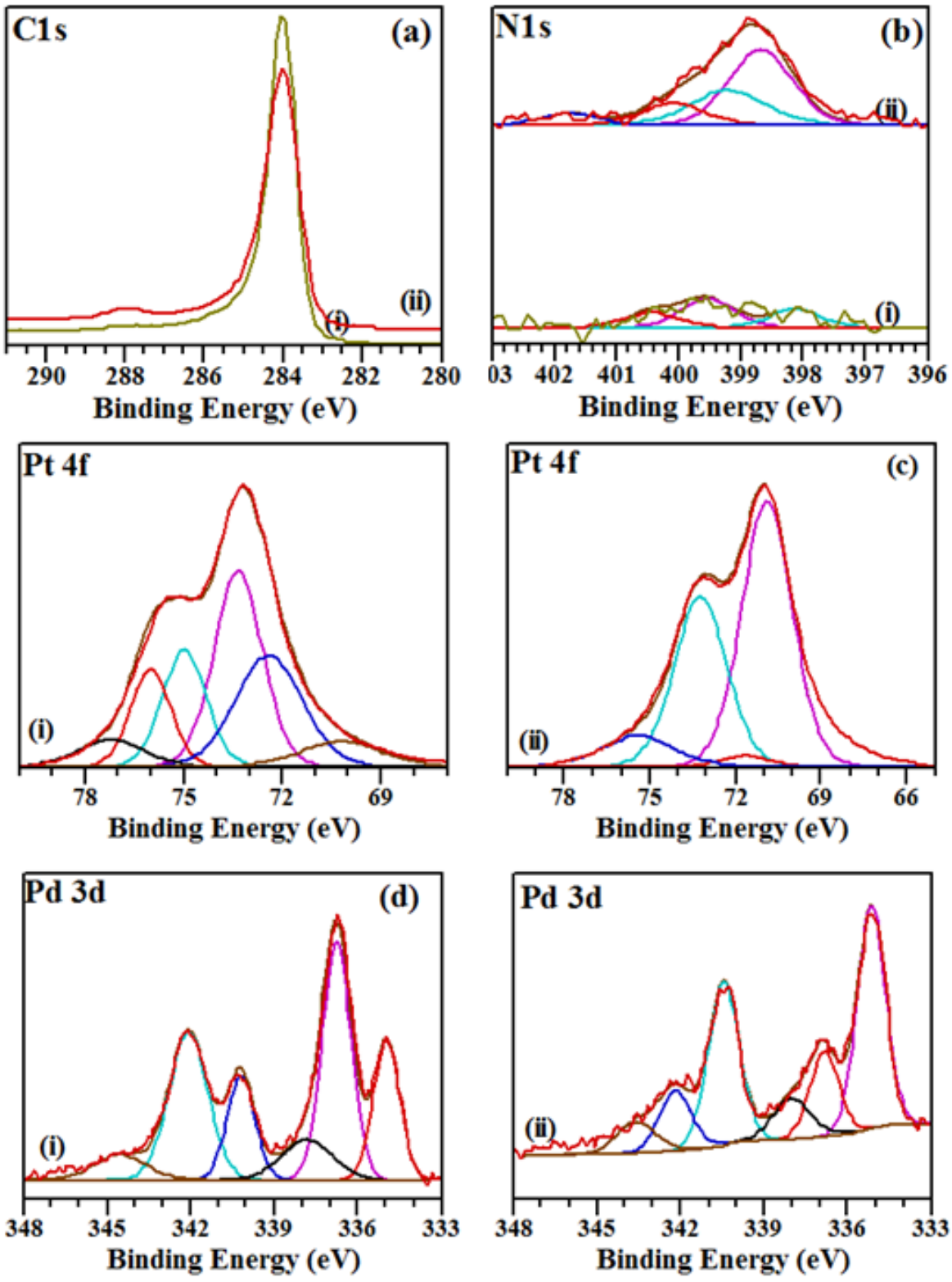

Figure 7.2: Core-shell XPS spectra of (a) C1s, (b) N1s, (c) Pt 4f, and (d) Pd 3d for the composites of (i) pristine (ii) N-doped graphene films.

Table 7.2: Peak positions for the oxidation states of Pt on the graphene/N-graphene composites

Sample	Positions of Pd oxidation states (eV)					
	Pt $4f_{7/2}$			Pt $4f_{5/2}$		
	Pt^0	Pt^{2+}	Pt^{4+}	Pt^0	Pt^{2+}	Pt^{4+}
Pt-Gr	70.9	73.3	76.1	71.8	75.1	77.2
Pt-NGr	71.2	73.2	-	72.4	75.4	-

Table 7.3: Peak positions for the oxidation states of Pd on the graphene/N-graphene composites

Sample	Positions of Pd oxidation states (eV)					
	Pd $3d_{5/2}$			Pd $3d_{3/2}$		
	Pd^0	Pd^{2+}	Pd^{4+}	Pd^0	Pd^{2+}	Pd^{4+}
Pd-Gr	334.8	336.6	337.2	340.1	341.9	343.7
Pd-NGr	335.1	336.7	337.7	340.3	342.1	343.2

7.3.2 Electrochemical behaviour of the modified electrodes

The electrochemical activity of the graphene-metal nanoparticle composite-based ITO electrodes/sensors was studied by investigating the cyclic voltammetric responses for the electrocatalytic reactions of the $[Fe(CN)_6]^{3-/4-}$ redox couple. Figure 7.3 shows the CVs of unmodified and modified ITO electrodes in 4.0 mM potassium ferricyanide solution at a scan rate of 50 mV s^{-1}. At the bare ITO electrode, the oxidation peak ascribed to the oxidation of $[Fe(CN)_6]^{4-}$ and the reduction peak attributed to reduction of $[Fe(CN)_6]^{3-}$ were observed at 363.6 mV and 197.3 mV, respectively. The oxidation peak potential (ΔEp) of 166.3 mV (Table 7.4) indicated a quasi-reversible reaction for the $[Fe(CN)_6]^{3-/4-}$ redox couple at the bare ITO electrode. Upon modification with graphene-metal nanoparticle composites, different voltammetric responses were observed. For instance, the Pt/Gr/ITO electrode exhibited

enhancement in both anodic (Ipa = 114.2 µA) and cathodic (Ipc = -129.5 µA) peak currents in comparison to the anodic peak currents of 81.8 µA, 72.1 µA, µA, 89.7 µA, and 98.9 µA as well as cathodic peak currents of -89.3 µA, -82.2 µA, -101.4 µA, -108.2 µA for Pd/Gr/ITO, Pt/NGr/ITO, Pd/NGr/ITO and bare ITO electrode respectively. The enhanced peak currents for the Pt/Gr/ITO electrode indicates that this sensor has the best electrochemical activity towards the $[Fe(CN)_6]^{3-/4-}$ redox couple. On the other hand, the decreased current responses of Pd/Gr/ITO, Pt/NGr/ITO, and Pd/NGr/ITO electrodes versus the bare ITO electrode can be attributed to the presence of oxygen functional groups on the graphene films, which repelled the negatively charged ferricyanide molecules.

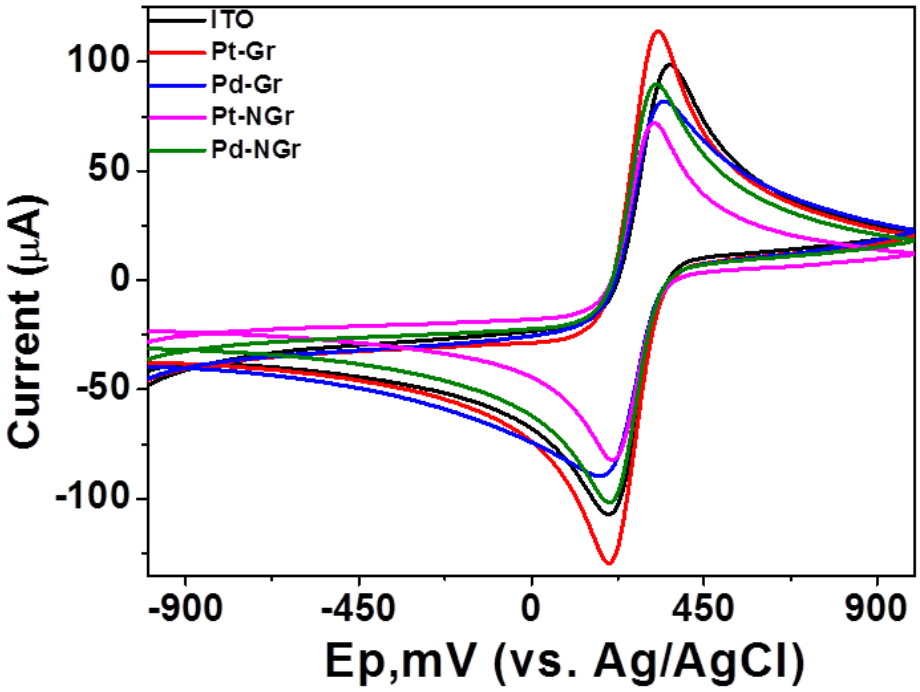

Figure 7.3: Electrochemical behaviour of $[Fe(CN)_6]^{3-/-4}$ on bare and modified ITO electrodes at scan rate of 50 mV s^{-1}.

Meanwhile, a narrower peak-to-peak separation (ΔEp = 109.2 mV, Table 7.4) is observed for the Pt/NGr/ITO electrode, suggesting a much higher efficiency for electron transfer at the interface of the Pt/NGr/ITO electrode in comparison with the other three electrodes. The results thus indicate improved electrochemical activity due an increased number of active sites provided by both nitrogen atoms and the smaller platinum nanoparticles. Furthermore, the excellent conductivity of both N-doped graphene films and the platinum nanoparticles contribute to an accelerated electron transfer rate between the $[Fe(CN)_6]^{3-/4-}$ redox couple and the Pt/NGr/ITO electrode surface. Similarly, the Pd/NGr/ITO electrode exhibited a narrower

peak-to-peak separation (ΔEp = 122.4 mV, Table 7.4) when compared with its undoped counterpart (i.e. Pd/Gr/ITO, ΔEp = 228.6, Table 7.4). In general, the results indicated that the presence of both nitrogen atoms and metal nanoparticles on the electrode surface greatly enhanced the electrocatalytic activity of the $[Fe(CN)_6]^{3-/4-}$ redox couple. Thus for good sensing applications, a composite made from Pt and/or Pd nanoparticles and N-graphene films should be a better candidate for modifying the electrode surface.

Table 7.4: Peak potentials and currents of $[Fe(CN)6]^{3-/-4}$ on bare and modified ITO electrodes at scan rate of 50 mV $^{s-1}$

Sample	Ep (mV)		Ip (μA)		ΔE
	Ep_a	Ep_c	Ip_a	Ip_c	
ITO	363.6	197.3	98.89	-108.2	166.3
Gr	341.3	215.7	95.71	-112.7	125.6
NGr	355.1	250.5	198.7	-287.2	156.4
Pt-Gr	330.2	201.4	114.2	-129.5	128.8
Pd-Gr	346.1	177.5	81.78	-89.31	228.6
Pt-NGr	320.2	211.0	72.11	-82.21	109.2
Pd-NGr	326.0	203.6	89.67	-101.4	122.4

7.3.3 Cyclic voltammetric detection of DA and UA

The electrocatalytic activities of the bare and modified ITO electrodes were investigated towards the reduction and oxidation of dopamine (DA) and uric acid (UA) using cyclic voltammetry. The corresponding CVs of 0.13 mM solutions of DA and UA (Figs. 7.4a and b) in 0.1 M phosphate buffer solution of pH = 6.02 at scan rate 50 mV s^{-1} at bare and modified ITO electrodes. For comparison purposes, the peak potential and currents for the non-composite ITO electrodes are listed in Table 7.5 for the voltammetric responses of DA and UA. From figure 7.4 (a), the oxidation peak currents for DA are observed to be 6.939 μA, 6.126 μA, 9.304 μA, and 10.67 μA, whereas the reduction peak currents are observed at 3.579 μA, 3.337 μA, 4.573 μA, and 5.839 μA for the redox reaction of DA at the surface of

Pt/Gr, Pd/Gr, Pt/NGr, and Pd/NGr modified electrodes, respectively. The significantly greater/larger oxidation peak currents at the Pt/NGr/ITO and Pd/NGr/ITO electrodes demonstrated enhanced electrocatalytic activity toward the oxidation of DA. This can be attributed to the unique characteristics of the electrode material such as superior electron conductivity contributed by both metal nanoparticles and N-atoms, the large amount of edge- and plane defects due to the incorporation of nitrogen atoms, and the increased surface to volume ratio of the nanoparticles.

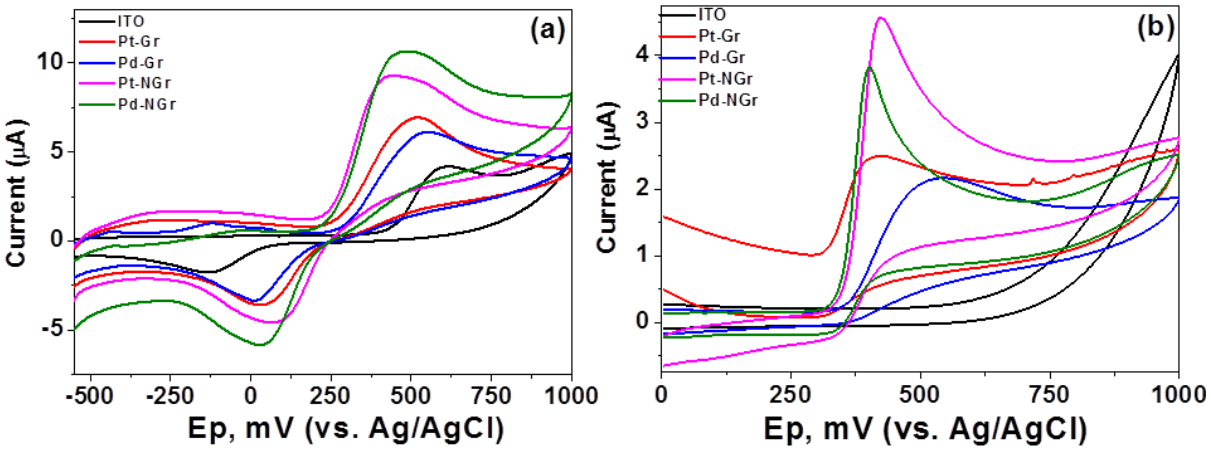

Figure 7.4: Electrochemical behaviour of (a) DA and (b) UA on bare and modified ITO electrodes at buffer pH 6.02 at scan rate of 50 mVs^{-1}.

Oxidation peak potentials corresponding to the oxidation of DA into an open-chain quinine (dopaquinone) [64], were observed at 520.1 mV, 553.1 mV, 443.3 mV, and 488.9 mV on the electrode surfaces of Pt/Gr, Pd/Gr, Pt/NGr, and Pd/NGr, respectively. Moreover, the reduction peak potentials indicating the reduction of the quinine back to DA (Scheme 7.2) were observed at 29.11 mV, 10.72 mV, 65.90 mV, and 28.44 mV for the redox reaction occurring for DA at the surface of Pt/Gr, Pd/Gr, Pt/NGr, and Pd/NGr modified electrodes, respectively. The electrocatalytic performance of the modified electrodes was investigated by determining the values of the peak potential separations (ΔEp) for the redox reactions of DA. The values were calculated as 491.0 mV (Pt/Gr), 542.4 mV (Pd/Gr), 377.4 mV (Pt/NGr), and 460.5 mV (Pd/NGr). The results revealed that the reversibility of DA was significantly improved at the surfaces of Pt and Pd supported on N-doped graphene films. In addition, the anodic and cathodic peak potentials of DA at Pt/NGr and Pd/NGr were observed to have shifted negatively and positively, respectively (Table 7.5); in comparison with those of DA at the surface of ITO electrodes modified with N-doped graphene films only. The improved electrocatalytic activity can be attributed to the presence of metal nanoparticles, which increased the surface area as well as the number of binding sites for DA.

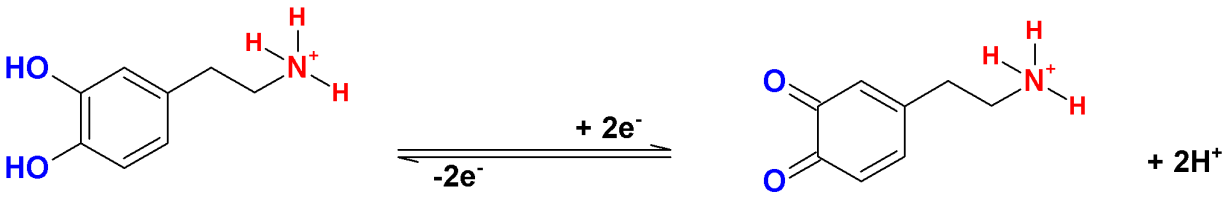

Scheme 7.2: A schematic representation of redox of dopamine to dopaquinone.

Figure 7.4b depicts the cyclic voltammetric response of 0.13 mM UA at the surfaces of Pt/Gr, Pd/Gr, Pt/NGr, and Pd/NGr modified ITO electrodes. It can be seen that strong oxidation peaks were observed for the electrochemical oxidation of UA on the surfaces of Pt/NGr/ITO (4.59 µA) and Pd/NGr/ITO (3.83 µA) electrodes. This indicated that a combination of nitrogen atoms and metal nanoparticles greatly enhanced the electrocatalytic activity toward the oxidation of UA. A similar trend was observed for the electrocatalytic activity of DA on Pt/NGr/ITO and Pd/NGr/ITO electrodes, and this was attributed to the increased surface to volume ratio of the small Pt and Pd nanoparticles as well as the large amount of edge-and plane defects due to the incorporation of nitrogen atoms. The oxidation peak potentials for the oxidation of UA [65] at the surface of Pt/Gr, Pd/Gr, Pt/NGr, and Pd/NGr modified ITO electrodes are observed to be 424.2 mV, 546.6 mV, 422.6 mV, and 400.8 mV, respectively (Table 7.5). Owing to the increased electrical conductivity due to the presence of nitrogen atoms and metal nanoparticles on the electrode surface, a negative shift is observed for the oxidation peak potentials of UA at Pt/NGr and Pd/NGr modified ITO electrodes. Interestingly, appproximatetly 0.4% shift in the oxidation peak potential was observed on Pt/NGr/ITO electrode, whereas ~27% shift was observed on Pd/NGr/ITO electrode. The results suggest an enhanced electrochemical activity for the oxidation of UA on Pd/NGrITO; which is ascribed to improved interaction between uric caid and the N-graphene films. Similar trend for detection of uric acid on pristine and N-doped graphene films was observed (see chapter 6). Generally, the negative shift indicates a decreased overpotential, hence suggesting that an easy and quick oxidation process occurs on these electrode surfaces.

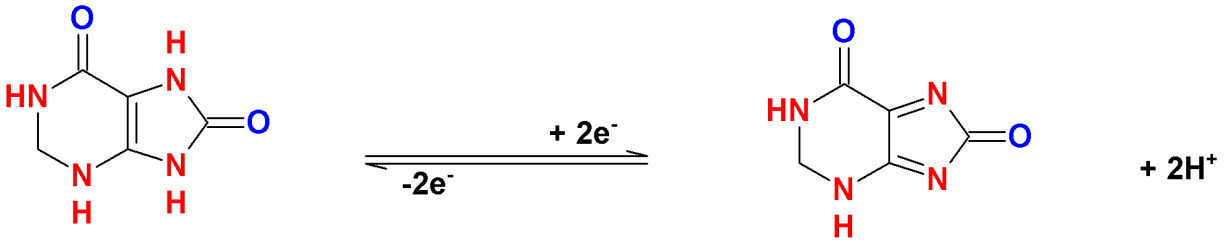

Scheme 7.3: A schematic representation of redox of uric acid to uric acid-4,5 diol.

Table 7.5: Peak potentials and currents of 0.13 mM solutions of DA and UA at bare and modified ITO electrodes at scan rate of 50 mV $^{s-1}$

Sample	Dopamine					Uric Acid	
	Ep (mV)		Ip_{max} (µA)		ΔE (mV)	Ep_a (mV)	Ip_a (µA)
	Ep_a	Ep_c	Ip_a	Ip_c			
ITO	566.5	-80.72	0.647	-0.8354	647.2	1113.8	2.317
Gr	550.3	-27.19	7.530	-3.288	577.5	550.3	1.555
Pt-Gr	520.1	29.11	6.939	-3.579	491.0	424.2	2.494
Pd-Gr	553.1	10.72	6.126	-3.337	542.4	546.6	2.174
NGr	566.8	-73.96	12.22	-4.258	640.8	424.1	3.819
Pt-NGr	443.3	65.90	9.304	-4.573	377.4	422.6	4.588
Pd-NGr	488.9	28.44	10.67	-5.839	460.5	400.8	3.832

7.3.4 Electrochemical parameters for DA at Pt and Pd-graphene modified electrodes

The influence of different scan rates (υ) on the electrochemical responses of DA at its different as-fabricated metal composite electrodes was studied using cyclic voltammetry. Figure 7.5 illustrates the cyclic voltammograms of 0.13 mM DA in 0.1 M PBS (pH = 6.02) at Pt/Gr, Pd/Gr, Pt/NGr, and Pd/NGr modified ITO electrodes, respectively, during the variation of scan rates from 10 to 100 mV s^{-1}. A pair of well-defined redox peaks for the electrocatalytic reactions of DA was observed at different scan rates on all modified ITO electrodes. The anodic (Epc) and cathodic (Epa) peak potentials gradually shifted to positive and negative values with increasing scan rate in the range of 10 to 100 mV s^{-1}, respectively. The shift in peak potentials indicates that there is no adsorption of DA and/or products of the redox reactions of DA on the electrode surface. The shift in peak potentials also generated an increasing potential separation (ΔE), which is characteristic of a quasi-reversible reaction. Moreover, the anodic (Ipa) and cathodic (Ipc,) peak currents were observed to increase with

the scan rate increment in the 10 to 100 mV s^{-1}, respectively. This relationship between the peak currents and an increase of the scan rate can be attributed to the heterogeneous kinetics of DA at the different electrode surfaces [50, 51, 66].

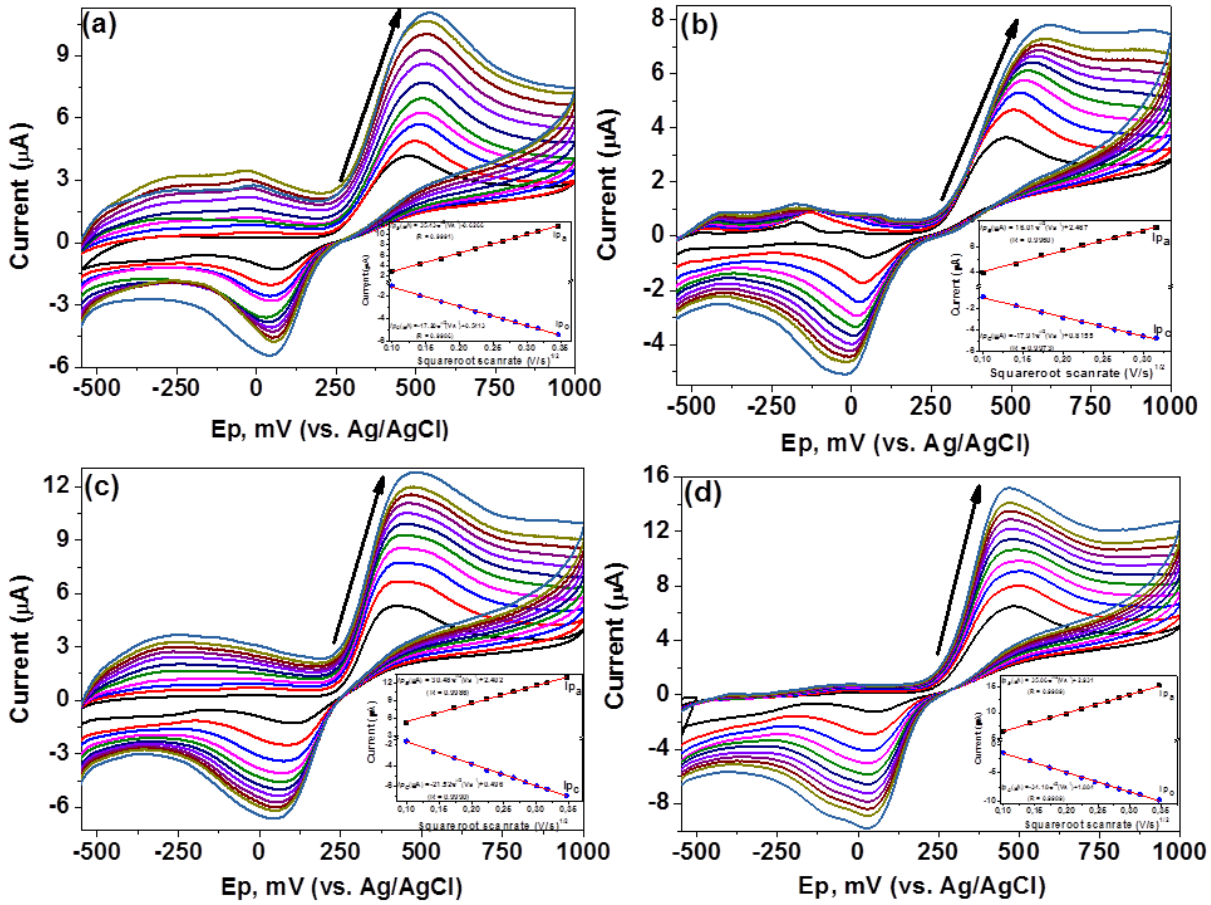

Figure 7.5: Influence of scan rate on the redox reactions of DA in PBS (pH 6.02) at (a) Pt/GR, (b) Pd/Gr, (c) Pt/NGr, and (d) Pd/NGr modified ITO electrodes. Inserts: Linear relationship between peak currents and square root of scan rate.

Further analysis of figure 7.5 revealed that a good linear dependence of the redox peak currents of DA (Ipa and Ipc) with the square root of the scan rate (√υ), was obtained (Inserts of figure 7.5), hence indicating a diffusion-controlled process for the detection of DA on all metal composite-modified ITO electrodes. Table 7.6 shows the linear regression equations for the relationship between the redox peak currents of DA (Ipa and Ipc) and the square root of the scan rate (√υ). Regression equations with positive slopes represent the relationship of anodic peak currents (Ipa), whereas the regression equations with negative slopes signifies the relationship of the cathodic peak currents (Ipc). The relatively large slope for the linear regression equation of DA at Pt/NGr indicated that the diffusion of DA molecules and the

resultant electrochemical redox reactions of DA at the electrode surface occurred faster due to increased conductivity induced by both nitrogen atoms and Pt nanoparticles. Moreover, the linear plot of log υ vs. log Ipa gave transfer coefficients (α) of 0.456, 0.436, 0.497, and 0.475 for DA at Pt/Gr, Pd/Gr, Pt/NGr, and Pd/NGr modified ITO electrodes, respectively. The calculated transfer coefficients (α) are very close to the theoretical value of 0.5 for a quasi-reversible process, hence suggesting that the electrochemical redox reactions of DA at the surface of these modified electrodes are associated with quasi-reversible process [50, 51, 65, 66].

Table 7.6: The relationships between scan rate and peak currents as well as peak potentials for detection of DA on modified ITO electrodes

Sample	Peak currents (*Ip, μA)*	Peak potentials (*Ep, mV*)
	Linear regression	**Linear regression**
Pt-Gr	$35.43\nu^{1/2}(Vs^{-1}) - 0.6266(R^2 = 0.9991)$ $-17.21\nu^{1/2}(Vs^{-1}) + 0.5413(R^2 = 0.9986)$	$24.67\ln\nu(Vs^{-1}) + 595.3(R^2 = 0.9994)$ $-24.81\ln\nu(Vs^{-1}) - 53.58(R^2 = 0.9989)$
Pd-Gr	$35.06\nu^{1/2}(Vs^{-1}) + 2.931(R^2 = 0.9989)$ $-34.18\nu^{1/2}(Vs^{-1}) + 1.884(R^2 = 0.9989)$	$26.51\ln\nu(Vs^{-1}) + 560.6(R^2 = 0.9982)$ $-25.57\ln\nu(Vs^{-1}) - 23.20(R^2 = 0.9995)$
Pt-NGr	$30.48\nu^{1/2}(Vs^{-1}) + 2.402(R^2 = 0.9986)$ $-21.51\nu^{1/2}(Vs^{-1}) + 0.496(R^2 = 0.9990)$	$25.09\ln\nu(Vs^{-1}) + 523.7(R^2 = 0.9991)$ $-22.36\ln\nu(Vs^{-1}) - 2.650(R^2 = 0.9993)$
Pd-NGr	$16.01\nu^{1/2}(Vs^{-1}) + 2.467(R^2 = 0.9960)$ $-17.91\nu^{1/2}(Vs^{-1}) + 0.8155(R^2 = 0.9973)$	$31.35\ln\nu(Vs^{-1}) + 743.02(R^2 = 0.9988)$ $-20.68\ln\nu(Vs^{-1}) - 82.53(R^2 = 0.9991)$

7.3.5 Influence of scan rate on the detection of UA

In order to evaluate the effect of the electrode kinetics for the electro-oxidation of UA at the differently modified ITO electrodes, cyclic voltammograms were recorded at scan rates of potentials between 10 and 300 mV s^{-1}. Figure 7.6 illustrates CVs obtained at Pt/Gr (a), Pd/Gr (b), Pt/NGr (c), and Pd/NGr (d) modified ITO electrodes in PBS (pH 6.02) containing 0.13

mM UA at different scan rates (10 and 300 mV s^{-1}). As the scan rate was increased, the Ipa was observed to increase while the Epa shifted slightly in the positive direction. The observed relationship between the peak currents and an increase of the scan rate can be attributed to the heterogeneous kinetics of UA at the different electrode surfaces. Furthermore, the shift in peak potentials indicates that there is no adsorption of UA and/or products of the redox reactions of UA on the electrode surface. On the other hand, the Pt/Gr/ITO is an exception since the occurrence of different reaction kinetics on the Pt/Gr/ITO electrode was indicated by the presence of other peak currents are more negative peak potentials (~-150 mV). This could suggest the adsorption of pre-oxidation products on the electrode surface [50, 51, 65, 66]. Therefore, further studies with other techniques will need to be performed to confirm the nature of adsorbed materials/compounds.

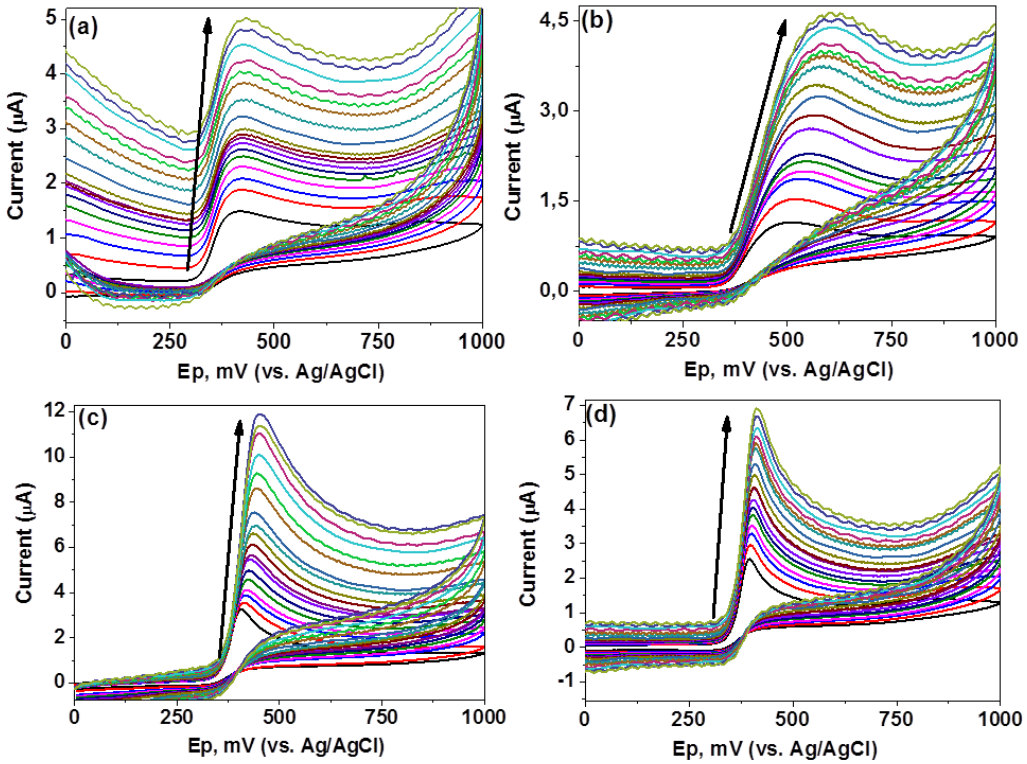

Figure 7.6: Influence of scan rate on redox reactions of UA in PBS (pH 6.02) at (a) Pt/GR, (b) Pd/Gr, (c) Pt/NGr, and (d) Pd/NGr modified ITO electrodes.

A good linearity between the anodic peak current (Ipa) and the square root of the scan rate (√υ) was obtained for UA (Fig. 7.7) and this indicated that the charge transfer on the modified electrodes is a diffusion-controlled process [50, 51, 65, 66]. Table 7.6 shows the linear regression equations used to establish the relationship between the oxidation peak currents and potentials of UA (Ipa) and the square root of the scan rate (√υ). Similarly linear regression equations for the relationship between the oxidation peak potentials (Epa) and ln υ,

as shown in inserts of figure 7.7. The relatively large slope for the linear regression equation of UA at Pt/NGr/ITO electrode indicated that the diffusion of UA molecules and electrochemical oxidation of UA at the electrode surface occurred faster due to increased conductivity induced by both nitrogen atoms and Pt nanoparticles.

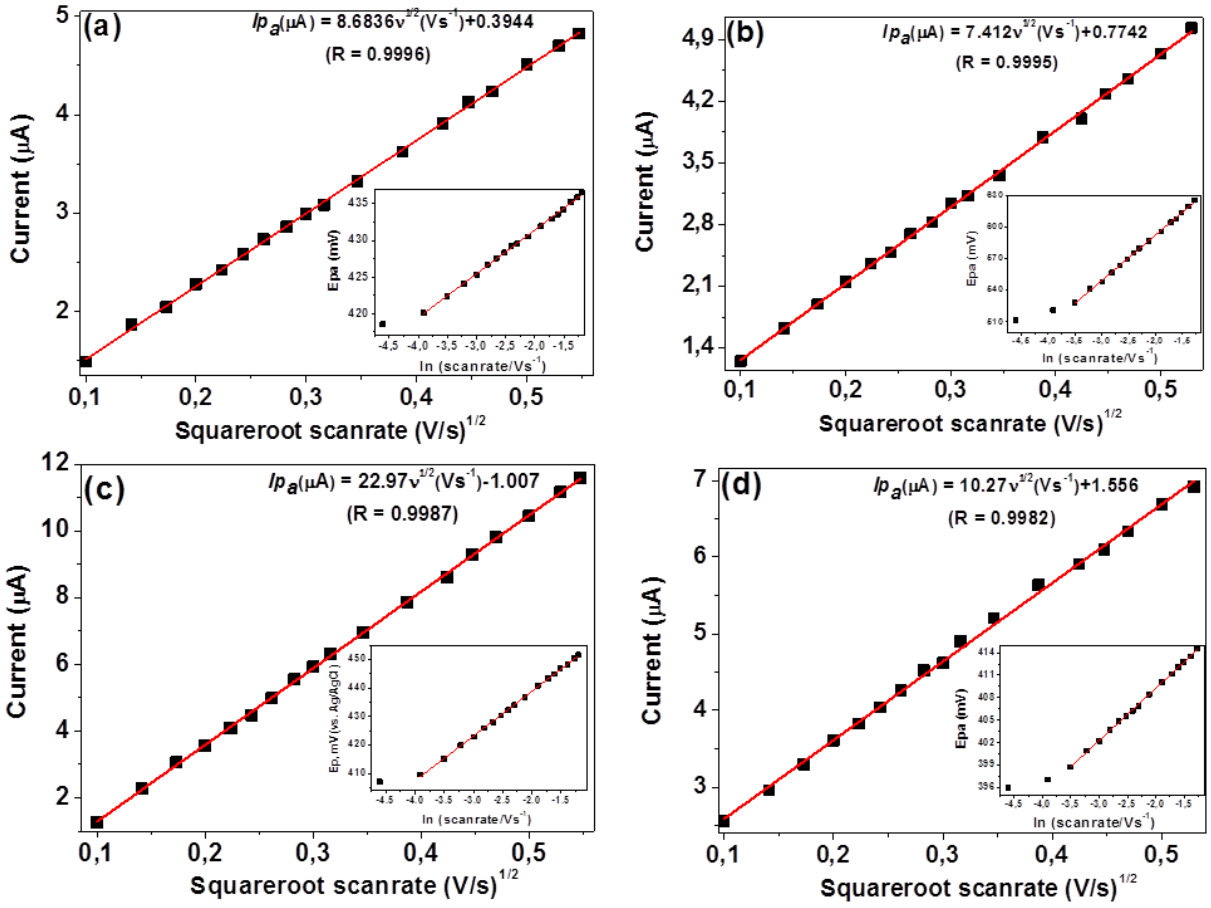

Figure 7.7: Linear relationship between peak currents and the square root of scan rate (√υ) of UA at (a) Pt/Gr, (b) Pd/Gr, (c) Pt/NGr, and (d) Pd/NGr-modified ITO electrodes. Inserts: Linear relationship of Ep and ln scan rate (υ).

Table 7.7: The relationships between scan rate and peak currents and peak potentials for detection of UA on modified ITO electrodes

Sample	Peak currents (*Ip, μA)*	Peak potentials (*Ep, mV*)
	Linear regression	**Linear regression**
Pt-Gr	$8.684\nu^{1/2}(Vs^{-1}) + 0.3944(R^2 = 0.9996)$	$43.12\ln\nu(Vs^{-1}) + 678.6(R^2 = 0.9986)$
Pd-Gr	$7.412\nu^{1/2}(Vs^{-1}) + 0.7742(R^2 = 0.9995)$	$5.987\ln\nu(Vs^{-1}) + 443.4(R^2 = 0.9989)$
Pt-NGr	$22.97\nu^{1/2}(Vs^{-1}) - 1.007(R^2 = 0.9987)$	$15.65\ln\nu(Vs^{-1}) + 470.1(R^2 = 0.9993)$
Pd-NGr	$10.271\nu^{1/2}(Vs^{-1}) + 1.556(R^2 = 0.9982)$	$6.978\ln\nu(Vs^{-1}) + 423.2(R^2 = 0.9991)$

7.3.6 Sensitivity and detection limits of DA and UA at modified electrodes

The sensitivity of ITO electrodes modified with composites of graphene or N-graphene films and Pt or Pd nanoparticles for the electrochemical detection of DA and UA was investigated using differential pulse voltammetry (DPV) technique. DPV was used for the determination of the linear detection limits of DA and UA due to the higher sensitivity and better signal-to-noise ratio of this technique. The DPV curves obtained for the responses on the surfaces of the Pt-Gr (a), Pd-Gr (b), Pt-NGr (c), and Pd-NGr (d) modified ITO electrodes in the presence of 1.0 mM phosphate buffer solution containing different concentrations of DA are shown in figure 7.8. The peak currents attributed to the oxidation of DA were observed to increase linearly with the increasing concentrations of DA in the ranges of 4 - 36 μM, 6 – 360 μM, 4 – 90 μM, and 8 – 140 μM for detection on Pt-Gr, Pd-Gr, Pt-NGr, and Pd-NGr modified ITO electrodes, respectively. The corresponding linear regression plots for the oxidation peak currents (Ipa) and the increasing DA concentrations are depicted in supplementary figure S7.5a.

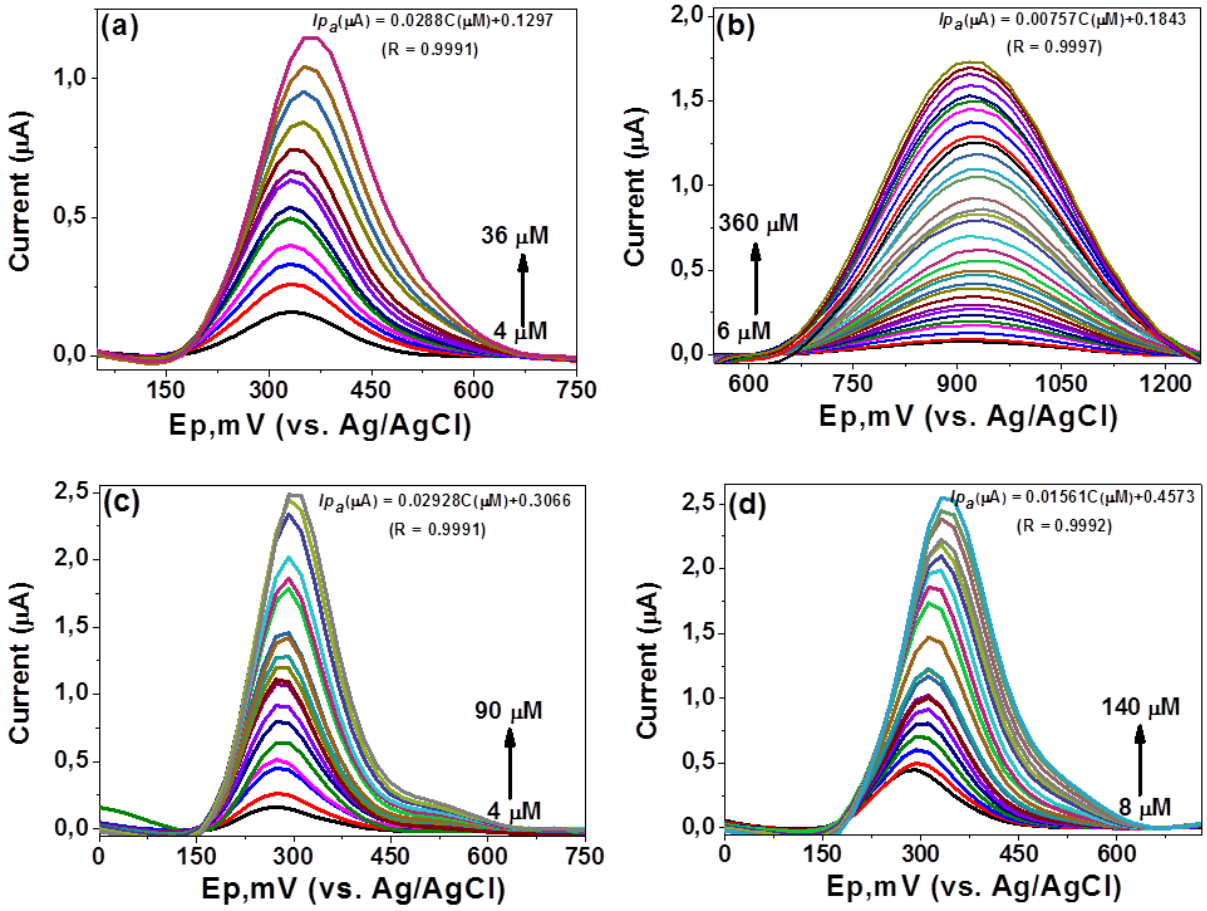

Figure 7.8: Concentration studies of DA on (a) Pt-Gr, (b) Pd-Gr, (c) Pt-NGr, and (d) Pd-NGr modified ITO electrodes at buffer pH 6.02.

Using the linear relationships between Ipa and DA concentration (C) on the modified ITO electrodes (Fig. 7.8: inserts), the detection limits were determined to be 0.76 μM, 0.29 μM, 0.075 μM, and 0.14 μM on ITO electrodes modified with Pt-Gr, Pd-Gr, Pt-NGr, and Pd-NGr films, respectively. From table 7.8, it can be seen that the determination of DA at a Pt/NGr/ITO electrode exhibited better sensitivity (0.09 $\mu A \mu M^{-1} cm^{-2}$), which can be attributed to the unique structural properties of the Pt/NGr/ITO electrode. The improved sensitivity for the electrocatalytic oxidation of DA on the Pt/Gr/ITO electrodes (0.07 $\mu A \mu M^{-1} cm^{-2}$) can be ascribed to the presence of Pt nanoparticles. Determination of DA at ITO electrodes modified with palladium composites revealed low sensitivities, viz. (0.02 $\mu A \mu M^{-1} cm^{-2}$(Pd/Gr) and 0.05 $\mu A \mu M^{-1} cm^{-2}$ (Pd/NGr)). This can be attributed to the presence of the large nanoclusters (54 ± 13 nm), which would then decrease the electrochemical performance of the Pd/Gr/ITO electrodes. Interestingly, a significant negative shift in oxidation peak potentials is observed on detection of DA on a Pd/NGr/ITO electrode (331 mV) as compared to the determination

of DA on a Pd/Gr/ITO electrode (917 mV). The results indicated that incorporation of nitrogen atoms into the graphene lattice as well as the presence of small Pd nanoparticles (7 ± 3 nm) led to an increased electron conductivity and surface-to-volume ratio. Therefore, less energy is used to facilitate the oxidation of DA at the Pd/NGr/ITO electrode (Scheme 7.2) [64].

Table 7.8: Linear ranges, detection limits and sensitivities for detection of DA

Electrode	Epa (mV)	Linear range (µM)	Detection Limit (µM)	Sensitivity ($\mu A.\mu M^{-1}.cm^{-2}$)
Gr	395	8 – 190	4.13	0.0294
Pt-Gr	351	4 - 36	0.76	0.0686
Pd-Gr	917	6 – 360	0.29	0.0180
NGr	297	2 - 150	0.15	0.0791
Pt-NGr	292	4 - 90	0.075	0.0897
Pd-NGr	331	8 - 140	0.14	0.0472

Similarly, the differential pulse voltammetry technique was used to investigate the influence of concentration on the voltammetric responses of UA at the electrode surfaces of Pt/Gr, Pd/Gr, Pt/NGr, and Pd/NGr modified ITO electrodes. Figure 7.9 illustrated the corresponding DPVs of 1.0 mM phosphate buffer solution containing various concentrations of UA at the different electrode surfaces. A linear enhancement in the oxidation peak currents was observed over a concentration range of 50 – 400 µM, 50 – 480 µM, 8 – 160 µM, and 10- 170 µM for the detection of UA at the Pt/Gr, Pd/Gr, Pt/NGr, and Pd/NGr modified ITO electrodes, respectively. The corresponding linear regression plots for the oxidation peak currents (Ipa) and the increasing UA concentrations are depicted in supplementary figure S7.5b.

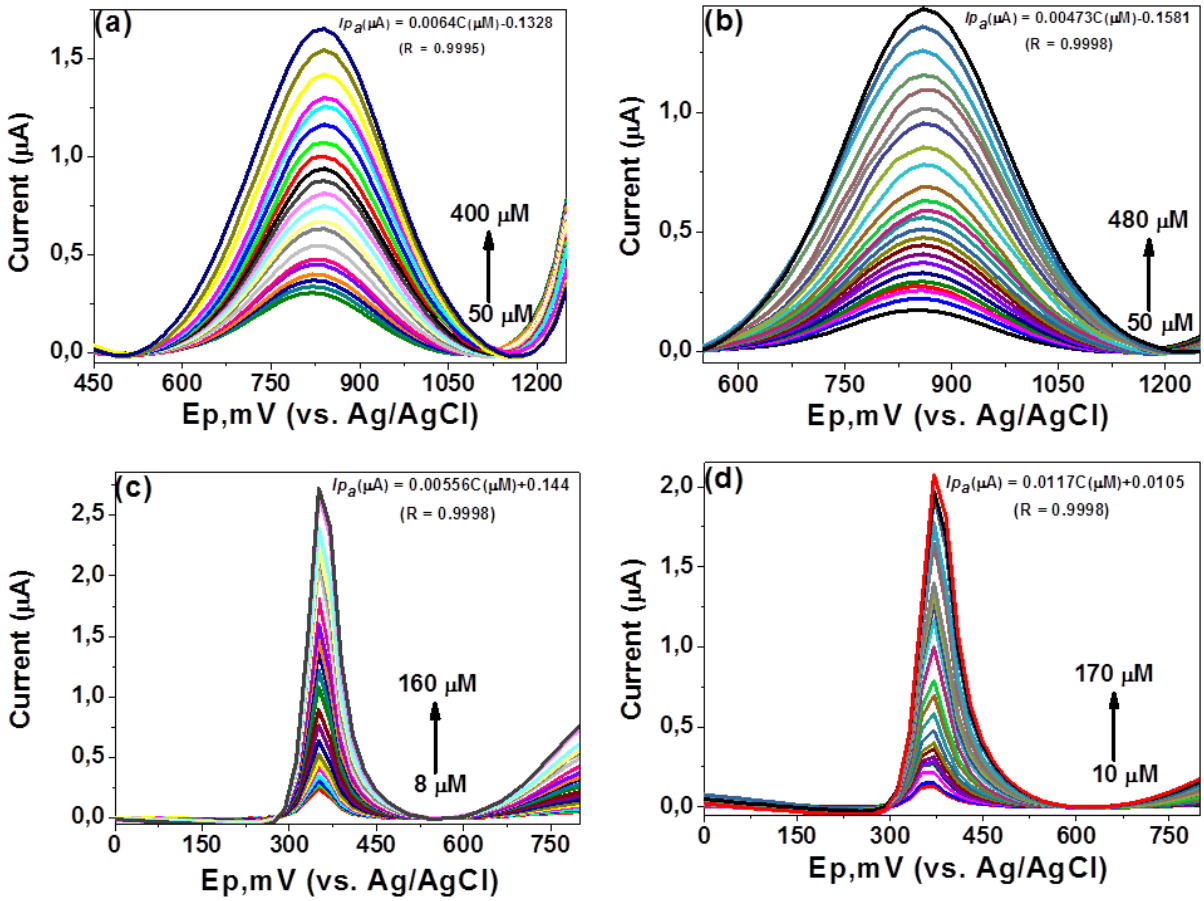

Figure 7.9: Concentration studies of UA on (a) Pt-Gr, (b) Pd-Gr, (c) Pt-NGr, and (d) Pd-NGr modified ITO electrodes at buffer pH 6.02.

Under optimized DPV conditions for quantitative determination of UA, the calibration curves were used to determine the detection limits (S/N=3) of UA on ITO electrodes modified with different composite materials. These were calculated to be 0.32 μM, 0.47 μM, 0.14 μM, and 0.29 μM for electrocatalytic oxidation of UA on Pt/Gr, Pd/Gr, Pt/NGr, and Pd/NGr modified ITO electrodes, respectively. Division of the slope of the calibration curve with the geometrical area of the electrode (0.42 cm^2) resulted in calculations of the sensitivities of the modified electrodes towards detection of UA (Table 7.9). It can be seen that the introduction of Pt and Pd nanoparticles onto the surface of the pristine graphene led to an increased sensitivity towards detection of UA. A similar trend was observed for the sensitivities of Pt/NGr/ITO and Pd/NGr/ITO electrodes towards the electrochemical oxidation of UA. This can be attributed to the increased electron conductivity due to the presence of metal nanoparticles as well as nitrogen atoms, and the increased surface-to-volume ratio due to the presence of small nanoparticles. As a result, it can be seen that increased sensitivity led to decreased detection limits for the ITO electrodes modified with composites materials as

compared to the non-composites modified ITO electrodes. Furthermore, the oxidation peak potentials of UA at the different composite electrode surfaces shifted negatively when compared with non-composite electrode surfaces; i.e. Pt/Gr (840 mV), Pd/Gr (859 mV), and Pt/NGr (351 mV) as compared with Gr (863 mV) and NGr (356 mV). The exception was observed for the oxidation peak potentials of the Pd/NGr/ITO electrode (370 mV), which shifted positively versus the peak potentials on the NGr/ITO electrode. The results could suggest that there is adsorption of UA oxidation products on the Pd/NGr/ITO electrode surface; thus more energy is required to facilitate oxidation of the UA (Scheme 7.3) [65]. This is also shown by the slightly broad voltammograms for Pd/NGr/ITO versus those of Pt/NGr/TIO; thus indicating slower electron transfer kinetics on Pd/NGr/ITO electrode.

Table 7.9: Linear ranges, detection limits and sensitivities for detection of UA

Electrode	Ep_a (mV)	Linear range (µM)	Detection Limit (µM)	Sensitivity ($\mu A.\mu M^{-1}.cm^{-2}$)
Gr	863	40 – 560	5.94	0.0063
Pt-Gr	840	50 – 400	0.32	0.0154
Pd-Gr	859	50 – 480	0.47	0.0113
NGr	356	6 – 140	0.73	0.0513
Pt-NGr/ITO	351	8 – 160	0.14	0.0932
Pd-NGr/ITO	370	10 – 170	0.29	0.0579

The as-synthesized ITO-based electrochemical sensors exhibited better or comparable analytical performances to other reported electrode materials based on platinum and palladium composite for the electrochemical detection of DA (Table 7.10) and UA (Table 7.11). In general, it can be seen that electrochemical oxidation of DA and/or UA on composites materials prepared with platinum nanoparticles and graphene or other carbon nanostructures exhibited satisfactory linear concentration ranges with very low detection limits. This good electrocatalytic performance of platinum nanoparticles immobilized on the carbon nanostructures was ascribed to the better dispersion of very small Pt nanoparticles on

these nanostructures, thus enhancing the surface area and facilitating faster electron transfer. For instance, in this study, a good dispersion of small Pt nanoparticles was observed on nitrogen doped graphene films. Furthermore, the good electrocatalytic performance can be ascribed to the excellent electrocatalytic activity of the carbon nanostructures (such as graphene and carbon nanotubes) as well as Pt nanoparticles towards the oxidation of DA and/or UA, due to the improved electrical conductivity contributed by the presence of carbon and Pt. As a result, ITO-based platinum/nitrogen-doped graphene composite sensors indicate potential for becoming promising candidates for application as electrochemical sensors. However, it is apparent more studies need to be performed so as to improve the selectively of this ITO-based sensors.

Table 7.10: Comparison of electrocatalytical data for the determination of DA

Electrode	Linear range (µM)	Detection limit (µM)	Reference
Pt-Gr/ITO	4 - 36	0.76	This study
Pd-Gr/ITO	6 – 360	0.29	This study
Pt-NGr/ITO	4 - 90	0.075	This study
Pd-NGr/ITO	8 - 140	0.14	This study
Pd-rGO/GCE	2 – 10	0.1	67
Pd-CNF/GCE	0.5 – 160	0.2	68
Pt-rGO/GCE	10 - 170	0.25	69
Pd_3Pt_1-PDDA-rGO/GCE	4 – 200	0.04	70
Pd-PEDOT-rGO/GCE	1 – 200	0.14	71
Pt-Gr/GCE	0.03 – 8.13	0.03	44

**Gr-> graphene films, ITO -> indium tin oxide, NGr -> N-doped graphene film, rGO -> reduced graphene oxide nanosheets, GCE -> glassy carbon electrode, NrGO -> N-doped reduced graphene oxide nanosheets, CNF -> carbon nanoflowers, Pt -> platinum nanoparticles, Pd -> palladium nanoparticles, PEDOT -> poly (3,4-ethylenedioxythiophene), PDDA-> poly (diallyldimethylammonium) chloride.*

Table 7.11: Comparison of electrocatalytical data for the determination of UA

Electrode	Linear range (µM)	Detection limit (µM)	Reference
Pt-Gr/ITO	110 – 400	0.32	This study
Pd-Gr/ITO	50 – 480	0.47	This study
Pt-NGr/ITO	8 – 160	0.14	This study
Pd-NGr/ITO	10 – 170	0.29	This study
Pd_3Pt_1-PDDA-rGO/GCE	4 – 400	0.10	70
Pt-rGO/GCE	10 - 130	0.45	67
Pt-Gr-CNT/GCE	0.1 - 50	0.1	72
Pt-Gr/GCE	0.05 – 11.85	0.05	73
cubic-Pd-rGO/GCE	6 – 469.5	1.6	43

**Gr-> graphene films, ITO -> indium tin oxide, NGr -> N-doped graphene film, rGO -> reduced graphene oxide nanosheets, GCE -> glassy carbon electrode, NrGO -> N-doped reduced graphene oxide nanosheets, CNT -> carbon nanotubes, Pt -> platinum nanoparticles, Pd -> palladium nanoparticles, PDDA-> poly (diallyldimethylammonium) chloride.*

7.3.7 Influence of the buffer solution pH

The influence of the solution acidity and alkalinity on the electrochemical oxidation peak potentials and currents of 0.13 mM DA and 0.13 mM UA was investigated by running DPVs at different PBS pH from 3.05 to 9.04. The pH studies were performed since both DA and UA are known to exhibit a two electron and two proton processes on the modified electrodes (Schemes 7.1 and 7.2) [64, 65]. As a result, the PBS buffer acidity should have great impact on the electrocatalytic responses of DA and UA. Figure 7.10 shows the oxidation peak potentials (Epa) of DA and UA in different phosphate buffer solution pH values at ITO electrodes modified with Pt and Pd nanoparticles immobilized on pristine and N-doped graphene films.

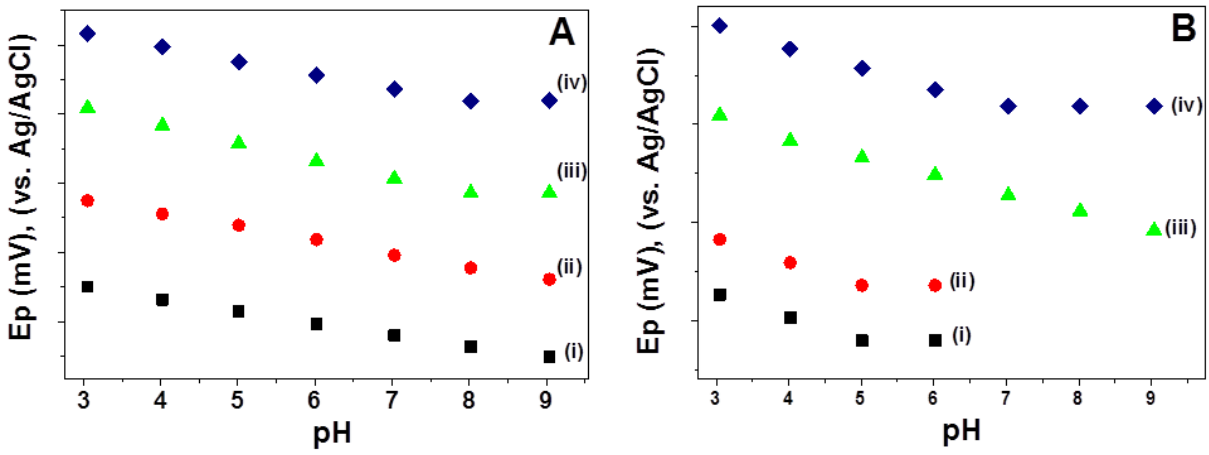

Figure 7.10: Oxidation peak potentials of (a) DA and (b) UA in different buffer pH values at ITO electrodes modified with (i) Pt/Gr, (ii) Pd/Gr, (iii) Pt/NGr, and (iv) Pd/NGr, respectively.

As shown in figures 7.10a and b, the oxidation peak potentials of DA and UA decreased gradually with increasing pH, thus suggesting less energy is required to facilitate electrocatalytic oxidation of DA and UA at higher pH values. The regression equations for the linear relationships of the oxidation peak potentials of DA and UA with the PBS pH values are shown in tables 7.12. The slopes of the linear plots were determined to be -51.3 mV pH^{-1}, -58.0 mV pH^{-1}, -74.9 mV pH^{-1} and -60.2 mV pH^{-1} for the electrochemical oxidation of DA at Pt/Gr, Pd/Gr, Pt/NGr, and Pd/NGr- ITO electrodes, respectively (Fig. 7.10a). The slopes for the voltammetric responses of DA at Pt/Gr and Pd/Gr-ITO electrodes were close to the theoretical Nernst value of -59 mV pH^{-1}, indicating that electron transfer in electrochemical oxidation of DA is equal to the number of protons [64]. However, the slopes for the voltammetric responses of DA at Pt/NGr and Pd/NGr-ITO electrodes were larger than the Nernst value, suggesting that faster electron transfer kinetics were involved in electrode reactions for oxidation of DA [64]. On the other hand, the slopes of all linear plots of the electrochemical oxidation of UA at different PBS pH values at Pt/Gr (-59.7 mV pH^{-1}), Pd/Gr (-58.8 mV pH^{-1}), Pt/NGr (-57.6 mV pH^{-1}), and Pd/NGr (-51.4 mV pH^{-1}), were close to the theoretical Nernst value, as shown in figure 7.10b. The results indicated that an equal number of electrons and protons were involved during the electrochemical oxidation of UA [65].

Table 7.12: The relationship between peak potentials and pH for detection of DA and UA

Electrode	Dopamine (DA)		Uric Acid (UA)	
	Linear regression	**pH range**	**Linear regression**	**pH range**
Pt-Gr	$-51.30(mV)\,pH + 667.2$ ($R^2 = 0.9984$)	3.05 – 9.04	$-59.69(mV)\,pH + 728.7$ ($R^2 = 0.9998$)	3.05 – 5.01
Pd-Gr	$-58.02(mV)\,pH + 724.0$ ($R^2 = 0.9981$)	3.05 – 9.04	$-58.69(mV)\,pH + 728.6$ ($R^2 = 0.9996$)	3.05 – 5.01
Pt-NGr	$-74.89(mV)\,pH + 729.2$ ($R^2 = 0.9984$)	3.05 – 8.02	$-57.61(mV)\,pH + 651.7$ ($R^2 = 0.9957$)	3.05 – 9.04
Pd-NGr	$-60.24(mV)\,pH + 683.5$ ($R^2 = 0.9983$)	3.05 – 8.02	$-51.38(mV)\,pH + 668.9$ ($R^2 = 0.9955$)	3.05 – 7.03

7.3.8 Stability and reproducibility of the modified electrodes

The stability of the ITO electrodes modified with composite materials was investigated using differential pulse voltammograms of 0.13 mM solutions of DA and UA. The DPVs were recorded on modified electrodes after two weeks of room temperature storage in ambeit conditions, and the average peak current loss was recorded for the voltammetric responses of both DA and UA (Table 7.13). In summary, the electrocatalytic oxidation of both DA and UA showed excellent stability at the surfaces of Pt/NGr/ITO electrodes, since only a 1.54 % and 1.78 % loss of the peak current was determined for DA and UA, respectively. Generally, the trend of the stability of the modified electrodes towards electrochemical oxidation of DA and UA was influenced by the particle sizes of Pt and Pd nanoparticles. For instance, Pd/Gr/ITO electrodes exhibited poor stability for the electrocatalytic oxidation of both DA and UA, with the loss of the peak currents recorded at 4.51% and 4.73 %, respectively.

Furthermore, five independent composite/ITO electrodes, prepared using a similar procedure, were used to evaluate the reproducibility from the DPVs of PBS containing 0.13 mM DA and 0.13 mM UA. Relative standard deviations (RSDs) of 2.52%, 3.21%, 1.02% and 1.53% were calculated for the voltammetric responses of DA at Pt/Gr, Pd/Gr, Pt/NGr, and Pd/NGr

modified ITO electrodes, respectively. In addition, RSDs of 1.34%, 2.58%, 1.89% and 2.03% were determined for the oxidation voltammetric responses of UA at Pt/Gr, Pd/Gr, Pt/NGr, and Pd/NGr modified ITO electrodes, respectively. In summary, as shown in Table 7.13, ITO electrodes modified with Pt and Pd nanoparticles supported on N-graphene films demonstrated good stability and reproducibility as compared to ITO electrodes modified with metal nanoparticles immobilised on their undoped graphene counterparts. Thus, the results indicate that the electrochemical performance of ITO electrodes, based on modification with composites of graphene and metal nanoparticles, appears to be dependent on the structural and electronic properties of graphene, as well as the sizes of the metal nanoparticles.

Table 7.13: Stability and reproducibility studies of DA and UA on modified ITO

Electrode	Stability (% Loss)[a]		Reproducibility (RSD, %)[b]	
	DA	**UA**	**DA**	**UA**
Pt-Gr	2.31	2.77	2.52	1.34
Pd-Gr	4.51	4.73	3.21	2.58
Pt-NGr	1.54	1.78	1.02	1.89
Pd-NGr	1.92	2.15	1.53	2.03

[a] *-> % loss in DPVs after two weeks of storage.*

[b] *-> % relative standard deviation of five independent electrodes.*

7.4 Conclusions

In summary, Pt/Pd-graphene and Pt/Pd-nitrogen doped graphene composites materials were successfully prepared by the electroless deposition of the metal nanoparticles from their salt solution. The electrochemical sensing application of both pristine- and N-graphene-composites for the sensitive detection of dopamine and uric acid was performed based on the modification of ITO electrodes. High resolution TEM analysis showed that incorporation of nitrogen atoms into the graphene lattice provided several advantages, including immobilization of platinum and palladium nanoparticles with decreased particle sizes (3 ± 1 nm for Pt and 7 ± 3 nm for Pd); fast electron transfer kinetics and good electron conductivity due to high surface-to-volume ratio induced by the small nanoparticles and nitrogen

configurations; enhanced electrocatalytic activity as a result of electrochemical surface area and increased amount of chemically active/binding sites for uric acid and dopamine. Furthermore, the electrochemical performances and stability of these composite-based ITO electrodes appeared to be dependent on the structural and electronic properties of graphene and the sizes of the metal nanoparticles. For instance, ITO electrodes modified with Pt and Pd nanoparticles supported on N-graphene films demonstrated good stability and reproducibility as compared to ITO electrodes modified with metal nanoparticles immobilised on their undoped graphene counterparts. Under optimized DPV conditions, the as-prepared composite-based ITO electrodes exhibited better or comparable limits of detection (S/N =3) to other reported research studies for electrochemical determination of dopamine and uric acid. However, more studies need to be performed to investigate the influence of same-sized Pt and Pd nanoparticles on the detectionof DA and UA. In general, the study provided a simple and cost-effective method for designing high performance the electrochemical sensors based on ITO electrodes modified with composites of graphene and noble metal nanoparticles. However, it is apparent that more work is required to enhance the selectivity of the electrodes.

References

1. Dennis, M. A., K. Michael, M. M. Khodabakhsh, N. Stuart, W. Michael. *Anal. Chem.*, **1989**, *61*, 2603-2608.
2. Ye, F., C. Feng, J. Jiang, S. Han. *Electrochim. Acta*, **2015,** *182*, 935–945.
3. Wightman, R. M., L. J. May, A. C. Michael. *Anal. Chem*., **1988**, *60*, 769A–793A.
4. Kapur, S., D. Mamo. *Prog. Neuro-Psychopharmacol. Biol. Psychiatry*, **2003**, *27*, 1081.
5. Volkow, N. D., J. S. Fowler, G. J. Wang. *Behav. Pharmacol*. **2002**, *13*, 355.
6. Kim, J. H., J. M. Auerbach, J. A. R. Gomez, I. Velasco, D. Gavin, N. Lumelsky, S. H. Lee, J. Nguyen, R. S. Pernaute, K. Bankiewicz, R. McKay. *Nature*, **2002**, *418*, 50.
7. Gowrishankar, R., M. K. Hahn, R. D. Blakely. *Neurochem. Int.* **2014**, *73*, 42–48.
8. Camardese, G., D. Giuda, M. Nicola, F. Cocciolillo, A. Giordano, L. Janiri, R. Guglielmo. *J. Psychiatr. Res.* **2014**, *51*, 7–18.
9. Liu, S., X. Xing, J. Yu, W. Lian, J. Li, M. Cui, J. Huang. *Biosens. Bioelectron*. **2012**, *36*, 186–191.
10. Dutt, V. V. S. E., H. A. Mottola. *Anal. Chem*. **1974**, *46*, 1777–1781.

11. Chen, X., G. Wu, Z. Cai, M. Oyama, X. Chen. *Microchimica Acta*, **2014,** *181*, 689–705.
12. Yu, J., S. Wang, L. Ge, S. Ge. *Biosensors and Bioelectronics*, **2011,** *26*, 3284–3289.
13. Kim, Y. R., S. Bong, Y.-J. Kang, Y. Yang, R. K. Mahajan, J. S. Kim, H. Kim. *Biosens. Bioelectron.* **2010,** *25*, 2366–2369.
14. Qi, S., B. Zhao, H. Tang, X. Jiang. *Electrochim. Acta*. **2015,** *161*, 395–402.
15. Jackowska, K., P. Krysinski. *Anal. Bioanal. Chem.* **2012,** *405*, 3753–3771.
16. Niu, L. M., K. Q. Lian, H. M. Shi, Y. B. Wu, W. J. Kang, S. Y. Bi. *Sensors Actuators B Chem.* **2013,** *178*, 10–18.
17. Sajid, M. S., M. K. Nazal, M. Mansha, A. Alsharaa, S. M. S. Jillani, C. Basheer. *TrAc Trends Anal. Chem*. **2016**, *76*, 15–29.
18. Dutt, V. V. S. E., H. A. Mottola. *Anal. Chem*. **1974**, *46*, 1777–1781.
19. Chen, X., G. Wu, Z. Cai, M. Oyama, X. Chen. *Microchimica Acta*, **2014,** *181*, 689–705.
20. Yu, J., S. Wang, L. Ge, S. Ge. *Biosensors and Bioelectronics*, **2011,** *26*, 3284–3289.
21. Sheng, Z. H., X. Q. Zheng, J. Y. Xu, W. J. Bao, F. B. Wang, X. H. Xia. *Biosens. Bioelectron.* **2012**, *34*, 125–131.
22. Wang, L., X. Lu, C. When, Y. Xie, L. Miao, S. Chen, H. Li, P. Li, Y. Song, *J. Mater. Chem. A*, **2015**, *3*, 608–616.
23. Cinti, S., F. Ardunini, M. Carbone, L. Sansone, I. Cacciotti, D. Moscone, G. Palleschi. *Electroanalysis* **2015**, *27*, 2230–2238.
24. Shakkthivel, P., S. Chen. *Biosens. Bioelectron*. **2007**, *22*, 1680–1687.
25. Jiang, G. T. Jiang, H. Zhou, J. Yao, X. Kong. *RSC Adv***.,** 2015, **5**¸9064-9068.
26. Welch, C.W., R. G. Compton. *Anal. Bioanal. Chem*. **2006**, *384*, 601–619.
27. Kalimuthu, P., S. A. John. *Talanta*, **2010**, *80*, 1686–1691.
28. Abdelwahab, A. A., Y.-B. Shim. *Sensors Actuators B Chem*. **2015,** *221*, 659–665.
29. Novoselov, K. S., A. K Geim, S. V. Morozov, D. Jang, Y. Zhang, D. Jang, Y. Zhang, S. V. Dubonos, I. V. Grigorieva, A. A. Firsov. *Science*, **2004**, *306***,** 666-669.
30. Geim, A. K., K. S. Novoselov. *Nat. Mater*, **2007**, *6,* 183-191.
31. Geim, A. K. *Science*, **2009**, *324***,** 1530-1534.
32. Geim, A.K., K. S. Novoselov, S. Morozov, D. Jiang, M. I. Katsnelson, S. Dubonos, I. Grigorieva, A. Firsov. *Nature*, **2005**, *438*, 197-200.
33. Pumera, M., A. Ambrosi, A. Bonanni, E. L. K. Cheng, H. L. Poh. *TrAC, Trends Anal. Chem.*, **2010**, *29*, 954.

34. Brownson, D. A. C., D. K. Kampouris, C. E. Banks. *Chem. Soc. Rev.*, **2012**, *41*, 6944.
35. Shuang, R., H. Wang, Y. Zhang, Y. Sun, L. Li, H. Zhang, Z. Shi, M. Li, M. Li. *Analyst,* **2016,** *141*, 2741-2747.
36. Huang, C. C., C. Li, G. Q. Shi, *Energy Environ. Sci.*, **2012,** *5*, 8848.
37. Ghanbari, K. H., N. Hajheidari, *Anal. Biochem.*, **2015**, *473*,53.
38. Soleymani, J., *Trends Anal. Chem*., **2015**, *72*, 27.
39. Cheng, W., R. G. Compton, *Trends Anal. Chem.*, **2014**, *58*, 79.
40. Kang, Y. J., C. B. Murray, *J. Am. Chem. Soc.*, **2010**, *132*,7568.
41. Christopher, B. J., P. M. Jennifer and V. B. Jill, *Anal. Chim. Acta,* **2010,** *622*, 105.
42. Annesh, P. K., S. R. Nambiar, T. P. Rao, A. Ajayaghosh. *Anal. Methods*, **2014**¸*6*, 5322-5330.
43. Wang, J., B. Yang, J. Zhang, B. Yan, K. Zhang, C. Zhai, Y. Shiraishi, Y. Du, P. Yang. *J. Colloid and Interface Science,* **2017,** *497,* 172-180.
44. Sun, C. L., H.H. Lee, J. M. Yang, C. C Wu. *Biosens Bioelectron,* **2011,** *26*, 3450-3455.
45. Han, D. X., T. T. Han, C. S. Shan, A. Ivaska, L. Nui. *Electroanalysis***, 2010**, *22*, 2001-2008.
46. Wu, L., L. Feng, J. Ren, X. Qu, *Biosens Bioelectron,* **2012,** *34*,57-62.
47. Liu, G., W. Ma, Y. Luo, D. M., Sun, S. Shao. *J. Anal. Methods. Chem*., **2014**¸ *984314*, 1-10.
48. Matsoso, B. J., K. Ranganathan, B. K. Mutuma, T. Lerotholi, G. Jones, N. J. Coville. *RSC Adv.*, **2016**, *6*, 106916-106920.
49. Gutes, A., B. Hsia, A. Sussman, W. Mickelson, A. Zettl, C. Carraro, R. Maboudian, *Nanoscale*, **2012,** *4*, 438-440.
50. Wang, Y., Y. Zheng, X. Xu, E. Dubuisson, Q. Bao, J. Lu, K. P. Loh. *ACS Nano*. **2011**, 5, 9927-9933.
51. Zhang, Y. Y. Ji, z. Wang, S. Liu, T. Zhang. *RSC Adv.*, **2015,** *5*, 106307-106314.
52. Yang, J., J. R. Strickler, S. Gunasekaran. *Nanoscale*, **2012,** *4*, 4594-4602.
53. Zaniewski, A. M., C. J. Trimble, R. J. Nemanich, *Appl. Phys. Lett.***, 2015,** *106*, 123104.
54. N'Diaye, J., S. Poorahong, O. Hmam, R. Izquierd, M. Siaj, *J. of Electroanalytical Chemistry,* **2017,** *789,* 85-91.
55. Li, X., Y. Wu, H. Song, S. Yoo, W. Lin, X. Wang, *J. Mater. Sci.: Materials in Electronics,* **2015,** *26,* 1500-1506.

56. Jansen, R. J. J., H. Vanbekkum, *Carbon*, **1995**, *33*, 1021-1027.
57. Nakayama, Y., F. Soeda, A. Ishitani, *Carbon*, **1990**, *28*, 21-26.
58. Lv, R. T., Q. Li, A.R. Botello-Me´ndez, T. Hayashi, B. Wang, A. Berkdemir. *Sci Rep*., **2012**, *2*, 586-1-8.
59. Venezuela, P., M. Lazzeri, F. Mauri, *Phys Rev B.*, **2011**, *84*, 035433-1-25.
60. Xie, W., N. M. Kai, L. T. Weng, C. M. Chan. *RSC. Adv*, **2016**, *6*, 80649-80654.
61. Ewels, C. P., M. Glerup, *J Nanosci Nanotechnol*., **2005**, *5*, 1345-1363.
62. Guo, B., Q. Liu, E. Chen, *et al., Nano Lett.*, **2010**, *10*, 4975-4980.
63. Qu, L., Y. Liu, J. B. Baek, L. Dai, *ACS Nano*, **2010**, *4*, 1321-1326.
64. Medintz, I. L., M. H. Stewart, S. A. Trammell, K. Susumu, J. B. Delehanty, B. C. Mei, J. S. Melinger, J. B. Blanco-Canosa, P. E. Dawson, H. Mattoussi, *Nat. Mater.*, **2010,** *9*, 676-684.
65. Jayakumar, C., C. M. Magdalane, K. Kanimozhi, K. Kaviyarasu, B. Jeyaraj, *J. Nanostruct¸***2017,** *7*, 155-164.
66. Thiagarajan, S., S. M. Chen, *Talanta,* **2007,** *74*, 212-222.
67. Palanisamy, S., S. Ku, S. M. Chen, *Microchim Acta,* **2013,** *180*, 1037-1042.
68. Huang, J., Y. Liu, H. Hou, T. You, *Biosens. Bioelectron.*, **2008,** *37*, 632.
69. Xu, T. Q., Q. L. Zhang, J. N. Zheng, Z. Y. Lv, J. Wei, J. J. Feng, *Electrochem Acta,* **2014,** *115*, 109-115.
70. Yan, J., S. Lin, Z. Zhang, G. He, P. Zhan, H. Liang, L. tian, X. Zhan, H. Jiang, *Colloids Surfs. B.*, **2013,** *111*, 392-397.
71. Choe, J. E., M. S. Ahmed, S. Jeon, *J. of Elcetrochem. Soc.*, **2016,** *163*, B113-B118.
72. Ramakrishnan, S., K. R. Pradeep, A. Raghul, R. Senthikumar, M. Rangarajan, N. K. Kothurkar, *Anal. Methods,* **2015,** *7*, 779-786.
73. Sun, C. L., H. H. Lee, J. M. Yang, C. C. Wu, *Biosens. Bioelectron.*, **2011,** *26*, 3450-3455.

Chapter 8

Time-dependent evolution of N-configurations in N-doped graphene films

8.1 Introduction

Graphene, a two dimensional (2D) crystalline allotrope of carbon[1], has attracted great interest for applications in the field of energy and storage devices due to its unique properties[1-3]. These unique properties include high chemical stability, high electrical conductivity, and large surface area[1, 4-10]; thereby enabling graphene to have potential applications in supercapacitors, photovoltaics, sensors, electronics, or Li batteries[11-14]. However, being a zero band gap 2D material[2, 15], graphene is not ready for its application in the next generation electronic devices because its electrical conductivity cannot be completely controlled when compared with the classical semiconductors (such as silicon, germanium, gallium arsenide, silicon carbide, etc.). Reports have however shown that graphene can compete with commercial semiconductors if its electrochemical properties are tuned. This can be achieved by either functionalization of the surface of graphene with gaseous molecules, metals, organic molecules, or by the chemical substitution of foreign atoms into the graphene lattice[16-19]. Theoretical and experimental attempts have indicated that chemical doping of graphene with heteroatoms is the most efficient technique for tailoring the electronic, chemical, optical and magnetic properties of graphene[20-22]; to broaden its applications. Doping with heteroatoms, such as nitrogen, phosphorus, sulphur, nitrogen/sulphur, or nitrogen/boron, allows graphene to have an open band gap; hence leading to the transformation of graphene into a p- or n-type semiconductor[23, 24]. It has been shown that the chemical doping influences the properties of graphene according to the at least two features of the dopant element, namely: (1) size of the dopant, and (2) dopant atom electronegativity[24]. These features play a significant role in determining the application of the doped graphene as well as in choosing the appropriate dopant.

Recent success in N-atom doping of carbon nanotubes (CNTs) to give N-CNTs[25] by chemical vapour deposition (CVD), arc discharge, and ammonia post-treatment techniques has

encouraged attempts for the chemical N-doping of graphene films. This is because nitrogen (65 pm) has a comparable atomic size to that of C (70 pm), thus making its incorporation into the graphene lattice possible. Additionally, nitrogen has an extra electron in its outer shell, which plays a significant role in predicting the applications of the N-doped graphene by either inducing n- or p-type semiconducting behaviour[24]. Typically, in most reports on synthesized N-doped graphene, X-ray photoelectron spectroscopy (XPS) studies have shown that N atoms can be bonded to the C atoms in graphene in at least four bonding configurations (Scheme 8.1).

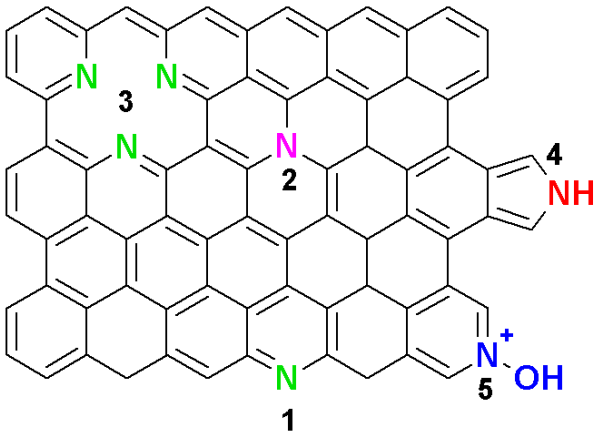

Scheme 8.1: Typical configurations of nitrogen atoms in graphene: (1) pyridinic N, (2) substitutional or graphitic N, (3) triple vacancy pyridinic N, (4) pyrrolic N, and (5) oxidized pyridinic-N (NOx).

The bonding configurations are as follows: pyridinic-N (398.1-398.3 eV), pyrrolic-N (399.8-400.2 eV), quaternary or graphitic-N (401.1-402.7 eV), and oxidised pyridinic-N (403-405 eV) [14, 22, 25-27]. Pyridinic-N is bonded to two C atoms at the edges of the graphene domains. Due to its sp^2-hybridisation, the pyridinic-N atoms contribute an extra p-electron to the delocalised π-system of graphene lattice[25-28]. In addition, pyrrolic-N atoms are sp^2-hybridised and are also bonded to two C atoms at the domain edges. Finally, graphitic-N atoms exhibit sp^2-hybridisation and introduce the remaining two electrons to the delocalised π- system[25-28]. For the oxidised pyridinic-N configurations, the N atoms are bonded to two C atoms and an O atom [25]. Thus, it can be concluded that each of the N-configurations affects the electronic and transport properties of graphene differently. For instance, theoretical studies have indicated that since both pyridinic and pyrrolic N-configurations occur at defects, and high concentrations of these configurations induce p-type semiconductor behaviour in nitrogen

doped graphene because they withdraw electrons from the graphene film[29, 30]. Additionally, the graphitic N-configuration was found to induce n-type conductivity, since one electron becomes engaged in a π bond while the fifth electron forms a partial π*-bonding state of the conduction band. Each graphitic N-configuration contributes to the π system of the graphene lattice, hence preserving the high mobility of charge carriers in N-doped graphene[29-30]. Contrary to theoretical predictions, experimental work by Li *et al.* showed that a crossover behaviour from p- to n-type could be observed in N-graphene with increasing degree of N-doping, especially for graphene films dominated by pyridinic and pyrrolic N-configurations[31]. Schiros and co-workers attributed this crossover behaviour to the hydrogenation of both pyridinic and pyrrolic N atoms, which then transforms them from p-type to n-type semiconducting behaviour[32].

Similar to N-CNTs, two approaches have been used for the synthesis of N-doped graphene. These include; (1) direct or in-situ doping during the synthesis of the graphene films and (2) post-doping of the as-synthesized graphene films with a nitrogen source. The latter doping method leads to surface-functionalization of graphene, whereas the former leads to the introduction of heteroatoms into the carbon lattice of graphene, thus resulting in the formation of homogeneously doped graphene films. In-situ N-doping is the preferred approach and it can be achieved via synthesis techniques such as chemical vapour deposition (CVD), segregation growth, solvo-thermal, laser ablation, microwave irradiation, and arc-discharge[22, 33-35]. Among the in-situ synthesis methods, the CVD technique has been extensively studied for the growth of large area N-doped graphene films from gaseous mixtures[22], liquid organic precursors[34], and solid precursors[35]. Apart from its easy scalability, CVD enables an easy approach for controlling the nitrogen content in a reaction by changing the flowrate, the ratio between the carbon and nitrogen sources, the growth temperature, as well as the metal catalysts[22, 36-37]. For instance, Qu *et al.*[36] showed that growth of N-graphene films on a Ni catalyst at 1000 ^{o}C using a 5:1 CH_4/NH_3 precursor gas mixture produced films consisting mainly of pyridinic and pyrrolic N configurations. On the other hand, Wei and co-workers[22] reported that the graphitic-N configuration was predominately found in N-graphene films grown at 800 ^{o}C on a Cu foil using a 1:1 CH_4/NH_3 gas mixture. Additionally, Luo *et al.*[37] synthesized pyridinic-N rich nitrogen doped graphene films on a Cu foil by using 1:1 and 3:1 C_2H_4/NH_3 mixture at 900 ^{o}C.

Interestingly, most reports indicated that successful CVD synthesis of N-doped graphene with varying nitrogen content is dependent on the concentration of the N-precursors material,

metal catalyst and the growth temperature. However, the evolution of the N-configurations with time (i.e. to study the evolution of the N configurations with time) has been little studied. Therefore, this investigation reports the facile method for an in-depth study and understanding of the of time-dependent APCVD N-doped graphene film growth using ammonia.

8.2 Experimental

8.2.1 Starting Materials

The reagents used in all experiments were of analytical grade. Acetone (99%, ACE, gold line (CP)) and methanol (MeOH, 99.5%), were bought from Sigma-Aldrich (South Africa). The argon (Ar, 99.9%), methane (CH_4, 99.98%), ammonia (NH_3, 10% in Ar) and hydrogen (H_2, 99.98 %) gases were supplied by Afrox, South Africa. Other materials include a copper foil (25 µm, 99.98%) from Sigma Aldrich (RSA), poly(methyl methacrylate) (PMMA, Mw ~999 000, crystalline, Sigma Aldrich), a silicon substrate with 300 nm silicon oxide layer (Sigma-Aldrich), and copper plate and iron wire (University of the Witwatersrand workshop). Distilled water was used throughout the experiments.

8.2.2 Synthesis and transfer of N-doped graphene films

The in-situ N-doping of graphene films was achieved using APCVD on a copper foil in a quartz tube furnace. All the films were grown using 10 sccm CH_4, 3 sccm H_2, 300 sccm Ar, and 5 sccm NH_3. An electrochemically cleaned[38] Cu foil was placed at the center of the cylindrical quartz tube (100 cm × 20 cm), and the tube was then inserted in a horizontal furnace. The furnace was heated to 1000 ^oC at a ramping rate of 10 ^oC/min under atmospheres of H_2 and Ar, and then held at the designated temperature for 30 minutes. The growth of the in-situ N-doped graphene films was carried out for varying times (2, 5, 10, and 20 min) under 10 sccm of CH_4 and 5 sccm of NH_3. In the control experiments, pristine graphene films were grown for the same times (2, 5, 10, and 20 min) using 10 sccm CH_4. Finally the reactor was *rapidly* cooled to room temperature by pushing the quartz tube outside the reactor.

After growth, both pristine and N-doped graphene films were then transferred onto the 300 nm SiO_2/Si substrate using the PMMA-assisted electrochemical delamination method [38]. Initially, a 1 cm × 1 cm square of the as-grown film on Cu was spin coated with a thin layer of PMMA at 2000 rpm for 60 sec, after which it was baked at 80 ^oC for 5 min to ensure good

adhesion of the PMMA on the graphene/Cu. From the electrolysis of water, the PMMA/graphene film was then detached from the Cu foil by the generated hydrogen bubbles. After the detachment of the PMMA/graphene film, the floating PMMA/graphene film was transferred onto the SiO_2/Si substrate. The transferred film was baked at 50 ^oC for 30 minutes to enable good adherence of PMMA/graphene onto the substrate. Finally, the PMMA was dissolved with warm acetone and the residual PMMA/acetone on the films was removed by washing the films with multiple volumes of methanol and distilled water.

8.2.3 Characterization

The structural characterization of the as-synthesized pristine and N-doped graphene films on 300 nm SiO_2/Si substrates was studied by Raman spectroscopy. Raman spectra of all films were collected on a Bruker Raman Senterra spectrophotometer (Bruker, South Arica) using a 532 nm excitation laser and at a very low laser power (0.5 mW) to avoid laser-induced heating which can damage the films. Optical imaging was captured by a 50x optical objective lens. The chemical composition of the prepared films was studied by X-ray photoelectron spectroscopy (XPS) at the Thermo Scientific factory in UK. The ex-situ XPS study was carried out on films grown on Cu foil with a Thermo Escalab 250. The radiation used was a monochromatised aluminium Kα radiation with a 400 μm spot size and a 'pass' energy of 60 eV was used.

8.3 Results and Discussions

The structural characterization of the as-grown films was determined by studying their optical images and Raman spectra; while the degree of N-doping and type of N-configurations were confirmed by studying their XPS spectra.

8.3.1 Microstructural analysis of the films

Optical micrographs (Fig.8.1) of N-doped graphene films transferred onto a 300 nm SiO_2/Si substrate showed large-area, continuous and uniform films. In comparison with their pristine graphene counter-parts (Fig. S8.1), N-doped graphene films exhibited regions of multilayers embedded within a uniform and continuous film. The multilayer regions can be ascertained by the dark spots. This is because for pristine graphene films on a 300 nm SiO_2/Si substrate the thickness can be verified by the colour contrast of the substrate due to the light interference effect[2, 3]. Therefore, the darker colour contrast of the substrates indicates a thicker film.

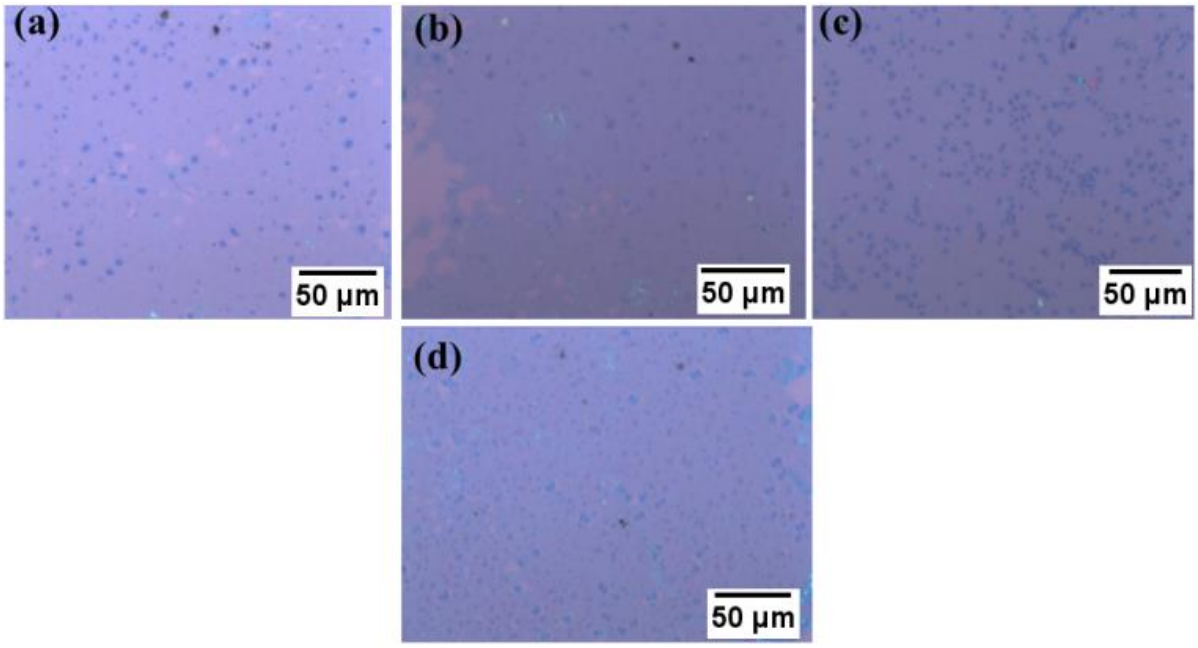

Figure 8.1: Optical images of N-doped graphene films grown at (a) 2 min, (b) 5 min, (c) 10 min, and (d) 20 min.

8.3.2 Raman Analysis of the films

To study the structural and electronic properties of the as-grown N-graphene films, Raman spectroscopy was used since it is a non-destructive and powerful technique for characterizing carbon materials[39-46]. Figure 8.2 shows the Raman spectra of both pristine and N-doped graphene films on a 300 nm SiO_2/Si substrate synthesized under the same growth conditions. The pristine graphene films (Fig. 8.2a) exhibited three Raman peaks, which are assigned to D (~ 1340 cm^{-1}), G (~ 1583 cm^{-1}) and 2D (~ 2675 cm^{-1}) bands, respectively[43, 44]. Interestingly, the relative intensity of the D band was found to decrease with increasing growth time (2-20 min). This is indicative of an improved quality of the graphene films with prolonged growth time. The Raman spectra of N-doped graphene films (Fig. 8.2b) showed four peaks, which can be assigned to D (~ 1350 cm^{-1}), G (~ 1590 cm^{-1}), D* (~ 1623 cm^{-1}), and 2D (~ 2678 cm^{-1}) bands. Furthermore, the pronounced D band relative intensity across the growth regime is an indication of graphene lattice distortion by N atoms. However, it can be seen that the relative D band intensity was not significantly affected by time.

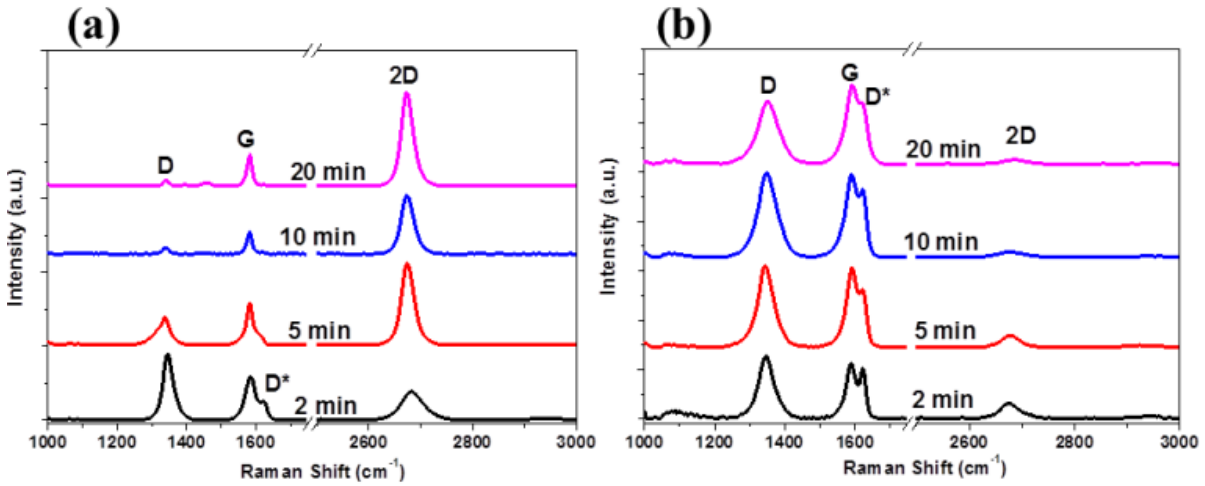

Figure 8.2: Raman spectra of pristine (a) and N-doped (b) graphene films grown at varying times.

Understanding of the graphene lattice distortion due to N-doping was done by assessing the observed Raman peaks (Fig. 8.2b). The existence of a strong defect-induced D band (~ 1350 cm^{-1}) in all N-doped graphene Raman spectra is indicative of the successful incorporation of N atoms into the graphene matrix, hence leading to a broken symmetry of the graphene lattice. The emergence of the D* band (~ 1623 cm^{-1}) on the shoulder of the G band is also considered as another Raman feature induced by defects. The D* band occurs through an intravalley double resonant scattering process, in which the defects provide the missing momentum required to satisfy the resonant process[39, 40, 43-45]. The relative intensities of these defect-induced peaks indicate the presence of substantial amount of defects; either in the form of in-plane heteroatom substitution, ad atoms, vacancies, and/or grain boundaries/edges. In contrast to both D and D* bands, the relative intensity of the lattice-defect sensitive 2D band (~ 2678 cm^{-1}) is significantly supressed across the growth regime. The 2D band originates from a two-phonon double resonant process and it does not require a defect to fulfil the resonant conditions[41, 47]. During N-doping, nitrogen atoms create lattice defects and introduce electron doping; and both of these processes increase the electron/hole scattering rate in N-doped graphene which then leads to the diminished 2D band intensity.

To further understand the degree of lattice distortion and the electronic properties of our films, the positions of the graphitic Raman peak (G band) were studied in detail. These peak positions were observed to have blue shifted by a maximum of ~ 9.5 cm^{-1} (red line in Fig. 8.3a), as compared to their graphene counterparts (black line in Fig. 8.3a). This blue shifting of the G band could be attributed to the increased electron doping, since this leads to

stiffening of the phonons for the G band[41, 46, 48]. In addition to the position of the G band, the position of the 2D band is another important parameter for an in-depth investigation of the electronic and structural properties of N-doped carbon materials[40, 41]. This is because the 2D band position is affected by the modification of the equilibrium lattice parameter as a result of lattice distortion by nitrogen dopants[41]. Figure 8.3b (red line) shows that the 2D band position in N-graphene films are blue shifted by a maximum of ~12.4 cm^{-1}. The strong blue shift observed in both G and 2D band positions signifies that not only electron doping contributes to the electronic, but also compressive/tensile strains on the C-C bonds could play an important role in the observed blue shifting of both peaks. Earlier theoretical calculations by Allen's group indicated that during N-doping different N-configurations lead to compressive strain on C-C bonds[50]. Their results showed that since pyridinic and pyrrolic bonding configurations have shorter bond lengths (~ 1.32 Å and ~ 1.37 Å respectively) than that of C-C (~ 1.42 Å), then a high concentration of these configurations result in a compressive strain on C-C bonds, thereby leading to a blue shift in 2D band instead of the well-known red shift. To support the finding by Allen *et al.,* Dettori and co-workers[51] showed that even for defected graphene, defects associated with bond reconstruction do lead to lattice deformation and stress/strain fields. Therefore based on the above analysis, we can ascertain that both electron doping and compressive strain on C-C bonds strongly contribute to the blue shifting of both G and 2D bands.

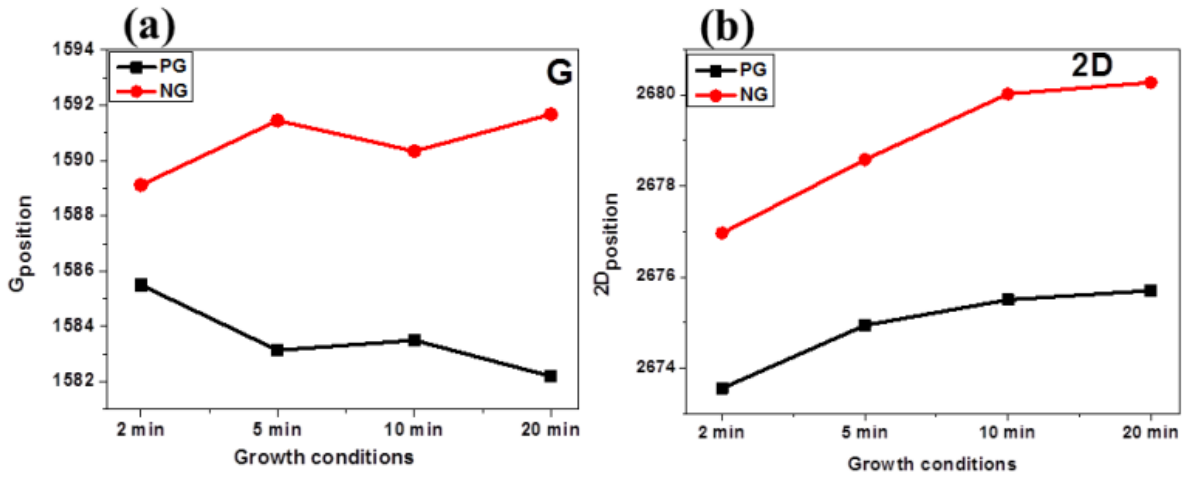

Figure 8.3: Peak positions for the G (a) and 2D (b) bands for both pristine and N-doped graphene films.

Commonly, the ratio of the relative intensity of D band to G band (I_D/I_G) is used to determine the quality or degree of disorder for as-grown pristine graphene[39, 40]. Figure 9.4a (black line)

shows that the level of disorder in pristine graphene films decreases with increasing growth time. Upon N-doping of graphene films, the I_D/I_G values (Fig. 8.4a, red line) are observed to be larger than those of pristine films, and this is due to the structural defects induced by introducing nitrogen dopants into the graphene lattice. Similarly, the I_D/I_G ratio is seen to decrease with increasing growth time; with the lowest intensity ratio found at 20 min growth time (I_D/I_G = 0.87). Ferrari and Robertson[49] attributed this phenomenon to the different arrangements of defects in sp^2 carbon materials. The high I_D/I_G ratio values signify the formation of nanocrystalline graphite domains. However, with increasing growth time, these nanocrystallites become smaller until they open up to form a matrix made up of sp^2 carbon clusters containing low sp^3 amorphous carbon domains. The loss in the sp^2 ring in graphite nanocrystallites decreases the intensity of the D band relative to that of the G band; hence the observed decrease in the I_D/I_G ratio. Therefore, the results indicate fewer lattice distortions are produced with increasing growth time. Recently, Eckmann and co-workers[42] indicated that the nature of defects in graphene films can be determined by Raman spectroscopy by using the intensity ratio of the defect-activated bands (I_D/I_{D*}). They showed that the I_D/I_{D*} is at a maximum (~13) for sp^3 hybridisation defects at graphene/graphite edges and grains boundaries, and that the value decreases to ~7 for on-site/vacancy-like defects. It finally reaches a minimum of ~3.5 for defects located at grain/domain boundaries. Therefore, by using the I_D/I_{D*} ratio we can determine the nature of defects present in our N-doped graphene films. Figure 8.4b shows that the maximum defect-sensitive intensity ratio I_D/I_{D*} is ~1.8, which suggests that the N-doped graphene films contain predominately grain/domain boundary defects.

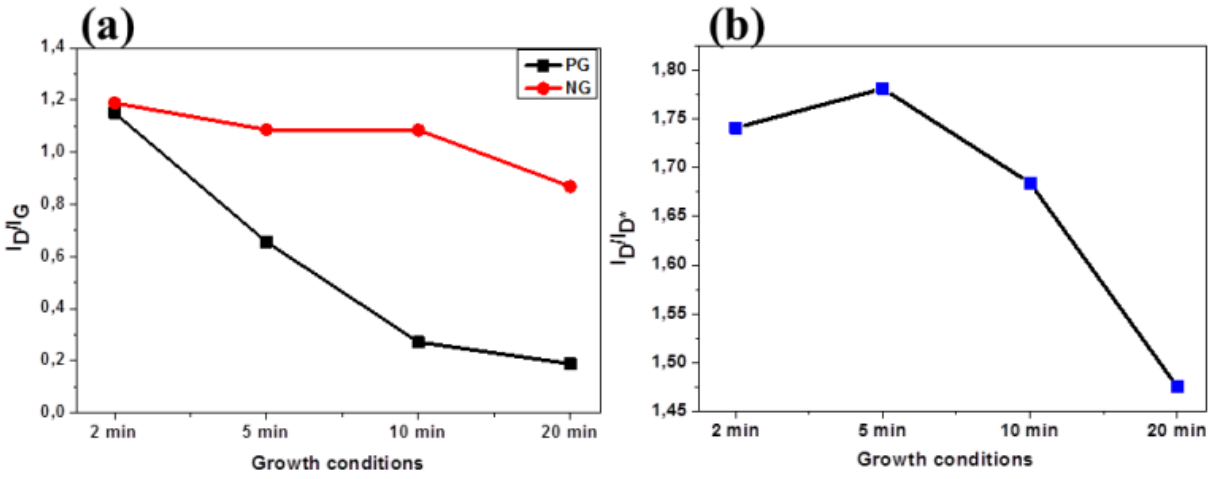

Figure 8.4: Evolution of I_D/I_G (a) with increasing growth time for both pristine and N-doped graphene films and I_D/I_{D*} (b) for N-doped graphene films.

8.3.3 XPS Analysis of the films

The XPS analysis was used as a surface sensitive and standard technique for determining the overall degree of N-doping and the different N-configurations in our films. The overall percentage concentrations of the carbon, nitrogen, and oxygen atoms (Fig. 8.5a) were determined by taking the integrated peak areas of the C1s, N1s, and O1s from the XPS survey spectra. It was seen that the carbon concentration increased (50.6%-71.9 at. %) while both nitrogen (2.3-2.0 at. %) and oxygen (47.0%-26.1 at. %) concentrations were found to decrease as the growth time increased. The ratio of the integrated peak area of N1s to that of the C1s (i.e. N/C ratio) was used to calculate the overall nitrogen content in the films, and this was found to be 4.68%, 3.75%, 3.25%, and 2.84% for the N-graphene films grown at 2, 5, 10, and 20 min, respectively (Fig. 8.5b). The results indicate that the nitrogen content was strongly dependent on the growth time of the as-synthesized films. The high degree of doping for films grown at 2 min (4.68 %) is in agreement with the largest defect intensity ratio (I_D/I_G) observed in figure 8.4a. Likewise, the low N-content for films grown at 20 min (2.84 %) correlated well with the low I_D/I_G ratio (0.87). The results indicate that short growth time (2 min) results in the formation of many poorly connected graphene domains, hence permitting a large incorporation of N atoms at the edges or grain boundaries. However, at a longer growth time the graphene domains have started to coalesce into bigger graphene domains, hence making incorporation of more N atoms into the graphene lattice more difficult. Compared to the pristine graphene films (Fig. S8.2), the increased oxygen content in the N-doped graphene films indicates a stronger oxygen adsorption ability on N-graphene films, hence demonstrating a potential application of N-graphene films in fuel cells[36].

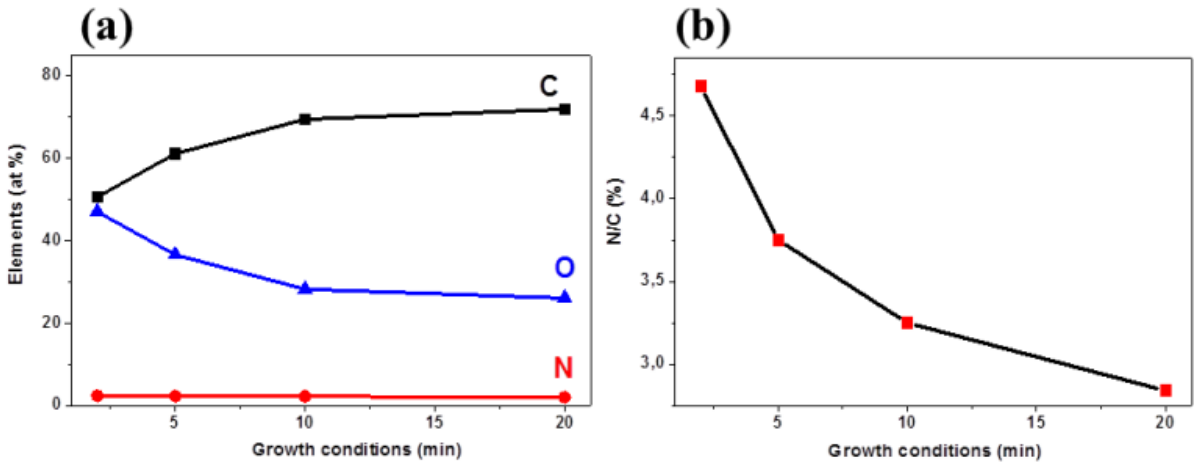

Figure 8.5: (a) Atomic composition analysis from the XPS survey spectra and (b) N/C content in N-doped graphene films grown using 10 sccm CH_4 and 5 sccm NH_3.

The deconvolution of the N1s XPS spectra was performed to determine the different bonding states (N-configurations) of nitrogen atoms in our N-doped graphene films (Figs 8.6 and S8.3 – S8.5). Figure 6.6 shows that the N1s spectra can be deconvoluted into at least four component peaks attributed to pyridinic-N (397.6-398.1 eV), pyrrolic-N (399.0-399.7 eV), substitutional/graphitic-N (400.6-401.7 eV), and the oxidised pyridinic-N (NO_x, 402.7-404. 6 eV), respectively[22, 25-28, 52]. The different relative intensities of the N-configurations indicate that the formation of N-graphene films rich in one N-configuration can be controlled by adjusting the growth time. The different chemical environments for the C atoms within the N-doped graphene films were determined by deconvoluting the high-resolution XPS C1s scan, as shown in figure 8.6 and figures S8.3-S8.5. All C1s XPS spectra exhibited an asymmetrical and tailing peak, which is indicative of different bonding states for C atoms. The main component located at 284.6-284.8 eV corresponds to the presence of C atoms in graphite-like sp^2 C-C bonds[25-27, 53]. When compared with the peak position of sp^2 C-C in graphite[53] and of the pristine graphene films grown under the same conditions (Table S8.2), the main component peak in N-doped graphene films is seen to shift to higher binding energies and this is attributed to the bonding of C atoms (*ca.* 2.55) to the more electronegative N atoms (*ca.* 3.04). Its high intensity indicates that most of the carbon atoms within the N-doped films remain bonded together in a conjugated honeycomb lattice. Two component peaks centred at 285.2-285.7 eV and 286.2-286.9 eV can be assigned to the contribution from N-sp^2-C (graphitic, pyridinic, and/or pyrrolic) and N-sp^3-C (defected sp^3-C bonds) respectively[25-27, 35, 53]. Finally, the peak at higher binding energies (288.3-288.5 eV) is attributed to the formation of C-O bonds from the oxygen at the edges of graphene domains[36, 47].

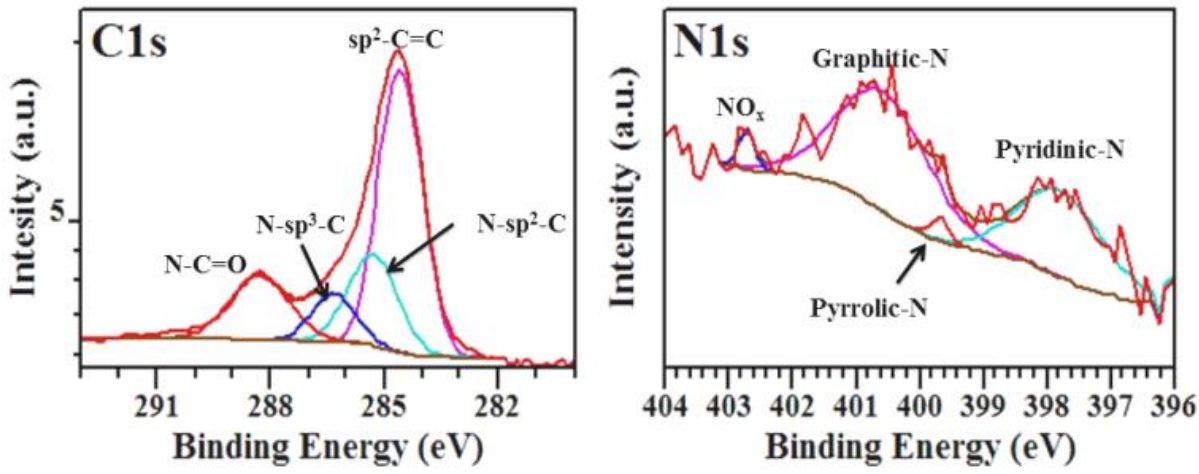

Figure 8.6: C1s and N1s core-shell XPS spectra of N-doped graphene films grown at 10 min.

The effect of growth time on the N-configurations was further investigated by determining the % concentrations of all configurations in the N-graphene films, as well as calculating the % amounts of each configuration per N-content (Figs. 8.7a and b). At 2 min and 5 min growth times the predominant N-configurations are the pyridinic- and pyrrolic-types; which indicate that most of the N atoms are located at the edges or on the defected sites on the graphene domains. Lack of any substitutionally incorporated N atoms confirms the existence of small graphene domains based on the stability for the formation of different bonding states (C=C (6.24 eV) > C-C (3.71 eV) > C-N (2.83 eV))[54]; thereby making incorporation of N atoms into the graphene domains difficult. At 10 min growth time, there is almost an equal rate of growth to give both graphitic-N and pyridinic-N bonding states. Finally, at a longer growth time (20 min), the pyridinic-N bonding states reach a maximum of 2.36 at %/ total N-content, while growth of both pyrrolic- and graphitic-N was found to be at almost the same rate. The absence of NO_x suggests that all the N atoms are perfectly incorporated into the graphene lattice. The observations indicate that prolonged growth time can cause healing of the graphene lattice to form more stable sp^2 bonds, therefore leading to the breakage of the C-N bonds and removal of nitrogen atoms[52]. The results are also in good agreement with theoretical calculations which indicate that N atoms are more thermodynamically stable at graphene edges, and with the pyridinic-type being the most stable [20-22, 51].

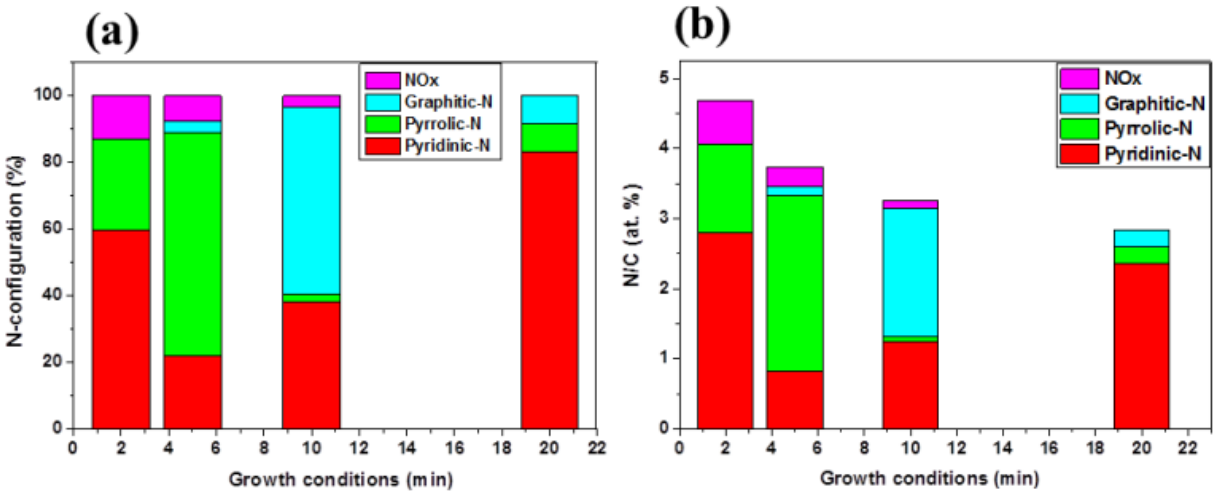

Figure 8.7: (a) % N-configurations and (b) contents of pyridinic-N, pyrrolic-N, graphitic-N and NOx as a function of growth time.

8.3.4 Growth mechanism of our samples

Based on the above characterization and analysis, we can, therefore, conclude that the time-dependent growth of N-doped graphene films follows at least a three-stage growth

mechanism (Scheme 8.2). In stage 1 (2 min and 5 min), the N-graphene films contain predominantly pyridinic and pyrrolic-N configurations along with some oxidised pyridinic-N type species. Interestingly, there are little or no graphitic-N type configurations detected, indicating that both pyridinic and pyrrolic-N atoms are found at the graphene domain edges and on defective sites. As a result, high defect density ratio values (I_D/I_G = 1.19 and 1.09 for 2 min and 5 min, respectively) were observed at this stage. The high relative intensity of the pyridinic-N configurations at 2 min growth time could be attributed to the different ways in which the pyridinic-N atoms are placed around the defects (i.e. to give mono-, di-, tri- and tetramerized pyridinic defects[55, 56]. In stage 2 (10 min), the N-graphene films consisted mainly of graphitic-N type bonding states with minimum amounts of pyridinic-N type atoms. This indicates that there is sufficient time in the doping reaction to permit the successful substitution of C atoms with N atoms, as well as to allow coalescence of graphene domains, as reflected by the slightly lower I_D/I_G value (1.05). At stage 3 (20 min), the N-graphene films consisted mostly of pyridinic-N, with a small amounts of graphitic and pyrrolic-N atoms and no oxidised pyridinic-N atoms. Unexpectedly, the film exhibited a low defect density ratio (I_D/I_G = 0.87), although pyridinic-N type are expected to increase the defect density. However, this improved quality indicates that prolonged growth time plays a significant role regarding the re-arrangement of pyridinic-N atoms. Since pyridinic-N atoms are bonded to sp^2 hybridized C atoms, we can suggest that at stage 3, most of the pyridinic-N atoms are located at the edges of the graphene domains with some of the N atoms located at defective sites to contribute to the defect density ratio.

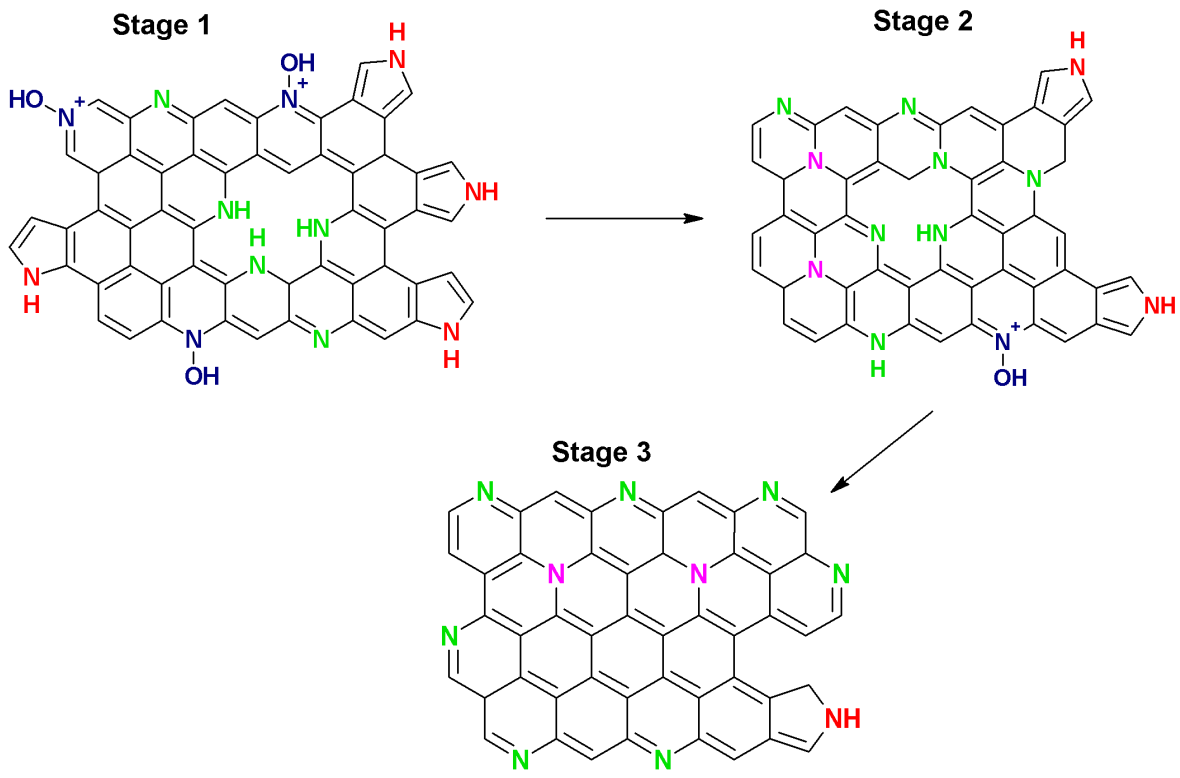

Scheme 8.2: Growth mechanism of N-doped graphene films with increasing growth time (Stages 1-3: pyridinic-N, pyrrolic-N, graphitic-N, oxidized pyridinic-N)

8.4 Conclusions

We have successfully synthesized continuous and large area N-doped graphene films using the co-growth of ammonia and methane gases via the APCVD technique. We used optical microscopy, Raman spectroscopy and X-ray photoelectron spectroscopy (XPS) to characterize the N-graphene films and to compare them with their pristine graphene counterparts. Nitrogen atoms were incorporated into graphene and the maximum N/C content of 4.68 at% was noted at a short growth time; while a minimum N/C content of 2.84 at% was observed at longer growth times. Furthermore, the type and amount of the N configurations (pyridinic, pyrrolic, graphitic and NO_x were found to be time-dependent. At 2 min and 5 min times, pyridinic, pyrrolic-N and NO_x bonding configurations dominated. A 10 min growth time led to the formation of graphitic-N-rich films, which also contained small amounts of pyrrolic-N and NO_x. In contrast, the longer growth time (20 min) produced N-graphene films rich in pyridinic-N with some graphitic-N bonding states. The films lacked NO_x bonding types and few pyrrolic-N configurations were observed.

References

1. Novoselov, K. S., A. K Geim, S.V. Morozov, D. Jang, Y. Zhang, *et al. Science*, **2004**, *306*, 666-669.
2. Geim, A. K., K. S. Novoselov, *Nat. Mater*, **2007**, *6*, 183-191.
3. Geim, A. K. *Science*. **2009**, ***324,*** 1530-1534.
4. Castro Neto, A. H., F. Guinea, N. M. R. Peres, K. S. Novoselov, A. K. Geim, *Rev. Mod. Phys.*, **2009**, *81*, 109-162.
5. Balandin, A. A., S. Ghosh, W. Bao, *et al.*, *Nano Lett*., **2008**, *8*, 902-907.
6. Balandin, A. A. *Nat Mater*., **2011**, *10*, 569-581.
7. Nika, D. L., A. A. Balandin, *J Phys Condens Matter*, **2012**, *24*, 23320-23323.
8. Chen, S. D., Y. Zhang, J. Wang, *et al*., *Sci China-Phys Mech Astron*., **2013**, *56*, 1466-1471.
9. Novoselov, K. S., Z. Jiang, Y. Zhang, *et al*., *Science*, **2007,** *315*, 1379-1381.
10. Li, X. L., G. L. Zhang, X.D. Bai, X. M. Sun, X. R. Wang, E. Wang, *et al*., *Nat Nanotechnol*., **2008**, *3*, 538-542.
11. Li, S. S., K. H. Tu, C. C. Lin, C. W. Chen, M. Chhowalla, *ACS Nano*, **2010**, *4*, 3169-3174.
12. Cheng, R., J. Bai, L. Liao, H. Zhou, Y. Chen, L. Liu, *et.al.*, *Proc. Nat. Acad. Sci.*, **2012**, *109*, 11588-11592.
13. Liu, C., Z. Yu, D. Neff, A. Zhamu, and B. Z. Jang, *Nano Lett.*, **2010**, *10*, 4863-4868.
14. Reddy, A. L. M., A. Srivastava, S. R. Gowda, H. Gullapalli, M. Dubey, P. M. Ajayan, *ACS Nano*, **2010**, *4*, 6337-6342.
15. Schedin, F., A. K. Geim, S. V. Morozov, E. W. Hill, P. Blake, M. I. Katsnelson, *et al.*, *Nat Mater*., **2007**, *6*, 652-655.
16. Giovannetti, G., P. A. Khomyakov, G. Brocks, V. M. Karpan, J. van den Brink, P. J. Kelly, *Phys Rev Lett*., **2008**, *101*, 026803-1-4.
17. Dong, X. C., D. L. Fu, W. J. Fang, Y. M. Shi, P. Chen, L. J. Li. *Small*, **2009**, *5*, 1422-1426.
18. Pablo, A. D. *Chem Phys Lett*., **2010**, *492*, 251-257.
19. Shinde, P. P., V. Kumar. *Phys. Rev. B*, **2011**, *84*, 125401.
20. Deifallah, M., P. F. McMillan, F. Cora, *J Phys Chem C*., **2008**, *112*, 5447-5453.
21. Panchakarla, L. S., K. S. Subrahmanyam, S. K. Saha, A. Govindaraj, H. R. Krishnamurthy, U. V. Waghmare, *et al.*, *Adv Mater*., **2009**, *21*, 4726-4730.

22. Wei, D. C., Y. Q. Liu, Y. Wang, H. L. Zhang, L. P. Huang, G. Yu, *Nano Lett.*, **2009**, *9,* 1752-1758.
23. Hou, Y. X., X. M. Geng, Y. Z. Li, *et al*., *Sci China-Phys Mech Astron*., **2011**, *54,* 416-419.
24. Duclaux, L. *Carbon*, **2002**, *40,* 1751-1764.
25. Ewels, C. P., M. Glerup, *J Nanosci Nanotechnol*., **2005**, *5,* 1345-1363.
26. Jansen, R. J. J., H. Vanbekkum, *Carbon*, **1995**, *33*, 1021-1027.
27. Nakayama, Y., F. Soeda, A. Ishitani, *Carbon*, **1990**, *28*, 21-26.
28. Casanovas, J., J. M. Ricart, J. Rubio, F. Illas, J. M. Jimenez-Mateos, *J. Am. Chem. Soc.,* **1996**, *118,* 8071-8074.
29. Jalili, S., R. Vaziri, *Mol. Phys.*, **2011**, *109*, 687-694.
30. Hou, Z. F., X. L. Wang, T. Ikeda, K. Terakura, M. Oshima, M. Kakimoto, *Phys. Rev. B: Condens. Matter Mater. Phys.,* **2013**, *87,* 165401-1654403.
31. Lu, Y. F., S. T. Lo, J. C. Lin, W. J. Zhang, J. Y. Lu, F. H. Liu, *et al., ACS Nano,* **2013**, *7*, 6522-6532.
32. Schiros, T., D. Nordlund, L. Palova, D. Prezzi, L.Y. Zhao, K. S. Kim, *et al., Nano Lett.*, **2012**, *12*, 4025-4031.
33. Ito, Y., C. Christodoulou, M.V. Nardi, *et al., ACS Nano*, **2014**, *8,* 3337- 3339.
34. Wang, Z., P. Li, Y, Chen, *et al*., *J Mater Chem C*., **2014**, *2*, 7396-7401.
35. Guo, B., Q. Liu, E. Chen, *et al., Nano Lett.*, **2010**, *10*, 4975-4980.
36. Qu, L., Y. Liu, J. B. Baek, L. Dai, *ACS Nano*, **2010**, *4*, 1321-1326.
37. Luo, Z., S. Lim, Z. Tian, J. Shang, L. Lai, B. MacDonald, *et al.,* J. *Mater. Chem.*, **2011**, *21,* 8038-8044.
38. Wang, Y., Y. Zheng, X. Xu, E. Dubuisson, Q. Bao, J. Lu, and K. P. Loh, *ACS Nano,* **2011**, *5*, 9927-9933.
39. Malard, L. M., M. A. Pimenta, G. Dresselhaus, M. S. Dresselhaus, *Phys Rep*., **2009**, *473*, 51-87.
40. Cancado, L. G., A. Jorio, E .H. Martins Ferreira, F. Stavale, C.A. Achete, R. B. Capaz, *et al*., *Nano Lett*., **2011**, *11*, 3190-3196.
41. Das, S. Pisana, B. Chakraborty, S. Piscanec, S.K. Saha, U.V. Waghmare, *et al., Nat Nanotechnol*., **2008**, *3*, 210-215.
42. Eckmann, A. Felten, A. Mishchenko, L. Britnell, R. Krupke, K.S. Novoselov, *et al., Nano Lett*., **2012,** *12,* 3925-3930.
43. Ferrari, A. C., *Solid State Commun.,* **2007**, *143,* 47-57.

44. Ferrari, A. C., J. C. Meyer, V. Scardaci, C. Casiraghi, M. Lazzeri, F. Mauri, *et al.*, *Phys. Rev. Lett.*, **2006**, *97*, 187401.
45. Casiraghi, S. Pisana, K. S. Novoselov, A. K. Geim, A.C. Ferrari, *Appl. Phys. Lett.*,**2007**, *91*, 233108.
46. Ni, Z. H., T. Yu, Y. H. Lu, Y. Y. Wang, Y. P. Feng, Z. X. Shen, *ACS Nano*, **2008**, *2*, 2301-2305.
47. Venezuela, P., M. Lazzeri, F. Mauri, *Phys Rev B.*, **2011**, *84*, 035433-1-25.
48. Zafar, Z., Z. H. Ni, X. Wu, Z. X. Shi, H. Y. Nan, J. Ba, *et al*., *Carbon*, **2013**, *61*, 57-62.
49. Maciel, I. O., N. Anderson, M.A. Pimenta, A. Hartschuh, H.H. Qian, M. Terrones, *et al.*, *Nat Mater.*, **2008**, *7*, 878-883.
50. Ferrari, A. C., J. Robertson. *Phys. Rev. B.* **2000**, *61*, 14095-14107.
51. Allen, F. H., O. Kennard, D. G. Watson, L. Brammer, A. G. Orpen, R. Taylor, *J Chem Soc, Perkin Trans 2*, **1987**, *12*, S1-S19.
52. Dettori, R., E. Cadelano, L. Colombo, *J Phys: Condens Matter.*, **2012**, *24*, 104020-1-10.
53. Lv, R. T., Q. Li, A. R. Botello-Me´ndez, T. Hayashi, B. Wang, A. Berkdemir, *et al.*, *Sci Rep*., **2012**, *2*, 586-1-8.
54. Wang, H., T. Maiyalagan, X. Wang, *ACS Catal*., **2012**, *2*, 781-794.
55. Ding, X. *J. Mater. Chem*., **2014**, *2*, 3717-3722.
56. Lin, C. K. *J. Phys. Chem. C.*, **2015**, *119*, 27131-27144.
57. Joucken, F., Y. Tison, J. Lagoute, J. Dumont, D. Cabosart, B. Zheng, *et al*., *Phys. Rev. B.*, **2012**, *85*, 161408 (R).

Chapter 9

The effect of N-configurations on the detection of dopamine at N-doped graphene modified ITO electrodes

9.1 Introduction

The electrochemical sensors have been widely studied as inexpensive materials for the selective and sensitive detection of various electroactive biomolecules in biological matrixes, such as blood, urine as well as extracellular fluids. Among the studied biomolecules, dopamine (DA) or 4-(2-aminoethyl) benzene-1,2-diol (Scheme 1), an important catecholamine found in the brain that acts as neurotransmitter, has received considerable attention in clinical and/or pharmaceutical researches due to its indispensable role in the renal, cardio vascular, hormonal and central nervous systems of humans [1-3]. An abnormal production of DA in the brain has been associated with the progression as well as the severity of neurological and neurodegenerative diseases such as aging of the brain, Alzheimer's, as Parkinson's, attention-deficient hyperactivity disorder (ADHD), schizophrenia, and Hunting's [4-9]. Thus, rapid and accurate detection of DA at nanomolar concentrations [1-8] is important not only for clinical diagnosis but also for the prevention of disorders arising from the abnormal control of DA concentrations. As such many conventional techniques have been developed for detection of DA in biological samples [10-18]. Among these techniques, electrochemical methods are widely used for the detection and determination of DA biological samples due to the electroactive behaviour of DA [15-20].

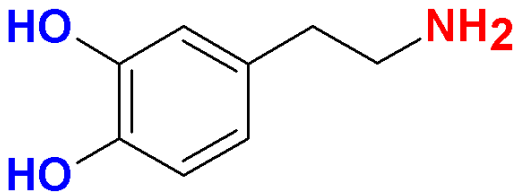

Scheme 9.1: Structure of dopamine or 4-(2-aminoethyl) benzene-1,2-diol

Owing to the ease for electro-oxidation of DA coupled with the excellent advantages of the electroanalysis techniques, numerous conducting materials including metal and metal oxides [21], carbon-based nanomaterials [22-28], quantum dots [29], magnetic nanoparticles [30], and polymeric nanoparticles [31], have been developed and used for the

direct determination of dopamine on traditional electrodes. Although, many carbon based nanomaterials have shown to be promising candidates [22-28], most electroanalytical techniques based on carbon nanomaterials are time-consuming, tedious, and require pre-concentration of the analytes. Thus, the development of new carbons for replacement or improvement of the already known and used carbon nanomaterials is necessary. One of these materials is graphene[32-34] and has been used for electrochemical determination of electroactive biomolecules such as dopamine, uric acid, and ascorbic acid [23-25, 31, 35, 36]. In spite of the extraordinary properties exhibited by graphene, the main drawback for practical applications of graphene lies in the production of graphene nanostructures with carefully controlled microstructural properties, such as functional groups, domain sizes and edge defects [23-25, 31, 35, 36].

Theoretical and experimental reports have indicated that chemical incorporation or doping of nitrogen atoms and other non-metallic elements (boron, or both nitrogen and boron) into the graphene lattice is a feasible approach for effectively tailoring the physicochemical properties of graphene [37-41]. Most importantly, nitrogen doping effectively changes the spin density and charge distribution of neighbouring carbons, thus enhancing electronic properties in N-doped graphene. Furthermore, the presence of nitrogen atoms in the graphene lattice enhances the biocompatibility and sensitivity for biosensing applications, by providing abundant binding sites for dopamine, uric acid, ascorbic acid, glucose, etc. [35-37]. Besides tailoring of graphene's intrinsic properties by doping with nitrogen atoms, the various ways in which nitrogen atoms become incorporated into graphene's lattice (Scheme 2), enables the electrical conductivity of N-doped graphene to be easily tuned by controlling the amount of the nitrogen dopant [37-41]. This is because each of the N-configurations affects the electronic and transport properties of graphene differently. As a result, substantial research effort is currently focused on investigating the electrocatalytic properties of nitrogen doped graphene-based electrodes towards the oxidation of biomolecules [19, 35, 36]. However, little attention has been paid to the influence and/or contribution as well as the importance of the content of each N-configuration on the electrocatalytic activity of graphene nanomaterials towards the oxidation of biomolecules such as dopamine. This may be ascribed to lack of simple and effective synthetic procedure to reproducibly grow graphene nanomaterials with the controlled content of one N-configuration.

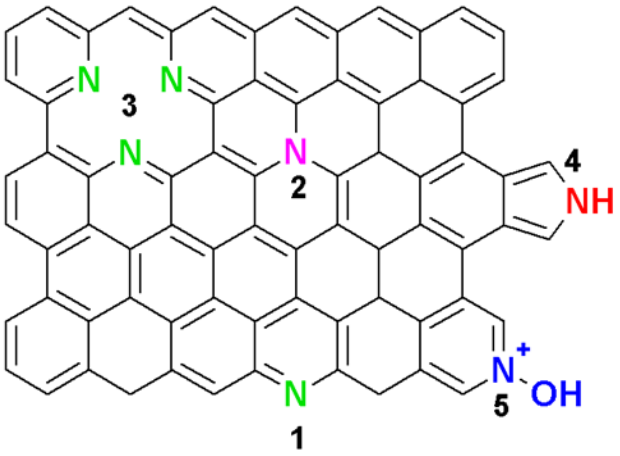

Scheme 9.2: Typical configurations of nitrogen atoms in graphene: (1) pyridinic N, (2) substitutional or graphitic N, (3) triple vacancy pyridinic N, (4) pyrrolic N, and (5) oxidized pyridinic-N (NOx) [39].

Therefore, a facile time-dependent technique to grow large-area N-doped graphene films on a Cu foil by atmospheric pressure chemical vapour deposition (APCVD) method was used[39]. The N-configurations in the as-grown N-graphene films were effectively controlled by varying the growth time during the CVD growth process [39]. In this study a link between the N-configurations, the amount of N-doping, the microstructural properties, and the inherent electrocatalytic oxidation of dopamine using an ITO electrode surface modified with the as-synthesized N-graphene films was investigated. In particular, in our study we have shown a correlation between N-configurations of graphene and the sensing behaviour of the N-graphene/ITO electrodes. Thin films of N-graphene were synthesized and transferred onto indium-doped tin oxide-coated glass (ITO) electrodes. ITO is a suitable low-cost photoelectric material due to its excellent optical transparency and satisfactory electrical conductivity. Consequently, ITO electrodes have found large scale application in various fields, such as light-emitting diodes (LEDs), solar cells, transistors, biosensors, electroluminescence devices, and liquid crystal displays (LCDs).

9.2 Experimental

9.2.1 Materials and reagents

The analytical grade reagents, which were used without prior purification, as well as substrates were purchased from Sigma-Aldrich, South Africa, and this included: dopamine hydrochloride (DA, ≥ 99%), sodium hydroxide pellets (98%, Merk), potassium dihydrogen

phosphate (KH_2PO_4, 99.99%), hydrochloric acid (HCl, 32.0 w/v %), potassium ferricyanide ($K_3[Fe(CN)_6]$, Merck, 99.98%), potassium chloride (KCl, Merck, 98.5%) and indium tin oxide (ITO)-coated glass slides (surface resistance 30 to 60 Ω/sq., thickness 1.1 mm, and optical transmittance of > 84%, refractive index of 1.517). N_2 (99.98%) gas was supplied by Afrox, South Africa. All voltammetric experiments used deionized water (> 18.2 MΩ.cm^2) that was purified through a Millipore ultrapure (type 1) water system (Bedford, MA, USA). A $K_3[Fe(CN)_6]$ stock solution (4 mM) was prepared with 1.0 M KCl, while stock solutions of DA (4 mM) and UA (4 mM) were prepared in a 0.1 M phosphate buffer solution ((PBS) at pH 6.02. The PBS was prepared by dissolving KH_2PO_4 in deionized water and the pH was adjusted by addition of 0.1 M NaOH or 0.1 M HCl solutions. Other standard solutions of DA were prepared by appropriate dilution of the stock solutions in PBS.

9.2.2 Instrumentation

Cyclic voltammetry (CV) and differential pulse voltammetry (DPV) were performed using a μAutolab potentiostat/galvanostat, running with the GPES software (version 4.900B) from Eco Chemie (Utrecht, Netherlands). The conventional three-electrode cell assembly consisted of an Ag/AgCl (3 M KCl) reference electrode, a platinum wire auxiliary electrode, and a working electrode made from the ITO-coated glass modified with N-doped graphene films (geometric area = 0.42 cm^2). The pH measurements of the PBS were performed on a Eutech Instruments bench pH/ion/mV-meter (Model pH/ion 510, Singapore). Prior to the electrochemical measurement, the N-doped graphene films, as electrode modifying materials, were characterised using a Thermo Escalab 250 X-ray photoelectron spectroscopy (XPS) [39].

9.2.3 Preparation of electrodes and procedure for electrochemical studies

Different N-doped graphene films were grown using APCVD on a copper foil in a quartz tube furnace. All the films were grown for various growth times (2, 10, and 20 min) using 10 sccm CH_4, 3 sccm H_2, 300 sccm Ar, and 5 sccm NH_3[39]. An ITO-coated glass electrode was cut into 0.60 cm × 0.70 cm pieces and sonicated in a solution mixture of acetone, ethanol and distilled water. The as-grown graphene films were transferred onto an ITO-coated glass electrode, using the PMMA assisted electrochemical delamination method [42]. In this process, the floating PMMA/graphene film was transferred onto the electrode. PMMA was then dissolved with acetone and the modified electrode was cleaned with multiple volumes of methanol and water. These electrodes were then labelled as NGr-2, NGr-10, and NGr-20 for ITO electrodes modified with N-doped graphene films grown at 2 min, 10 min, and 20 min, respectively.

In a typical experimental measurement, 20.0 mL of 0.1 M PBS (pH 6.02), as supporting electrolyte, was deoxygenated by purging with nitrogen gas for 30 min. Electrochemical behaviour and voltammetric detection of DA was obtained by addition of a defined volume of the stock solution to the electrochemical cell. The cyclic voltammograms were recorded by scanning two cycles between -1.0 V and 1.0 V at the step potential of 0.004889 V. The operating parameters for obtaining the quantitative analysis of DA by DPV were set as follows: modulation amplitude of 25.05 mV, initial potential of -0.25 V, end potential of 1.0 V, step increment potential of 1.95 mV, and sensitivity of 100 nA V^{-1}. Electrochemical behaviour and the voltammetric detection of DA were obtained by addition of a defined volume of the respective stock solution to the electrochemical cell. The voltammograms were then recorded. The detection limit (DL) was determined from, $DL = \frac{3\sigma}{s}$, where σ is the standard deviation of three low concentration measurements, and *s* is the slope of the linear relationship plot of anodic peak current (Ipa) vs. concentration (C) [43]. Furthermore, the sensitivities of the modified electrodes were calculated by dividing the slope of the calibration curve by the geometrical area of the electrode (0.42 cm^2) [44].

9.3 Results and discussions

The successful growth of nitrogen-doped graphene films with different compositions using the APCVD technique was achieved by varying the growth time [39]. The degree of doping and the different types of N-configurations of the as-grown films were determined by XPS characterization techniques [39]. The electrocatalytic activity of ITO electrodes modified with the as-synthesized N-doped graphene films towards the oxidation of dopamine was investigated by both cyclic voltammetry (CV) and differential pulse voltammetry (DPV) techniques.

9.3.1 Electrochemical behaviour of the modified electrodes

The determination of the different N-configurations in nitrogen doped graphene films, grown at different times (2, 10 and 20 min), were investigated using XPS. XPS results of the N-graphene films grown at different times (2, 10 and 20 min) showed that the 10 and 20 min samples exhibited similar pyridinic (38.1- 83.1%), pyrrolic (3.5-3.96%), graphitic (13.4-59.6%) and NOx (1.91%) configurations; while after 2 min the values were ~ 59.6%, ~31.2%, and ~9.17% for pyridinic, pyrrolic, and NOx-N-

configurations. (Fig. S9.1)[39]. The electrochemical behaviour of the different NGr/ITO electrodes was investigated in a ferricyanide solution by cyclic voltammetry. Figure 9.1 shows the corresponding CVs of 4.0 mM potassium ferricyanide solution (scan rate of 50 mV s^{-1}) at NGr-2/ITO (red line), NGr-10/ITO (pink line) and NGr-20/ITO (green line) electrodes in comparison with the bare ITO electrode (black line). On the bare electrode, the oxidation peak ascribed to the oxidation of $[Fe(CN)_6]^{4-}$ and the reduction peak attributed to reduction of $[Fe(CN)_6]^{3-}$ were observed at 363.6 mV and 197.3 mV, respectively. Upon modification of the ITO electrode with N-graphene films, the electrochemical responses for the $[Fe(CN)_6]^{3-/4-}$ redox couple showed an interesting trend, with an enhancement in both oxidation and reduction peak currents. In particular, the NGr-10/ITO electrode exhibited higher redox peak currents (Fig. 9.1 (pink line)), followed by the NGr-2/ITO electrode, and finally the NGr-20/ITO electrode Table 9.1.

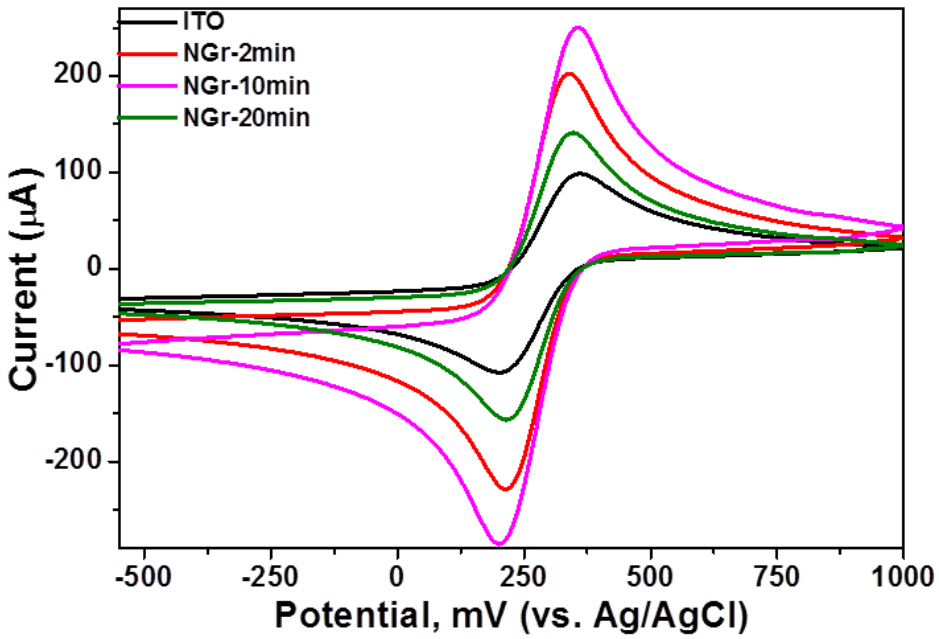

Figure 9.1: Electrochemical behaviour of DA on bare and NGr-modified ITO electrodes at buffer pH 6.02.

The significantly large peak currents at the NGr-10/ITO and NGr-2/ITO electrodes indicate that these electrodes are better oxidants and/or reductants for the $[Fe(CN)_6]^{3-/4-}$ redox couple in comparison with the bare and NGr-20/ITO electrodes. Although an enhancement in peak currents was observed for the NGr-10/ITO electrode, a large peak-to-peak separation (ΔEp = 156.4 mV) was also obtained. This indicated a slow electron transfer process between the redox couple and the electrode surface. On the

other hand, a faster electron transfer process was observed between the $[Fe(CN)_6]^{3-/4-}$ redox couple and the surface of NGr-2/ITO and NGr-20/ITO electrodes, as indicated by the ΔEp values of 126.9 mV and 135.8 mV, respectively.

The accelerated electron transfer process on the NGr-2/ITO electrode can be correlated with the presence of a large amount of defects as determined by Raman spectroscopy (I_D/I_G = 1.21, figure S9.1 [39]). The defects provide easy transport channels for the electrons to move from the $[Fe(CN)_6]^{4-}$ species to the hole-rich ITO surface during the oxidation process, as well as from the electron-rich ITO surface to the $[Fe(CN)_6]^{3-}$ species during the reduction process. Furthermore, the NGr-2/ITO electrode contained a relatively large concentration of pyrrolic N-configurations (59.6%). As pyrrolic-N atoms are sp^2-hybridised and bonded to two C atoms at the domain edges in a five-membered ring, theoretical studies have shown that high concentration of this N-configuration can withdraw electrons from the graphene film [45, 46]. As such, an electron rich environment is formed around pyrrolic-N atoms, and more electrons are thus available to be exchanged during the redox process of $[Fe(CN)_6]^{3-/4-}$ at the surface of the NGr-2/ITO electrodes. Thus, the results suggest that the presence of pyrrolic N-configurations on N-doped graphene surfaces influenced the charge transfer kinetics and enhanced the electrocatalytic activity of the $[Fe(CN)_6]^{3-/4-}$ redox couple.

Table 9.1: Peak potentials and currents of $[Fe(CN)6]^{3-/4-}$ on bare and modified ITO electrodes at scan rate of 50 mV s^{-1}

Electrode	Ep (mV)		Ip (μA)		ΔE
	Ep_a	Ep_c	Ip_a	Ip_c	
ITO	363.6	197.3	98.9	-108.2	166.3
NGr-2min/ITO	338.4	211.5	205.8	-226.8	126.9
NGr-10min/ITO	355.1	250.5	198.7	-287.2	156.4
NGr-20min/ITO	349.1	213.8	144.8	-152.9	135.8

9.3.2 Detection and electrochemical behaviour of dopamine

The electrocatalytic activity of bare and different N-doped graphene modified ITO electrodes against the redox of dopamine (DA) was investigated by cyclic voltammetry. Figure 9.2 shows the cyclic voltammetric (CV) responses of PBS (pH = 6.02) containing 0.13 mM DA at bare and the modified ITO electrodes. At the bare

ITO electrode, a peak current of 3.71 µA, ascribed to the oxidation of DA to dopaquinone was observed at 564.4 mV, and the peak current of -0.808 µA, which is associated to the reduction of the dopaquinone back to DA was located at -82.55 mV (Scheme 9.3).

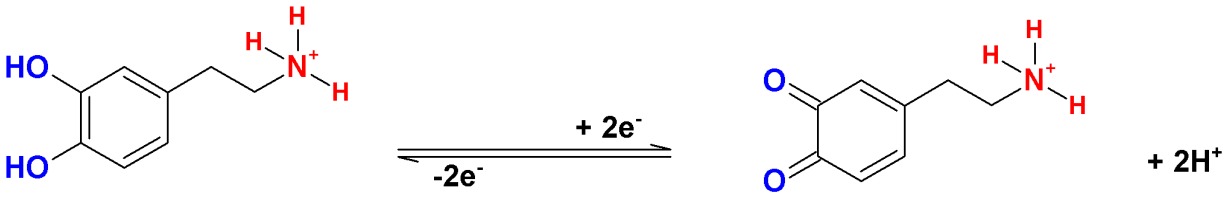

Scheme 9.3: A schematic representation of redox of dopamine to dopaquinone.

Modification of the ITO electrode with the doped graphene films led to enhanced electron transfer processes and improved electrocatalytic activity, as observed by the increased redox peak currents as well as negatively and positively shifted peak potentials, respectively (Table 9.2). For instance, both NGr-10 (pink line) and NGr-20 (green line) modified ITO electrodes exhibited higher oxidation peak currents, suggesting enhanced electron transfer. However, the large peak-to-peak separations (i.e. ΔE = 452.4 $mV_{NGr\text{-}10min}$ and 450.3 $mV_{NGr\text{-}20min}$) indicated slow reaction kinetics during oxidation and reduction of DA at the surface of NGr-10/ITO and NGr-20/ITO modified electrodes. These electrodes had fewer electrochemical actives sites in the form of pyrrolic N-configurations (i.e. $3.96\%_{NGr\text{-}10min}$ and $3.50\%_{NGr\text{-}20min}$) as well as basal and edge defects (I_D/I_G = $1.15_{NGr\text{-}10min}$ and $0.87_{NGr\text{-}20min}$). The high concentrations of pyrrolic N-configurations have been shown to increase the charge transfer kinetics by improving the π-π interaction between an N-graphene surface and the hydroxyl and amine groups on the DA molecule [35, 36]. Consequently, NGr-2/ITO electrode exhibited improved electrochemical activity against oxidation and reduction of DA, as shown by the ΔEp value of 175.7 mV. This electrode had relatively large concentration of pyrrolic N-configuration (~31.2%) and the large number of defects as indicated by the I_D/I_G value of ~1.21.

From our previous work, the maximum defect-sensitive intensity ratio (I_D/I_{D*}) for the NGr-2 min graphene films was determined to be approximately 1.8, which suggests that the NGr-2 min graphene films contain predominately grain/domain boundary defects [39]. Therefore, the edge defects (I_D/I_{D*} = 1.8, Fig.S9.2) in combination with pyrrolic N-configuration (~31.2%) provided binding sites for adsorption of DA species. This facilitated a faster electrocatalytic oxidation of DA at NGr-2 min modified working electrodes. In addition to pyrrolic N-

configuration, the presence of oxidized pyridinic N-configuration (NOx, ~9.17%) could also contribute to the improved electrocatalytic activity of the NGr-2/ITO electrode towards oxidation of DA. The NOx-configurations contribute to the enhanced activity through the increased hydrogen bonding between the DA molecule and the NGr-2/ITO electrode [35, 36]. To ascertain the role of pyrrolic and NOx-N-configurations towards the detection of dopamine, an experiment was conducted using N-graphene films grown at 5 min (data not shown here). XPS analysis showed that the values for the N-configuration in this NGr-5 min sample were ~24.89%, ~66.98%, ~2.32% and ~5.81% for pyridinic, pyrrolic, graphitic, and NOx-N-configurations [39]. Electrochemical detection studies indicated a greatly improved performance of the NGr-5/ITO electrode towards the electrochemical detection of DA as shown by the narrow peak-to-peak separation (ΔE = 166.2 mV); again confirming the importance of pyrrolic N-configuration in the reaction. In summary, it can be seen that by tuning the relative concentrations of different N-configurations in the graphene lattice, the subsequent electrochemical performance of N-doped graphene based electrodes towards detection of DA can be evaluated.

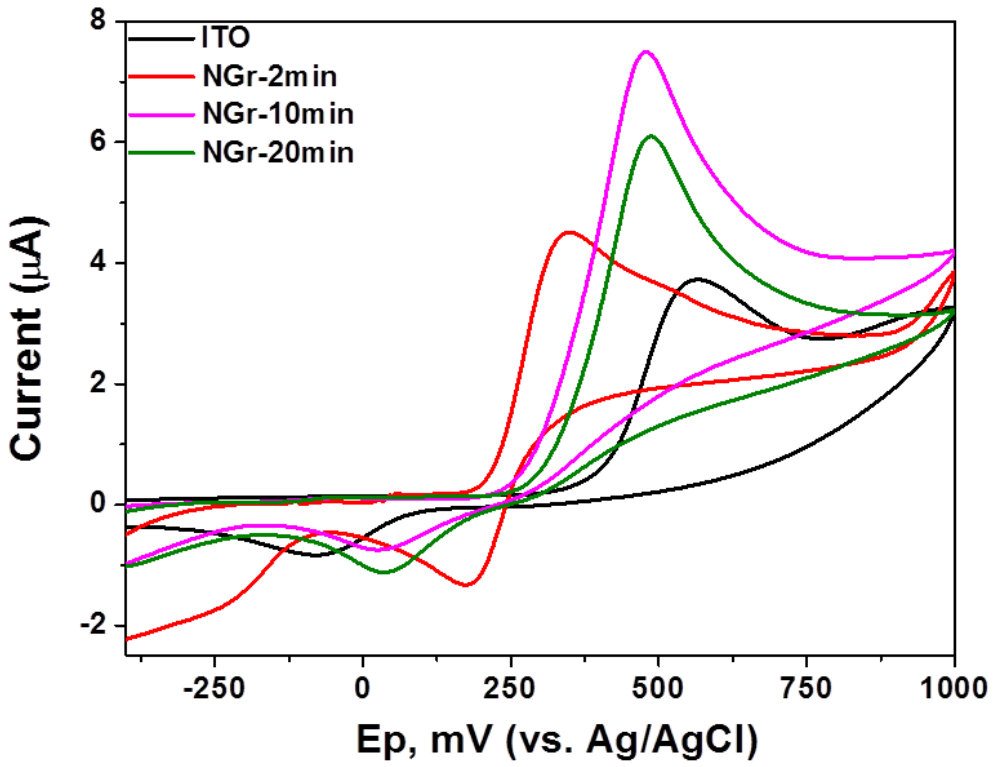

Figure 9.2: Electrochemical behaviour of DA on bare and NGr-modified ITO electrodes at buffer pH 6.02 and scanrate of 10 mV s^{-1}.

Table 9.2: Peak potentials and currents of 0.130 mM DA on bare and modified ITO electrodes at a scan rate of 10 mV s^{-1}

Electrode	Ep (mV)		Ip (µA)		ΔE
	Ep_a	Ep_c	Ip_a	Ip_c	
ITO	564.4	-82.55	3.713	-0.8075	647.0
NGr-2min/ITO	348.4	172.7	4.538	-1.307	175.7
NGr-10min/ITO	477.3	24.92	7.508	-0.7432	452.4
NGr-20min/ITO	486.7	36.42	6.107	-1.109	450.3

9.3.3 Influence of scan rate on the detection of DA

The reaction kinetics of ITO electrodes modified with the N-doped graphene films were investigated by studying the influence of scan rate (υ) on the electrochemical responses of DA redox process (Fig. 9.3). As the scan rate is increased, the redox peak currents (Ipa and Ipc) were observed to increase, while the redox peak potentials (Epa and Epc) shifted to more negative and positive values. The increasing shift in peak potentials with increasing scan rate generated large potential separations (ΔE), which is characteristic of a quasi-reversible reaction[46-48]. Interestingly, the oxidation peak currents of DA at NGr-10/ITO and NGr-20/ITO electrodes (Figs. 3b and c) increased linearly in the scan rate range of 10-40 mV s^{-1} and 10-100 mV s^{-1}, respectively. On the other hand, the oxidation peak currents of DA at NGr-2/ITO electrode (Fig. 9.3a) increased linearly over a wide scan rate range, with the cut-off value for this work being set at 300 mV s^{-1}. The results could indicate supersaturation of charge on the electrode surface during the oxidation process. Thus for the NGr-10/ITO electrode, supersaturation is reached earlier (~40 mV s^{-1}) due to the presence of more graphitic-N boding states, whereas at the NGr-20/ITO electrode, supersaturation is reached later (~100 mV s^{-1}) due to the presence of fewer graphitic-N boding states (Fig. S1). This is because graphitic-N configurations exhibit sp^2-hybridisation and introduce an extra two electrons to the delocalised π- system [45, 46]. This increases the mobility of charge carriers on the electrode surface. On the contrary, lack of graphitic N-bonding states at the NGr-2/ITO electrode suggests that there is a free exchange of charge between the electrode surface and the DA redox couple with increasing scan rate. The results indicate that modification of ITO electrodes with defective N-doped graphene films

(NGr-2min) leads to development of more stable N-graphene-based sensors for investigating the oxidation of DA at higher scan rates.

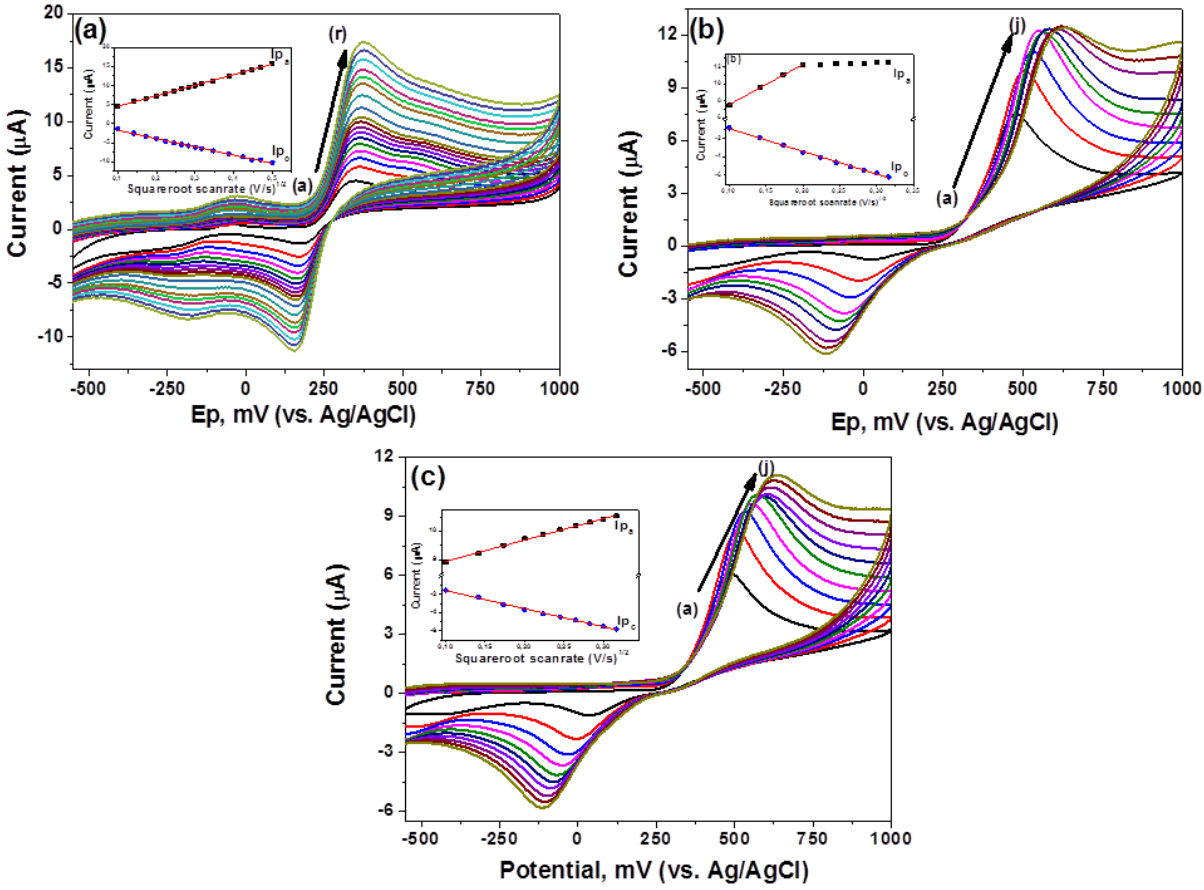

Figure 9.3: Scan rate studies of DA in PBS (pH 6.02) on (a) NGr-2 min, (b) NGr-10 min, and (c) NGr-20 min. Inserts: Linear relationship between peak currents and square root of scan rate.

As the scan rate was increased, a good linear relationship of the redox peak currents (Ipa and Ipc) with the square root of the scan rate ($\sqrt{\upsilon}$), was obtained (Fig. 9.3 inserts). This is characteristic of a diffusion-controlled process at all modified electrodes [46-49]. Moreover, from the linear plots of log Ipa vs. log υ, the transfer coefficients (α) were determined to be 0.460, 0.453, and 0.368 for NGr-2 min, NGr-10 min and NGr-20 min modified ITO electrodes, respectively (Table 3), which are close to the theoretical value of 0.5 for a quasi-reversible process [46-49]. Furthermore, a linear dependence of the redox peak potentials (Epa and Epc) with ln υ for the electrocatalytic oxidation and reduction of DA at the N-graphene modified ITO electrodes is shown in figure 4. By assuming a two electron – two proton redox process (Scheme 9.3) and using the Nicholson's equation [50, 51], the apparent heterogeneous transfer rate constant (k_s) for

the redox process of DA at the electrode surface of NGr-2/ITO, NGr-10/ITO and NGr-20/ITO electrodes were calculated to be 402.9×10^{-3} s^{-1}, 10.1×10^{-3} s^{-1}, and 7.92×10^{-3} s^{-1}, respectively. The heterogeneous electron transfer (HET) rate constant is a measure of the transfer of electrons from/to the electrode surface and to/from the DA molecule [23-25]. This rate constant is known to be correlated not only to the biomolecule of interest but also to the amount of defects, functional groups and impurities present on the N-graphene modified electrode surface [23-25].

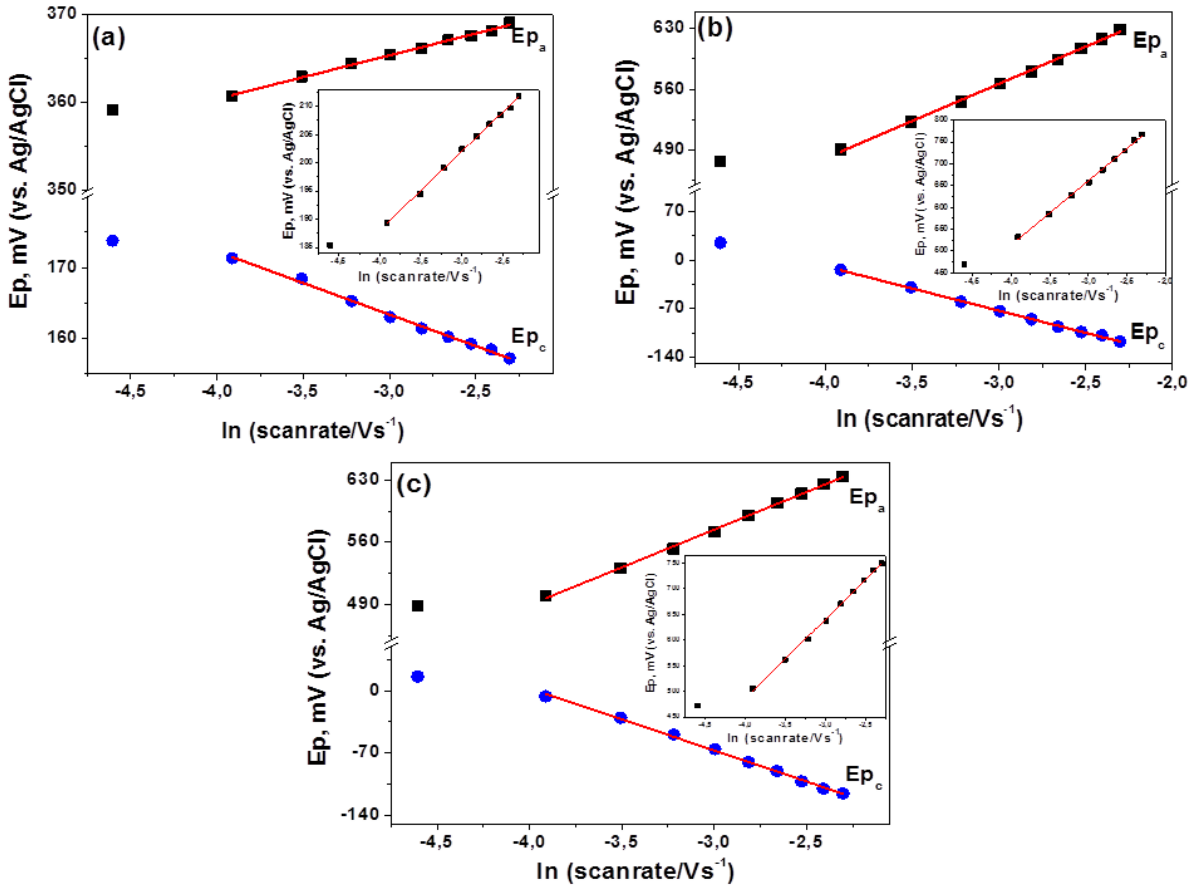

Figure 9.4: Linear relationships between Ep and ln scan rate (υ) on (a) NGr-2 min, (b) NGr-10 min, and (c) NGr-20 min. Inserts: Linear relationship ΔEp vs. ln υ.

The significantly large HET rate constant of DA at the NGr-2/ITO electrode (402.9×10^{-3} s^{-1}) can be attributed to the unique structural properties of the N-graphene films, such as the large amount of edge defects ($I_D/I_{D*} \approx 1.8$, Fig. S9.2) as well as the large concentrations of pyrrolic N-configuration (~31.2%) and oxidized pyridinic N-configuration (NOx, ~9.17%). Consequently, the results are in good agreement with reports that have shown that the HET rates of edge and basal planes of graphene are dramatically different for the redox reaction of ferro/ferricyanide, $Fe^{2+/3+}$, dopamine,

uric acid, and ascorbic acid; with the edge planes exhibiting faster HET rates than the basal planes [23-25].

Table 9.3: The electrochemical parameters of DA on modified electrodes

Electrode	α	k_s (s^{-1})
NGr-2 min/ITO	0.460	402.9×10^{-3}
NGr-10 min/ITO	0.453	10.14×10^{-3}
NGr-20 min/ITO	0.368	7.923×10^{-3}

9.3.4 Influence of pH of the buffer solution

In order to investigate the influence of the pH of the phosphate buffer solution on the electrochemical oxidation of dopamine at NGr/ITO electrodes, differential pulse voltammograms (DPVs) of 0.13 mM DA were recorded in the pH range of 3.05 to 9.03 (Fig. 9.5). The pH studies were conducted since electrochemical oxidation of DA is a two-electron and two-proton processes (scheme 9.3) [47], thus, any changes in pH of the supporting electrolyte should have an impact on the electrocatalytic responses of dopamine. As shown in figures 9.5a-c, no major deviations in the oxidation behaviour of DA at the NGr/ITO electrodes was observed, indicating similar oxidation processes occurred on the electrode surfaces at different PBS pH values. The oxidation peak currents of DA increased with increasing pH, indicating that high pH values favour the oxidation reaction of DA to form *o*-dopaquinone by the loss of two protons from the hydroxyl groups and loss of two electrons (Scheme 9.4, step 1). Furthermore, the oxidation peak potentials shifted to the more negative values with increasing buffer pH, indicating an increased electron transfer and easier oxidation of DA due to reduced overpotentials. A linear relationship between the oxidation potentials (Epa) and PBS pH values was obtained in the range of 3.05 – 8.02 for all NGr/ITO electrodes. The slopes of the linear plots were calculated to be -84.0 mV pH^{-1}, -81.8 mV pH^{-1}, and -75.6 mV pH^{-1} for NGr-2/ITO, NGr-10/ITO, and NGr-20/ITO electrodes, respectively. The measured slopes were found to be larger than the theoretical Nernst value (-59 mV pH^{-1}) [48, 52, 53], implying that the oxidation process of DA at all NGr/ITO electrodes occurred more rapidly. Most importantly, the value of the linear slope for NGr-2/ITO electrode (-84.0 mV pH^{-1}) was larger than that of the other modified electrodes. This corroborated the significantly large HET rate constant (402.9×10^{-3} s^{-1}).

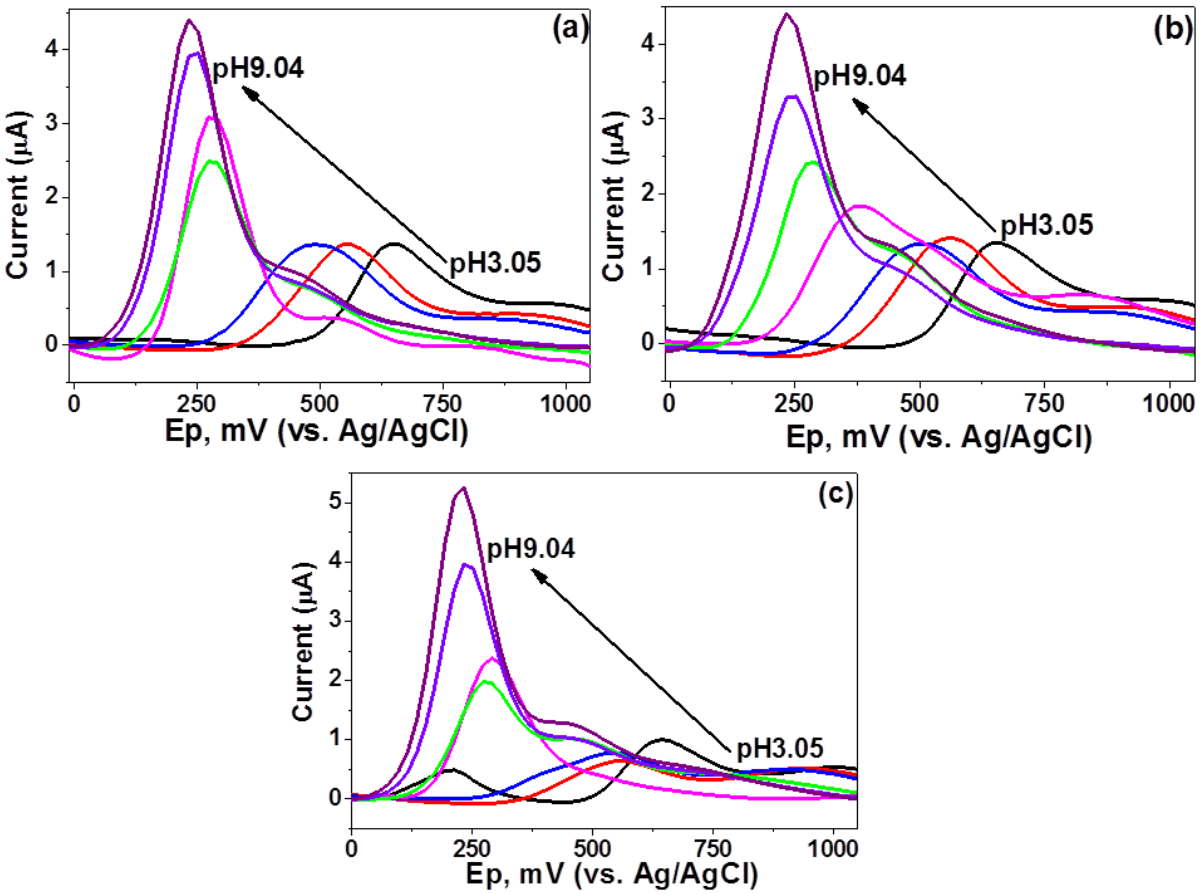

Figure 9.5: DPVs of DA on (a) NGr-2/ITO, (b) NGr-10/ITO, and (c) NGr-20/ITO electrodes at different buffer pH values.

The general mechanism depicting the electrochemical behaviour of DA on the modified electrodes in buffer solutions with different pH values can be shown in scheme 9.4. Initially, the parent DA molecule is oxidized to form *o*-dopaquinone by the loss of two protons from the hydroxyl groups, which is then accompanied by loss of two electrons, while *o*-dopaquinone is easily reduced back to dopamine (step 1) [47]. However, during the oxidation of dopamine in buffer solutions of neutral and alkaline pH values (7.03 – 9.04); there is an increased production of OH^- species which leads to a major deprotonation of the *o*-dopaquinone [48, 52, 53]. Reports have indicated that the presence of OH^- groups leads to the deprotonation of o-dopaquinone by a cyclization reaction to form leucodopaminochrome through a proton-assisted intramolecular 1,4-Michael addition reaction (step 2) [48, 52, 53]. The resultant leucodopaminochrome is more easily oxidized than the parent DA molecule, and undergoes a further two-electron oxidation to form dopaminochrome (step 3) [48, 52, 53]. As it is expected that the electrochemical responses for the oxidation of DA at the modified

electrodes is dependent on pH media of the buffer solution, then voltammograms depicting varying electrochemical responses are expected to be observed at different PBS pH values. Consequently, in acidic media (pH 3.05 – 5.01), slightly increasing oxidation peak currents were observed for the oxidation of DA at all NGr/ITO electrodes. This can be attributed to the dissociation of the surface-bound acidic groups as well as the increased electrostatic attraction between the DA molecules and the modified electrodes. However, in neutral to alkaline media (pH 7.03 – 9.04), an increase in oxidation peak is observed, suggesting that the oxidation reaction leading to the formation of dopaminochrome is more favourable. Interestingly, when the PBS media has a pH = 9.03, no further negative shift was observed for the oxidation peak potentials, whereas the oxidation peak currents were observed to increase. This can be attributed to the pKa value of dopamine (*ca*. 8.93), which suggests that in more alkaline media dopamine remains in its neutral form.

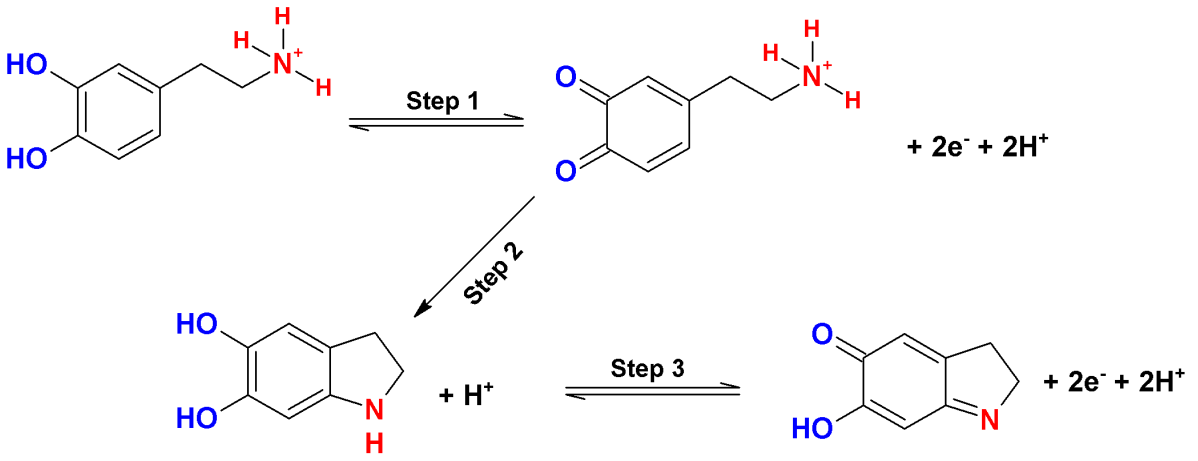

Scheme 9. 4: The general mechanism for the electrochemical oxidation of DA at different pH values of the buffer solution.

9.3.5 Concentration studies

The quantitative analysis of DA at the NGr/ITO electrodes was investigated using differential pulse voltammetry (DPV) through the determination of the linear detection ranges as well as the limits of detection. The corresponding DPV plots of the electrochemical responses at NGr/ITO electrodes versus the concentration of DA in a phosphate buffer solution of pH 6.02 are illustrated in figure 9.6. The oxidation peak currents, centred at 238 mV, 297 mV, and 248 mV, increased linearly with increasing concentration for the detection of DA at NGr-2/ITO, NGr-10/ITO and NGr-20/ITO electrodes, respectively. The negatively shifted peak potentials on NGr-2/ITO electrodes indicate the facile electrochemical oxidation of DA. A linear relationship

between the oxidation peak currents (Ipa) and the concentration of DA was obtained in the concentration ranges of 2 – 240 µM, 2 – 150 µM and 4 – 40 µM for DA at NGr-2/ITO, NGr-10/ITO and NGr-20/ITO electrodes, respectively. From these linear plots, the detection limits of DA, with the signal to noise ratio of 3, were determined to be 0.131 µM (NGr-2/ITO), 0.153 µM (NGr-10/ITO), and 0.645 µM (NGr-20/ITO). Moreover, the sensitivities of the modified electrodes were determined to be 0.0923 $\mu A.\mu M^{-1}cm^{-2}$, 0.0791 $\mu A.\mu M^{-1}.cm^{-2}$, and 0.0188 $\mu A.\mu M^{-1}cm^{-2}$ for NGr-2/ITO, NGr-10 min and NGr-20/ITO electrodes, respectively. The results indicated that the NGr-2 min/ITO electrode was the most sensitive of all electrodes towards the electrochemical oxidation of dopamine over a large concentration range. Thus, based on the criteria for the classification of a high performance sensor, which includes very low detection limit, good sensitivity, large detection range, and fast electron transfer kinetics, it can be argued that NGr-2 min/ITO electrode is the best electrode, of those studied, for the determination of DA.

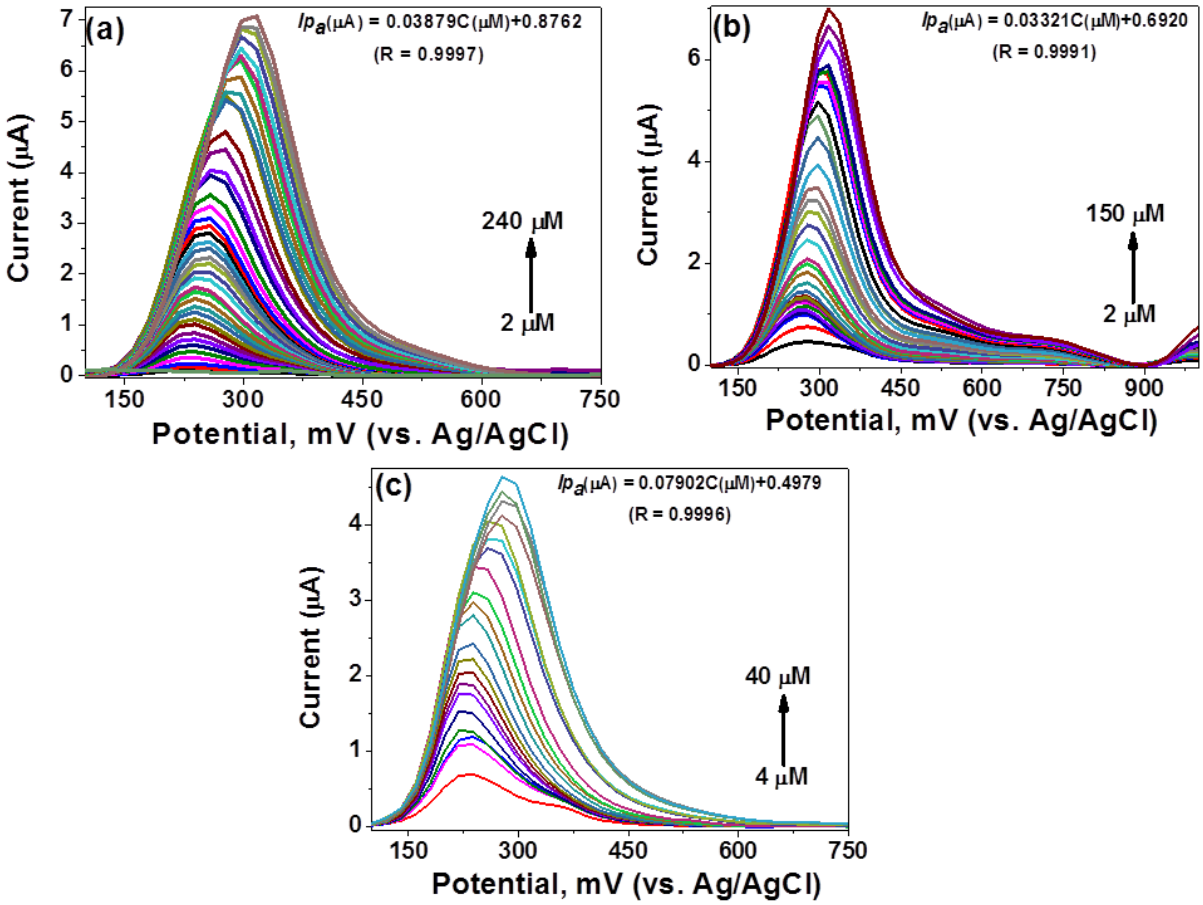

Figure 9.6: Concentration studies of DA on (a) NGr-2min, (b) NGr-10 min, and (c) NGr-20 min modified ITO electrodes at buffer pH 6.02.

Table 9.4: The detection limit, sensitivity and linear ranges for determination of DA

Electrode	Ep_a (mV)	Sensitivity ($\mu A.\mu M^{-1}.cm^{-2}$)	Linear range (µM)	Detection Limit (µM)
NGr-2 min/ITO	238	0.0923	2 - 240	0.131
NGr-10 min/ITO	297	0.0791	2 - 150	0.153
NGr-20 min/ITO	248	0.0188	4 - 40	0.645

The calculated limits of detection of DA at the NGr/ITO were compared to the reported data (Table 9.5). In particular, the detection limits of DA on the NGr-2/ITO electrode was smaller than the detection limits of DA at glassy carbon electrodes (GCE) modified with N-doped reduced graphene oxide nanosheets[19] as well as at GCE modified with other nitrogen doped carbonaceous materials [59, 61]. On the other hand, dopamine electrochemical sensors based on other nitrogen doped carbon based nanomaterials [54, 55, 56-58, 60] exhibited very low detection limits over wide linear concentration ranges. For instance, Nsabimana *et al.* [55] ascribed the enhanced electrocatalytic performance to the presence of the conducting porous structure which facilitated improved mass transport for dopamine molecules as well as the enhancement of the electron transfer rates between dopamine species and the nitrogen doped carbon lattice. Additionally, a relatively high density of oxygen functional groups increased the hydrogen bonding and improved the π-π interaction between DA and the carbon interface, hence promoting faster charge transfer [54, 55, 56-58, 60]. In general, it can be observed that the presence of defects and defective nitrogen configurations on the electrode surface greatly enhanced the electrocatalytic activity and sensitivity of the ITO electrodes towards oxidation of DA.

Table 9.5: Comparison of electrocatalytical data for detection of DA

Electrode	Linear range (µM)	Detection Limit (µM)	Predominant N-config.	N/C (%)	Reference
NGr-2 min/ITO	2 - 240	0.131	pyrrolic (27.4%), pyridinic (59.6 %)	4.68	This study
NGr-10 min/ITO	2 - 150	0.153	graphitic (56.3%), pyridinic (38.1%)	3.25	This study
NGr-20 min/ITO	4 - 40	0.645	pyridinic (83.1 %)	2.84	This study
NGF/GCE	0.1 – 80	0.030	pyridinic, pyrrolic	2.3	54
NGO/GCE	0.5 – 170	0.25	pyridinic, pyrrolic	N/A	19
3D-NHPC/GCE	0.05 – 14.5	0.020	pyrrolic	2.01	55
MNC/GCE	0.001 – 30	0.001	pyridinic, pyrrolic	12.2	56
3D-NGO/GCE	3 – 100	0.001	pyridinic, graphitic	2.79	57
NCQDs/GCE	0 - 100	0.001	pyridinic, pyrrolic	32.5	58
N-HCS/GCE	1 - 400	0.30	graphitic, pyridinic	N/A	59
NPCNP/GCE	0.5 – 30	0.011	graphitic, pyridinic	1.67	60
NCNF/GCE	1 – 10	0.5	pyridinic, pyrrolic	N/A	61

**ITO -> indium tin oxide, NGr -> N-doped graphene film, NGO -> N-doped reduced graphene oxide nanosheets, GCE -> glassy carbon electrode, NGF-> nitrogen doped graphene fibres, NHPC->nitrogen doped hierarchically porous carbon, MNC -> mesoporous nitrogen doped carbon, NCQDs -> nitrogen doped carbon quantum dots, NHCS -> nitrogen doped hollow carbon spheres, NPCNP-> nitrogen doped porous carbon nanopolyhedra, NCNF -> nitrogen doped carbon nanofibers.*

9.4 Conclusions

In summary, nitrogen doped graphene films containing different N-configurations were successfully used for fabrication of modified ITO-based sensors. The electrocatalytic activity of the NGr-modified ITO electrodes towards the oxidation of dopamine was investigated. The results indicated that structural and electronic properties of N-doped graphene films influenced the electrochemical oxidation of DA differently. For instance, DA was detected in the concentration range of 2 – 240 µM, with a limit of detection of 0.131 µM (S/N = 3) and sensitivity of 0.0923 µA μM^{-1} cm^{-}

^{2} at the NGr-2/ITO electrode. Moreover, faster apparent heterogeneous transfer rate constant (k_s) of 402.9×10^{-3} s^{-1} and high sensitivity at the NGr-2/ITO electrode was attributed to the presence of more defective N-configurations (pyrrolic-N, pyridinic-N, and NO_x) on NGr-2 min films. The results suggested that controlled incorporation of nitrogen atoms into graphene lattice resulted in different electrocatalytic performances of N-graphene-based ITO electrodes towards oxidation of dopamine. Moreover, the high content of pyrrolic N-configuration improved the electrocatalytic activity through enhanced π-π interaction between DA and the carbon interface and increased charges transfer rate. In general, the study provided insight into understanding how different structural and electronic properties of graphene arising from the incorporation of nitrogen atoms impacted its electrocatalytic activity for determination of dopamine.

References

1. Gottas, A., A. Ripel, F. Boix, V. Vindenes, J. Moland, E. L. Oiestad, *J. Pharmacological and Toxicological Methods,* **2015,** *74,* 75-79.

2. Floresco, S. B., A. R. West, B. Ash, H. Moore, A. A. Grace, *Nature Neurosciences,* **2003,** *6,* 968-973.

3. Sano, I., T. Gamo, Y. Kakimoto, K. Taniguchi, M. Takesada, K. Nishinuma, *Biochim. Biophys. Acta.* **1959,** *32,* 586-587.

4. Wightman, R. M., L. J. May, A. C. Michael. *Anal. Chem*., **1988**, *60*, 769A–793A.

5. Kapur, S., D. Mamo. *Prog. Neuro-Psychopharmacol. Biol. Psychiatry*, **2003**, *27*, 1081.

6. Mobbs, C. V., P. R. Hof, *Handbook of the neuroscience of aging,* **2009,** Amsterdam: Elsevier/Academic Press.

7. Kim, J. H., J. M. Auerbach, J. A. R. Gomez, I. Velasco, D. Gavin, N. Lumelsky, S. H. Lee, J. Nguyen, R. S. Pernaute, K. Bankiewicz, R. McKay. *Nature*, **2002**, *418*, 50.

8. Gowrishankar, R., M. K. Hahn, R. D. Blakely. *Neurochem. Int.* **2014**, *73*, 42–48.

9. Montagu, K. A., *Nature,* **1957,** *180,* 244-250.

10. Abbaspour, A., A. Khajehzadeh, A. Ghaffarinejad. *Analyst*, **2009,** *134*, 1692–1698.

11. Chen, J. L., X.-P. Yan, K. Meng, S.-F. Wang. *Anal. Chem*., **2011,** *83,* 8787–8793.

12. Szantai, E., A. Szilagyi, A. Guttman, M. Sasvari-Szekely, Z. Ronai. *J. Chromatogr. A,* **2004**, *1053*, 241–245.

13. Huang, C., X. Chen, Y. Lu, H. Yang, W. Yang. *Biosens. Bioelectron*. **2015**, *63*, 478–482.

14. Watson, C. J., B. J. Venton, R. T. Kennedy. *Anal. Chem*. **2006,** *78*, 1391–1399.

15. Kim, Y. R., S. Bong, Y.-J. Kang, Y. Yang, R. K. Mahajan, J. S. Kim, H. Kim. *Biosens. Bioelectron.* **2010,** *25*, 2366–2369.

16. Qi, S., B. Zhao, H. Tang, X. Jiang. *Electrochim. Acta*. **2015,** *161*, 395–402.

17. Jackowska, K., P. Krysinski. *Anal. Bioanal. Chem.* **2012,** *405*, 3753–3771.

18. Sajid, M. S., M. K. Nazal, M. Mansha, A. Alsharaa, S. M. S. Jillani, C. Basheer. *TrAc Trends Anal. Chem*. **2016**, *76*, 15–29.

19. Sheng, Z. H., X. Q. Zheng, J. Y. Xu, W. J. Bao, F. B. Wang, X. H. Xia. *Biosens. Bioelectron.* **2012**, *34*, 125–131.

20. Wang, L., X. Lu, C. When, Y. Xie, L. Miao, S. Chen, H. Li, P. Li, Y. Song, *J. Mater. Chem. A,* **2015**, *3*, 608–616.

21. Shakkthivel, P., S. Chen. *Biosens. Bioelectron*. **2007**, *22*, 1680–1687.

22. Cinti, S., F. Ardunini, M. Carbone, L. Sansone, I. Cacciotti, D. Moscone, G. Palleschi. *Electroanalysis* **2015**, *27*, 2230–2238.

23. Ambrosi, A., C. K. Chua, A. Bonnani, M. Pumera. *Chem.Rev.* **2014,** *114,* 7150-7188.

24. Ambrosi, A., C. K. Chua, N. M. Latiff, A. H. Loo, C. H. A. Wong, A. Y. S. Eng, A. Bonanni, M. Pumera, *Chem Soc. Rev,* **2016, *45,*** 2458-2493**.**

25. Pumera, M., B. Smid, K. Veltruska, *J. Nanosci. Nanotechnol.* **2009,** *9,* 2671.

26. Abdelwahab, A. A., Y.-B. Shim. *Sensors Actuators B Chem*. **2015,** *221*, 659–665.

27. Komathi, S., A. I. Gopalan, K. P. Lee, *Analyst*, **2010,** *135*, 397-404.

28. Cheemalapati, S., S. Palanisamy, V. Mani, S. M. Chen, *Talanta*, **2013,** *117*, 297-304.

29. Jiang, G. T. Jiang, H. Zhou, J. Yao, X. Kong. *RSC Adv***.,** 2015, ***5*****,**9064-9068.

30. Welch, C.W., R. G. Compton. *Anal. Bioanal. Chem*. **2006**, *384*, 601–619.

31. Kalimuthu, P., S. A. John. *Talanta*, **2010**, *80*, 1686–1691.

32. Novoselov, K. S., A K Geim, S. V. Morozov, D. Jang, Y. Zhang, D. Jang, Y. Zhang, S. V. Dubonos, I. V. Grigorieva, A. A. Firsov. *Science*, **2004**, *306***,** 666-669.

33. Geim, A. K., K. S. Novoselov. *Nat. Mater*, **2007**, *6***,** 183-191.

34. Geim, A. K. *Science*, **2009**, *324***,** 1530-1534.

35. Pumera, M., A. Ambrosi, A. Bonanni, E. L. K. Cheng, H. L. Poh. *TrAC, Trends Anal. Chem.*, **2010**, *29*, 954.

36. Brownson, D. A. C., D. K. Kampouris, C. E. Banks. *Chem. Soc. Rev.*, **2012**, *41*, 6944.

37. Dong, X. C., D.L. Fu, W.J. Fang, Y.M. Shi, P. Chen, L.J. Li. *Small*, **2009**, *5*, 1422-1426.

38. Lv, R., M. Terrones. *Mater. Lett*. **2012**, *78*, 209−218.

39. Matsoso, B. J., K. Ranganathan, B. K. Mutuma, T. Lerotholi, G. Jones, N. J. Coville. *RSC Adv.*, **2016**, *6*, 106916-106920.

40. Chang, C. K., S. Kataria, C. C. Kuo, A. Ganguly, B. Y. Wang, J. Y. Hwang, W. H. Yang, S. B. Wang, C. H. Chuang, M. Chen. *ACS Nano*, **2013**, *7*, 1331-1341.

41. Shinde, P. P., V. Kumar. *Phys. Rev. B.* **2011**, *84*, 125401.

42. Wang, Y., Y. Zheng, X. Xu, E. Dubuisson, Q. Bao, J. Lu, K. P. Loh, *ACS Nano*, **2011**, *5*, 9927-9933.

43. Zhang, Y. Y. Ji, z. Wang, S. Liu, T. Zhang. *RSC Adv.*, **2015**, *5*, 106307-106314.

44. Yang, J., J. R. Strickler, S. Gunasekaran. *Nanoscale*, **2012**, *4*, 4594-4602.

45. Ewels, C. P., M. Glerup, J Nanosci *Nanotechnol.*, **2005**, *5*, 1345-1363.

46. Casanovas, J., J. M. Ricart, J. Rubio, F. Illas, J. M. Jimenez-Mateos, *J. Am. Chem. Soc.*, **1996,** *118*, 8071-8074.

47. Medintz, I. L., M. H. Stewart, S. A. Trammell, K. Susumu, J. B. Delehanty, B. C. Mei, J. S. Melinger, J. B. Blanco-Canosa, P. E. Dawson, H. Mattoussi, *Nat. Mater.*, **2010,** *9*, 676-684.

48. Yang, J., J. R. Strickler, S. Gunasekaran. *Nanoscale*, **2012,** *4*, 4594-4602.

49. Zhang, Y. Y. Ji, z. Wang, S. Liu, T. Zhang. *RSC Adv.*, **2015,** *5*, 106307-106314.

50. Nicholson, R. S., S. Irving. *Anal Chem*., **1964,** *36*, 706–723.

51. Wang, W. C., S. Gong, W. Sun, G. Li, Y. Lu, J. Yu, L. Dong, *Chem. Acta.*, **2016,** *89*, 323-330.

52. Wang, X., B. JIn, X. Lin, *Anla, Sci.*, **2002,** *18*, 931-933.

53. Bernmann, F., V. Ball, F. d. r. Addiego, A. Ponche, M. Michel, J. J. d. A. Gracio, V. r. Toniazzo, D. Ruch, *Langmuir*, **2011,** *27*, 2819-2825.

54. Ding, X., J. Bai, T. Xu, C. Li, H. M. Zhang, L. Qu, *Electrochem. Commun*, **2016,** *72*, 122-125.

55. Nsabimana, A., J. Lai, S. Li, P. Hui, Z. Liu, G. Xu, *Analyst*, **2017,** *142*, 478-484.

56. Joshi, A., W. Schuhmann, T. C. Nagaiah, *Sensors and Actuators B.: Chemical*, **2016,** *230*, 544-555.

57. Feng, X., Y. Zhang, J. Zhou, Y. Li, S. Chen, L. Zhang, Y. Ma, L. Wang, X. Yan, *Nanoscale*, **2015,** *7*, 2427-2432.

58. Jiang, G., T. Jiang, H. Zhou, J. Yao, X. Kong, *RSC Adv.*, **2015,** *5*, 9064-9068.

59. Li, Y., M. Yao, T. T. Li, Y. Y. Song, Y. J. Zhang, S. Q. Liu, *Anal Methods*, **2013**, *5*, 3635-3638.

60. Gai, P. B., H. J. Zhang, Y. S. Zhang, W. Liu, G. B. Zhu, X. H. Zhang, *J. Mater. Chem B.*, **2013**, *1*, 2742-2749.

61. Sun, J., L. Li, X. Zhang, D. Liu, S. Lv, D. Zhu, T. You, *RSC Adv.*, **2015**, *5*, 11925-11932.

Chapter 10

Single-step synthesis of crystalline *h*-BN nano-dots and quantum dots embedded in BCN hybrid films.

10.1 Introduction

Graphene, a monatomic two-dimensional (2D) allotrope of carbon, has attracted tremendous attention from both theoretical and experimental scientists due to its unique properties and promising applications in a variety of fields such as energy storage and conversion, sensors, ultracapacitors, field effect transistors, and electronic devices [1-9]. However, as a band gap free material, graphene has a very poor on/off current ratio, thus limiting its application in electrochemical devices. As a result, researchers have developed various methods to open up its band gap energy so as to improve its semiconductor properties. For instance, methods such as the use of certain substrates [10, 11], electrical gating [8, 12], inorganic and/or organic molecules [13, 14], fabrication of graphene quantum dots [15], and doping with heteroatoms [16-20], have proved to be suitable for tailoring the properties of graphene. One of the most straightforward and widely used techniques for tailoring the semiconducting properties of graphene is doping with heteroatoms. Heteroatom doping of graphene with nitrogen, boron, and nitrogen/boron has been achieved by using techniques such as chemical vapour deposition (CVD), thermal annealing, hydrothermal treatment, chemical treatment, etc. [16-20] For instance, Bepete *et al.* [16] incorporated small BN domains into a graphene structure via a low pressure CVD method using methane, boric acid and nitrogen. Additionally, Müllen and co-workers [18] prepared a B and N co-doped graphene by the hydrothermal method using ammonia boron trifluoride. Both research groups showed the possibility of incorporating small BN –domains into the graphene lattice.

Often times, co-doping of graphene with B and N atoms leads to the atomic mixing of B, N, and C atoms, which then results in the formation of a layered structure known as boron carbonitride (BCN) [21-24]. Recently, the BCN materials have raised much interest due to their electronic structure that can be tailored by adjusting the stoichiometry of the constituent atoms [22-26]. Both experimental and theoretical studies have shown that depending on the

atomic composition, BCN materials possess mechanical, optical and electrical properties that are in between those of the insulator hexagonal boron nitride (*h*-BN) and the semimetallic graphene [22-35]. Due to their tunable electronic properties, BCN materials have demonstrated great potential for applications in electronic, hydrogen storage, field-emission, optoelectronic devices and supercapacitors [24-45].

Similar to graphene, synthesis techniques such as chemical vapour deposition (CVD), thermal annealing, hydrothermal treatment, and chemical treatment can be employed to grow BCN materials. For example, from a low pressure chemical vapour deposition (LPCVD) system, Ajayan and co- workers [26] pioneered the growth of large-area BCN films by investigating the influence of the amount of the precursor material on the composition and structure of the BCN films. They indicated that adjusting the amount of ammonia borane (source of B and N) by varying the temperature led to the formation of large-area layers of a *h*-BCN material, which consisted of randomly distributed domains of pure *h*-BN in a graphene lattice. The different heating temperatures of ammonia borane led to different sizes of the pure h-BN and graphene domains, which in turn resulted in tuned electrical and optical properties of their as-synthesized BCN films.

Apart from doping graphene, the synthesis of graphene quantum dots (GQDs) can also be used to control and improve the semiconducting properties of graphene. GQDs have attracted much interest due to their unique optical, electrical, spin, photoelectric properties, and tunable band gap which is induced by the quantum confinement effect and the edge effect [36-40]. GQDs are an alternative to traditional semiconductor quantum dots, e.g. cadmium selenide (CdSe) and cadmium telluride (CdTe), due to their non-toxicity, tunable photoluminescence, high solubility, and high chemical- and photo-stability [36]. Similar to graphene, doping of the GQDs with heteroatoms such as nitrogen [41], boron [42], and nitrogen/boron [43] has proved to be an effective route for tuning the properties of GQDs. Pristine and doped GQDs have shown applications in bioimaging [44], supercapacitors [45], OPV solar cells [46], and oxygen reduction reactions [43]. However, the synthesis techniques for producing GQDs are tedious and result in low yields. Furthermore, these methods require special equipment, and lack scalability and reproducibility, especially when considering the controlled GQDs size [37-46]. To circumvent the problems associated with the QDs synthesis method, Ding and co-workers [37] reported the successful fabrication and characterization of large-area GQDs on *h*-BN films by CVD. By

adjusting the experimental parameters, their GQDs possessed excellent morphology, a well-ordered arrangement, and a thickness-dependent photoluminescence (PL).As a result, this successful synthesis and characterization of GQDs on *h*-BN films has laid a good foundation for the understanding, fabrication and properties of new hybrid materials consisting of QDs and 2D semiconducting films.

Based on the above background, it is clear that there is a lack of information regarding the synthesis of *h*-BN QDs embedded in graphene films. Here, we report a safe and efficient technique for the one-step growth of large-area *h*-BN QDs/NDs in BCN hybrid films. We also present their *h*-BN QDs/NDs dependent optical properties. The films were grown by an atmospheric pressure chemical vapour deposition (APCVD) technique and this method provides a cheap, facile and safe procedure for growing the 2D materials.

10.2 Experimental

10.2.1 Materials

All reagents used in the experiments were of analytical grade. Acetone (99%, gold line, ACE) and methanol (MeOH, 99.5 %) were bought from Sigma-Aldrich (SA). The gases were supplied by Afrox (South Africa), and they include argon (Ar, 99.9%), methane (CH_4, 99.98%), ammonia (NH_3, 10% in Ar), and hydrogen (H_2, 99.98 %). Other materials included a copper foil (25 µm, 99.98%) from Sigma Aldrich (RSA), poly(methyl methacrylate) (PMMA, Mw ~999 000, Sigma Aldrich), a silicon substrate with a 300 nm silicon oxide layer (Sigma-Aldrich), and a copper plate and an iron wire (University of the Witwatersrand workshop). Distilled water was used in all the experiments.

10.2.2 Synthesis and transfer of films

The films were synthesized by atmospheric pressure CVD (APCVD) on a copper foil in a quartz tube furnace (Fig. S10.1a). All the samples were grown with CH_4, H_2, Ar, NH_3 (10 % in Ar), and H_3BO_3 powder. An electropolished [47] Cu foil was placed at the center (herein hot zone, temp = ~ 1000 ^oC) of the quartz tube, and a quartz boat containing 100 mg boric acid powder was placed at 2 cm-12 cm distances from the hot zone (see Fig. S10.1c for the temperatures). The furnace was heated to 1000 ^oC at a ramping rate of 10 ^oC/min in 10 sccm H_2 and 300 sccm Ar atmospheres, after which the Cu substrate was annealed for 30 min. Methane (10 sccm) and ammonia (5 sccm) were introduced into the reaction chamber for 10

min, and then the reactor was ***rapidly*** cooled to room temperature by pushing the quartz tube to the outside of the furnace. After growth and for characterization purposes, the as-synthesized hybrid films were transferred onto different substrates (SiO_2/Si, Cu grids, and fused silica) using the PMMA- assisted electrochemical delamination method [47].

10.2.3 Characterization

The structural characterization of the films was studied by Raman spectroscopy on films transferred onto a 300 nm SiO_2/Si substrate. A Bruker Raman Senterra spectrometer equipped with a 50x optical objective and a 532 nm excitation laser was used for accumulating the films' spectra. The topological images and the estimated film thickness of the as-synthesized films were carried out on a Veeco Di3100 Atomic Force Microscope (AFM) in a tapping mode. The morphology of the films transferred onto a carbon coated Cu grid was determined using a FEI Tecnai T12 TEM, while both HR-TEM and selected area electron diffraction (SAED) images were accumulated using a JEOL JEM 2100 High Resolution TEM (JEOL, Japan) fitted with a LaB_6 gun. Images were captured at 200 kV using a Gatan Ultrascan camera (Gatan, USA). The ex-situ XPS study was carried out on films grown on a Cu foil with a Thermo Escalab 250 Spectrometer (Johnson Matthey Technology Centre, UK). The radiation used was a monochromatised aluminium Kα radiation with a 650 μm spot size. Charge compensation was provided by the in-lens electron flood gun at a 2 eV setting and the "401" unit for "zero energy" argon ions. Finally, optical absorption measurements were carried out on the films transferred onto a fused silica substrate using a Cary 500 Scan UV-vis-NIR spectrophotometer. For the analysis, the measurements were accumulated in the 190-800 nm wavelength range.

10.3 Results and Discussions

To grow the *h*-BN QDs/NDs in BCN films, a thermal catalytic APCVD technique using a Cu catalyst was employed, in which the C, N, and B-rich precursors were methane, ammonia, and boric acid. The thermal catalytic CVD technique was chosen due to the successful use of Cu foil for the large-area growth of graphene and *h*-BN films [11, 26, 48]. The experimental parameters which were studied in detail included the influence of the $B_2O_{2\,(g)}$ concentration and the heating temperature of the H_3BO_3. These were achieved by placing the H_3BO_3 at varying positions (2 cm-12 cm) from the hot zone, as shown in figure S10.1c. The quality of the as-grown films was characterized by studying their microstructural features, and their Raman, XPS, and UV-vis spectra. For this report, only films grown at the two extremes (i.e. 2

cm and 12 cm) will be discussed in detail; for other films see the supplementary information. The data for the studies carried out at different distances (i.e. 4, 6, 8, and 10 cm) from the Cu foil showed the trends expected from samples grown between the two extreme distances (2 and 12 cm).

10.3.1 Microstructure measurements of the films

The as-synthesized films were transferred onto a 300 nm SiO_2/Si substrate for both optical and atomic force microscopy characterization. Figure 10.1 shows the optical micrographs of the *h*-BN QDs/NDs in BCN films grown at 2 cm and 12 cm separation distances from the hot zone. The images revealed that the films were smooth, continuous and uniform over a large area (~ 50 μm).

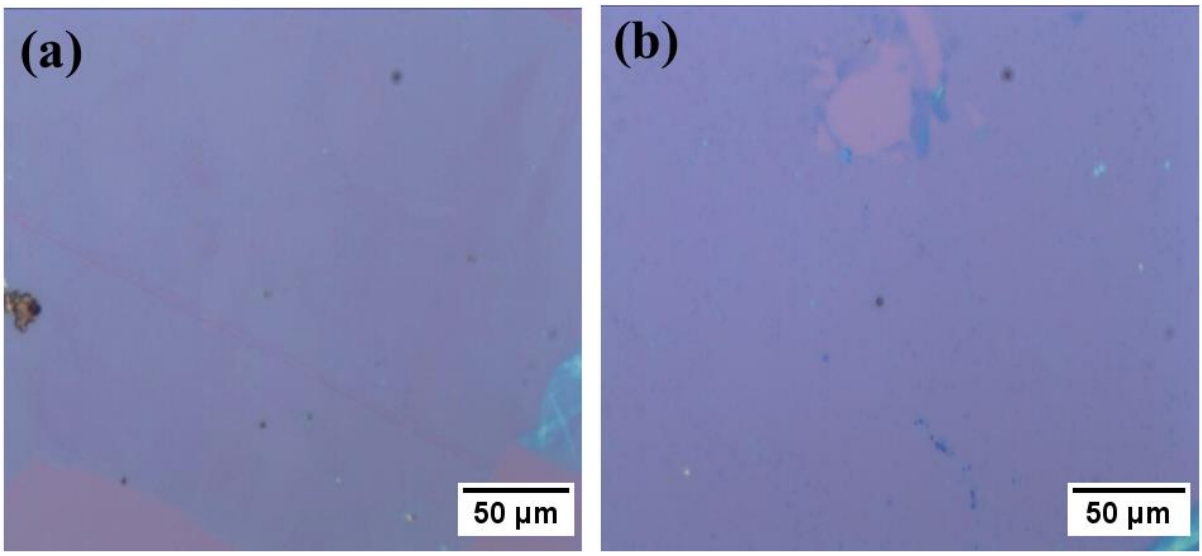

Figure 10.1: Optical images of *h*-BN QDs/NDs-BCN hybrid films transferred on a 300 nm SiO_2/Si substrate: (a) 2 cm and (b) 12 cm *h*-BN QDs/NDs-BCN hybrid films.

However AFM images showed that the *h*-BN QDs/NDs in the BCN films (Fig. 10.2b and 10.2c) consisted of a continuous distribution of the *h*-BN quantum/nanodots. Comparison of the hybrid films with the control sample (pristine graphene film, Fig. 10.2a), pristine graphene film exhibited wrinkles which occur during the transfer process of the films onto the substrate. It is noteworthy to mention that AFM was chosen as the best characterization technique for determining the distribution of the *h*-BN QDs/NDs in the BCN films. This is because under low magnification under SEM analysis (Fig. S10.3) the dots were barely visible. Further AFM analysis of the hybrid films indicated that the hybrid films became thinner with increasing distance from the hot zone. The estimated film thicknesses were found to be ~ 4.74 ± 0.20 nm and ~ 2.81 ± 0.03 nm for the 2 cm and 12 cm *h*-BN QDs/NDs-

BCN hybrid films, respectively (Figs. 10.2 (e-f)). This suggests that hybrid films are few- and multilayered [26]. The estimated film thickness profile and topographs for all *h*-BN QDs/NDs in the BCN films are found in figure S10.4b.

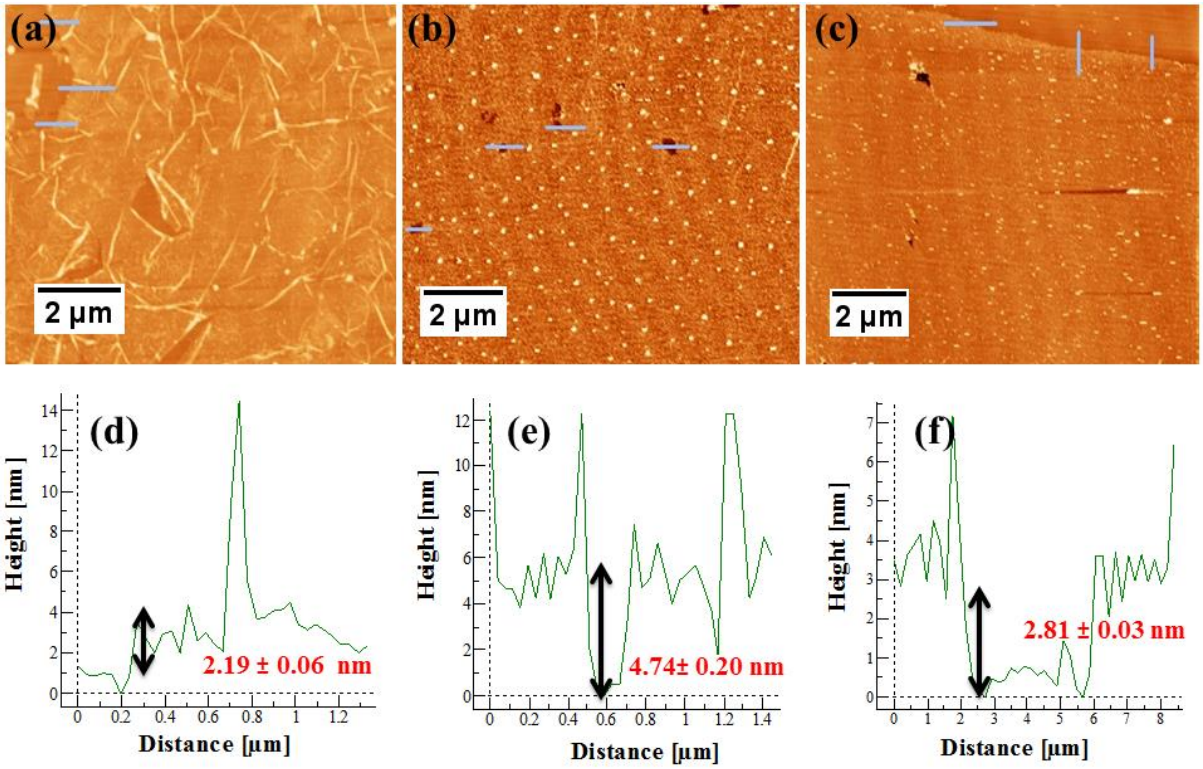

Figure 10.2: AFM images of (a) pristine graphene, (b) 2 cm and (c) 12 cm *h*-BN QDs/NDs-BCN hybrid films. (d-f) Thickness profiles of the same films.

Transmission electron microscopy (TEM, Fig. 10.3 (a-b)) observations indicated that the hybrid films were composed of *h*-BN quantum/nanodots embedded within a continuous film. The average size distribution was calculated to be 224 ± 8 nm and 11.1 ± 1.6 nm for the 2 cm and 12 cm *h*-BN QDs/NDs-BCN films, respectively (Fig. S10.2). The TEM-EDS analysis (Fig. S10.6 (a-c)) confirmed that the surrounding film was composed mainly of amorphous C as well as trace amounts of B and N atoms. High resolution TEM analysis (Fig. 10.3c), indicated that the *h*-BN dots were crystalline with a lattice spacing of ~ 2.5 Å, which corresponded to *h*-BN (002) [49]. To further evaluate the structure of the *h*-BN domains, selected-area electron diffraction patterns, (SAED, Fig. 10.3 (c) insert), indicated the distinctive hexagonal structure of the *h*-BN dots. The surrounding matrix was found to be amorphous because incorporation of both B and N atoms into the orderly sp^2-lattice carbon lattice leads to a distortion of the graphene lattice which then generated the amorphous structure [16-20].

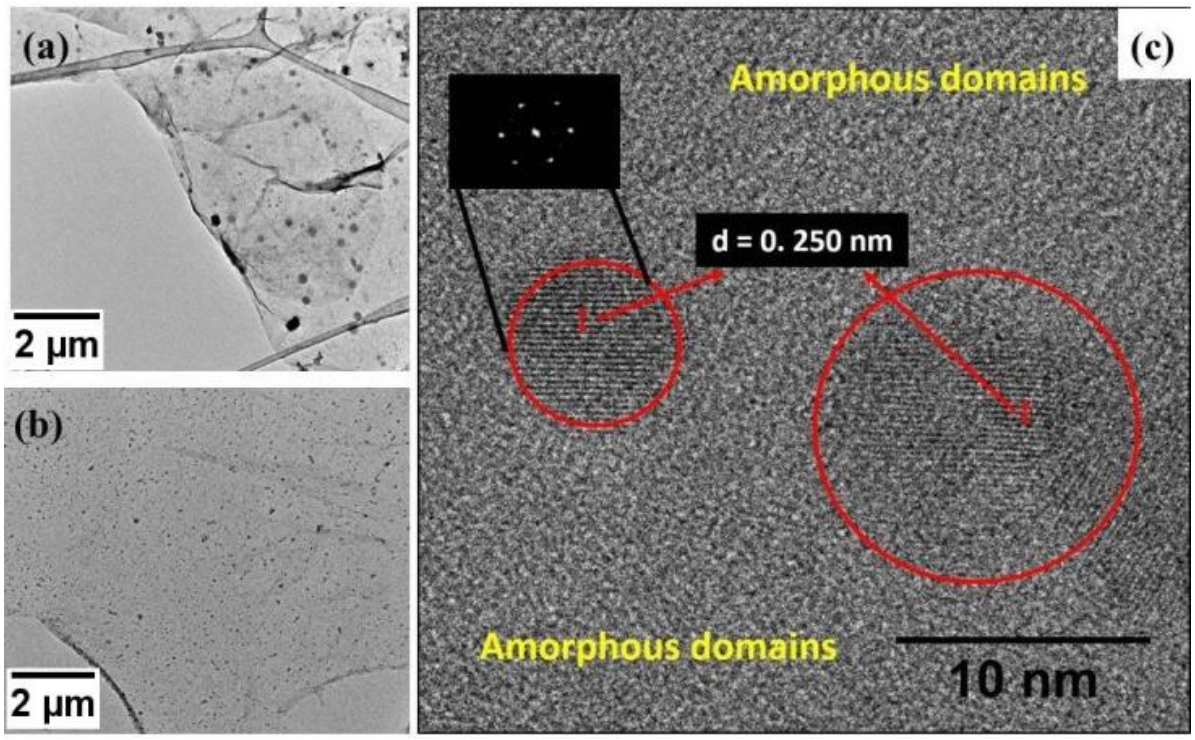

Figure 10.3: Low magnification TEM images of (a) 2 cm and (b) 12 cm *h*-BN QDs/NDs-BCN hybrid films, (c) HRTEM image, indicating *h*-BN QDs/NDs. Insert (c) shows the corresponding SAED image.

10.3.2 Raman analysis of the hybrid films

Figure 10.4a shows the Raman spectra for pristine graphene and *h*-BN QDs/NDs-BCN films (2 cm and 12 cm) films. The spectra of the as-synthesized hybrid films were found to be similar to spectra of the previously reported BCN and BCN-related materials, such as BCN nanotubes, atomically thin BCN films, and C-doped *h*-BN QDs [26, 31, 50]. The observed Raman peak positions are shown in Table 10.1. Compared to pristine graphene spectra, the Raman spectra of the *h*-BN QDs/NDs in the BCN films exhibited a broader and more intense D peak which was located ~ 1346 cm^{-1} (Fig. 10.4a) [51-53]. The presence of the D peak in the films signifies structural defects and disordered structures at the edges of the sp^2 domains as a result of single-phonon intervalley scattering processes [51-55]. Therefore, the very pronounced D peak in the *h*-BN QDs/NDs in the BCN films indicates the formation of a highly distorted BCN lattice with short range order due to the atomic mixing of B, C, and N [51-58]. Deconvolution of the D peaks for *h*-BN QDs/NDs in BCN films (Fig. 10.4b) showed the presence of B-C modes (~1336 cm^{-1}), the defect-induced peak of graphene (~1350 cm-1), and the B-N vibrational modes (~ 1369 cm^{-1}) [26,58]. This indicated the existence of different

domains within the hybrid films, which was later confirmed by XPS. Comparison of Raman profiles of all the hybrid films versus the pristine graphene film is shown in figure S10.7.

Further analysis of the Raman spectra (Fig. 10.4a) showed a broad G peak for the 2 cm *h*-BN QDs/NDs-BCN films; while the G peak of the 12 cm *h*-BN QDs/NDs-BCN films exhibited a peak splitting. Deconvolution of the G peak for the 2 cm *h*-BN QDs/NDs-BCN hybrid films (Fig. 10.4c) also exhibited a peak splitting, and this can be attributed to intravalley, defect-induced double-resonance processes [51-55]. The D* band (~ 1620 cm^{-1}) is known to originate from a further lattice distortion resulting from the intercalation process which leads to the formation of a finite crystal size within the as-synthesized films [51-55]. Furthermore, the observed upshift of the G peak in our hybrid films is attributed to the in-plane bond stretching of all sp^2-bonded pairs and these including C-C, B-C, N-C, and B-N bonds [56-59].

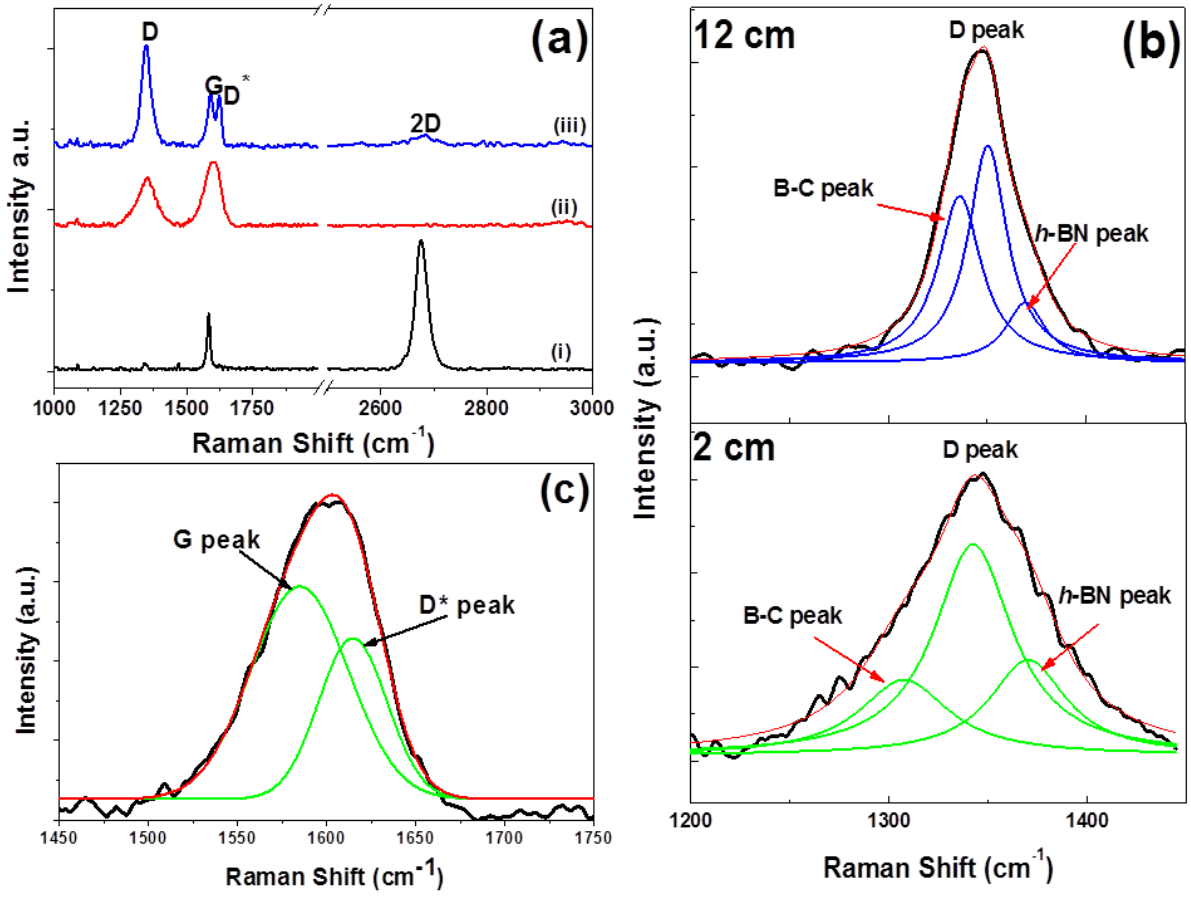

Figure 10.4: (a) Raman spectra of (i) pristine graphene and (ii) 2 cm *h*-BN QDs/NDs-BCN hybrid films, and (iii) 12 cm *h*-BN QDs/NDs-BCN hybrid films, (b) deconvolution of D peaks of the hybrid films, and (c) deconvolution of the G peak of the 2 cm *h*-BN QDs/NDs-BCN hybrid films.

For pristine graphene films, the relative intensity of the D peak with respect to the G peak (I_D/I_G) was used to determine the crystallization and quality, as well as the degree of doping for the chemically doped graphene [51-55, 58-60]. The 12 cm *h*-BN QDs/NDs in the BCN films exhibited the highest I_D/I_G ratio value (2.1), while the 2 cm *h*-BN QDs/NDs-BCN hybrid films gave an I_D/I_G value of 1.0 (shown in Table 10.1). The results suggest more structural defects are generated within the BCN lattice due to the formation of the *h*-BN quantum/nanodot structures. On the other hand, a small I_D/I_G value for pristine graphene indicates the formation of high quality graphene.

Table 10.1: Raman peak positions of pristine and *h*-BN quantum/nanodots-BCN hybrid films

Samples	**Raman Shift (cm^{-1})**				
	D	**G**	**D***	**2D**	**I_D/I_G**
Pristine graphene	1342.4	1583.2	-	2676.4	0.12
2 cm *h*-BN-BCN	1348.7	1586.3	1620.8	-	1.0
12 cm *h*-BN-BCN	1346.4	1590.2	1623.4	2679.4	2.1

10.3.3 XPS measurements of the hybrid films

The vaporization temperature of the boric acid was adjusted by varying its distance from the Cu substrate. This enabled us to tune the elemental composition (at %) of the as-synthesized *h*-BN QDs/NDs in the BCN films. Table 10.2 shows the atomic compositions of both 2 cm and 12 cm *h*-BN QDs/NDs-BCN hybrid films as compared to the pristine graphene films grown under the same conditions. The values of the atomic compositions were determined from the integrated peak areas of the XPS survey spectra (see table S10.1 for other films). As expected, pristine graphene is mainly made up of carbon atoms with some oxygen atoms. On the other hand, our *h*-BN QDs/NDs-BCN hybrid films showed an increasing C content with increasing distance of H_3BO_3 from the hot zone; the reverse trend was observed for the B and N contents. The B/N ratio for all the samples (2, 4, 6, 8, 10, 12 cm) was always close to unity. The significantly large O content for *h*-BN QDs/NDs in the BCN films indicates the high affinity of these films for oxygen atoms due to high lattice distortions [28, 32, 61, 62].

Table 10.2: Atomic compositions from XPS of pristine and *h*-BN quantum/nanodots-BCN hybrid films

Samples	Elements (at. %)			
	C	**B**	**N**	**O**
Pristine graphene	93	-	-	7
2 cm *h*-BN-BCN	42	19	14	25
12 cm *h*-BN-BCN	62	8	7	23

High resolution XPS was used to investigate the chemical environments of the B, C, and N atoms in the as-synthesized hybrid films. Figure 10.5 shows the XPS spectra of the 2 cm and 12 cm *h*-BN QDs/NDs-BCN hybrid films. The B1s exhibited a broad spectral peak with a full width at half maximum (FWHM) was in the range of 1.8 – 2.7 eV (Fig. 10.5a). This is wider than the reported FWHM value for B in *h*-BN (0.92 eV) [61, 62]. This signifies the presence of different bonding states for B atoms. To determine the chemical environments of the B atoms in our hybrid films, the B1s spectral peak was deconvoluted into three component peaks centered at 189.3 - 189.5, 189.7 - 189.9 and 191.2 eV respectively. These peaks can be assigned to formation of B-C bonds (either in the form of B_4C and BC_3), sp^2-B-C-N bonds, and sp^2B-N bonds within the crystalline *h*-BN quantum/nanodots [22 -35, 61, 62]. The absence of a component peak at relatively higher binding energy (192.0 eV), which is assigned to B-O bonds in B_2O_3 [61, 62], indicates the full conversion of the boric acid to BN dots during the growth process. Similarly, the C1s spectra (Fig. 10.5b) exhibited a broad and tailing peak with a significantly larger FWHM (1.29 - 1.35 eV) than that of graphite [23-35, 62]. To understand the bonding states of the C atoms, the peak for the C1s spectra was deconvoluted into at least five component peaks, located at 283.1 - 283.3 eV, 284.1 - 284.5 eV, 285.4 - 285.7 eV, 286.5 - 286.8 eV, and 288.0 - 288.8 eV, respectively. The peaks were attributed to the presence of C-B, sp^2C-C, sp^2C-N (either in the form of sp^2C-N [27], C=N [34], and/ or C≡N [28]), C=O and O-C=O bonds [22-35]. It was observed that many of the C atoms within the film are still bonded together to form graphene domains as shown by the predominant peak at 284.1 - 284.5 eV.

Confirmation of the bonding states obtained from both C1s and B1s was supported by the deconvolution of the XPS N1s spectra (Fig. 10.5c). At least three component peaks centered at 398.1 - 398.3, 399.3 - 399.4, and 400.1 - 400.5 eV, were observed and these were ascribed

to the formation of sp^2N-B, N-C and N=C bonding configurations [16, 48, 57, 62]. Finally, figure 5d shows that oxygen atoms are bonded mainly to the carbon, which compliments the C1s data and indicates that the oxygen atoms are only found at the edges and defective sites in the graphene domains. In summary, XPS spectra suggest that under our growth conditions (methane, boric acid (at varying separation distances from hot zone), and ammonia), the as-synthesized films are composed of different B-N, B-C, and C-N bonding configurations that form a continuous hybrid system consisting of *h*-BN QDs/NDs and BCN domains. Additionally, lack of B-O and N-O bonds in the B1s and N1s spectra also confirms the successful controlled growth of the high quality *h*-BN QDs/NDs-BCN hybrid films. The data for other films grown at 4, 6, 8 and 10 cm distances of H_3BO_3 from the Cu foil are entirely in agreement with the above results (Fig. S10.8).

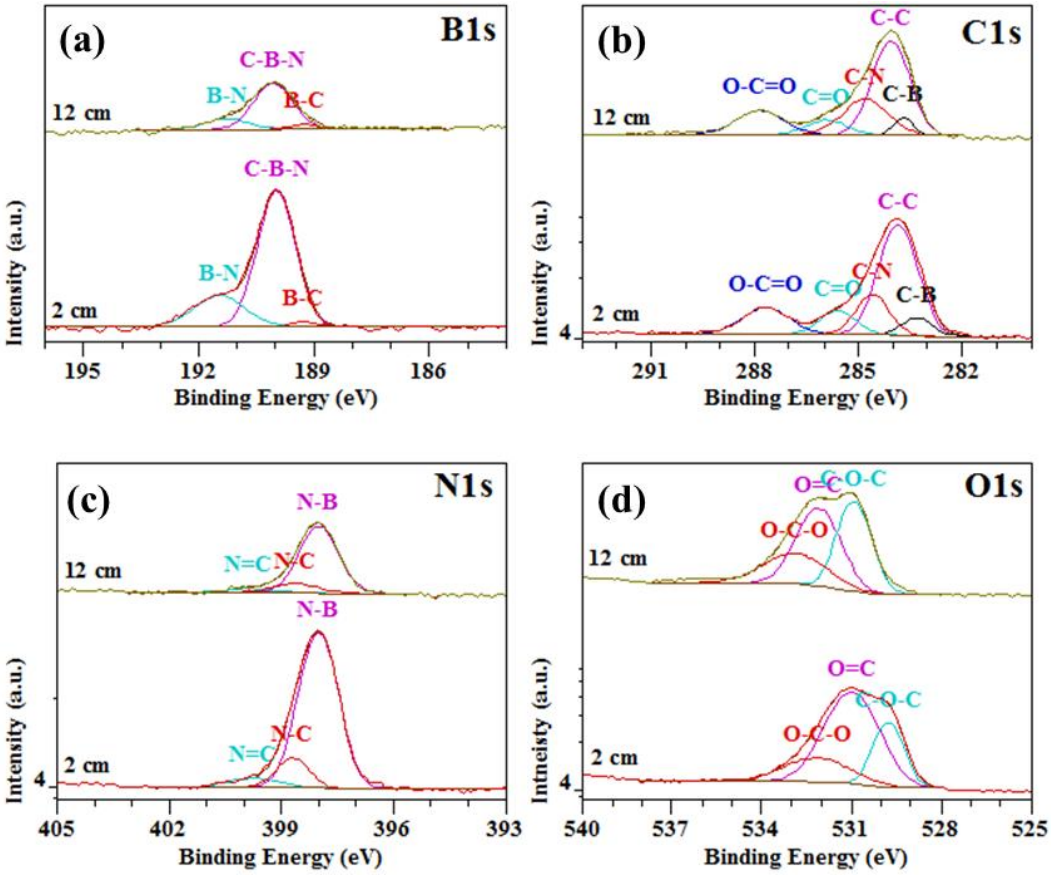

Figure 10.5: XPS spectra showing deconvoluted curves for (a) B1s, (b) C1s, (c) N1s, and O1s (d) of the 2 cm and 12 cm prepared *h*-BN QDs/NDs-BCN hybrid films.

10.3.4 UV-vis analysis of the samples

The UV-vis absorption spectra (Fig. 10.6a) of the *h*-BN QDs/NDs in the BCN hybrid films transferred onto a fused silica substrate were measured to investigate the optical energy band gap of the films. Figure 10.6a shows that the *h*-BN QDs-BCN hybrid film (12 cm) exhibited a higher absorption intensity in the visible range in comparison to the *h*-BN NDs-BCN hybrid films (2 cm). This can be attributed to a quantum confinement effect due to the large coverage of the small *h*-BN quantum dots (11.1 ± 1.6 nm) in films grown at d = 12 cm, as compared to the large nanodots (224 ± 8 nm) *h*-BN grown at d = 2 cm. The optical band gap energies for *h*-BN QDs/NDs in the BCN films were determined on the basis of the Tauc's formulation [63] (see Fig. S10.9 for Tauc's formulation). From a plot of $\varepsilon^{1/2}/\lambda$ versus λ^{-1} (Fig. 10.6b), the optical band gap energies were calculated to be 5.68 eV and 5.90 eV for the 2 cm and 12 cm *h*-BN QDs/NDs-BCN hybrid films, respectively.

Based on previous investigations, BCN hybrid films are expected to exhibit optical properties which are located between those of graphene (semi-metallic) and monolayered *h*-BN (~ 6.0 eV) [26, 31, 32, 57]. It is also reported that these properties can be varied by tuning the atomic configurations and compositions of BCN hybrid films [26, 32]. For instance, Ci *et al.* showed that increasing the C-content from 65 at. % to 84 at.% in BCN films decreased the band gap energy from 4.48 eV to 3.85 eV [26]. Additionally, Lei and co-workers reported the narrowing of the band gap energy for BCN films when the concentration of carbons atoms is increased from 40 at. % (2.00 eV) to 55 at. % (1.48 eV) [31]. Furthermore, Xue *et al.* also showed that doping BN QDs with carbon atom in order to form BCNO QDs tuned the band gap energy from 3.02 eV (BN QDs) to 2.98 eV (BCNO QDs) [64]. Theoretical calculations by Nascimento *et al.* have also shown that widening of the graphene band gap opening can be achieved by adjusting the BN concentration (c_{BN}) from 2.08 % (0.05 eV) to 10.42 % (0.30 eV) [65]. Interestingly, in our case the 12 cm *h*-BN QDs-BCN hybrid films, which contained a high C content (~ 65 at. %) and very low B (~ 7.79 at. %) and N (~ 6.95 at. %) contents, exhibited a large optical band gap energy. This suggests that the *h*-BN domains in the 12 cm *h*-BN QDs-BCN hybrid films mainly contributed to the optical properties and suppressed the effect of the C-content. The results also indicated the successful incorporation of discrete domains of *h*-BN QDs/NDs within the BCN hybrid films.

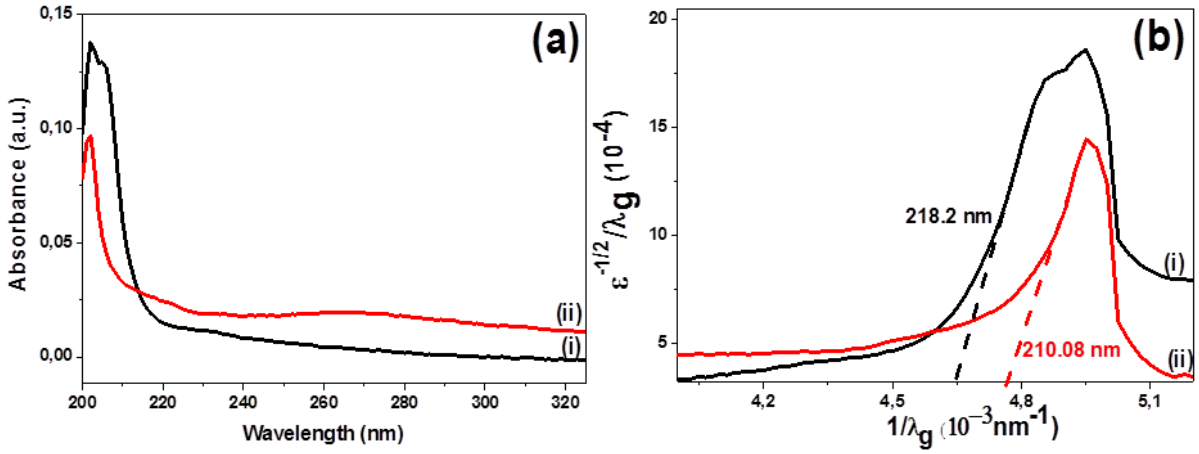

Figure 10.6: (a) UV-vis absorption spectra and (b) Tauc's plot of the (i) 2 cm *h*-BN NDs-BCN and (ii) 12 cm *h*-BN QDs-BCN hybrid films.

10.3.5 Proposed growth mechanism

From the above characterization results and analyses of our *h*-BN QDs/NDs in BCN films, we can propose a growth mechanism for the synthesis of our materials using the APCVD technique. During the ramping and annealing steps, $H_3BO_{3(s)}$ sublimes into gaseous $H_3BO_{3\,(g)}$, which is then carried and deposited as a thin film onto the Cu substrate by the Ar gas. Once on the Cu substrate, the thin film of $H_3BO_{3\,(g)}$ decomposes into a mixture of the dehydrated metaboric acid (HBO_2) and the incomplete oxidation intermediate product of boron, known as boron sub-oxide or diboron dioxide ($B_2O_{2\,(g)}$) [66]. The reactions are shown in equations 1 and 2. The metaboric acid can further dehydrate at ≈ 300 ^oC to form pyroboric acid ($H_2B_4O_7$, equation 3), which finally dehydrates into a thin film of diboron dioxide ($B_2O_{2\,(g)}$, equation 4) at ≤ 1000 ^oC.

Due to the different thermal coefficients of the Cu foil and the B_2O_2 film, most of the B_2O_2 collapses, segregates and agglomerates into quantum dots or nanodots embedded within a continuous B_2O_2 film. Depending on the distance between the B-source and the Cu substrate, varying thicknesses of the B_2O_2 film are formed on the Cu foil leading to the formation of different sizes of the B_2O_2 dots. Thus, the size variation of the dots can be related to the amount of H_3BO_3 vapour required for the B_2O_2 thin film formation, agglomeration and growth of the dots. For instance, at a 2 cm separation distance there is sufficient H_3BO_3 vapour to lead to the formation of a thick B_2O_2 film, which then results in the formation of larger sized nanodots. However, at a 12 cm separation distance most of the H_3BO_3 vapour is

diluted by the carrier gas and therefore is not used. This results in the formation of thinner B_2O_2 films, which consequently leads to the production of smaller sized quantum dots.

During the growth step, the addition of CH_4 and NH_3 (equations 6 and 7) results in the production of active C and N species, which then react with the B_2O_2 dots and film to generate B-C [67] species as well as B-N domains (equation 8). Further introduction of NH_3 and CH_4 leads to the formation of BCN hybrid configurations (equation 9). Scheme 10.2 shows a graphical representation of the proposed growth mechanism of the *h*-BN QDs/NDs-BCN hybrid films by the APCVD technique.

$$H_3BO_{3(s)} \xrightarrow{\leq 170^oC} HBO_{2(g)} + H_2O_{(g)} \quad [1]$$

$$2H_3BO_{3(g)} \xrightarrow{\leq 1000^oC} B_2O_{2(g)} + 3H_{2(g)} + 2O_{2(g)} \quad [2]$$

$$4HBO_{2(g)} \xrightarrow{\approx 300^oC} H_2B_4O_{7(g)} + H_2O_{(g)} \quad [3]$$

$$H_2B_4O_{7(g)} \xrightarrow{\geq 500^oC} 2B_2O_{2(g)} + H_{2(g)} + \tfrac{3}{2}O_{2(g)} \quad [4]$$

$$B_2O_{2(g)} \xrightarrow{\Delta(1000^oC)} Cu / B_2O_{2(s)} \quad [5]$$

$$CH_{4(g)} + H_{2(g)} \rightarrow C_{(g)} + 3H_{2(g)} \quad [6]$$

$$2NH_{3(g)} + H_{2(g)} \rightarrow N_{2(g)} + 4H_{2(g)} \quad [7]$$

$$2B_2O_{2(s)} + 5C_{(g)} \rightarrow B_4C_{(s)} + 4CO_{(g)}$$

or

$$B_2O_{2(s)} + N_{2(g)} \rightarrow 2BN_{(s)} + O_{2(g)} \quad [8]$$

$$B_2O_{2(s)} + 2NH_{3(g)} + 2CH_{4(g)} \rightarrow 2BCN_{(s)} + 2O_{(g)} + 7H_{2(g)} \quad [9]$$

Scheme 10.1: Summary of reactions leading to the formation of the *h*-BN quantum/nanodots embedded in the BCN films.

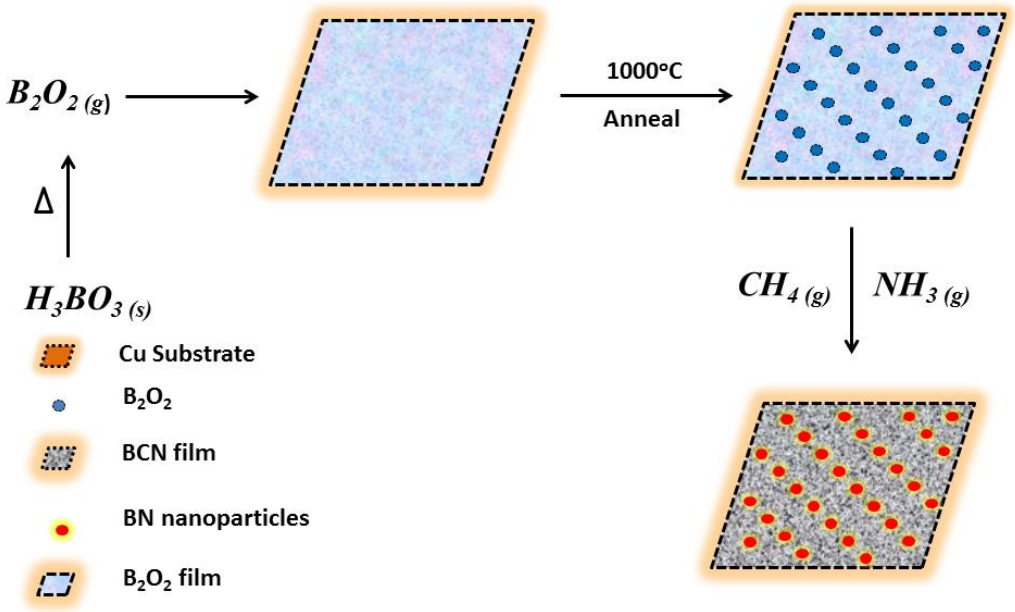

Scheme 10.2: Graphical representation of the growth mechanism for *h*-BN quantum/nanodots embedded in BCN films.

10.4 Conclusions

The controlled H_3BO_3 vaporization temperature- and B_2O_2 concentration-dependent growth of *h*-BN QDs/NDs in BCN hybrid films was successfully realized using the APCVD technique. This was achieved by placing the boron source at varying distances from the hot zone. Raman spectra indicated that the lattice distortion increased with the formation of *h*-BN quantum dots; i.e. as the distance between the B-source and the Cu substrate is increased. AFM, TEM, and HRTEM analyses indicated the presence of crystalline *h*-BN QDs/NDs of varying sizes embedded into the BCN lattice. The survey XPS spectra showed that the atomic compositions of the hybrid films can be tuned by adjusting the position of the B-source. Furthermore, core-shell XPS spectra indicated that the films consisted of various B-N, B-C, and C-N bonding configurations. Interestingly, depending on the vaporization temperature and the concentration of B_2O_2, these new *h*-BN QDs/NDs in BCN films were found to exhibit optical properties that have not been previously reported for these three component systems.

References

1. Novoselov, K. S., A. K Geim, S.V. Morozov, D. Jang, Y. Zhang, S. V. Dubonos, I. V. Grigorieva, A. A. Firsov, *Science*, **2004**, *306*, 666-669.
2. Geim, A. K. Novoselov, K. S. *Nat. Mater,* **2007**, *6*, 183-191.

3. Wu, Y., K. A. Jenkins, A. Valdes-Garcia, D. B. Farmer, Y. Zhu, A. A. Bol, C. Dimitrakopoulos, W. Zhu, F. Xia, P. Avouris, Y. M. Lin. *Nano Lett.,* **2012,** *12*, 3062-3067.
4. Castro Neto, A. H., F. Guinea, N. M. R. Peres, K. S. Novoselov, A. K. Geim. *Rev. Mod. Phys.*, **2009**, *81*, 109-162.
5. Stamfer, C. S., Fringes, J. Guttinger, F. Molitor, C. Volk, B. Terres, J. Dauber, S. Engels, S. Schnez, A. Jacobsen, S. Droscher, T. Ihn, K. Ensslin. *Front. Phys.,* **2011**, *6,* 271-293.
6. Zhu, Y., S. Murali, W. Cai, X. Li, J. W. Suk, J. R. Potts, R. S. Ruoff. *Adv. Mater.*, **2010**, *22*, 3906-3924.
7. Li, S. S., K. H. Tu, C. C. Lin, C. W. Chen, M. Chhowalla. *ACS Nano*, **2010**, *4*, 3169-3174.
8. Cheng, R., J. Bai, L. Liao, H. Zhou, Y. Chen, L. Liu, Y. C. Lin, S. Jiang, Y. Huang, X. Duan. *Proc. Nat. Acad. Sci.*, **2012**, *109,* 11588-11592.
9. Liu, C., Z. Yu, D. Neff, A. Zhamu, B. Z. Jang. *Nano Lett*., **2010**, *10*, 4863.
10. Giovannetti, G., P. A. Khomyakov, G. Brocks, P. J. Kelly, J. van de Brink. *Phys. Rev B.*, **2007**, *76*, 073103.
11. Reina, A., X. Jia, J. Ho, D. Nezich, H. Son, V. Bulovic, M. S. Dresselhaus. *Nano Lett.*, **2009**, *9*, 30-35.
12. Wang, F., Y. Zhang, C. Tian, C. Girit, A. Zettl, M. Crommie, Y.R. Shen. *Science*, **2008**, *320*, 206-209.
13. Berashevich, J., T. Chakraborty. *Phys Rev B.*, **2009**, *80*, 033404.
14. Huang, H., S. Chen, X. Gao, W. Chen, A.T. S. Wee. *ACS Nano*, **2009**, *3*, 3431-3436.
15. Ritter, K. A., J.W. Lyding. *Nature Materials*, **2009**, *8*, 235–242.
16. Bepete, G., D. Voiry, M. Chhowalla, Z. Chiguvare, N. J. Coville. *Nanoscale*, **2013**, *5*, 6552-6557.
17. Chang, C. K., S. Kataria, C. C. Kuo, A. Ganguly, B. Y. Wang, J. Y. Hwang, W. H. Yang, S. B. Wang, C. H. Chuang, M. Chen, *et.al*. *ACS Nano,* **2013**, *7*, 1331-1341.
18. Wu, Z. Z., A. Winter, L. Chen, Y. Sun, A. Turchanin, X. Feng, K. Mullen. *Adv. Mater.*, **2012**, *24*, 5130.
19. Jeong, H M, J. W. Lee, W. H. Shin, Y. J. Choi, H. J. Shin, J. K. Kang, J. W. Choi. *Nano Lett.,* **2011**, *11*, 24727.
20. Shinde, P. P., V. Kumar. *Phys. Rev. B.*, **2011**, *84*, 125401.

21. Kaner, R. B., J. Kouvetakis, C. E. Warble, M. L. Sattler, N. Bartlett. *Mater Res Bull*., **1987**, *22*, 399-401.
22. Kang, Y., Z. Chu, D. Zhang, G. Li, Z. Jiang, H. Cheng, X. Li. *Carbon*, **2013**, *61*, 200-208.
23. Lin, T. W., C. Y. Su, X. Q. Zhang, W. Zhang, Y. H. Lee, H. Y. Li, C. W. Chu, M. T. Chang, F. R. Chen. *Small*, **2012**, *8*, 1384-91.
24. Gong, Y., G. Shi, Z. Zhang, W. Zhou, J. Jung, W. Gao, L. Ma, Y. Yang, S. Tang, G. You, R. Vajtai, *et.al*. *Nature Communications*, **2014**, *5*, 3193.
25. Dou, S., X. Huang, Z. Ma, J. Wu, S. Wang. *Nanotechnology,* **2015**, *26*, 045402.
26. Ci, L., L. Song, C. Jin, D. Jariwala, D. Wu, Y. Li, A. Srivastava, Z. F. Wang, K. Storr, L. Balicas, F. Liu, P. M. Ajayan. *Nature Mater*., **2010**, *9*, 430-435.
27. Yang, Q., C. B. Wang, S. Zhang, D. M. Zhang, Q. Shen, L. M. Zhang. *Surface & Coating Technology*, **2010**, *204*, 1863-1867.
28. Mannan, M. A., M. Nagano, T. Kida, N. Hirao, Y. Baba. *Journal of Physics and Chemistry of Solids*, **2009**, *70*, 20-25.
29. Mannan, M. A., H. Noguchi, T. Kida, M. Nagano, N. Hirao, Y. Baba. *Thin Solid Films*, **2010**, *518*, 4163-4169.
30. Raidongia, K., A. Nag, K. P. Hembram, U. V. Waghmare, R. Datta, C. N. Rao. *Chem Eur. J*., **2010**, *16*, 149–57.
31. Lei, M. K., Q. Li, Z. F. Zhou, I. Bello, C. S. Lee, S. T. L,. *Thin Solid Films* **2001**, *389*, 194-199.
32. Essafti, A., E. Ech-chamikh. *J Mater Sci*., **2011**, *46*, 5847-5850.
33. Watanabe, M. O., T. Sasaki, S. Itoh, K. Mizushima. *Thin Solid Films*, **1996**, *282*, 334-336.
34. Mannan, M. A., H. Noguchi, T. Kida, M. Nagano, N. Hirao, Y. Baba. *Materials Science and Semiconductor Processing*, **2008**, *11*, 100-105.
35. Mannan, M. A., H. Noguchi, T. Kida, M. Nagano, N. Hirao, Y. Baba. *Materials Sciences and Applications*, **2013**, *4*, 11-19.
36. Güçlü, A. D., P. Potasz, P. Hawrylak. *Physical Review B*., **2011**, *84*, 035425-1-5.
37. Ding, X. *J.Mater.Chem*., **2014**, *2*, 3717-3722.
38. Anikeeva, P. O., J. E. Halpert, M. G. Bawende, V. Bulovic. *Nano Lett*., **2009**, *9*, 2532–2536.
39. Wu, X., H. Liu, J. Liu, K. N. Haley, J. A. Treadway, J. P. Larson, N. Ge, F. Peale, M. P. Bruchez. *Nat. Biotechnol*., **2003**, *21*, 41–46.

40. Wang, X., G. Sun, N. Li, P. Chen. *Chem Soc. Rev,* **2016**, *34,* 567-572.
41. Qu, D., M. Zheng, L. G. Zhang, H. F. Zhao, Z. G. Xie, X. B. Jing, R. E. Haddad, H. Fan, Z. Sun. *Sci. Rep*., **2014**, *4,* 5294-5313.
42. Zhang, Li., Z. Y. Zhang, R. P. Liang, Y. H. Li, J. D. Qui. *Anal. Chem*., **2014**, *86,* 4423-4430.
43. Fei, H., R. Ye, G. Ye, Y. Gong, Z. Peng, X. Fan, E. L. G. Samuel, P. M. Ajayan, J. M. Tour. *ACS Nano,* **2014**, *8,* 10837-10843.
44. Ananthanarayanan, A., Y. Wang, P. Routh, A. Than, M. Jin, J. Zhang, J. Chen, H. Sun, P. Chen. *Nanoscale,* **2015**, *7,* 8159-8165.
45. Liu, W. W., Y. Q. Feng, X. B. Yan, J. T. Chen, Q. J. Xue. *Adv. Funct. Mater*., **2013**, *23*, 4111–4122.
46. Li, M. M., W. Ni, B. Kan, X. J. Wan, L. Zhang, Q. Zhang, G. Long, Y. Zuo, Y. Chen. *Phys. Chem. Chem. Phys*., **2013**, *15*, 18973–18978.
47. Wang, Y., Y. Zheng, X. Xu, E. Dubuisson, Q. Bao, J. Lu, K. P. Loh. *ACS Nano,* **2011**, *5*, 9927-9933.
48. Shi, Y., C. Hamsen, X. Jia, K. K. Kim, A. Reina, M. Hofmann, A. L. Hsu, K. Zhang, H. Li, Z. Y. Juang, M. S. Dresselhaus, L. J. Li, J. Kong. *Nano Lett*., **2010**, *10*, 4134-9.
49. Lynch, R.W, H. G. J., Drickamer, *Chem. Phys*., **1966**, *44*, 181.
50. Xi, Y., X. Y. Zhao, A. Z. Wang, X. P. Wang, H. X. Bu, M. W. Zhao. *Physica E.*, **2013**, *49*, 52–60.
51. Ferrari, A. C. *Solid State Commun*., **2007**, *143*, 47-57.
52. Ferrari, A.C., J. C. Meyer, V. Scardaci, C. Casiraghi, M. Lazzeri, F. Mauri, S. Piscanec, D. Jiang, K. S. Novoselov, S. Roth, A. K. Geim. *Phys. Rev. Lett*., **2006**, *97*, 187401.
53. Casiraghi, C., S. Pisana, K. S. Novoselov, A. K. Geim, A. C. Ferrari. *Appl. Phys. Lett*., **2007**, *91*, 233108.
54. Cancado, L. G., A. Jorio, E. H. Martins Ferreira, F. Stavale, C. A. Achete, R. B. Capaz, M. V. O. Moutinho, A. Lombardo, T. S. Kulmala, A. C. Ferrari. *Nano Lett*., **2011**, *11*, 3190-3196.
55. Malard, L. M., M. A. Pimenta, G. Dresselhaus, M. S. Dresselhaus. *Phys Rep*., **2009**, *473*, 51-87.
56. Watanabe, M. O., T. Sasaki, S. Itoh, K. Mizushima. *Applied Physics Letter,* **1996**, *68*, 2962-2964.

57. Kim, K. K., A. Hsu, X. Jia, S.M. Kim, Y. Shi, M. Hofmann, D. Nezich, J. F. Rodriguez-Nieva, M. S. Dresselhaus, T. Palacios, J. Kong. *Nano Lett*., **2011**, *12*, 161-166.
58. Reich, S., A. C. Ferrari, R. Arenal, A. Loiseau, I. Bello, J. Robertson. *Phys. Rev. B*., **2005**, *71*, 205201.
59. Brito, W. H., R. Kagimura, R. H. Miwa. *Phys. Rev. B*., **2012**, *85*, 035404.
60. Eckmann, A., A. Felten, A. Mishchenko, L. Britnell, R. Krupke, K. S. Novoselov, C. Casiraghi. *Nano Lett*., **2012**, *12*, 3925-3930.
61. Linss, V., F. Richter, S. E. Rodil, P. Reinke, M. G. Garnier, P. Oefhafen, U. Kreissig. *Thin Solid Films*, **2004**, *467*, 76-87.
62. Uddin, M. N., I. Shimoyama, Y. Baba, T. Sekiguchi, M. Nagano. *J. Vac. Sci. Technol. A*., **2005**, *3*, 497–502.
63. Tauc, J, R. Grigorovici, A. Vancu. *Phys. Stat. Sol*., **1966**, *3*, 627-637.
64. Xue, Q, H. Zhang, M. Zhu, Z. Wang, Z. Pei, Y. Huang, Y. Huang, X. Song, H. Zeng, C. Zhi. *RSC Adv.,* **2016**, *6*, 79090-79094.
65. Nascimento, R., J. R. Martins, R. J. C. Batista, H. Chacham. *J. Phys. Chem. C.,* **2015**, *119*, 5055-5061.
66. Heller, G. *Science,* **2013**, 3rd Supplement, Volume 2. Springer Science and Business media, 12-14.
67. Weimer, A. W., W. G. Moore, R. P. Roach, J. E. Hitt, R. S. Dixit, S. E. Pratsinis. *J. Am. Ceram. Soc.*, **1992**, *75*, 2509-2514.

Chapter 11

Synthesis and characterization of boron carbon oxynitride films with tunable composition using methane, boric acid and ammonia

11.1. Introduction

The successful isolation of a new two-dimensional carbon material, known as graphene, by Geim and Novoselov over a decade ago has ignited much interest in atomically thin two-dimensional nanomaterials[1-3]. Graphene has proved to be a promising material for future use in the fields of supercapacitors, gas adsorbents, and as a field effect transistor; due to its outstanding electronic, mechanical, and optical properties[1, 4-7]. Boron nitride (BN) which is isoelectronic to graphene[8, 9], is normally found in two forms. These are the cubic form (*c*-BN)[10], which is the second hardest material after synthetic diamond, and the exfoliated layered 2D hexagonal form (*h*-BN)[11], which has found useful applications as an effective adsorbent for metal ions, as a white solid lubricant, and in high power semiconductor devices[12-14]. Due to the structural similarities between graphene and *h*-BN, tremendous attention has been focused on the development of hybrid thin films of graphene and *h*-BN, to generate boron carbon nitride (BCN) [15-17]. These films can be achieved by either co-doping of graphene with boron and nitrogen atoms or incorporation of carbon atoms into the *h*-BN matrix[15, 17-19].

BCN materials are a new generation of 2D semiconductors with tunable electronic, optical, and magnetic properties; dependent on the B/C/N elemental ratio. Theoretical reports based on ab initio calculations have further indicated that depending on the atomic composition and arrangement, BCN materials are appealing semiconductors that have high oxidation resistance, very good electrical and mechanical properties, and have a variable band gaps[15-22]. For instance, different ratios of BN to carbon in BCN nanostructures have been shown to tune the optical band gap energy between that of the semi-metallic graphene and the qausi-direct band gap energy of *h*-BN (~ 6.0 ± 0.04 eV)[15, 17-21]. Due to these remarkable properties, BCN materials show a great potential to be applied in electronic and optoelectronic devices.

In addition to BCN films, another important semiconducting material is the oxygen containing BCN material, boron carbon oxynitride (BCNO). Theoretical calculations and experimental results have shown that BCNO materials also have a wide range of spectral emissions with tunable wavelengths[23]. Furthermore, they are found to behave like low cost and non-toxic metal free phosphors with a high external quantum efficiency. They can hence be applied in lighting technology as light emitting diodes (LEDs) [23-25]. Several techniques have been employed to synthesize BCNO materials, and these include catalytic chemical vapour deposition (CVD), solid state reactions and chemical synthesis[23, 24, 26-28]. For instance, Lei *et al.*[24] used an eutectic LiCl/KCl salt melt to synthesize BCNO phosphor nanoparticles with diameters of ~ 5 nm, which exhibited emission spectra in the 440-528 nm range. Additionally, Single's research group showed that changing the molar ratio of boric acid to melamine (1:1 to 2:1) in the chemical synthesis of nanophosphors led to the formation of highly crystalline and semi-crystalline BCNO particles[27]. Photoluminescence (PL) studies showed they had emission spectra at 357 nm (800 ^{o}C), which shifted to lower wavelengths at higher temperatures (1400 ^{o}C) due to a change in the crystal structure and atomic compositions of the BCNO. Using a chemical synthesis route, Rivera-Tapia *et. al.*[23] synthesized a wide band gap (3.22 eV) semiconducting BCNO material from a solid solution of urea and boric acid. Furthermore, the presence of hydroxyl groups that were formed on the BCNO nanoplatelets was found to facilitate their good dispersion in polar solvents. Apart from being used as tunable nanophosphors, BCNO materials have also shown potential applications in fields such as hydrogen storage, as chemical sensors, and as supercapacitors[28-31].

So far the most promising approach for synthesizing BCNO films with tunable composition and thickness has been found to be the CVD technique. For instance, Ozturk and co-workers successfully synthesized large-area atomically thin BCNO films over a Cu foil using methane gas, powdered ammonia borane and a gas mixture of 0.1 % O_2/Ar as precursors in a *low-pressure* CVD system[26]. They observed that the area coverage of graphene-rich BCNO domains and the overall compositions of the BCNO films can be controlled by varying the oxygen content in the reaction chamber. They also observed that the presence of nitrogen promoted the inclusion of oxygen into the BCN lattice, thereby leading to the formation of the BCNO materials. Despite the numerous reports on the synthesis of BCNO nanomaterials from graphene oxide, Ozturk's group showed that similar to graphene and BCN nanosheets, it is possible to make large-area and atomically thin BCNO films. However, to the best of our

knowledge, studies on the synthesis and characterization of BCNO films under an atmospheric pressure CVD (APCVD) system are yet to be reported. This is surprising since the APCVD technique is known to provide a cheap and safe procedure for growing graphene[32], *h*-BN[33] and *h*-BCN[15] films with adjustable compositions and properties.

In this work, the synthesis of 2D-BCNO films by the APCVD technique using carbon-rich methane, nitrogen-rich ammonia, and as well as the boron- and oxygen-rich boric acid as precursors is reported. The compositions and atomic configurations of the hybrid films were investigated by varying the total gas flux of B_2O_2 and monitoring the effect of this flux on the growth of the new material on the Cu foil substrate. The total gas flux of B_2O_2 was changed by varying the position of the $H_3BO_{3(s)}$ from the Cu substrate (i.e. 2 cm to 12 cm) [34]. The morphology, atomic compositions, structural and optical properties of the as-grown films was studied by optical microscopy, XPS, as well as Raman and UV-vis spectroscopies. Finally, a mechanism to explain the growth of BCNO films was proposed.

11.2. Experimental:

11.2.1 Starting Materials

Acetone (99%, gold line ACE), methanol (99.5 %), ethanol (absolute), iso-propanol (ACE, 99%), ortho-phosphoric acid (85%, LabChem), urea (99%, Promark Chemicals), boric acid (99.5%, Sigma Aldrich), chlorobenzene (99%, UniLab), sodium hydroxide pellets (98%, Merk) and poly(methyl methacrylate) (PMMA, Mw ~999 000) were purchased from Sigma-Aldrich, South Africa. The gases used included argon (Ar, 99%), methane (CH_4, 99.98%), ammonia (NH_3, 10% in Ar), and hydrogen (H_2, 99.98 %), and these were supplied by Afrox, South Africa. Other materials used included a copper foil (25 µm, 99.98%) from Sigma Aldrich (RSA), a silicon substrate with a 300 nm silicon oxide layer (Sigma-Aldrich), a copper plate and an iron wire (University of the Witwatersrand workshop). Distilled water was used in all the experiments.

11.2.2 Synthesis and transfer of films

Large area BCNO films were grown on a Cu substrate using an atmospheric pressure chemical vapour deposition method with CH_4, H_2, NH_3 (10% in Ar), and H_3BO_3 as precursor materials. Initially, the Cu foil was electrochemically cleaned for 90 sec in an aqueous mixture of 150 mL H_3PO_3, 150 mL ethanol, 30 mL iso-propanol and 3.0 g urea using a 12 V current[35]. The Cu foil was placed at the center of a 20 cm × 100 cm quartz tube, and a quartz

boat containing 100 mg of H_3BO_3 was placed at different distances (2, 4, 6, 8, 10, and 12 cm) from the Cu substrate. H_3BO_3 placed at these distances allowed the vaporization temperature of H_3BO_3 to be varied from ~ 300^oC to ~ 1000 ^oC. The quartz tube was then inserted in a horizontal CVD furnace[34] (Fig. S1), after which the furnace was heated to 1000 ^oC under H_2 and Ar atmospheres at the heating rate of 10 ^oC/min. After annealing for 30 min, growth of the BCNO films was achieved for 10 min by introducing 20 sccm CH_4 and 5 sccm NH_3 into the reaction chamber. For characterization purposes, the films were transferred onto a 300 nm SiO_2/Si substrate, TEM Cu grids, and fused silica substrates using the PMMA (4.6 % m/v in chlorobenzene) - assisted electrochemical delamination method[36]. The films were named according to the distance of the boric acid from the growth substrate in the reaction chamber, e.g. BCNO-2 stands for the BCNO films grown using boric acid placed at a 2 cm distance from the Cu foil.

11.2.3 Characterization

Raman spectroscopy was used to investigate the structural properties of the films that were transferred onto a 300 nm SiO_2/Si substrate. The analyses were performed on a Bruker Raman Senterra spectrometer using a 532 nm excitation laser and a laser power of 0.2 mW. The spectrometer was equipped with a 50x optical objective, which was used for optical imaging of the films at a 50 μm resolution. The surface topography of the BCNO films on a 300 nm SiO_2/Si substrate were recorded on a Veeco Di3100 AFM in a tapping mode with 256 scan lines at a scanning rate of 2.0 Hz and an amplitude set point of 1.20 V. The AFM machine was placed on an anti-vibration table and housed in a soundproof room so as to eliminate any vibrational and acoustic noise. A FEI Tecnai T12 TEM was used to determine the morphology of the films that were transferred onto the Cu grids. HR-TEM images were accumulated using a JEOL JEM 2100 High Resolution TEM (JEOL, Japan) fitted with a LaB_6 gun. Images were captured at 200 kV by tilting the stage by ~10^o and the imaging was performed at the edges of the films using a Gatan Ultrascan camera (Gatan, USA). Optical-absorption measurements in the 200-800 nm wavelength range (Cary 500 scan UV-vis-NIR spectrophotometer) were carried out on the BCNO films which were transferred onto a fused silica substrate. Finally, the chemical composition of the films on a Cu foil was determined by XPS using a Thermo Fisher Escalab 250. Monochromatised aluminium Kα radiation was used with a 650 μm spot size to maximise signal. Charge compensation was provided by an in-lens electron flood gun and separate low-energy argon ion source. The deconvolution of

the spectra was performed using the CasaXPS software and were fitted with Lorenztian-Guassian (GL30) peaks.

11.3. Results and Discussions

The growth of BCNO films using the APCVD technique was investigated by studying the role of heating temperature of the boric acid on the composition of the as-grown films. The quality, structural and compositional analyses of the as-grown films was determined by optical microscopy, AFM, Raman spectroscopy, TEM, and XPS characterization techniques. UV-vis characterization was used for determining the optical properties of the films.

11.3.1 Microstructural measurements of the films

The optical micrographs of the BCNO hybrid films (Fig.11.1) revealed that the films were continuous and uniform. Since BCNO films have similar structural features to graphene nanosheets, the colour contrast of the BCNO film after being transferred onto a 300 nm SiO_2/Si substrate was used to estimate their thickness, as was done with graphene films[18, 37, 38]. As a result, it can be seen that the as-grown BCNO films are fairly thick, as depicted by their very deep purple colour.

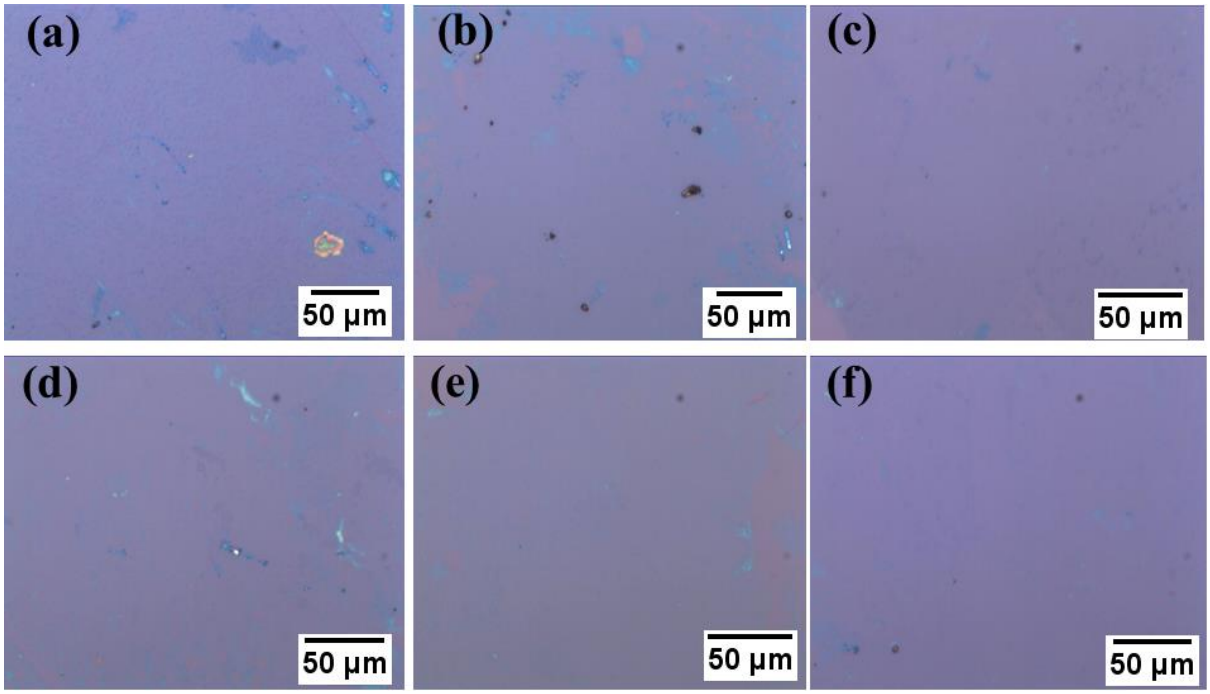

Figure 11.1: Optical images of BCNO hybrid films transferred onto 300 nm SiO_2/Si substrate and grown at (a) 2 cm, (b) 4 cm, (c) 6 cm, (d) 8 cm, (e) 10 cm, and (f) 12 cm, respectively.

The AFM analysis indicated that the estimated average film thickness was ~3.14 ± 0.05 nm for BCNO-2 films, ~4.00 ± 0.13 nm for BCNO-6 films and ~ 2.19 ± 0.08 nm for films BCNO-12 films. Therefore it can be concluded that the films grown at all distances were mostly multi-layered[37]. This was corroborated by the HRTEM images (Fig. 11.2 (a-f)) which confirmed that the films were of varying thickness. For instance, the BCNO-2 films were observed to have approximately five to seven layers thick. The thickness of the films was observed to be over ten layers for the BCNO-6 films, and this was in agreement with the AFM estimated thickness. Interestingly, as estimated by the AFM calculations, the films became thinner as shown by the approximately eight layers for BCNO-8 films and the two to three layer thick BNCO-12 films. Finally, low magnification TEM images of the films (inserts to Fig. 11.2 (a-f) and Fig. S11.3) showed that the films were a continuous phase with tears/holes which can be attributed to imperfections, shown by red circles (Fig. S11.3), due to the transference step.

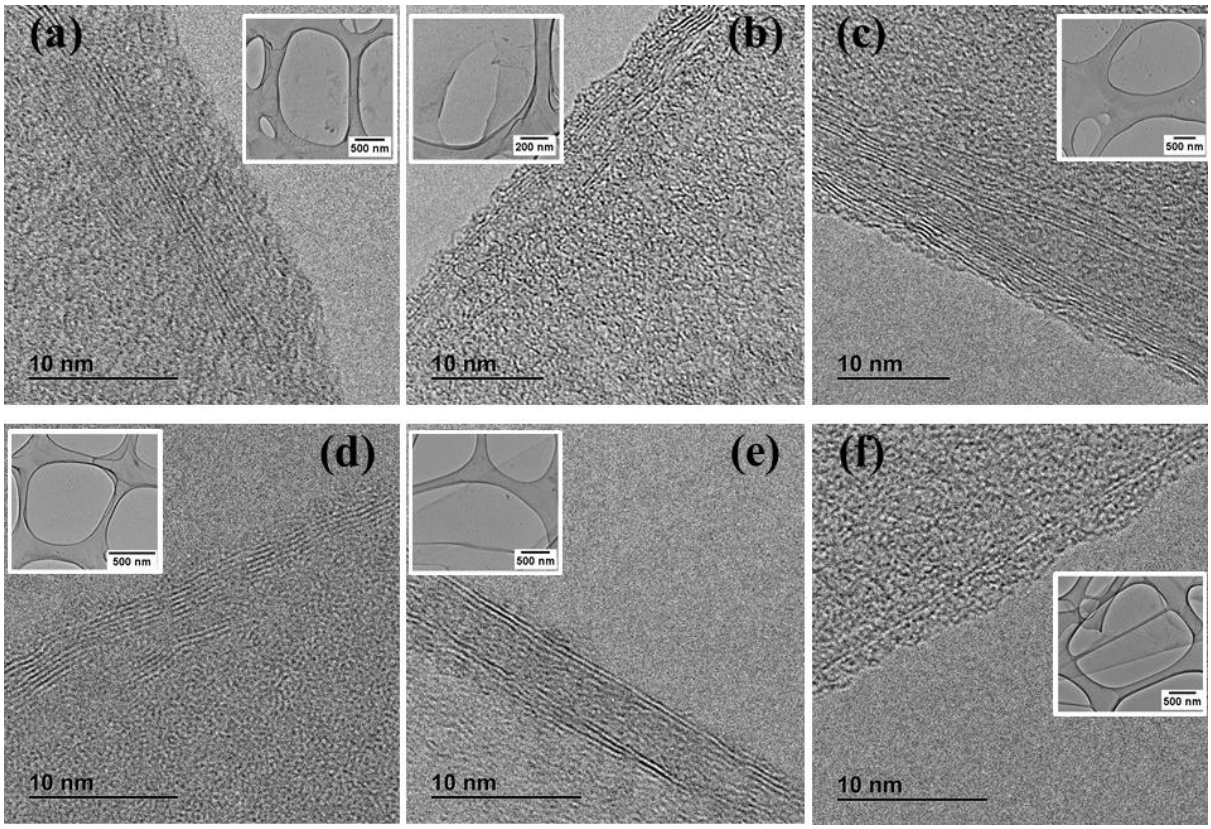

Figure 11.2: HRTEM images of BCNO hybrid films transferred onto Cu grids and grown at (a) 2 cm, (b) 4 cm, (c) 6 cm, (d) 8 cm, (e) 10 cm, and (f) 12 cm, respectively. Insert shows the TEM images of the respective BCNO films.

11.3.2 Raman analysis of BCNO films

The chemical and structural nature of the as-grown films was investigated using Raman spectroscopy (Fig. 11.3). The most prominent spectral signal was a broad D peak[38-40], located at ~ 1350 cm^{-1}. Detailed analysis of all D peaks (Fig. S11.4) showed that the deconvolution of the D peak into at least three component peaks was possible. The deconvolution showed the presence of a dominant defect-induced peak for graphitic carbon materials at ~ 1350 cm^{-1}, implying a contribution from regions of defective graphene domains[38-40]. The contribution from the B-N vibrational modes[41, 42] was verified by a component peak located at ~ 1370 cm^{-1}. Finally, the contribution of the B-C vibrational modes from carbon–rich amorphous regions of B_4C was shown by a component peak located at lower wavenumbers (~1330 cm^{-1}) [26, 43-45]. Relative intensities for each component peaks indicate the varying amounts of the graphene, *h*-BN, and B-C domains. In addition to the D peak (Fig. 11.3), Raman active bands for graphitic carbon (G and 2D) were observed at ~ 1590 cm^{-1} and ~ 2680 cm^{-1}, respectively[38-40]. For BCNO-2, the relative intensity of the 2D peak was suppressed almost to zero which implies the presence of large lattice distortions in this sample. On increasing the growth distance, the relative intensity of the 2D peak was observed to increase, indicating a reduction in the lattice distortions by restoration of the crystalline structure. The effect of the lattice distortions on the structure was further confirmed by the appearance of another defect-induced peak (D*) [38-40] located at ~1620 cm^{-1}.

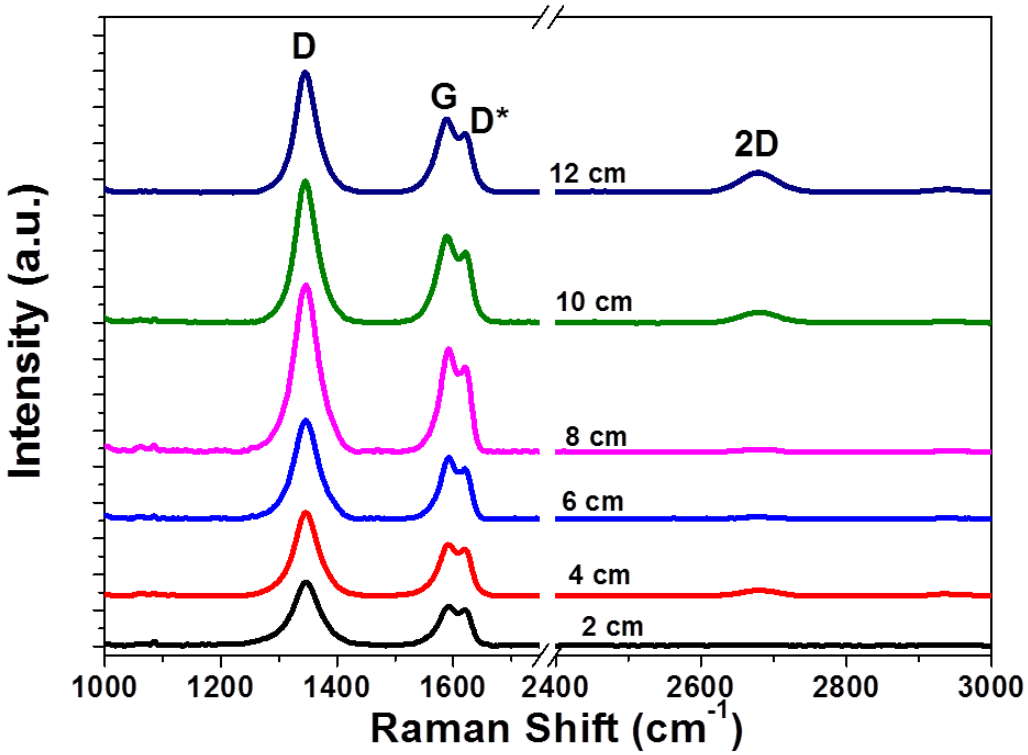

Figure 11.3: Raman spectra of BCNO films grown at (a) 2 cm, (b) 4 cm, (c) 6 cm, (d) 8 cm, (e) 10 cm, and (f) 12 cm growth positions from the hot zone.

In pristine graphene, the quantification of defects is determined by measuring the ratio between the relative intensities of the defect-induced D peak and the graphitic-G peak (I_D/I_G)[37-39, 46]; the larger the I_D/I_G ratio value, the higher the defect density. It was assumed that due to the structural similarities between graphene and BCNO films, the I_D/I_G ratio could also be used to quantify the degree of disorder for the as-grown BCNO films[23, 26]. Figure 11.4 (blue line) showed that the BCNO films exhibited large lattice distortions as indicated by the defect density ratio (I_D/I_G) value (~ 1.8). Interestingly, the G peak position was observed to be blue shifted in comparison to that of the CVD-grown graphene films[39, 46, 47] (Fig. 11.4, red line). The blue shift in the BCNO-2 to BCNO-6 films can be attributed to the contribution of all in-plane bond stretching of all sp^2-bonded pairs, including C=C (1580-1600 cm^{-1})[48], B-C (1570-1600 cm^{-1})[26, 43-45], and N=C (1600-1680 cm^{-1})[49]. However, the position of the G band was observed to slightly red shift towards the G position in CVD-graphene (~1580 cm^{-1})[39, 46] for the BCNO-8 to BCNO-12 films. The results therefore could suggest that there was formation of larger graphene domains as the B-source is placed further away from the Cu growth substrate.

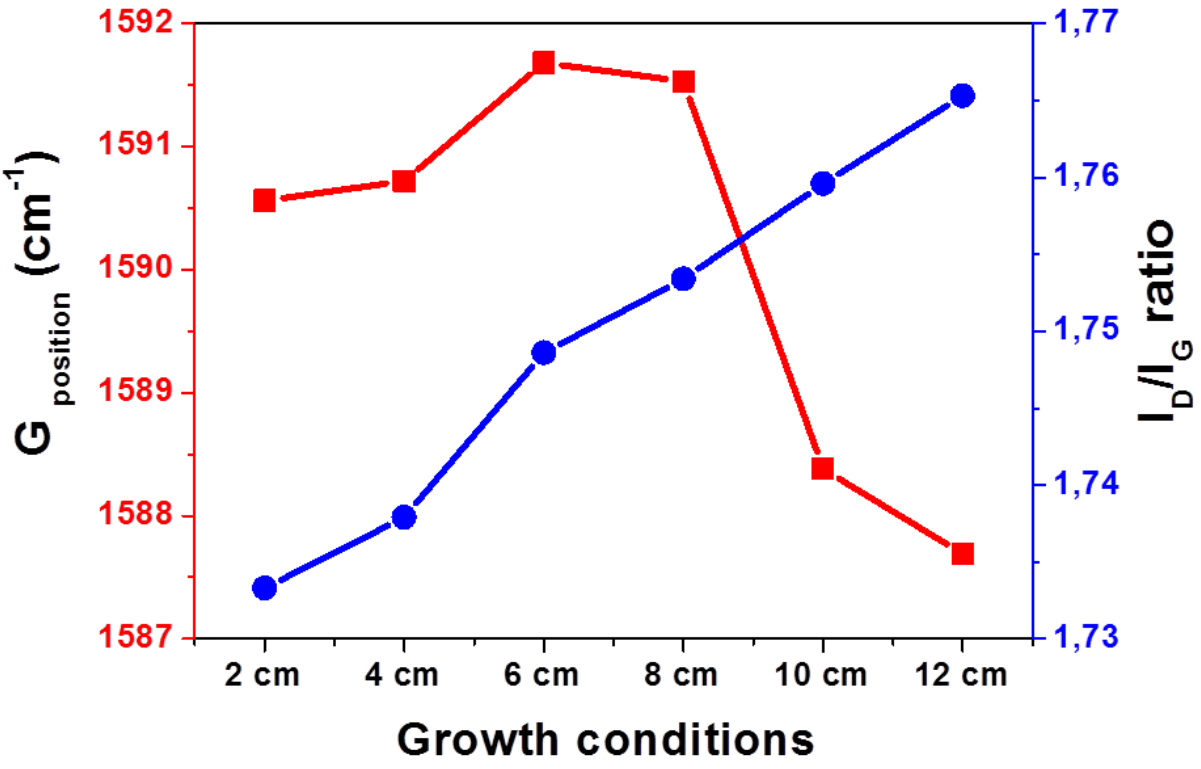

Figure 11.4: G peak positions (red line) and defect density ratio (I_D/I_G, blue line) of the BCNO films.

11.3.3 XPS measurements of the hybrid films

The surface elemental composition (at. %) of the as-synthesized BCNO films was determined by X-ray photoelectron spectroscopy (XPS). Figure 11.5a shows a typical XPS survey scan for the BCNO-2 films. The survey spectrum exhibited five peaks: two distinct peaks corresponding to C1s (284.7 eV) and O1s (531.1 eV), two weak peaks corresponding to B1s (190.1 eV) and N1s (397.9 eV), as well as another peak corresponding to Cu2p (933.1 eV). The atomic percentages of the constituent elements in the as-grown films are shown in figure 11.5b. It can be observed that the composition of the films changed with increasing distance from the hot zone; with the C and O showing an opposite trend to the N and B contents. The changing atomic compositions indicate that the deposition rate of B_2O_2 on the Cu foil as a function of distance from the hot-zone (heating temperature) plays a significant role in controlling the resultant compositions of the as-grown films.

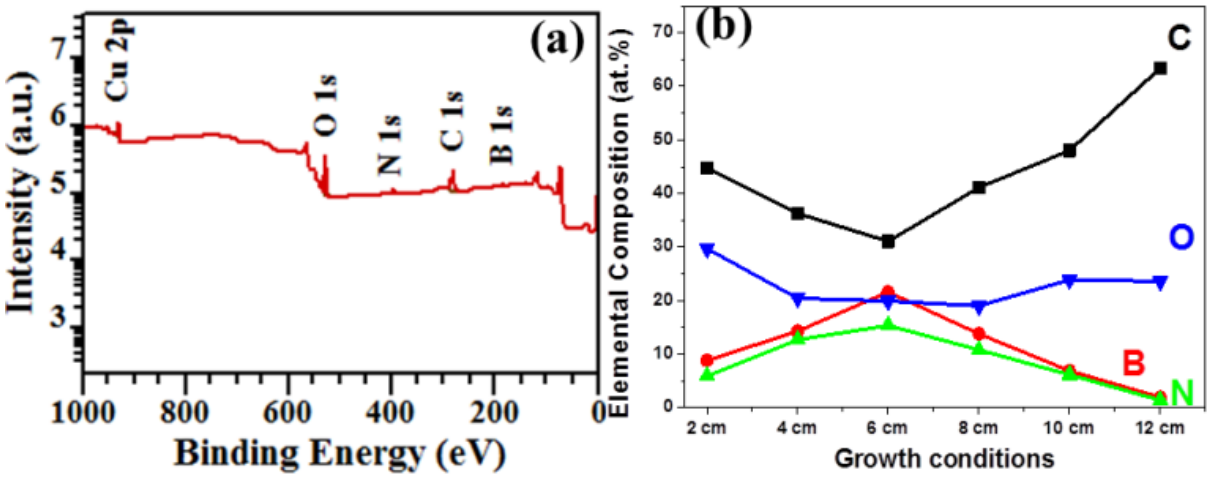

Figure 11.5: (a) XPS survey spectra and (b) the elemental composition of BCNO films grown at varying growth distances.

The bonding states for the constituents atoms (B, C, N, O) in the films were determined by deconvolution of the high resolution XPS spectra of the B1s, C1s, N1s, and O1s peaks. Figure 11.6 shows high-resolution XPS scans of the B1s, C1s, N1s, and O1s spectra for the BCNO-2 films (see Figs S5-S9 for spectra of other films). The B1s spectrum (Fig. 11.6a) was deconvoluted into four component peaks centered at 188.6, 189.9, 191.4, and 193.3 eV, respectively. These corresponded to the contribution from B-C, sp^2C-B-N, sp^2-BN, and B-O bonds, respectively[15, 17, 18, 50-54]. Interestingly, the positions of the B-O bonds were found to be red shifted with increasing distance from the hot zone, suggesting the existence of different bonding states around/within the B-O domains. For instance, the B-O peak position in BCNO-2 (~193.3 eV) was closer to that of B-O bonds in B_2O_2 (~192.55 ± 0.05 eV) [54, 55], indicating that at this growth condition, boron atoms are surrounded by oxygen atoms and formed regions of B_2O_2 domains. However, on increasing the distance from the hot zone, the B-O peak position red shifted, suggesting that there is substitution of the oxygen atoms in the B_2O_2 domains with carbon atoms. As a result, boron atoms tended to share only one bond with oxygen atoms the other with N and C atoms; leading to the formation of less saturated B_2O_2 domains.

The C1s spectra, on the other hand, exhibited at least five components centered at 283.5, 284.1, 284.9, 285.9, and 288.0 eV, respectively (Fig. 11.6b). The main component peak located at 284.1 eV, corresponded to the graphitic C-C bonds, and indicated that the majority of carbon atoms within the films retained the hexagonal crystalline lattice of graphene[15, 18, 51, 52]. The component peak at lower binding energies (283.5 eV) is assigned to formation of

boron carbide bonds either in the form of B_4C (282.9 eV) and/or BC_3 (284.3 eV) [51]. Additionally, the peak located at 284.9 eV represented the formation of various defect-induced C-N bonding states with either sp^2C-N [15], and/or C=N [53] bonding configurations. Finally, the two peaks located at higher binding energies (285.9 eV and 288.0 eV) are attributed to oxygenated C atoms (C=O and N-C=O/O-C=O) at the edges and/or defect sites of the graphene domains[50].

Deconvolution of the N1s signal (Fig.11. 6c) resulted in three component peaks corresponding to sp^2-N-B (398.0 eV), N-C (399.1 eV) and N=C (400.1 eV) respectively[52-54]. The presence of both N-C and N=C bonding configurations indicated that there are regions of pyrrolic and/or graphitic-N doped graphene domains within the BCNO films. In addition, the high affinity of nitrogen for boron atoms was clearly observed by the relatively high and prominent N-B peaks, which strongly indicates the existence of *h*-BN domains within the BNCO films. The presence of *h*-BN domains was also confirmed by the slightly high intensity of the B-N bonds in the B1s spectrum (Fig. 11.6a). Furthermore, the O1s spectra (Fig. 11.6d) was also deconvoluted into three peaks which were assigned to O=C and/or Cu_2O (530.4 eV), O-C (531.2 eV), and O-B (532.5 eV) bonds respectively. Interestingly, the component peak at 530.4 eV could be attributed to the presence of O-N bonds. The data analysis of the Cu2p spectra showed the presence of Cu_2O boding configurations (Fig. S11.10), thus indicating that few oxygen atoms are also bonded to the Cu foil[50, 51]. Moreover, the absence of any N-O bonds in the N1s spectra implies that all the oxygen atoms in the BCNO films are primarily bonded to C and B atoms only[50, 51]. The percentage concentrations of each bonding state for the constituent atoms (B, C, N, and O atoms) were determined (Figures S11.11 a–d). In general, and ignoring the predominance of C-C bonds, the results show that the preferred and stable bonding configurations within the BCNO films follow the theoretically determined bonding energies[56]:

B-N (4.00 eV) > C-C (3.71 eV) > N-C (2.83 eV) > B-C (2.59 eV)

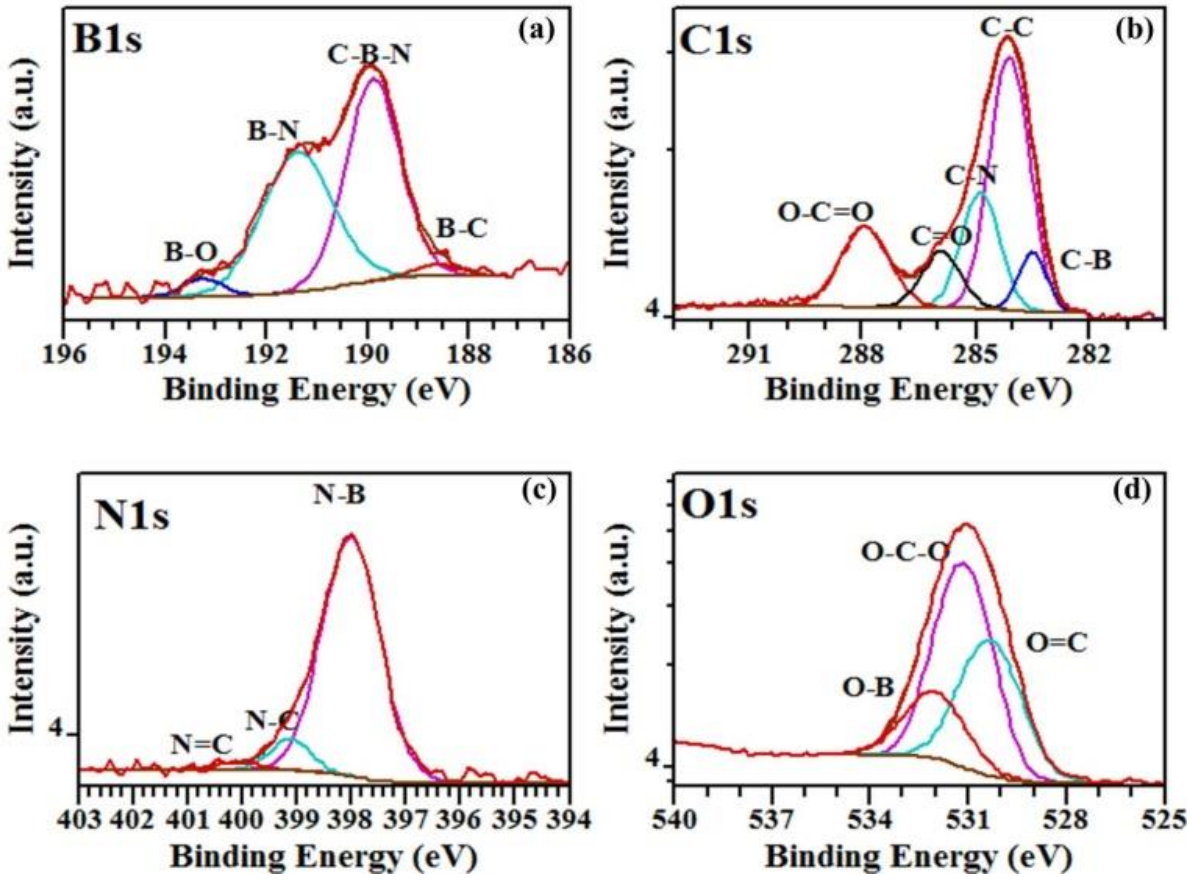

Figure 11.6: XPS spectra showing deconvoluted curves of (a) B1s, (b) C1s, (c) N1s, and (d) O1s BCNO films grown at 2 cm.

11.3.4 UV-vis analysis of the films

The UV-vis absorption spectra (Fig. 11.7a) were used to determine the optical band gap energies of the BCNO films. Since the as-synthesized films contained portions of graphene and *h*-BN, which are both direct band gap materials, the absorbance near the band edge can be determined. Previous reports have shown that the optical properties of the BCNO films are located between those of pure graphene and pure *h*-BN, which is found to be similar for that of boron carbonitride (BCN) films[17-21]. Furthermore these properties can also be tuned by adjusting their atomic configuration and composition. Tauc's equation[57] was used to determine the band gap energies (E_g) of the BCNO films (equation 1);

$$\omega^2 \varepsilon = (h\omega - E)^2, \qquad (1)$$

where ε is the optical absorbance and $\omega = 2\pi/\lambda$ is the angular frequency of the incident radiation. A plot of $\varepsilon^{1/2}$ versus $1/\lambda$ is expected to give a straight line with an x-axis intercept

at $1/\lambda$ and an optical band gap energy calculation based on $E = hc/\lambda$. The band gap energies determined from the calculations are listed in table 11.1.

Table 11.1: Optical band gap energies for the BCNO films

Sample Name	Band Energy (eV)		
	I	II	III
BCNO-2	5.87 ± 0.05	-	2.35 ± 0.06
BCNO-4	5.86 ± 0.04	5.76 ± 0.01	2.57 ± 0.02
BCNO-6	5.85 ± 0.02	5.72 ± 0.04	2.56 ± 0.01
BCNO-8	5.81 ± 0.03	5.61 ± 0.04	1.95 ± 0.05
BCNO-10	5.70 ± 0.01	5.57 ± 0.01	1.78 ± 0.02
BCNO-12	5.66 ± 0.06	5.22 ± 0.01	1.74 ± 0.04

Figure 11.7c shows that BCNO-2 exhibited two absorption edges at 210.1 nm and 518.8 nm, which correspond to band gap energies of 5.87 ± 0.05 eV and 2.35 ± 0.06 eV, respectively. This indicates that both *h*-BN and doped graphene domains contributed predominately to the electronic properties of the BCNO-2 films. The result correlated well with figures S11.11a and c which showed relatively high concentrations of both B-N and N-B bonds under those growth conditions. In addition, BCNO-12 films (Fig. 11.7d) exhibited three band gap energies at 5.66 ± 0.06 eV, 5.22 ± 0.01 eV and 1.74 ± 0.04 eV. The results showed that the *h*-BN, *h*-BCN, and doped graphene domains contributed to the optical properties of BCNO-12 films. The summary of band gap energies of all the BCNO films (Fig. 11.7b and S11.12) showed that *h*-BN, *h*-BCN and doped graphene domains all contributed to the electrical properties. Since XPS survey spectra (Fig.11.5a) showed an increasing C-content with growth distance, the effect of C-doping on the *h*-BN domains was indicated by the narrowing of the band gap energy of the *h*-BN domains with increasing growth distance (Fig. 7b-blue line). The effect of the increasing C-content was further shown by the red-shift of *h*-BCN domain band gap energy (Fig. 11.7b-green line), indicating the formation of fewer *h*-BCN domains (Fig. S11.11a). Finally, the red line in figure 11.7b shows that in BCNO-2 films band gap opening of the graphene domains (2.35 ± 0.06 eV) was due to incorporation of B and N atoms. Similar to the cases of *h*-BN and *h*-BCN domains, an increase in the C-content with growth distance led to the narrowing of the optical band to a minimum of 1.74 ± 0.04 eV for BCNO-12 films.

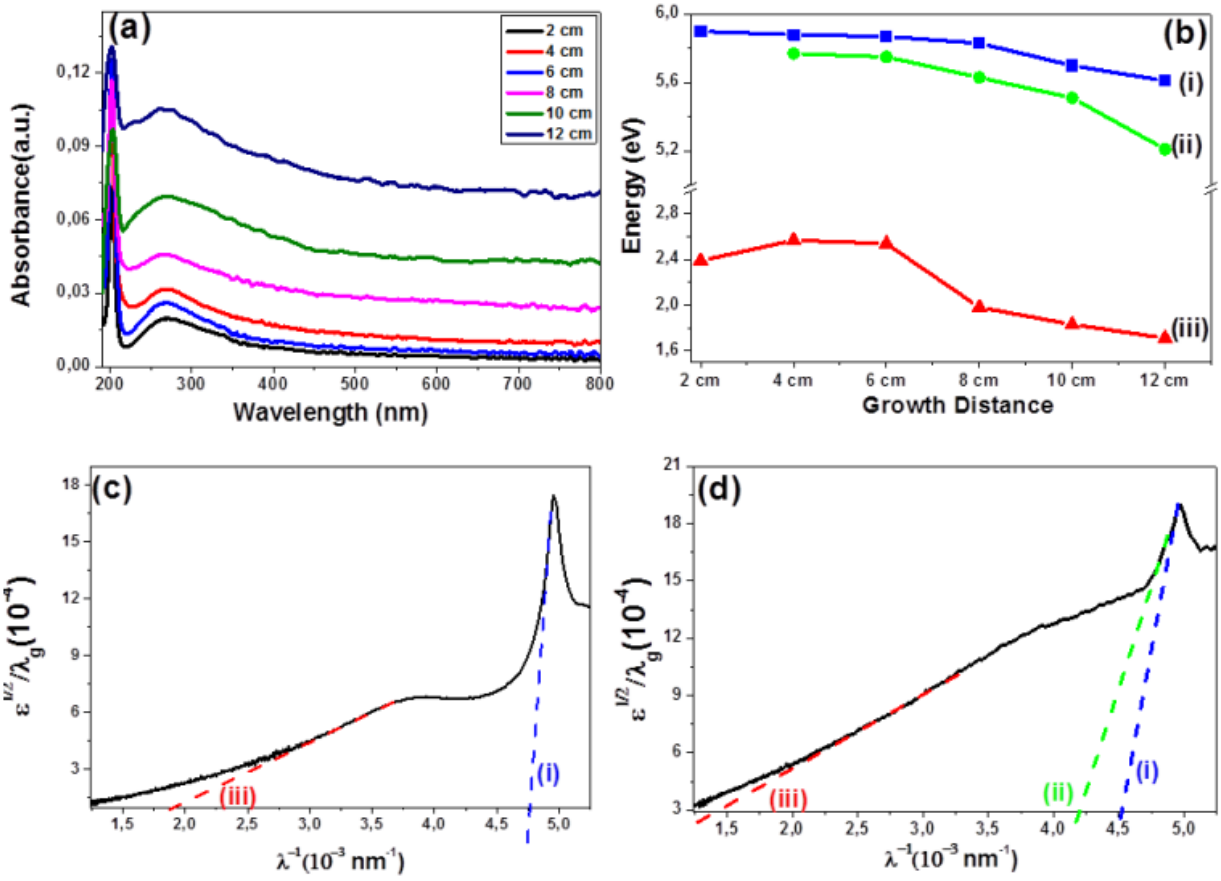

Figure 11.7: (a) UV-vis spectra of all films, (b) Band gap energies, and Tauc's plots of the BCNO hybrid films grown (c) 2 cm and (d) 12 cm, respectively.

11.3.5 Proposed growth mechanism

Based on the above analysis, we can propose a mechanism for understanding the formation of the BCNO films on varying the compositions (B, C, N, and O) of the films. From figures 11.5b and S11.9, the growth of films can be seen to follow at least three processes. Process 1 corresponds to the use of short distance (2 cm) and a large B_2O_2 flux, process 2 to a medium reaction temperature and lower flux (4 cm - 6 cm), and process 3 (8 cm – 12 cm) to lower B_2O_2 flux and reaction temperature. Scheme 11.1 shows a graphical representation of the materials formed in all stages. From our previous work[34], we showed that during the ramping and annealing step (Fig. S11.1a), the solid H_3BO_3 decomposed and vaporized to $B_2O_{2\,(g)}$, which was then deposited onto the Cu substrate. In process 1, due to the high flux of $B_2O_{2\,(g)}$ onto the Cu substrate, there is a tendency to form large B-rich domains of *h*-BN upon introduction of the $NH_{3\,(g)}$. This is shown by the B/N ratio which is almost 2 (Table S11.1). These domains were then surrounded by carbon atoms formed from $CH_{4\,(g)}$ to give a continuous sp^2-C-B-N matrix, while the rest of the C atoms formed B-, N- and pristine

graphene domains. In addition, the presence of unreacted B_2O_2 domains is indicated by the locations of both the B-O (193.3 eV) and O-B (532.5 eV) peaks from the B1s and O1s spectra. Although the presence of unreacted B_2O_2 domains were observed from XPS data, it was observed that the optical band energies from *h*-BN (5.87 ± 0.05 eV) and doped graphene (2.35 ± 0.06 eV) domains mainly contributed to the electronic properties of the BCNO-2 films. As a result, we can conclude that the formation of BCNO hybrid films in stage 1 is due to the presence of regions of N-doped, and B-doped graphene, as well as *h*-BN, *h*-BCN, and B_2O_2 domains.

During process 2 (4 cm – 6 cm), the flux of $B_2O_{2\,(g)}$ is lowered resulting in the formation of small *h*-BN domains with a B/N ratio that is close to unity (Table S11.1). Further analysis showed that the relative amounts of N-C and C-B-N bonds reached a maximum, while both B-N and N-B bonds were at their minimum (Figs. S11.11a and c). These results indicated that most of the N and B atoms contributed to the formation of N- and B-doped graphene and sp^2-C-B-N domains, thus reducing the number of N atoms present in *h*-BN domains. This phenomenon was supported by the widening of the band gap energies of the doped-graphene domains formed in the BCNO-4 and BCNO-6 hybrid films (Table 11.1I). Furthermore, a red shift that was observed for the B-O (~191.5 eV) and O-B (~533.5 eV) peaks in B1s and O1s spectra suggested the possible disintegration of the B_2O_2 domains by the atomic substitution of O atoms with C atoms leading to the formation of numerous individual B-O-B domains. Therefore, it can be summarized that the BCNO films synthesized during the process 2 growth regimes are composed of *h*-BN, *h*-BCN, sp^2-C-B-N, doped graphene, as well as less saturated B_2O_2 and B-O-B domains.

Finally in process 3, both the B (15.38 at % - 2.08 at %) and N (12.01 at % - 1.48 at %) contents had significantly decreased, while an increase in the C content (45.79 at % - 65.76 at %) was observed with increasing growth distance. The high C content led to an increase in the relative amount of C atoms that participated in the formation of the graphene grains, and this was observed by the narrowing of the band gap energy (Fig. 11.7b, red line) as well as an increase in the percentage concentration of C-C bonds (Fig. S11.11b). Moreover, since the increased distance from the hot zone resulted in a low $B_2O_{2\,(g)}$ flux onto the Cu substrate, this led to the formation of small *h*-BN domains with a B/N ratio close to unity. The presence of these *h*-BN domains was shown by the optical band gap energies of 5.81 ± 0.03 eV, 5.70 ± 0.01 eV and 5.66 ± 0.06 eV for the BCNO-8, BCNO-10 and BCNO-12 films, respectively. The calculated band gap energies of these films are lower than that of *h*-BN (~6.01 eV) [8, 9, 11,

[12] due to the incorporation of C atoms into the *h*-BN domains. In addition to this, formation of more C-C bonds restricted the growth of a continuous C-B-N matrix. Thus, a broadening of the optical energies (Table 11.1II) and sudden drop the percentage concentration of C-B-N bonds (Fig. S11.11b) was detected. A further red shift was observed for both B-O and O-B peaks in B1s and O1s spectra (Figs. S8 and 9), indicating the formation of numerous B-O-B domains. We therefore propose that the BCNO films grown in process 3 are made up of regions of pristine, N-doped, B-doped graphene, *h*-BN, and B-O-B domains.

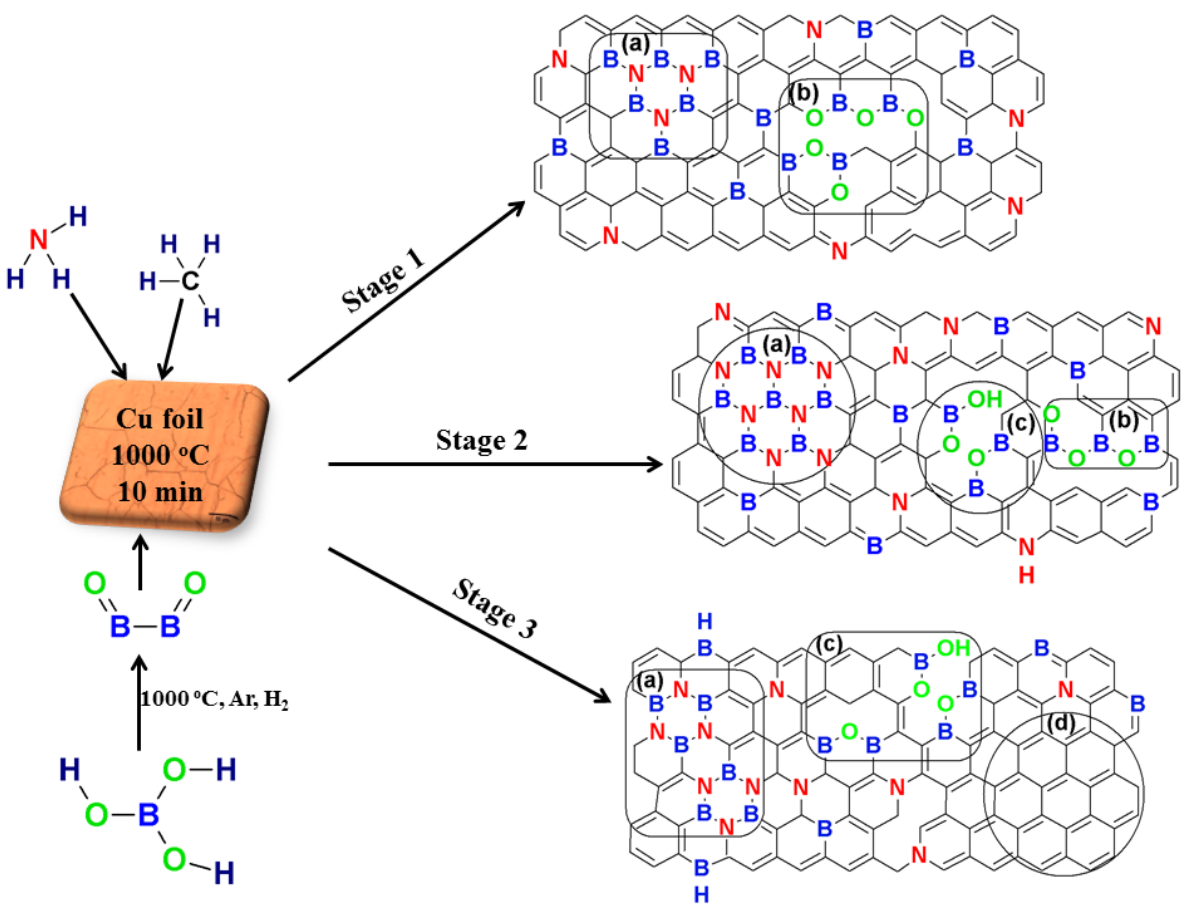

Scheme 11.1: Formation of BCNO films at stages 1-3: (a) *h*-BN, (b) B_2O_2, (c) discrete B-O-B, (d) pure graphene domains within a BCNO matrix.

In summary, it was observed that the total amount of $B_2O_{2\ (g)}$ within the growth chamber and reaction of $B_2O_{2\ (g)}$ with both CH_4 and NH_3 played a significant role in determining the overall composition of the BCNO film, its optical properties as well as influencing the formation of different domains (i.e. *h*-BN, B-O-B, or pristine and doped graphene domains). For instance, a high gas flux of B_2O_2 led to the formation of BNCO-2 films whose electronic properties were mainly influenced by the *h*-BN and N/B doped graphene domains.

Additionally, the presence of unreacted B_2O_2 domains was also confirmed by XPS analysis. On the other hand, a shift of the position of the B-source to 4 cm and 6 cm away from the Cu substrate, revealed that the three main domains, viz. *h*-BN, sp^2C-B-N and doped graphene domains, predominantly contributed to the optical properties of the as-grown BCNO films. Remarkably, shifting the B-source further away from the growth substrate (8 cm to 12 cm) resulted in the lowest total $B_2O_{2\,(g)}$ flux in the reaction chamber; which led to formation of *h*-BN, sp^2C-B-N, doped and pristine graphene domains, that contributed mainly to the observed optical properties of the BCNO films.

11.4. Conclusions

BCNO films with varying atomic compositions were successfully grown on Cu-growth substrate using an APCVD technique. Optical, AFM and TEM images showed that the as-grown BCNO films were continuous and uniform over a large area, with an estimated thickness in the range of ~2.19 ± 0.08 nm to ~4.00 ± 0.13 nm. HRTEM analysis confirmed that the films exhibited a different number of layers. Raman spectroscopy showed the presence of different bonding states in the form of B-C, pure/doped graphene and *h*-BN domains. XPS survey spectra indicated that the elemental compositions were dependent on the amount of $B_2O_{2\,(g)}$ in the reaction chamber. UV-vis analysis corroborated the Raman and XPS results and showed that the as-grown films exhibited three band gap energies corresponding to the *h*-BN (5.87 ± 0.05 – 5.66 ± 0.06 eV), *h*-BCN (5.76 ± 0.01 – 5.22 ± 0.01 eV) and doped graphene (2.35 ± 0.06 – 1.74 ± 0.04 eV) domains. The optical energies of all domains broadened with growth distance due to an increase of the C-content. This led to C-doping in *h*-BN and *h*-BCN domains, while on the other hand it resulted in growth of more graphene domains. Finally, an analysis of the data from all the characterization techniques assisted in developing a mechanism for the growth of the as-synthesized BCNO films.

References

1. Novoselov, K. S., A. K Geim, S.V. Morozov, D. Jang, Y. Zhang, *et.al. Science.* **2004,** *306*, 666-669.
2. Geim, A. K., K. S. Novoselov. *Nat. Mater.* **2007,** *6*, 183-191.
3. Castro Neto, A. H., F. Guinea, N. M. R. Peres, K. S. Novoselov, A. K. Geim. *Rev. Mod. Phys.*, **2009,** *81*, 109-162.

4. Li, S. S., K. H. Tu, C. C. Lin, C. W. Chen, M. Chhowalla. *ACS Nano*, **2010,** *4*, 3169-3174.
5. Zhu, Y., S. Murali, W. Cai, X. Li, J. W. Suk, J. R. Potts, *et.al*. *Adv. Mater.,* **2010,** *22*, 3906-3924.
6. Cheng, R., J. Bai, L. Liao, H. Zhou, Y. Chen, L. Liu, *et.al*. *Proc. Nat. Acad. Sci.* **2012,** *109*, 11588-11592.
7. Liu, C., Z. Yu, D. Neff, A. Zhamu, B. Z. Jang. *Nano Lett.* **2010,** *10*, 4863-4868.
8. Nag, A., K. Raidongia, K. P. S. S. Hembram, R. Datta, U. V. Waghmare, C. N. R. Rao. *ACS Nano*, **2010,** *4*, 1539-1544.
9. Corso, M., W. Auwärter, M. Muntwiler, A. Tamai, T. Greber, J. Osterwalder. *Science*, **2004,** *303*, 217-220.
10. Wentorf, R. H. *J. Chem. Phys.* **1961**, *34*, 809-812.
11. Stehle, Y., H. M. Meyer, R. R. Unocic, M. Kidder, G. Polizos, P. G. Datskos, R. Jackson, S. N. Smirnov, I. V. Vlassiouk. *Chem. Mater.*, **2015,** *27*, 8041-8047.
12. Kubota, Y., K. Watanabe, O. Tsuda, T. Taniguchi, *Science* **2007,** *317, 932*-934.
13. Watanabe, K., T. Taniguchi, H. Kanda, *Nat. Mater.* **2004**, *3*, 404-409.
14. Li, J., X. Xiao, X. Xu, J. Lin, Y. Huang, Y. Xue, P. Jin, J. Zou, C. Tang. *Sci. Rep*., **2013**, *3*, 3208-3214.
15. Ci, L., L. Song, C. Jin, D. Jariwala, D. Wu, Y. Li, *et.al*. *Nature Mater.* **2010,** *9*, 430-435.
16. Kaner, R. B., J. Kouvetakis, C. E. Warble, M. L. Sattler, N. Bartlett. *Mater Res Bull*. **1987**, *22*, 399-401.
17. Kang, Y., Z. Chu, D. Zhang, G. Li, Z. Jiang, H. Cheng, X. Li. *Carbon*. **2013**, *61*. 200-208.
18. Dou, S., X. Huang, Z. Ma, J. Wu, S. Wang. *Nanotechnology*. **2015,** *26*, 045402-045409.
19. Mannan, M. A., M. Nagano, N. Hirao, Y. Baba. *Chemistry Letter*, **2008,** *37*, 96-97.
20. Shinde, P. P., V. Kumar. *Phys. Rev. B.* **2011,** *84*, 125401 (1-6).
21. Essafti, A., E. Ech-chamikh. *J Mater Sci*. **2011,** *46*, 5847-5850.
22. Watanabe, M. O., T. Sasaki, S. Itoh, K. Mizushima. *Thin Solid Films*. **1996,** *282*, 334-336.
23. Rivera-Tapia, E. D., C. A. Fajardo, A. J. Avila-Vega, C. F. Avila, F. M. Sanchez-Arévalo, I. Chango-Villacís, F. J. Quiroz-Chavez, J. Santoyo-Salazar, R. C. Dante. *Fullerenes, Nanotubes and Carbon Nanostructures,* **2016,** 24, 8-12.

24. Lei, W., D. Portehault, R. Dimova, M. Antonietti. *J. Am. Chem. Soc*., **2011**, *133*, 7121-7127.
25. Zhang, X., Li, L., Lu, Z., Lin, J., Xu, X., Ma, Y., Yang, X., Meng, F., Zhao, J., C. Tang. *J. Am. Ceram. Soc.*, **2014,** *97*, 246-250.
26. Ozturk, B., A. de-Luna-Bugallo, E. Panaitescu, A. N. Chiaramonti, F. Liu, A. Vargas, X. Jiang, N. Kharche, O. Yavuzcetin, M. Alnaji, M. J. Ford, J. Lok, Y. Zhao, N. King, N. K. Dhar, M. Dubey, S. K. Nayak, S. Sridhar, S. Kar. *Science Advances.* ***2015,*** *31*, e1500094 (1-8).
27. Singh, L., V. Chopra. *J. Mater. Sci. Technol*. **2011,** *27*, 967-972.
28. Liu, X. F., S. Ye, Y.B. Qiao, G. P. Dong, Q. Zhang, J. R. Qiu. *Chem. Commun*. **2009,** 27, 4073-4075.
29. Kommo, H., T. Ito, M. Ushiro, K. Fushimi, K. Azumi. *J. Power Sources.* **2010,** *195*, 1739-1746.
30. Portehault. D., C. Giordano, C. Gervias, I. Senkovska, S. Kaskel. C. Snachez, M. Antonietti. *Adv. Funct. Mater.* **2010,** *20*, 1827-1833.
31. Liu, Q., P. Jiang, Z. Pu, A. M. Asiri, A. O. Al-Youbi, X. Sun. *Sensors and Actuators B: Chem.* **2014,** *194*, 492-497.
32. Reina, A., X. Jia, J. Ho, D. Nezich, H. Son, V. Bulovic, *et al*. *Nano Lett*. **2009,** *9*, 30-35.
33. Song, X., J. Gao, Y. Nie, T. Gao, J. Sun, D. Ma. . *Nano Res*. **2015,** *8*, 3164-3176.
34. Matsoso, B. J., K. Ranganathan, B. K. Mutuma, T. Lerotholi, G. Jones, N. J. Coville. *Nanotechnology*. **2017**, *28*, 105602 (1-11).
35. Dodoo-Arhin, D., F. Mopeli, A. Bello, N. Manyala. *Ind. Eg. Chem. Res.* **2013,** *52*, 14160-14168.
36. Wang, Y., Y. Zheng, X. Xu, E. Dubuisson, Q. Bao, J. Lu, K. P. Loh. *ACS Nano*. **2011,** *5*, 9927-9933.
37. Malard, L. M., M. A. Pimenta, G. Dresselhaus, M. S. Dresselhaus. *Phys Rep*. **2009,** *473***,** 51-87.
38. Ferrari, A. C. *Solid State Commun*. **2007,** *143*, 47-57.
39. Ferrari, A. C., J. C. Meyer, V. Scardaci, C. Casiraghi, M. Lazzeri, F. Mauri, *et.al. Phys. Rev. Lett*. **2006,** 97, 187401 (1-4).
40. Casiraghi, C., S. Pisana, K. S. Novoselov, A. K. Geim, A. C. Ferrari. *Appl. Phys. Lett.* **2007,** *91*, 233108 (1-3).

41. Reich, S., A. C. Ferrari, R. Arenal, A. Loiseau, I. Bello, J. Robertson. . *Phys. Rev. B.* **2005,** 71, 205201 (1-12).
42. Brito, W. H., R. Kagimura, R. H. Miwa. *Phys. Rev. B.* **2012,** 85, 035404.
43. Reddy, K. M., P. Liu, A. Hirata, T. Fujita, M. W. Chen. *Nat. Commun.* **2013,** *4:2483* (1-5).
44. Subhash, G., D. Ghosh, J. Blader, J. Q. Zheng, V. Halls, K. Masters. *Acta Materialia.* **2013**, *61*, 3888-3896.
45. Yan, X. Q., W. J. Li, T. Goto, M. W. Chen. *Appl. Phys. Lett.* **2006**, *88*, 131905 (1-3).
46. Cancado, L. G., A. Jorio, E. H. Martins Ferreira, F. Stavale, C. A. Achete, R. B. Capaz, *et al*. *Nano Lett*. **2011,** *11***,** 3190-3196.
47. Eckmann, A., A. Felten, A. Mishchenko, L. Britnell, R. Krupke, K.S. Novoselov, *et al. Nano Lett*. **2012,** *12***,** 3925-3930.
48. Lee, J. Y., S. J. Lee, K. S. Kim. *J. Chem. Phys.* **1997,** *107*, 4112-4117.
49. Wang, Y., R. A. Poirier. *J. Phys. Chem. A.* **1997,** *101*, 907-912.
50. Lin, T. W., C.Y. Su, X.Q. Zhang, W. Zhang, Y.H. Lee, H.Y. Li, *et.al. Small*. **2012,** *8*, 1384-1391.
51. Uddin, M. N., I. Shimoyama, Y. Baba, T. Sekiguchi, M. Nagano. X *J. Vac. Sci. Technol. A.* **2005,** *3*, 497–502.
52. Schild, B., S. Ulrich, J. Yeb, M. Stüber. *Solid State Sci*. **2010,** *12*, 1903–1906.
53. Mannan, M. A., M. Nagano, T. Kida, N. Hirao, Y. Baba. *J. Physics and Chemistry of Solids*. **2009,** *70*, 20-25.
54. Yang, Q., C. B. Wang, S. Zhang, D. M. Zhang, Q. Shen, L. M. Zhang. *Surface & Coating Technology*. **2010,** *204*. 1863-1867.
55. Hornyak, G. L., J. J. Moore, H. F. Tibbals, J. Dutta. *CRC Press, Taylor & Francis Group*. **2009**, London
56. Ding, X., *J. Mater. Chem*. **2014,** *2*, 3717-3722.
57. Tauc, J, R. Grigorovici, A. Vancu. *Phys. Stat. Sol*. **1966,** *3*, 627-637.

Chapter 12

General Conclusions and Recommendations

12.1 Conclusions

12.1.1 Synthesis of high quality graphene films by APCVD

- Optimization for the growth of high quality graphene films on a Cu catalyst using atmospheric pressure CVD was conducted by using different growth times (2, 10, and 20 min) and methane flow rates (5, 10, 15, 20, and 30 sccm). In all growth time regimes, the growth of graphene films was observed to be a self-limiting reaction mechanism.
- The medium growth time regime (10 min) led to formation of predominantly bilayered graphene films with very good quality, as indicated by the defect density in the range of $0.209 < I_D/I_G < 0.669$.
- Since the main objective was to obtain good growth conditions for the formation of good quality graphene films, the optimum growth conditions were selected to be as follows: CH_4 flow rate (10 sccm), growth time (10 min), and H_2 concentration (10 sccm).
- Under optimum growth conditions, the effect of the reducing atmosphere (H_2 flow rate) on the quality and thickness of the graphene films at three synthesis stages was studied; that is at annealing (A), growth (G), and both annealing/growth (A/G) stages. Different hydrogen flow rates (0, 3, 10, 50, and 100 sccm) were introduced into the reaction chamber at all synthesis stages.
- Low flow rates of H_2 (3 sccm) during (A/G) stage led to growth of monolayered ($I_G/I_{2D} = 0.265$) graphene films of very good quality ($I_D/I_G = 0.184$); while during (A) and (G) stages, it resulted in formation of good quality bilayered graphene films, as indicated by the ratios: $I_D/I_G = 0.433_{\boldsymbol{A}}$, $I_G/I_{2D} = 0.338_{\boldsymbol{A}}$, $I_D/I_G = 0.293_{\boldsymbol{G}}$, and $I_G/I_{2D} = 0.721_{\boldsymbol{G}}$.
- Although, medium H_2 flow rates (10 sccm) during the A/G step led to the formation of good quality and non-AB stacked bilayered graphene films ($I_D/I_G = \sim 0.206$ and $I_G/I_{2D} = \sim 0.362$), this flow rate together with high flow rates (50 and 100 sccm) during

A and G stages resulted in growth of highly defective and few to multilayered graphene films. This was attributed to the competitive adsorption and decomposition of both CH_4 and H_2 molecules on the available Cu active sites.

- Therefore, for growth of future graphene films on Cu catalysts by APCVD, the final growth conditions were selected to be as follows: CH_4 flow rate (10 sccm), growth time (10 min), and H_2 concentration (3 sccm).

12.1.2 Synthesis of nitrogen doped graphene

- The effect of doping of graphene films with nitrogen atoms via in-situ and post doping routes was investigated by using different flow rates of ammonia gas (5 sccm and 10 sccm).
- XPS results showed that the maximum N/C content of 3.25% was obtained for N-doped graphene films grown from an in-situ synthesis route using 5 sccm NH_3. Moreover, the lowest N/C content of 0.61% was obtained for the N-10sccm post doped graphene films. Thus, indicating that N/C content depends mainly on the flow rate of NH_3 ($N/C_{5sccm} > N/C_{10sccm}$), and to a lesser extent on the synthesis method ($N/C_{in\text{-}situ} > N/C_{post}$).
- Additionally, the type and amount of the N-configurations (pyridinic, pyrrolic, graphitic and NO_x) were found to be influenced by the flow rate of NH_3 as well as the synthesis route.
- Therefore, the optimum growth condition for synthesizing N-doped graphene films was chosen as the in-situ doping route with low flow rate of NH_3 (5 sccm).
- Finally, the effect of growth time (2, 5, 10, and 20 min) on the type of N-configurations and the total N/C ratio was investigated on N-doped graphene films grown using the in-situ route.
- XPS results showed that the maximum N/C content of 4.68 % was obtained at a short growth time; while a minimum N/C content of 2.84 % was observed at longer growth times.
- Additionally, the type and amount of the N configurations (pyridinic, pyrrolic, graphitic and NO_x) were found to be dependent on the growth time, with short growth time containing predominately pyridinic, pyrrolic-N and NO_x bonding configurations, while 10 min-growth time was found to lead to growth of graphitic-N-rich graphene

films. Contrarily, a longer growth time (20 min) resulted in pyridinic-N-rich graphene films with few graphitic-N and pyrrolic-N bonding states.

- In summary, the synthesis of large-area graphene films, either pristine or doped with nitrogen atoms, is technically and/or commercially beneficial based on the following factors:
    a. Ease of controlling the thickness and quality of graphene films.
    b. Recyclable of the Cu foil, since most processes in literature involve acid etching of the Cu foil.
    c. Lack of contaminants such as Fe from using $FeCl_3$ etching method.

12.1.3 Electrochemical oxidation properties of graphene and graphene/metal nanoparticle composites

- The successful application of pristine and N-doped graphene films in ITO –based electrochemical sensors for detection of DA and UA was presented. Additionally, graphene composites with Pt and Pd nanoparticles were investigated for application as electrochemical sensors for detection of DA and UA.
- The electrochemical behaviours of DA and UA were determined to be diffusion controlled at both Gr/ITO and NGr/ITO electrodes as well as at graphene-metal nanoparticle composites.
- Pristine graphene-based electrodes (either Gr/ITO or Gr-NPs/ITO) exhibited good selectivity for both DA and UA, however they both suffered from poor sensitivity and high detection limits (S/N =3).
- On the other hand, N-doped graphene-based (either NGr/ITO or NGr-NPs/ITO) exhibited good sensitivity and very low detection limits for both DA and UA, but with poor selectivity.
- Pt@Gr/ITO, Pd@NGr/ITO and Pt@NGr/ITO electrodes showed better stability and enhanced electrochemical responses in comparison with Gr/ITO electrodes, thus indicating increased charge transfer kinetics due to the presence of metal nanoparticles. However, Pd@Gr/ITO electrodes suffered fouling by the oxidation products, as determined by diminished electrochemical responses in comparison with NGr/ITO electrodes.

12.1.4 Synthesis of co-doped graphene to produce graphene hybrid films.

- Synthesis of *h*-BN QDs/NDs in BCN hybrid films by the APCVD technique was achieved by controlling the vaporization temperature of H_3BO_3, which was achieved by placing the boron source at varying distances from the hot zone.
- AFM analysis showed formation of *h*-BN QDs at distances closer to the hot zone, while *h*-BN NDs were found to form with increasing distance from the hot zone.
- Core-shell XPS spectra indicated that the hybrid films consisted of various B-N, B-C, and C-N bonding configurations.
- Similarly, synthesis of BCNO hybrid films with varying atomic compositions were successfully grown on a Cu-growth substrate using an APCVD technique, by controlling the vaporization temperature of H_3BO_3 and the flow rates of CH_4.
- Optical microscopy, AFM and TEM studies showed that the as-grown BCNO films were continuous and uniform over a large area, whereas HRTEM analysis confirmed that the films exhibited a different number of layers. Moreover, Raman and XPS data showed the presence of different bonding states in the form of B-C, pure/doped graphene and *h*-BN domains.
- UV-vis analysis showed that the as-grown hybrid films exhibited three band gap energies corresponding to the *h*-BN ($5.87 \pm 0.05 – 5.66 \pm 0.06$ eV), *h*-BCN ($5.76 \pm 0.01 – 5.22 \pm 0.01$ eV) and doped graphene ($2.35 \pm 0.06 – 1.74 \pm 0.04$ eV) domains.

12.2 Recommendations

12.2.1 Synthesis of nitrogen doped graphene films

- The determination of the optical properties of N-doped graphene films can be explored so as to broaden their applications, such as in solar cells.
- Additionally, the optical properties would assist in understanding their observed electrocatalytic behaviour towards oxidation of dopamine and uric acid.
- Techniques such as Scanning Tunneling Microscope (STM) are required to clearly quantify the positions of the nitrogen atoms within the graphene lattice.

12.2.2 Support of metal nanoparticles on pristine ad N-doped graphene

- Scanning Tunneling Microscope (STM) is highly recommended in order to clearly quantify the positions of the nitrogen atoms and metal nanoparticles within the graphene lattice.
- The nature of the interaction between the metal nanoparticle and the graphene surface can be determined by theoretical calculations as well as high resolution TEM.
- The nature of the interface properties, such as the charge-transfer resistance, of the metal-NGr composites can be studied using impedence spectroscopy.
- Finally, the ability of graphene and/or N-doped graphene films to stabilize the different metal nanoparticles prepared under various reaction conditions (thermal, pH) should be explored. This could help to further elucidate the metal-support interactions as well as to determine the correct media for fabrication of electrochemical sensors.

12.2.3 Electrochemical oxidation properties of graphene and metal nanoparticle composites

- Optical properties, via UV-vis spectroscopic analysis, would provide information to interpret the electrocatalytic behaviour towards oxidation of dopamine and uric acid.
- Since both dopamine and uric acid co-exist with numerous biomolecules and cations in the body fluids, then interference studies in the presence of K, Na, glucose, ascorbic acid, should be performed so as to determine the stability of these fabricated graphene-based electrodes in media resembling physiological conditions.
- More studies should be performed to improve the selectivity ability of N-doped graphene/ITO electrodes.
- Fabrication sensors based on a composite of graphene and an alloy of platinum and palladium can be performed and then applied in electrochemical sensing of dopamine and/or other biomolecules. This could assist in investigating the electrochemical behaviour of biomolecules at electrode surfaces modified with bimetallic materials.
- Finally, the sensitivity and selectivity of these electrodes towards detection of dopamine and uric acid in real clinical samples, such as urine and preserved meat, should be explored.
- In comparison with many research reports for the detection of dopamine and uric acid, the fabricated electrochemical sensors in this works showed better or comparable

sensitivity. The improved electrochemical performance was attributed to the 2D planar structure of the graphene films, which allows good exposure of electroactive sites. Therefore, it is further, recommended that further studies are conducted to elucidated issues such as scalability, reproducibility, selectivity, etc.

12.2.4 Synthesis of co-doped graphene to produce graphene hybrid films.

- Scanning Tunneling Microscope (STM) is highly recommended in order to clearly quantify the positions of both boron and nitrogen atoms within the hybrid films.
- Since the optical properties were found to be tunable, by varying the atomic compositions of the films, application of these hybrid films can be explored in fields such as FETs, solar cells, and sensors.

Supplementary Information

Appendix A: Electrochemical behaviour and detection of dopamine and uric acid over Pt and Pd- graphene/ITO composites

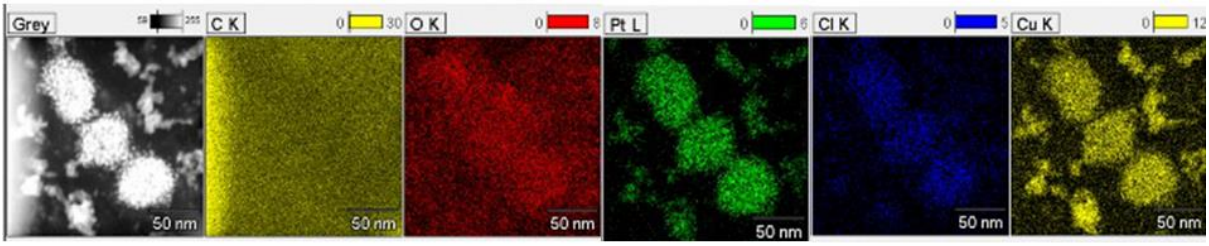

Figure S7.1: HAADF-STEM images of Pt nanoparticles on pristine graphene films.

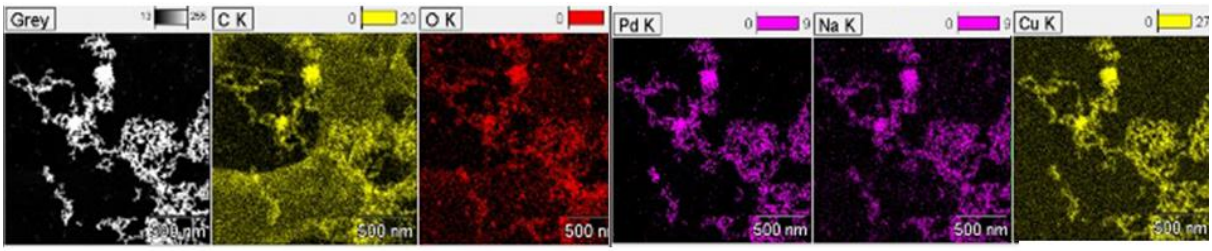

Figure S7.2: HAADF-STEM images of Pd nanoparticles on pristine graphene films.

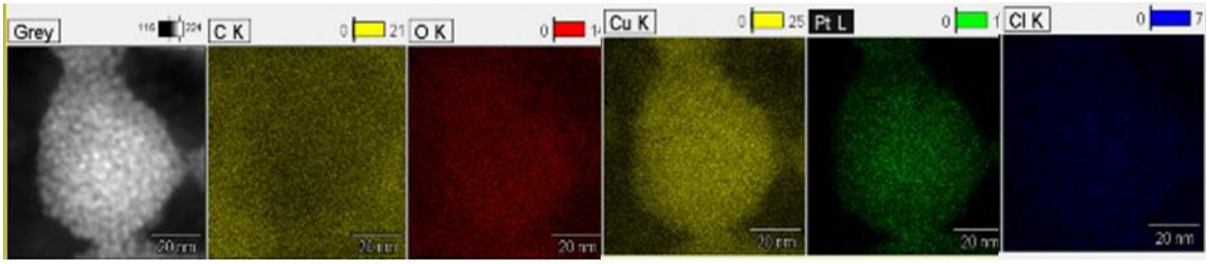

Figure S7.3: HAADF-STEM images of Pt nanoparticles on N-doped graphene films.

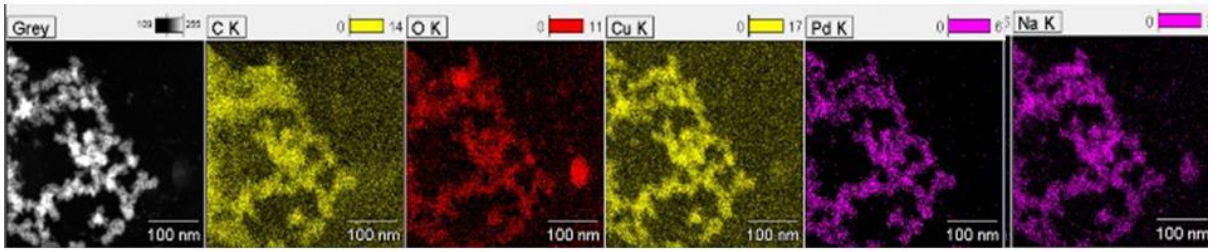

Figure S7.4: HAADF-STEM images of Pd nanoparticles on N-doped graphene films.

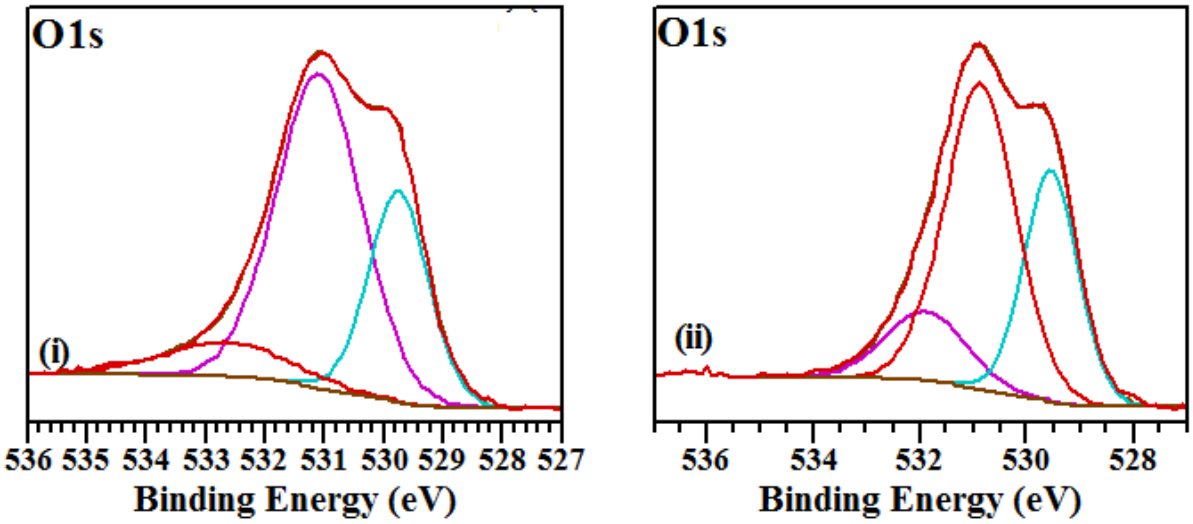

Figure S7.5: O1s XPS spectra of Pt and Pd-composites using (i) pristine and (ii) N-doped graphene.

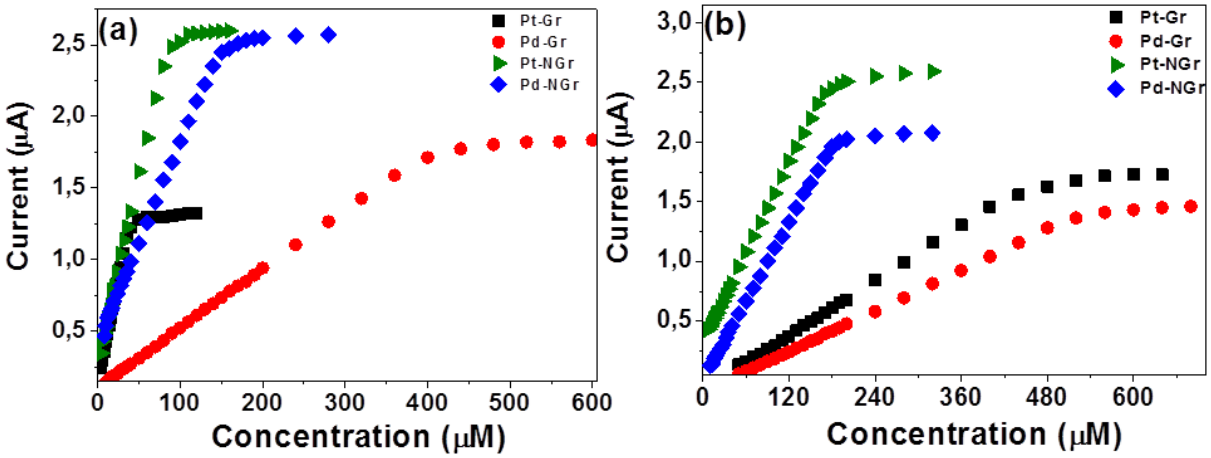

Figure S7.6: Linear concentration ranges of (a) DA and (b) UA on modified ITO electrodes at buffer pH 6.02.

Table S7.1: Relative concentrations of the oxidation states of Pt on the graphene/N-graphene composites

Sample	Positions of Pd oxidation states (eV)					
	Pt $4f_{7/2}$			Pt $4f_{5/2}$		
	Pt^0	Pt^{2+}	Pt^{4+}	Pt^0	Pt^{2+}	Pt^{4+}
Pt-Gr	6.89	31.79	13.03	24.99	17.20	6.10
Pt-NGr	53.81	36.73	-	1.83	8.62	-

Table S7.2: Relative concentrations of the oxidation states of Pd on the graphene/N-graphene composites

Sample	Relative % concentations					
	Pd $3d_{5/2}$			Pd $3d_{3/2}$		
	Pd^0	Pd^{2+}	Pd^{4+}	Pd^0	Pd^{2+}	Pd^{4+}
Pd-Gr	16.45	30.01	9.43	12.74	25.37	6.10
Pd-NGr	33.83	13.32	8.26	27.24	10.48	6.88

Appendix B: Time-dependent evolution of the nitrogen configuration in N-doped graphene films

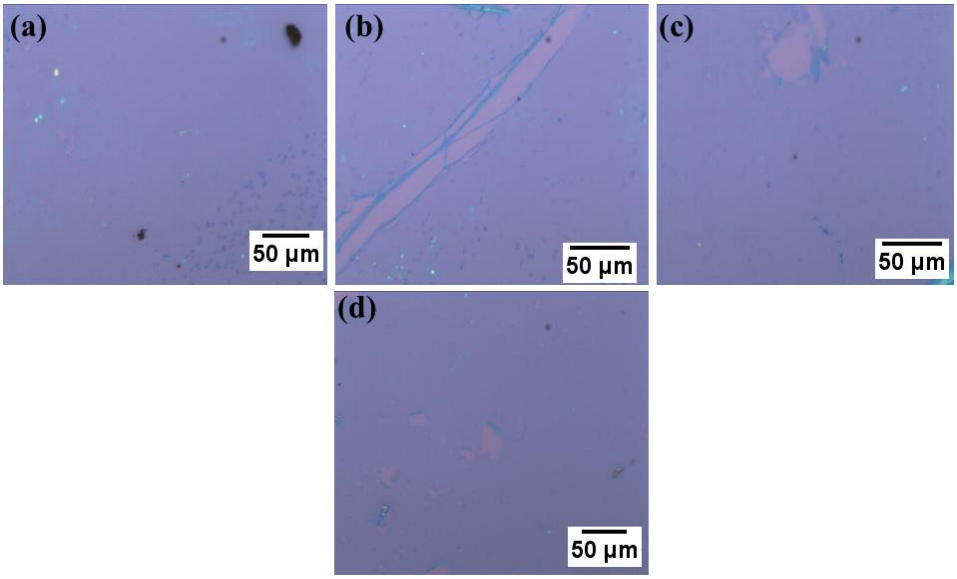

Figure S8.1: Optical images of pristine graphene films grown (2 min, (b) 5 min, (c) 10 min, and (d) 20 min growth times.

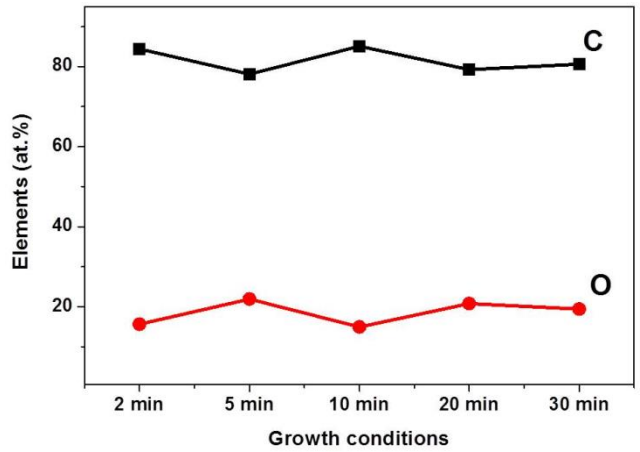

Sample	Elemental compositions (at. %)	
	C	O
2 min	84.4	15.6
5 min	78.1	21.9
10 min	85.1	14.9
20 min	79.2	20.8

Fig S8.2: Elemental plot and table of atomic compositions of pristine graphene films.

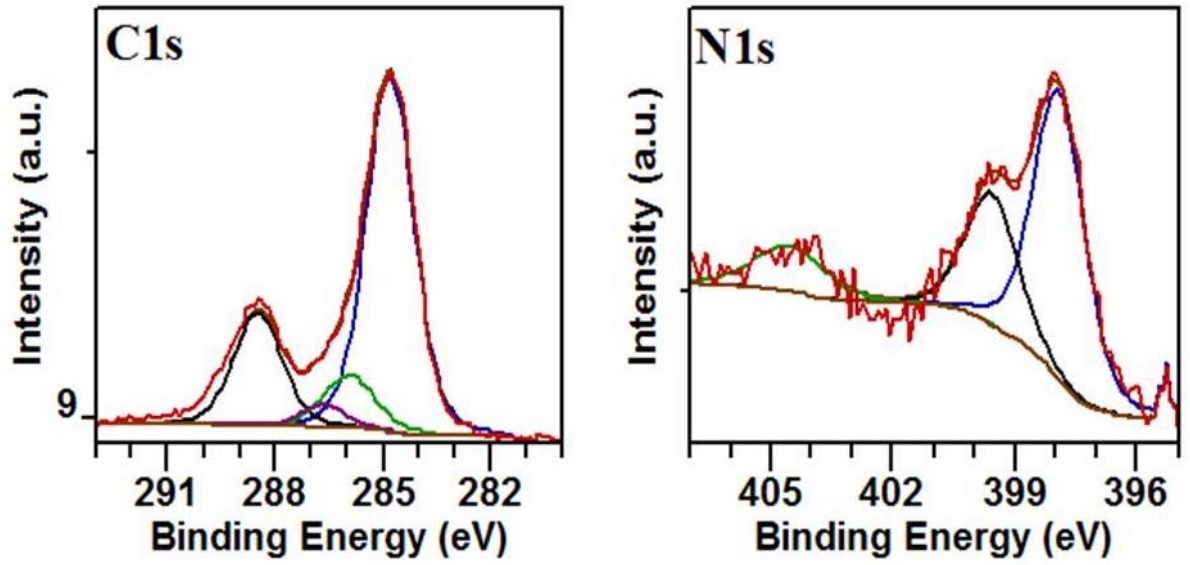

Figure S8.3: Core-shell XPS spectra of N-doped graphene films grown at 2 min with 10 sccm CH_4 and 5 sccm NH_3.

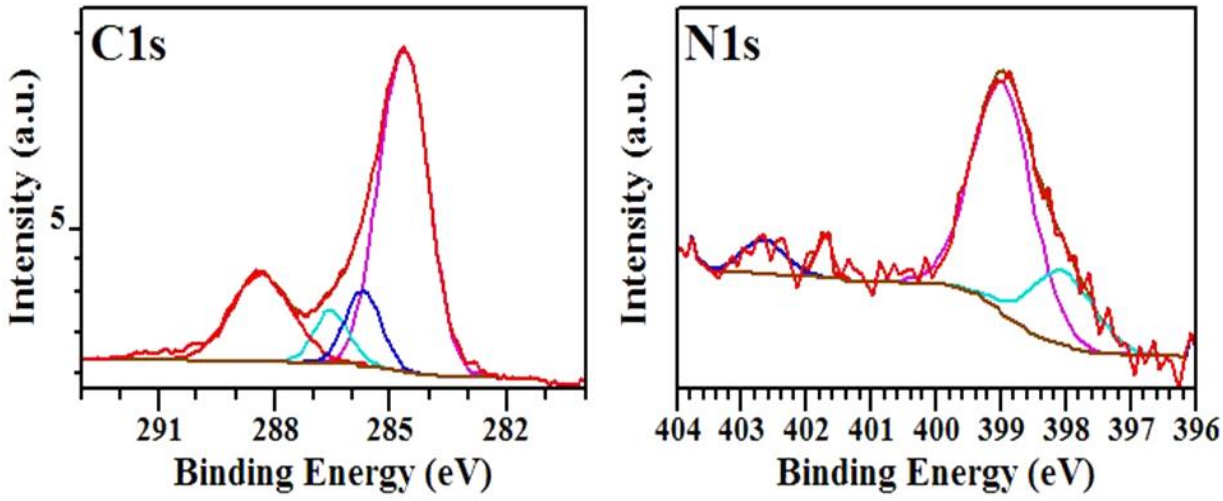

Figure S8.4: Core-shell XPS spectra of N-doped graphene films grown at 5 min with 10 sccm CH_4 and 5 sccm NH_3.

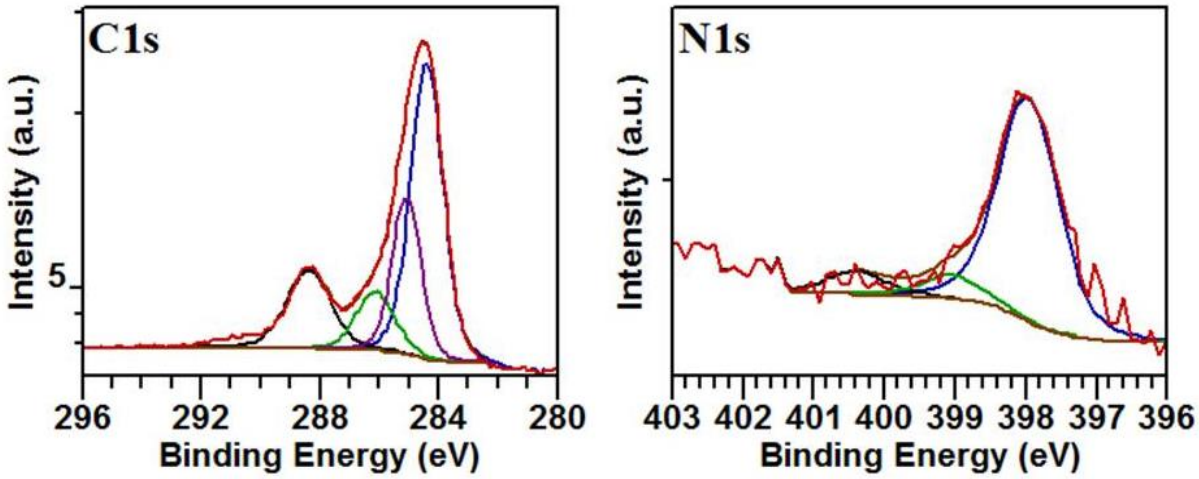

Figure S8.5: Core-shell XPS spectra of N-doped graphene films grown at 20 min with 10 sccm CH_4 and 5 sccm NH_3.

Table S8.1: Atomic compositions of N-doped graphene films

Sample	N-configurations/ N-content (N/C at. %)			
	Pyridinic-N	**Pyrrolic-N**	**Graphitic-N**	**NO_x**
2 min	2.79	1.28	0	0.61
5 min	0.82	2.51	0.13	0.28
10 min	1.24	0.081	1.83	0.11
20 min	2.36	0.24	0.24	0

Appendix C: The effect of N-configuration on the detection of dopamine at N-doped graphene-modified ITO electrodes

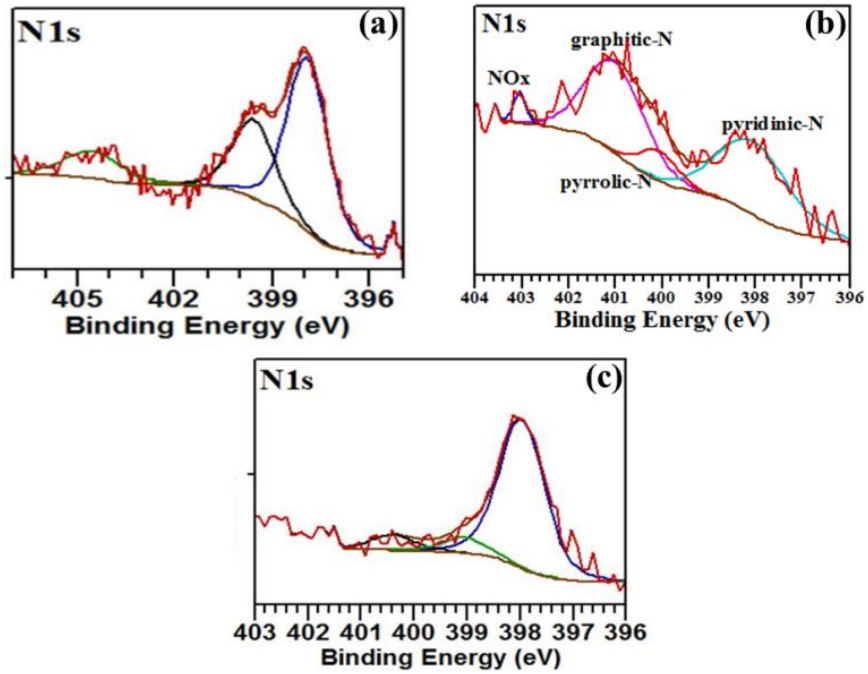

Figure S9.1: N1s core-shell XPS spectra of N-doped graphene films grown at (a) 2 min, (b) 10 min, and (c) 20 min[39].

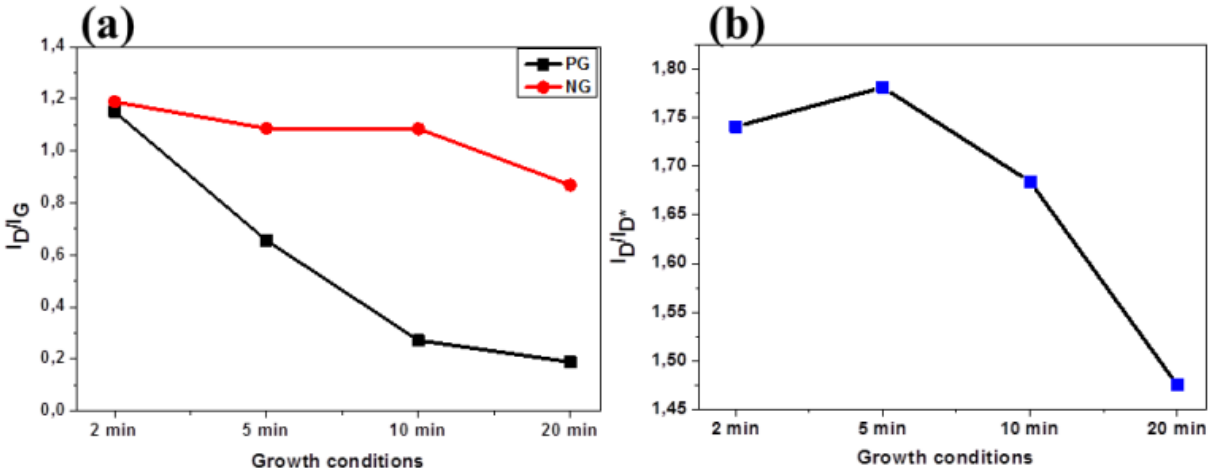

Figure S9.2: Evolution of I_D/I_G (a) with increasing growth time for both pristine and N-doped graphene films and I_D/I_{D^*} (b) for N-doped graphene films[39].

Appendix D: Single-step synthesis of crystalline *h*-BN quantum- and nanodots embedded in boron carbon nitride films

(a)

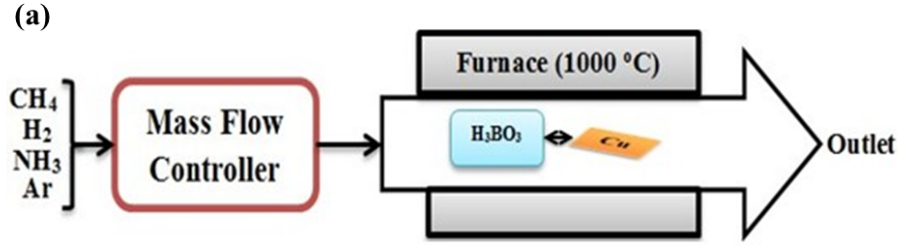

(b)

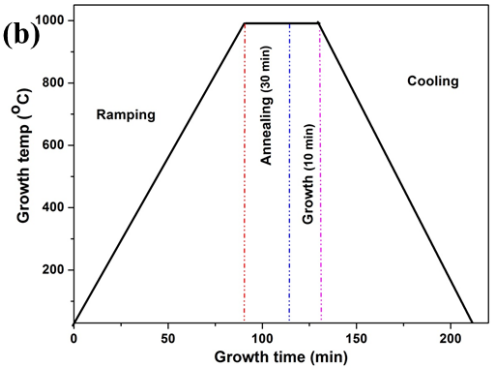

(c)

Distance (cm)	Temperature [a](°C)
2.0	970
4.0	900
6.0	840
8.0	750
10.0	580
12.0	390

Figure S10.1: Growth conditions for the *h*-BN QDs/NDs embedded in BCN films: (a) CVD set-up, (b) growth profile, and (c) temperature profile at different growth distances. [a]Temperature of H_3BO_3 in the tube.

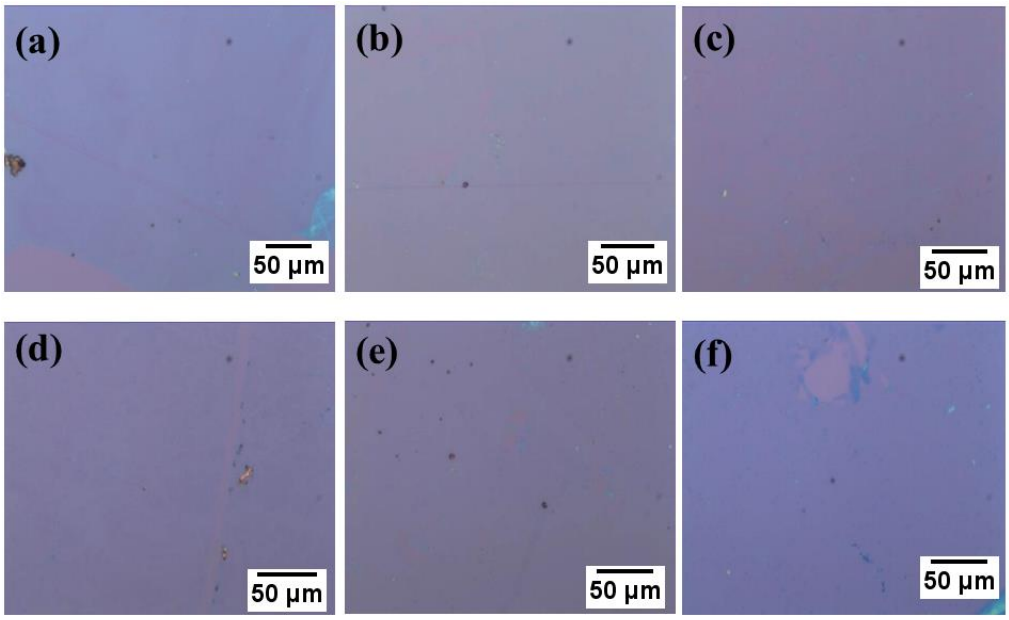

Figure S10.2: Optical images of the *h*-BN QDs/NDs in the BCN films grown at (a) 2 cm, (b) 4 cm, (c) 6 cm, (d) 8 cm, (e) 10 cm, and (f) 12 cm separation distances.

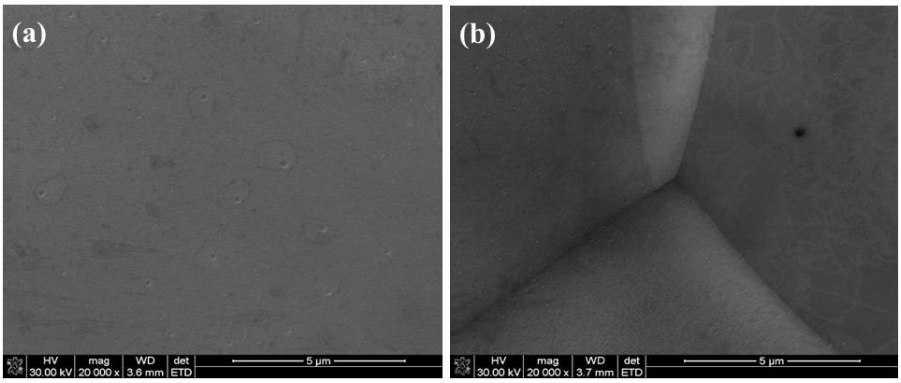

Figure S10.3: SEM images of the *h*-BN QDs/NDs in the BCN films grown at (a) 2 cm (b) 12 cm separation distances.

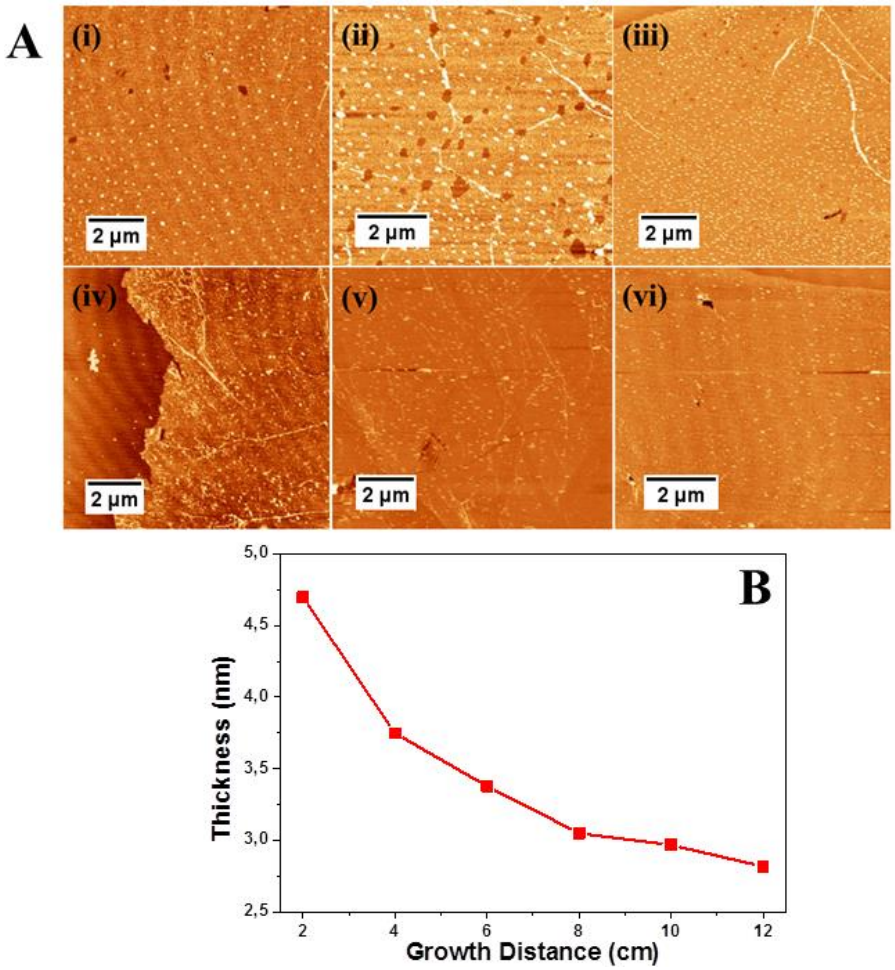

Figure S10.4: (A) AFM images and (B) thickness profile of the *h*-BN QDs/NDs-BCN films grown at (i) 2 cm, (ii) 4 cm, (iii) 6 cm, (iv) 8 cm, (v) 10 cm, and (vi) 12 cm separation distances.

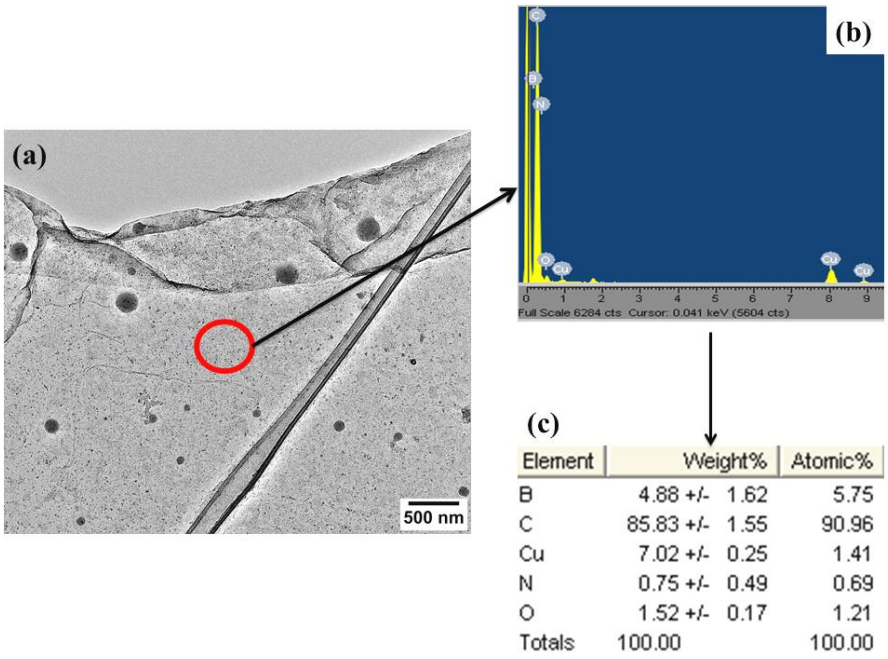

Element	Weight%	Atomic%
B	4.88 +/- 1.62	5.75
C	85.83 +/- 1.55	90.96
Cu	7.02 +/- 0.25	1.41
N	0.75 +/- 0.49	0.69
O	1.52 +/- 0.17	1.21
Totals	100.00	100.00

Figure S10.5: TEM-EDS images of the matrix surrounding the *h*-BN QDs/NDs.

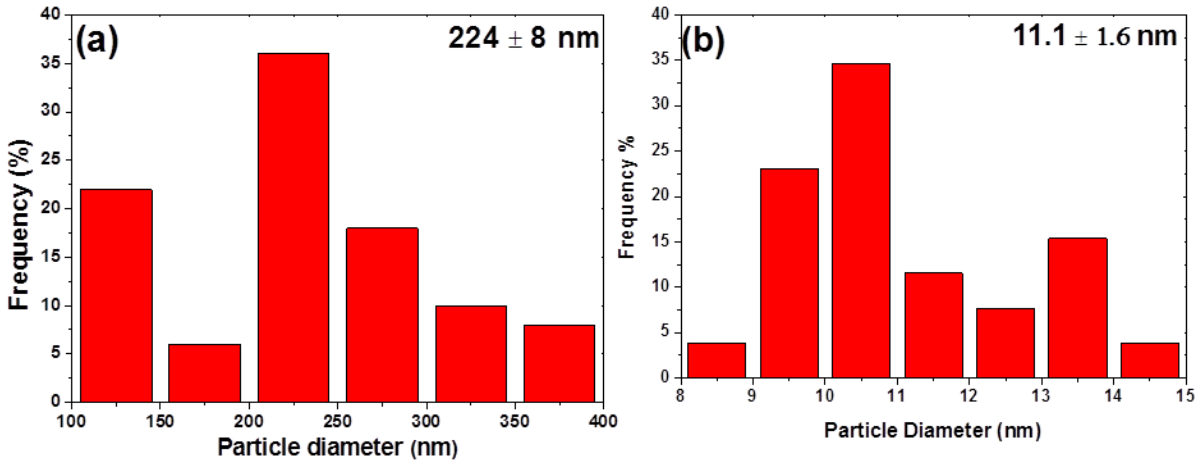

Figure S10.6: Particle size distribution of the *h*-BN QDs/NDs in the BCN films grown at (a) 2 cm (b) 12 cm separation distances.

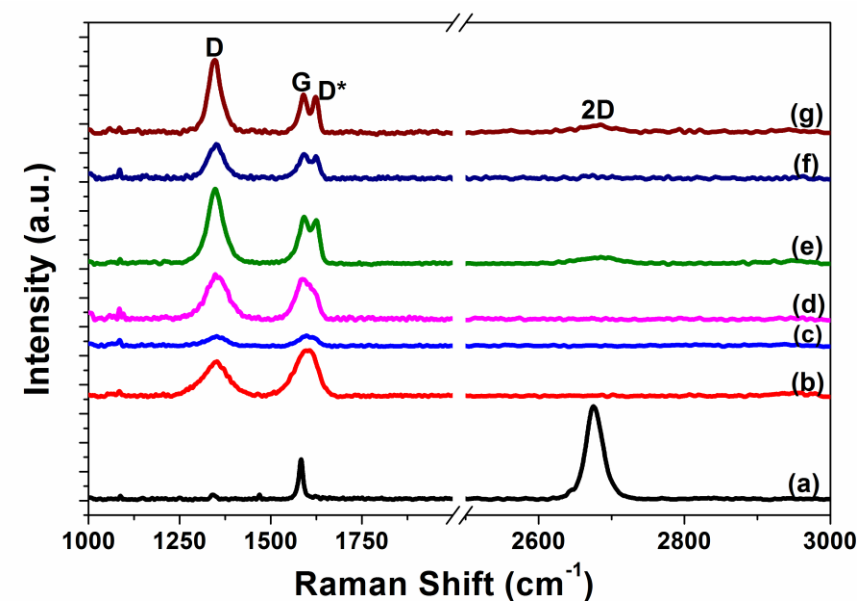

Figure S10.7: Raman spectra of pristine graphene (a) and the *h*-BN QDs/NDs-BCN films: (b) 2 cm, (c) 4 cm, (d) 6 cm, (e) 8 cm, (f) 10 cm, and (g) 12 cm.

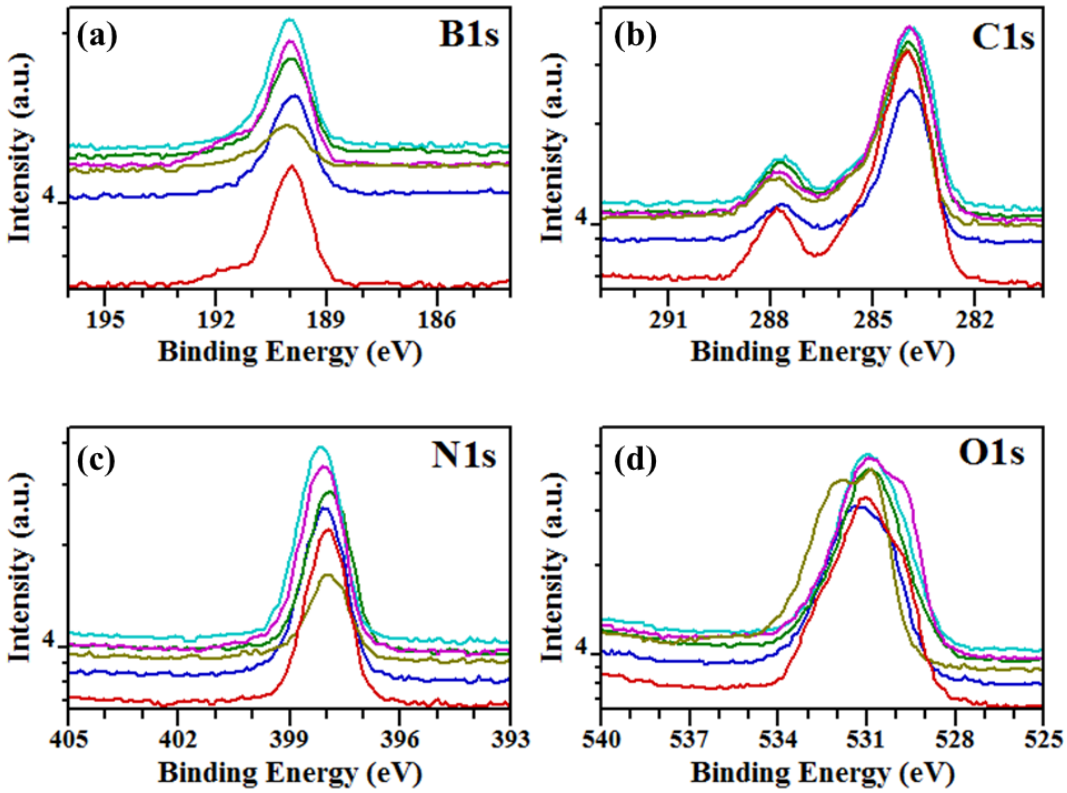

Figure S10.8: (a) B1s, (b) C1s, (c) N1s, and (d) O1s XPS spectra of *h*-BN QDs/NDs-BCN hybrid films grown at **2 cm**, **4 cm**, **6 cm**, **8 cm**, **10 cm,** and **12 cm** separation distances.

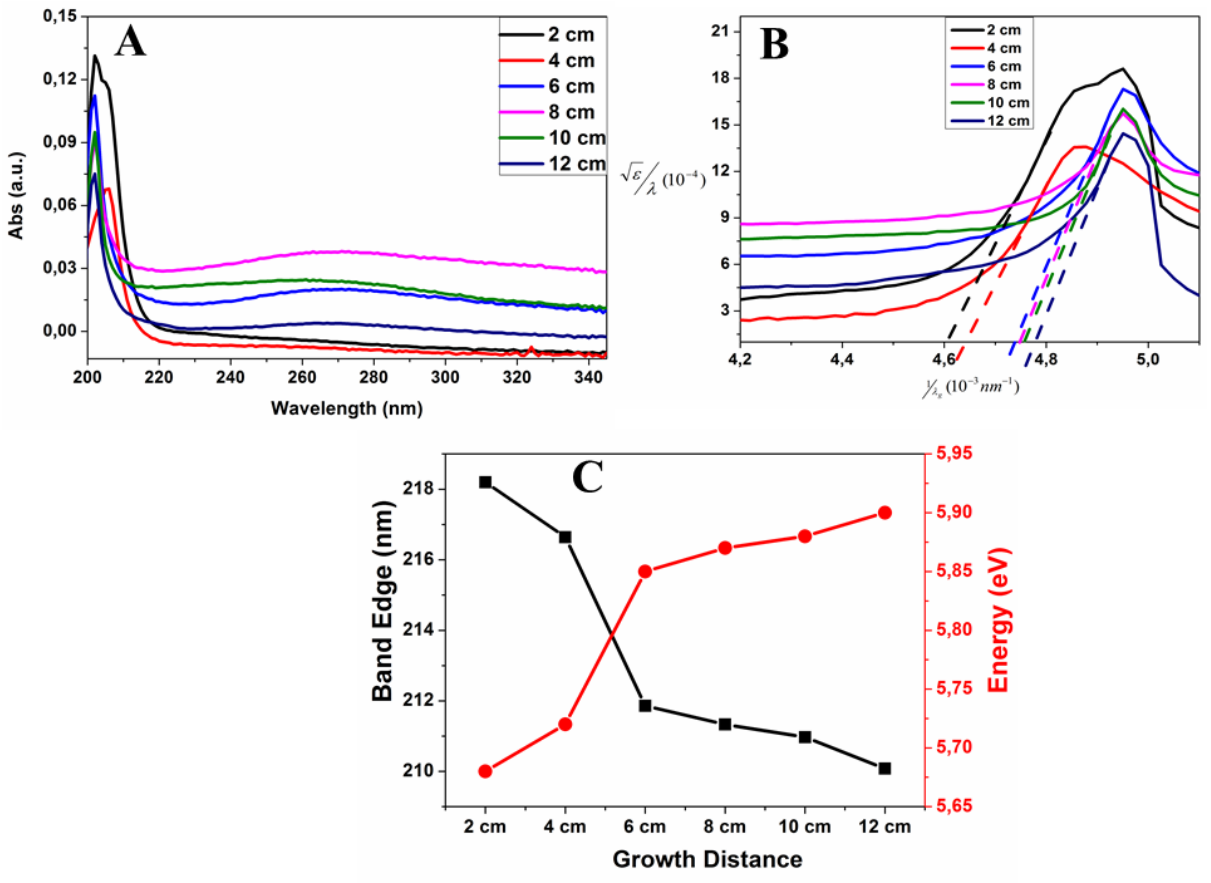

Figure S10.9: (a) UV-vis spectra, (b) Tauc's plot, and (c) Band gap energy profile of the *h*-BN QDs/NDs-BCN hybrid films grown at different separation distances.

The optical band gap energies of the films were determined using the following Tauc's equation[63]:

$$\omega^2 \varepsilon = (h\omega - E_g)^2 ,$$

where;

1) ε is the optical absorbance,
2) $\omega = 2\pi/\lambda$ is the angular frequency of incident radiation
3) E_g is the band gap energy
4) λ is the wavelength

Table S10.1: XPS survey spectra analysis of *h*-BN QDs/NDs embedded in BCN films.

Elements / Samples	C (at %)	B (at %)	N (at %)	O (at %)	N/C	B/N	B/C
2 cm	41.9	18.4	14.4	25.3	0.342	1.28	0.439
4cm	42.8	19.2	15.1	23.0	0.352	1.27	0.447
6 cm	45.6	16.7	13.0	24.7	0.286	1.28	0.366
8 cm	39.4	19.4	15.6	25.7	0.395	1.24	0.492
10 cm	47.8	14.1	13.3	24.8	0.278	1.06	0.295
12 cm	52.4	7.75	6.31	33.6	0.121	1.23	0.148

Appendix E: Synthesis and XPS characterization of boron carbon oxynitride films with tunable composition using methane, boric acid and ammonia

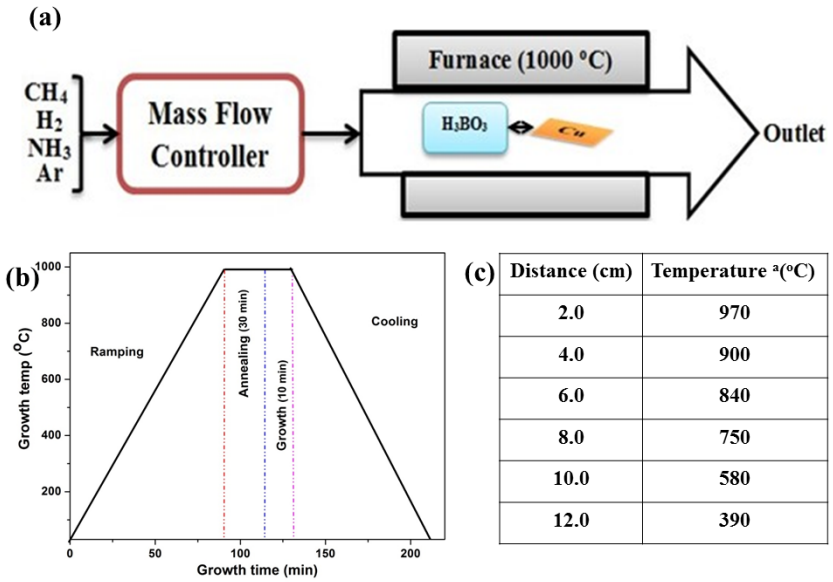

Distance (cm)	Temperature [a](°C)
2.0	970
4.0	900
6.0	840
8.0	750
10.0	580
12.0	390

Figure S11.1: (a) CVD setup, (b) growth profile and (c) temperature profile for the growth of the BCNO films.

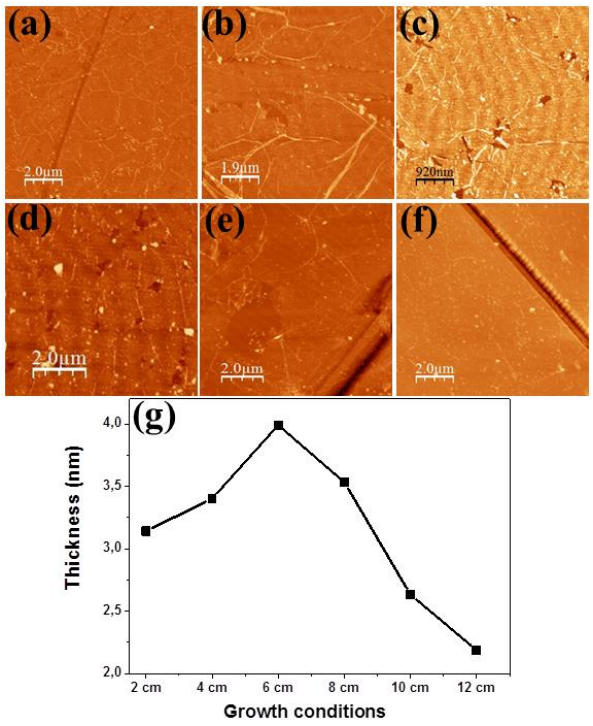

Figure S11.2: AFM topographic images (a – f) and estimated thickness plot (g) of BCNO films grown at 2 cm – 12 cm, respectively.

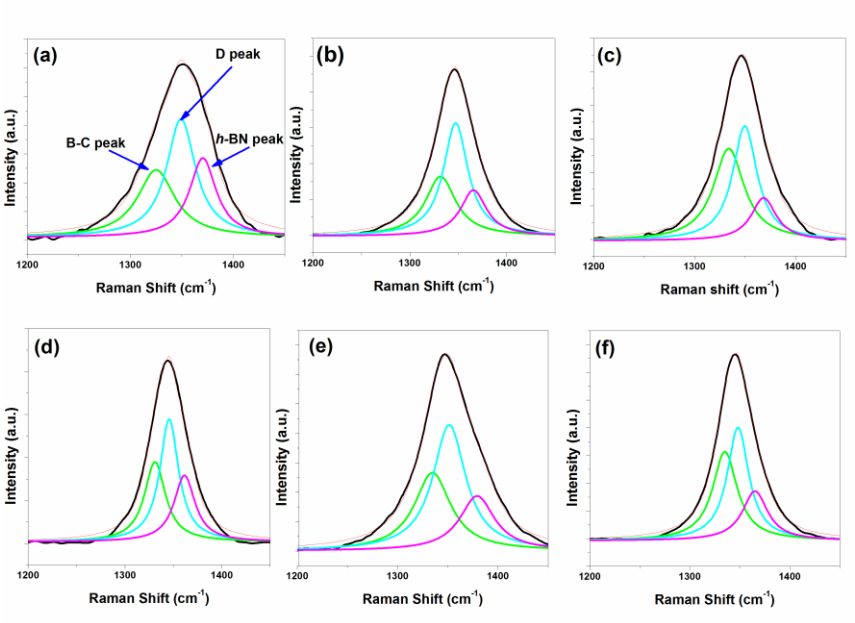

Figure S11.3: Deconvolution of defect induced D-bands for BCNO films grown at 2 cm -12 cm (a - f) showing the B-C, D, and the *h*-BN peaks, respectively.

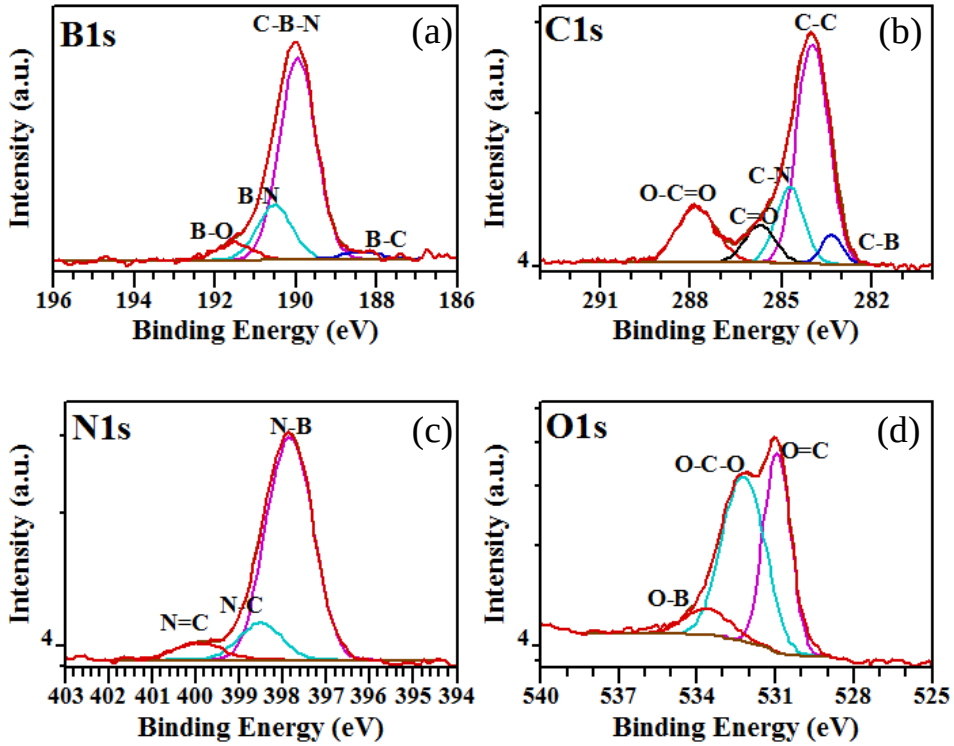

Figure S11.4: XPS spectra showing deconvoluted curves of (a) B1s, (b) C1s, (c) N1s, and O1s (d) of BN-doped graphene-BCN hybrid films grown at 4 cm using 100 mg H_3BO_3 and 20 sccm CH_4.

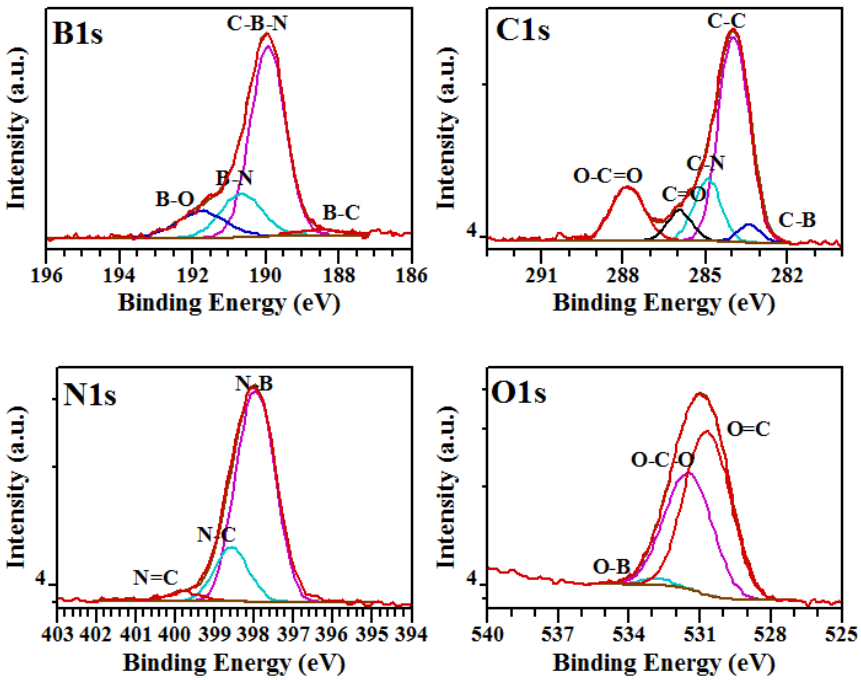

Figure S11.5: XPS spectra showing deconvoluted curves of (a) B1s, (b) C1s, (c) N1s, and O1s (d) of BN-doped graphene-BCN hybrid films grown at 6 cm using 100 mg H_3BO_3 and 20 sccm CH_4.

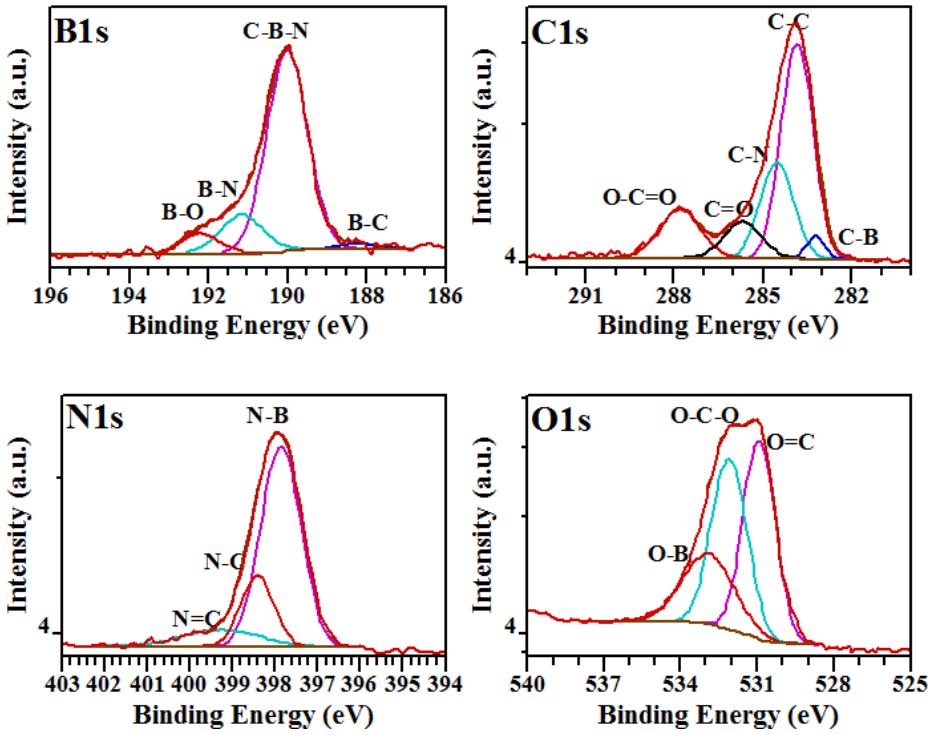

Figure S11.6: XPS spectra showing deconvoluted curves of (a) B1s, (b) C1s, (c) N1s, and O1s (d) of BN-doped graphene-BCN hybrid films grown at 8 cm using 100 mg H_3BO_3 and 20 sccm CH_4.

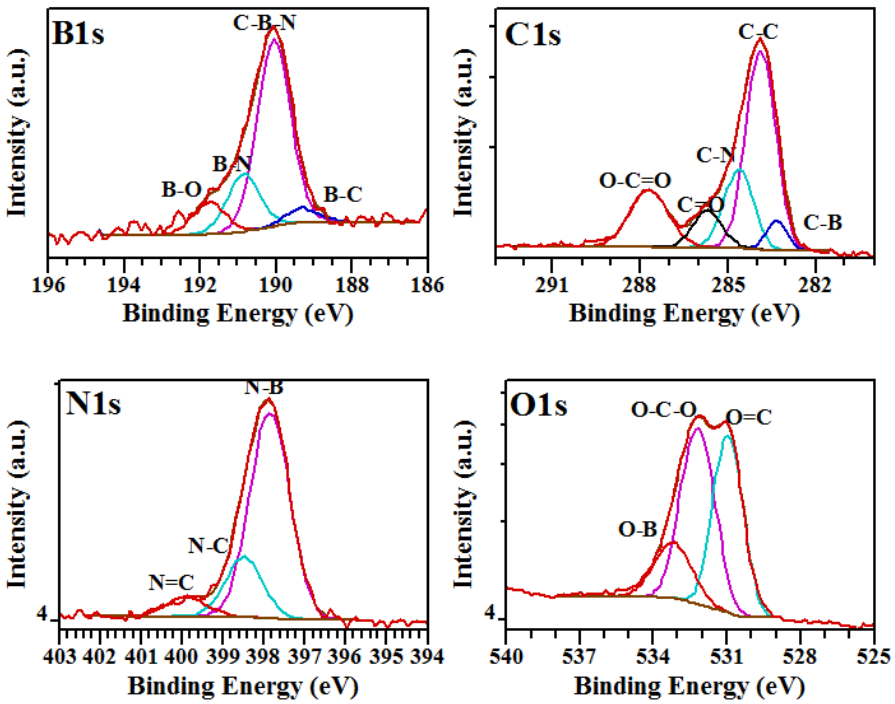

Figure S11.7: XPS spectra showing deconvoluted curves of (a) B1s, (b) C1s, (c) N1s, and O1s (d) of BN-doped graphene-BCN hybrid films grown at 10 cm using 100 mg H_3BO_3 and 20 sccm CH_4.

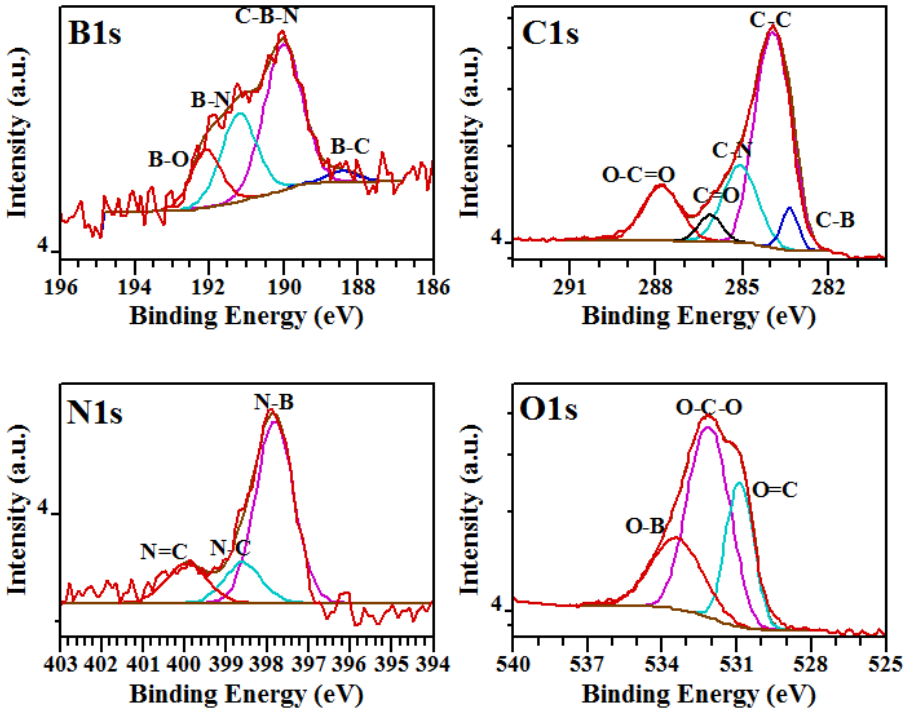

Figure S11.8: XPS spectra showing deconvoluted curves of (a) B1s, (b) C1s, (c) N1s, and O1s (d) of BN-doped graphene-BCN hybrid films grown at 12 cm using 100 mg H_3BO_3 and 20 sccm CH_4.

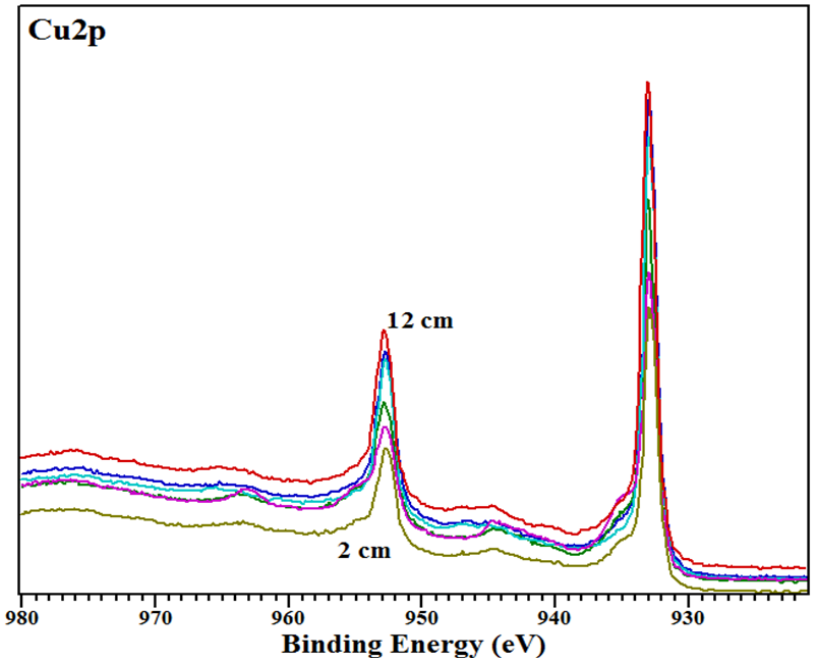

Figure S11.9: XPS spectra showing Cu2p of BCNO films grown at 2cm to 12 cm.

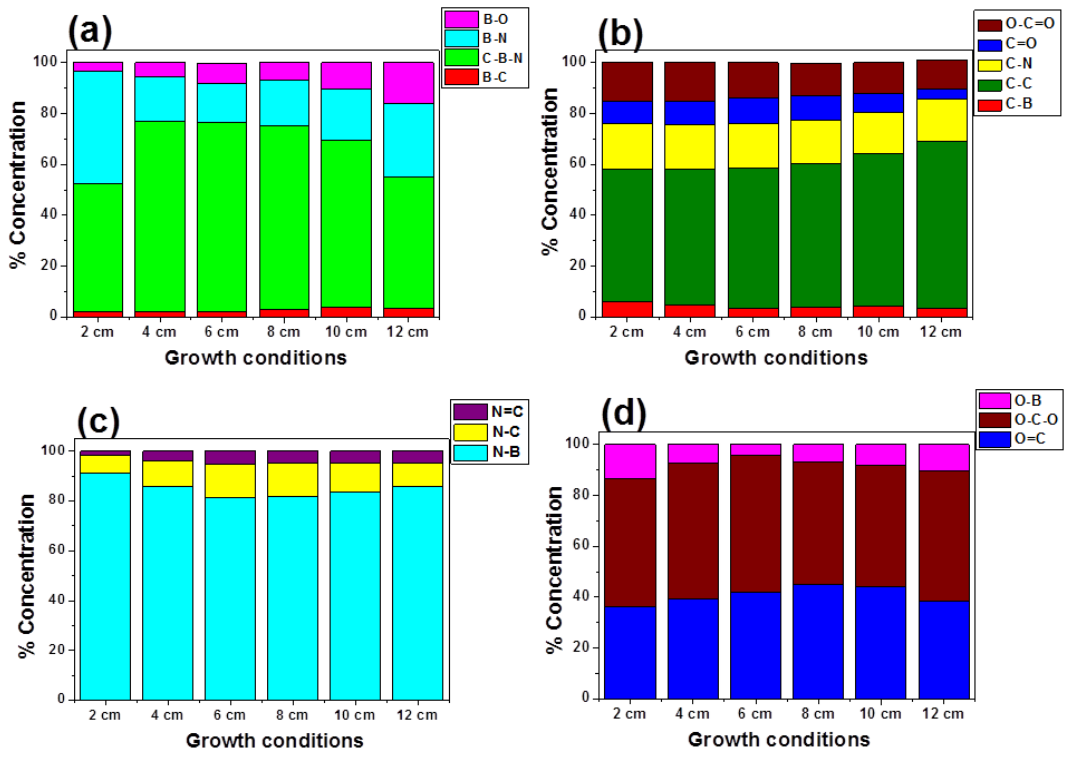

Figure S11.10: Evolution of bond concentration with increasing growth distance from the hot zone: a-d representing % concentrations of B, C, N and O atoms in (a) B1s, (b) C1s, (c) N1s and (d) O1s, respectively.

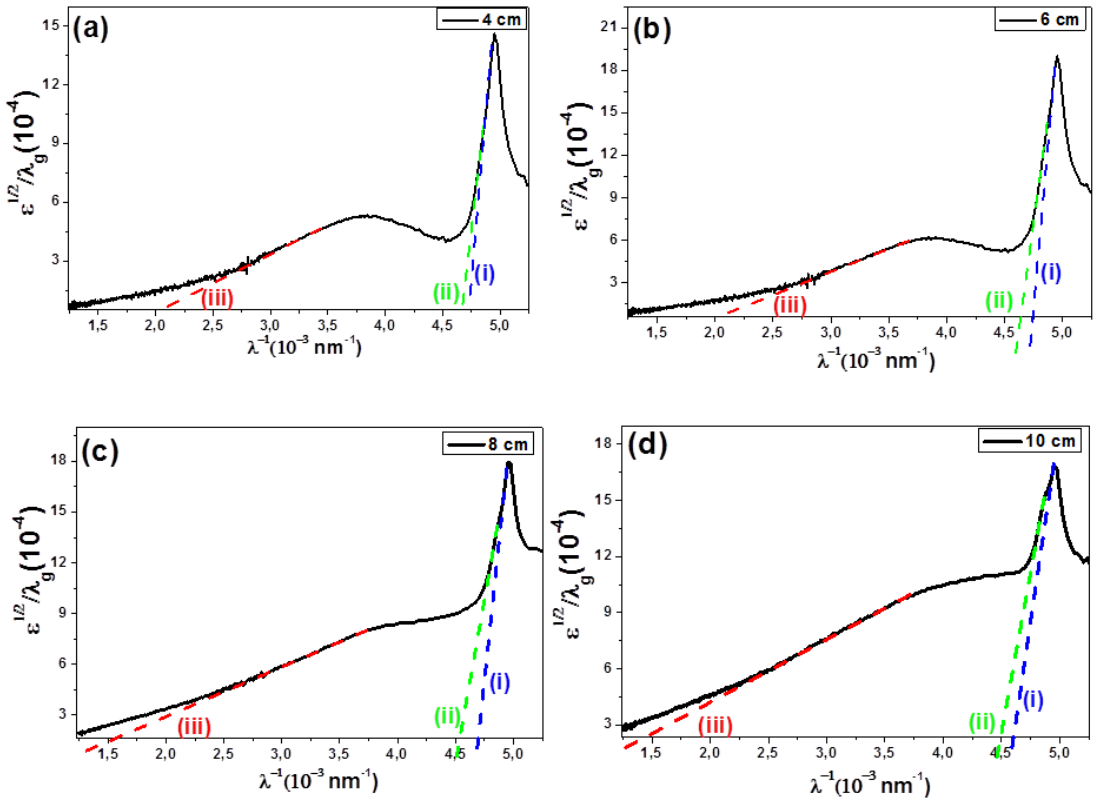

Figure S11.11: Tauc's plots of BCNO films grown at (a) 4 cm, (b) 6 cm, (c) 8 cm, and (d) 10 cm growth distances from the hot zone.

Table S11.1: Elemental ratio of all constituent atoms in the BCNO films

Growth distance	Elemental ratio (at. %)				
	B/N	B/C	N/C	B/O	O/C
2 cm	1,79	0,281	0,164	0,298	0,663
4 cm	1,01	0,408	0,0102	0,699	0,563
6 cm	1,40	0,695	0,495	1,083	0,642
8 cm	1,28	0,336	0,262	0,727	0,462
10 cm	1,12	0,138	0,124	0,288	0,498
12 cm	1,41	0,032	0,0225	0,0826	0,373